Advances in Electrochemical Science and Engineering

Volume 3

VCH

Advances in Electrochemical Science and Engineering

Volume 1

G. P. Evans, The Electrochemistry of Conducting Polymers
R. Kötz, Photoelectron Spectroscopy of Practical Electrode Materials
T. Iwasita-Vielstich, Progress in the Study of Methanol Oxidation by *In Situ,*
Ex Situ and On-Line Methods
Der-Tau Chin, Theory and Experimental Aspects of the Rotating Hemispherical
Electrode
J. Winnick, Electrochemical Separation of Gases
V. Brusic et al., Electrochemical Aspects of Thin-Film Storage Media

Volume 2

S. Trasatti, Electrocatalysis of Hydrogen Evolution: Progress in Cathode Activation
A. Hammou, Solid Oxide Fuel Cells
G. L. Richmond, Second Harmonic Generation as an In-situ Probe of Single Crystal
Electrode Surfaces
C. Deslouis, B. Tribollet, Flow Modulation Techniques in Electrochemistry

Advances in Electrochemical Science and Engineering

Volume 3

Edited by Heinz Gerischer
and Charles W. Tobias

Contributions from

W. P. Gomes, H. H. Goossens, Gent
Y. Okinaka, T. Osaka, New Jersey, Tokyo
J. O. Dukovic, Yorktown Heights
H. Lehmkuhl, K. Mehler, U. Landau,
Mülheim, Berlin
P. C. Andricacos, L.T. Romankiw,
Yorktown Heights

VCH

Editors:

Prof. Dr. Heinz Gerischer Fritz-Haber-Institut der MPG Faradayweg 4–6 D-14195 Berlin	Prof. Charles W. Tobias Dept. of Chemical Engineering University of California Berkeley, California 94720, USA

Published jointly by
VCH Verlagsgesellschaft mbH, Weinheim (Federal Republic of Germany)
VCH Publishers Inc., New York, NY (USA)

Editorial Director: Dr. Thomas Mager
Production Manager: Claudia Grössl

Library of Congress Card No. applied for

British Library Cataloguing-in-Publication Data
Advances in electrochemical science and engineering: Vol 3. –
(Advances in electrochemical science and engineering)
I. Gerischer, H. II. Tobias, C. W. III. Series
541.3
ISBN 3-527-29002-8

Deutsche Bibliothek Cataloguing-in-Publication Data
Advances in electrochemical science and engineering :
Weinheim ; Basel (Switzerland) ; Cambridge ; New York, NY : VCH
ISSN 0938-5193
Erscheint unregelmäßig. – Aufnahme nach Vol. 1 (1990)
Vol. 1. (1990) –

Printed on acid-free and low-chlorine paper

Composition: Filmsatz Unger & Sommer, D-69469 Weinheim. Printing: strauss offsetdruck GmbH, D-69509 Mörlenbach. Bookbinding: J. Schäffer, D-67269 Grünstadt
Printed in the Federal Republic of Germany

Distribution:
VCH, P. O. Box 10 1161, D-69451 Weinheim (Federal Republic of Germany)
Switzerland: VCH, P. O. Box, CH-4020 Basel (Switzerland)
United Kingdom and Ireland: VCH (UK) Ltd., 8 Wellington Court, Cambridge CB1 1HZ (England)
USA and Canada: VCH, 220 East 23rd Street, New York, NY 10010-4606 (USA)
Japan: VCH, Eikow Building, 10-9 Hongo 1-chome, Bunkyo-ku, Tokyo 113 (Japan)

ISBN 3-527-29002-8 (VCH, Weinheim)
ISBN 1-56081-282-8 (VCH, New York)
ISSN 0938-5193

Preface

The five chapters of this volume treat topics of great current significance, demonstrating how essential electrochemistry is for technological progress.

W. P. Gomes and H. H. Goossens analyze the kinetics of the electrochemical reactions used for etching gallium arsenide. The authors describe means by which information about the mechanisms may be obtained. Based on the understanding of the anodic dissolution of n-type and p-type GaAs, both in the dark and under illumination, etching mechanisms for different oxydants with and without current are derived.

H. Lehmkuhl, K. Mehler, and U. Landau provide a summary of the criteria and problems associated with the electrodeposition of aluminum at ambient temperature. Special emphasis is given to the organo-aluminum electrolyte developed in the laboratory of Karl Ziegler, winner of the Nobel prize in 1963. Although difficult to handle, these electrolytes offer some unique advantages for the deposition of aluminum.

Effects that cause non-uniformity in patterned electrodeposition of microscopic features are the subject of J. O. Dukovic's chapter. Mathematical models are used to identify process conditions which lead to flat profiled features of uniform height needed in electronic components. The emergence of computer-aided-design tools for electrochemical microfabrication is discussed.

Y. Okinaka and T. Osaka describe the fundamental aspects and technological applications of autocatalytic metal deposition processes. In view of that electroless deposition has found important applications in the manufacture of microelectronic devices, a review of the pertaning electrochemical fundamentals has been long overdue.

Following a concise review of direct access storage devices, a treatise on the properties and electrochemistry of magnetically soft materials is provided by P. C. Andricacos and L. T. Romankiw. The chapter is focused on the fundamentals of the magnetics and electrochemistry of Permalloy, a material which has similar importance in magnetic storage as has silicon in semiconductor devices.

Heinz Gerischer
Charles W. Tobias

Contents

List of Contributors

Panayotis C. Andricacos
IBM Research Division
Thomas J. Watson Research Center
Yorktown Heights, New York, 10598
USA

John O. Dukovic
IBM Research Division
Thomas J. Watson Research Center
Yorktown Heights, New York, 10598
USA

Walter P. Gomes
Laboratorium voor Fysische Scheikunde
Universiteit Gent
9000 Gent, Belgium

Hans H. Goossens
Laboratorium voor Fysische Scheikunde
Universiteit Gent
9000 Gent, Belgium

Uwe Landau
MIB-Metallurgie und Oberflächentechnik und Innovationen in Berlin GmbH & Co
Motzener Str. 5
12277 Berlin
Germany

Herbert Lehmkuhl
Max-Planck-Institut für Kohlenforschung
Kaiser-Wilhelm-Platz 1
45470 Mülheim a.d. Ruhr
Germany

Klaus Mehler
Max-Planck-Institut für Kohlenforschung
Kaiser-Wilhelm-Platz 1
45470 Mülheim a.d. Ruhr
Germany

Yutaka Okinaka
AT&T Bell Laboratories
Murray Hill
New Jersey
USA

Tetsuya Osaka
Department of Applied Chemistry
School of Science and Engineering
Kagami Memorial Laboratory for Materials Science and Technology
Waseda University
Tokyo
Japan

Lubomyr T. Romankiw
IBM Research Division
Thomas J. Watson Research Center
Yorktown Heights, New York, 10598
USA

Advances in Electrochemical Science and Engineering
Edited by Heinz Gerischer and Charles W. Tobias

Electrochemistry of III–V Compound Semiconductors: Dissolution Kinetics and Etching

Walter P. Gomes and Hans H. Goossens*

Laboratorium voor Fysische Chemie, Universiteit Gent, Krijgslaan 281,
B-9000 Gent, Belgium

* Research Assistant of the N.F.W.O. (National Fund for Scientific Research, Belgium)

Contents

List of Symbols and Abbreviations

c_i	concentration of species i in solution
C_H	Helmholtz layer capacitance
C_{sc}	depletion layer capacitance
C_{ss}	surface state capacitance
e	absolute value of the elementary charge
E^o	standard redox potential
E_g	semiconductor band gap
E_v^s	valence band edge at the surface
φ_H	potential drop over the Helmholtz layer
φ_{sc}	potential drop over the depletion layer
$h\nu$	photon energy
i	current density
i_a	anodic current density
i_c	cathodic current density
I_{redox}	partial current associated with oxidation of reducing agent
I_{tot}	total anodic photocurrent
k	rate constant
k_B	Boltzmann constant
K_c	equilibrium constant
n	number of hole capture steps
	electrochemical equivalence of anodic decomposition reaction of the semiconductor
ν_{th}	mean thermal velocity of holes
p_b	bulk concentration of holes
p_s	surface concentration of holes
r	etch rate
RRDE	rotating ring-disk electrode
s	stabilization ratio
t	time
T	absolute temperature
TMPD	tetramethyl-p-phenylenediamine
u	flow rate
V	electrode potential
V_{fb}	flat-band potential
V_r	rest potential
w	rotation velocity of the electrode
x_i	concentration of surface decomposition intermediate X_i
X_i	i-th surface decomposition intermediate (i = oxidation state)
Y	concentration of reducing agent Y
Y	reducing agent in solution
Z	oxidizing agent in solution

1 Introduction

The pioneering work by Brattain and Garrett [1] in the 1950s on the germanium electrode revealed that a semiconductor/electrolyte interface does not necessarily constitute a blocking contact but allows the transfer of charges under certain conditions of polarization and of illumination. This observation formed the starting point for the systematic study of these charge transfer processes. Soon thereafter, the theoretical basis for the understanding of the electrode behavior of semiconductors was established [2]. Since then, semiconductor (photo)electrochemistry has gradually developed into an important area in electrochemical science, the principles of which are presently familiar to a large part of the electrochemical community. Therefore, we will refrain from introducing these basic principles in the present chapter, and we will refer to several excellent literature sources for this purpose [3–5].

The interest in semiconductor (photo)electrochemistry was significantly stimulated in the 1970s by the search for alternative energy sources, and more specifically for photoelectrochemical solar energy converting systems. In 1972, Fujishima and Honda [6] proposed an electrochemical solar cell for the photoelectrolysis of H_2O, in which H_2O was oxidized to O_2 at an illuminated n-TiO_2 electrode and reduced to H_2 at a dark metal counterelectrode, the electrodes being short-circuited. Subsequently, Gerischer [7] proposed an alternative type of solar cell based upon semiconductor electrodes, called a regenerative cell, in which a dissolved reducing agent was photoanodically oxidized at an n-type semiconductor electrode, while the corresponding oxidizing agent was reduced again at a dark counterelectrode. In contrast to the Fujishima–Honda cell, here the electrodes were connected through a consumer, the purpose being to convert solar energy not to chemical free enthalpy, but to electrical energy. The idea seemed attractive, since less stringent conditions were imposed as far as the band-gap width and the band-edge position are concerned, so that semiconductor photoanodes with a less wide band gap, such as III–V compound semiconductors, could be used and the active part of the solar spectrum hence extended toward the visible and the infrared region. It soon appeared that one of the main problems with cells of the latter type was the stability of illuminated n-type semiconductors, such as the III–V compounds GaAs, GaP, and InP, as well as the II–VI compounds CdS and CdSe, with respect to photocorrosion. In other words, the fact that besides the photoanodic oxidation of the reducing agent in the solution also the oxidation of the semiconductor itself contributes to the current leads to deterioration of the cell. Investigations of the symmetrical type of cells, involving photocathodic reduction at an illuminated p-type semiconductor, revealed that here a different problem arises, i. e. the relatively high surface electron-hole recombination rate, resulting in a considerable loss in solar energy conversion efficiency. Therefore, most of the work on regenerative photoelectrochemical solar cells has concentrated on n-type semiconductor photoanodes. The detailed discussion of potentially useful photoelectrochemical cells evidently exceeds the scope of this chapter (for a review, see, e. g., ref. [8]). In the present context, however, it is important to realize that much effort has been spent on studying the competition between the photoanodic dissolution of the n-type semiconductor and the photoanodic oxidation of the reducing agent in the regenerative cell. Although the ultimate goal of investigations of this type was a practical one, i.e. to suppress the photoanodic dissolution of the semiconductor, these studies have greatly contributed to a more fundamental objective, i.e., to deepen the insight into the mechanisms of these reactions, especially of the anodic dissolution of III-V semiconductors. This point is treated in more detail in Sec. 2.

Whereas on the one hand the oxidative dissolution of III-V semiconductors constitutes one of the major problems in the application of these materials in photoelectrochemical solar cells, the electronics industry on the other hand utilizes these dissolution reactions in various ways. Etching (controlled dissolution) of semiconductors has indeed become an essential process in microelectronic device technology [9, 10]. Etching procedures are furthermore used to reveal different kinds of crystal defects, such as dislocations, impurity striations, and microprecipitates; in this way they constitute an important factor of quality control. Another application of etching is related to the fact that the surface morphology after etching often depends on the crystal orientation; this property is currently applied by crystallographers to identify crystal faces. Finally, etching procedures are very often used to remove different kinds of surface layers (e.g. oxide layers or damaged layers), which may result from pretreatment of the sample [11].

Besides "wet" etching, "dry" etching procedures are also utilized in practical applications. In the latter case, the active species are either charged or neutral gaseous particles, and the etching process is chemical and/or physical (ion bombardment) in character [12]. In the case of wet etching, on the other hand, the removal of material originates from an electrochemical and/or a chemical reaction at the semiconductor/electrolyte interface. It is evident that the present contribution only pertains to wet etching processes, since dry etching processes belong to the field of plasma chemistry and physics.

Sec. 3 of this chapter discusses the kinetics, the mechanisms, and the surface morphology of wet etching processes at III-V semiconductors. It is important to distinguish between wet etching with or without external current flow [13]. In the former case, etching amounts to anodic dissolution. Since this subject is treated in Sec. 2 as far as the kinetics and mechanisms are concerned, the discussion in Sec. 3 of this type of etching is restricted to the etching morphology. One of the main objectives of this chapter is to show that in the study of etching processes involving no net current flow, (photo)electrochemical methods also constitute a very powerful approach, not only to unravel the reaction mechanisms, but also to get more fundamental insight into the factors determining the surface morphology. Therefore, the discussion of anodic dissolution reactions precedes that of open-circuit etching processes.

2 Anodic Dissolution of III-V Compound Semiconductors

2.1 General

This discussion concerns the III-V semiconductors GaAs, GaP and InP with room-temperature band-gaps E_g of 1.43, 2.25, and 1.35 eV, respectively. The crystal structure of all three is of the zincblende type. The samples used in electrochemical and etching experiments are mostly single crystal slabs, cut perpendicularly either to the [100] axis, which is a tetragonal inversion axis, or to the [111] axis, which has trigonal symmetry. It is important to note that the [111] axis is polar, so that the (111) and $(\bar{1}\bar{1}\bar{1})$ faces, consisting of group III and group V atoms, respectively, may show different properties. Most of the work which is discussed in this context pertains to aqueous media at either low or high pH; since our main interest is in oxidative dissolution and etching, less attention is paid to the intermediate pH range. This is in view of the low solubility of certain oxidation products, such as $Ga(OH)_3$ [14] or In_2O_3, [15], in this pH range.

In order to simplify this discussion, Fig. 1 schematically represents the main features of the current density i vs. potential V behavior of n- and p-type III-V electrodes in indifferent electrolyte solutions at (a) low and (b) high pH, in the dark and under illumination ($h\nu > E_g$). This generalized representation is primarily based on experimental results reported for GaAs and GaP; for InP, less detailed data are available. Examples of actual experimental i-V curves are found in this text, as well as in the papers cited.

The dark i-V curves for n-type electrodes show the usual diode characteristics (Fig. 1(n) (a) and (b)). The forward current is predominantly associated with cathodic reduction of the solvent (H^+ or H_2O) by conduction band electrons, and for InP [16], but under certain circumstances also for GaP [17] and GaAs [18], to a small extent also with cathodic decomposition of the semiconductor. The anodic dark current density is low, i.e. typically on the order of 1 $\mu A \cdot cm^{-2}$. The anodic photocurrent in aqueous indifferent electrolytes is associated with the electrochemical dissolution of the semiconductor. Hence it follows that at least the first step of this multi-equivalent oxidation reaction requires a valence band hole. At not too high light intensities, the i-V curve under illumination first rises (region I) and eventually reaches a saturation region (region III), in which the photocurrent density is proportional to the light intensity. At high light intensities, however, some special features appear. In an acidic medium, a typical passivation behavior may be observed at sufficiently high potentials, indicating the formation of a product layer on the electrode surface (Fig. 1(n) (a), region II; see, e.g. refs. [19] and [20], respectively, for actual curves measured for GaAs and GaP). In an alkaline medium, a saturation regime is reached at high V (Fig. 1(n) (b), region II), in which the photocurrent is independent of the light intensity, but proportional to the OH^- concentration and to the square root of w, the rotation velocity of the electrode. Such behavior has been observed with GaAs [21, 22] as well as with GaP [23, 24] elec-

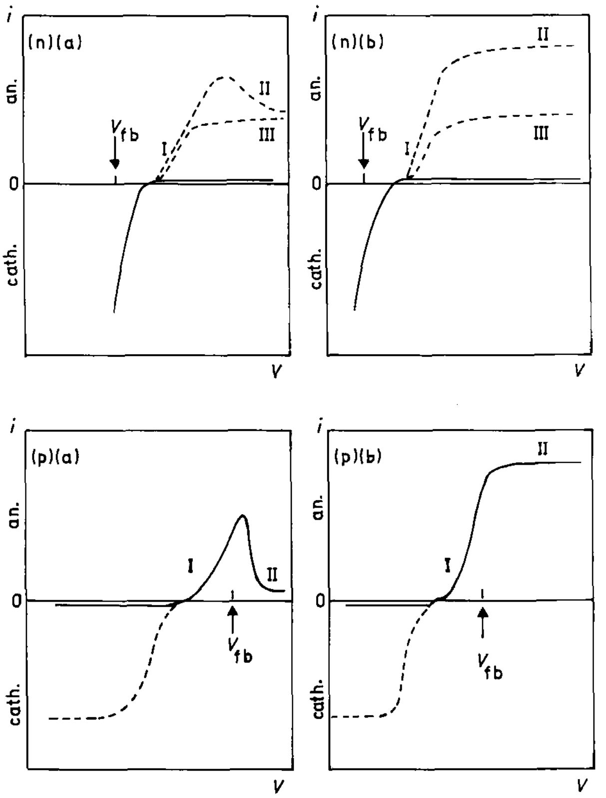

Fig. 1. Schematic representation of i–V curves at III–V semiconductor electrodes in indifferent aqueous media. ——— dark, ----- under illumination.
(n) (a): n-type, low pH (n) (b): n-type, high pH
(p) (a): p-type, low pH (p) (b): p-type, high pH

trodes. It is clear that under these circumstances, the anodic dissolution reaction is diffusion-controlled by OH^- and that this ion must be involved in the reaction.

At p-type electrodes (Fig. 1 (p) (a) and (b)), the cathodic dark current density is low (on the order of 1 $\mu A \cdot cm^{-2}$), indicating that hole-injection processes are negligible. The cathodic photocurrent is associated with the same reactions as those mentioned above for dark n-type cathodes. The dark anodic branch of the curve shows an exponentially increasing region (I), passing at higher potentials into a passivation region in acidic medium (Fig. 1 (p) (a), region II) and into a saturation region in alkaline medium (Fig. 1 (p) (b), region II); in the latter case, the current density is again controlled by OH^- diffusion (see, e. g., ref. [24]).

It is interesting to consider in some detail the exponential region I in the p-type case. An important remark is that this region is situated negatively with respect to flat-band potential V_{fb}, which implies that holes are being captured from a depletion layer. Assuming that the holes are at quasi-equilibrium in this layer, their concentration p_s at the surface is expected to be related to the bulk concentration p_b by the relationship:

$$p_s = p_b \exp(-e\varphi_{sc}/k_B T), \tag{1}$$

e being the absolute value of the elementary charge and k_B the Boltzmann constant. The potential drop over the depletion layer φ_{sc} is in the simplest case given by:

$$\varphi_{sc} = -(V - V_{fb}) \tag{2}$$

Assuming further that the anodic current density is proportional to p_s, i.e., that the following relation holds:

$$i = ekp_s \tag{3}$$

with k a rate constant, then the combination of Eqs. (1) to (3) leads to the expectation that the Tafel slope $dV/d\log i$ is $2.3\ k_B T/e \simeq 0.06$ V. This prediction is particularly well fulfilled for p-GaAs in acidic medium over a considerable current density range, as shown in Fig. 2 (reprinted from ref. [25]), which proves the validity of the simple Schottky-barrier model in this case. Note that the combined Eqs. (1) to (3) also explain the observed shift in the position of the anodic i-V curves towards lower potentials with increasing pH, which is attributable to the corresponding shift in V_{fb} as a function of the pH reported for III-V semiconductors, see, e.g., ref. [26].

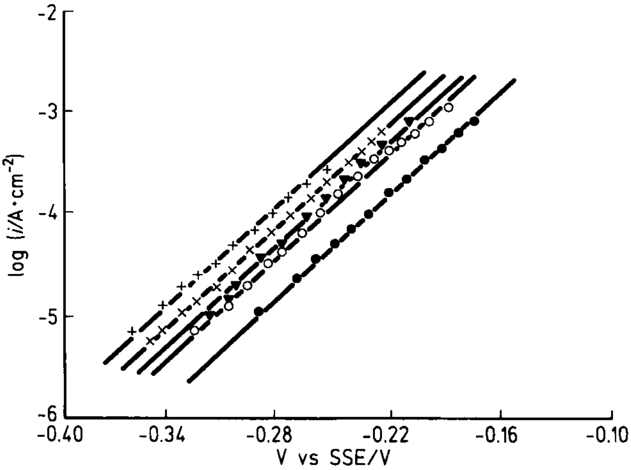

Fig. 2. Plot of log i vs. V. p-GaAs electrode, $(\bar{1}\bar{1}\bar{1})$-face, dark.
Electrolyte composition: 0.25 mol · l^{-1} $LiClO_4 + HClO_4$ in H_2O. ● pH = 0.9; ○ pH = 1.9; x pH = 2.5; ▲ 0.09 mol · l^{-1} TMPD added, pH = 2.5; + pH = 3.0.
(From ref. (25), by permission of VCH).

The multi-equivalent anodic oxidation of the semiconductor involves several consecutive electrochemical steps, the first of which can be symbolized as

$$X_0 + h^+ \xrightarrow{k_1} X_1 \tag{4}$$

where X_0 represents a normal surface bond and X_1 is a surface bond in which one electron is lacking, i.e., an electron-deficient surface intermediate. (For simplicity, the positive charge of X_1 has been omitted in the notation. The nature of X_1 is discussed in some more detail below). If the electrochemical steps mentioned are n consecutive irreversible hole-capture steps, the concentrations of the surface decomposition intermediates of subsequently higher oxidation states X_1, X_2 ... will, under steady-state conditions, adjust so that the rates of all steps are equal, and the constant k from Eq. (3) can be written as

$$k = nk_1 \tag{5}$$

in which k_1 includes the (quasi-constant) concentration of X_0 (see Eq. (4)). In the case of p-GaAs in an acidic medium, on the other hand, there are strong indications that reaction Eq. (4) constitutes the only step in which holes are consumed (see below). In the latter case, the constant k in Eq. (3) can be identified with the rate constant k_1. For p-GaAs, the numerical value of the constant k, hence of k_1, has been obtained from the i-V measurements shown in Fig. 2 and from impedance data on V_{fb} (see Eqs. (1) to (3)), and has been found to be of the order of 10 cm · s^{-1} [25]. From statistical physics, it is known that the number of holes hitting the surface per cm^2 and per second is $v_{th} \cdot p_s/\sqrt{6\pi}$, with the mean thermal velocity of holes $v_{th} \simeq 10^7$ cm · s^{-1}. According to Eq. (3) with $k = k_1$, only $k_1 p_s$ holes are captured to react at the surface which cm^2 and per second. Hence the ratio $k_1/v_{th} \cdot (6\pi)^{-1/2}$ represents the fraction of holes hitting the surface which will be captured. Inserting the values mentioned above, this fraction turns out to be ca. 10^{-5}. This result justifies the assumption of a free-hole "cloud" at quasi-equilibrium throughout the space-charge layer being present during anodic dissolution of p-type electrodes, hence the use of Eq. (1) under these circumstances.

In most cases, such as that of p-GaAs in alkaline medium [27] and that of p-GaP [20, 23, 28–31], the anodic Tafel slopes have been found to be higher than 0.06 V, i.e., typically between 0.09 and 0.15 V. Differences in the Tafel slopes depending on the crystal face have been reported; e.g., for p-GaP in an alkaline medium, values of 0.09–0.10 V have been measured at the $(\bar{1}\bar{1}\bar{1})$ face, of 0.10–0.11 V at the (100) face, and of 0.14–0.15 V at the (111) face [20]. Tafel slopes above 0.06 V have often been attributed to non-constancy of the Helmholtz potential drop φ_H and hence to the invalidity of Eq (2), originating from the filling or emptying of surface states. However, the relative changes of the depletion and Helmholtz layer potential drops can be easily shown to obey to the following expression:

$$d\varphi_H/d\varphi_{sc} = (C_{sc} + C_{ss})/C_H \tag{6}$$

in which C_{sc}, C_{ss}, and C_H represent the depletion layer, surface state and Helmholtz capacitance, respectively, so that [30]

$$\frac{d\varphi_{sc}}{dV} = -\frac{d\varphi_{sc}}{d\varphi_{sc} + d\varphi_H} = -\frac{1}{1 + (C_{sc} + C_{ss})/C_H} \tag{7}$$

From Eqns. (3), (1) and (7) it then follows:

$$\frac{dV}{d\log i} = \frac{2.3 k_B T}{e}\left[1 + \frac{C_{sc} + C_{ss}}{C_H}\right] \tag{8}$$

so that a linear $\log i$ vs. V plot with a Tafel slope above $2.3\ k_BT/e$ would imply the ratio $(C_{sc} + C_{ss})/C_H$ to be non-negligible with respect to 1 and to be constant when V varies. Since for a depletion layer $C_{sc} \ll C_H$, this means that C_{ss} should be non-negligible with respect to C_H and hence also that $C_{ss} \gg C_{sc}$, and that C_{ss} should be potential-independent within the range in which the Tafel slope is valid. The latter condition is unlikely to hold, and even if it was fulfilled, it would be hard to explain why Tafel slopes in semiconductor electrochemistry are very often between 0.09 and 0.15 V, implying that in all of these cases, C_{ss} happened to be between (1/2) C_H and (3/2) C_H. Hence, we can only state that to our knowledge, no satisfactory theory is at present available to account for Tafel slopes in semiconductor electrochemistry which are markedly above 0.06 V and constant over several orders of magnitude in current density.

The electrochemical equivalence n of the anodic dissolution reaction, i.e., the number of moles of elementary charges flowing through the external circuit per mole of semiconductor dissolved, has been determined by several authors. In the case of GaAs, n has been found to equal 6 [27,32]. The first report on GaP in this respect mentions $n = 6$ in acidic medium and $n = 3$ in alkaline medium [23]; in later papers, the equivalence was found to be 6, in acidic as well as in alkaline media [24, 28, 29]. In the case of InP, n was reported to be equal to 6 in acidic medium [33, 35]; in alkali, one source mentions n to be between 6 and 8 [36], whereas more recent results show that n is about 6 [35]. The general conclusion appears to be that n equals 6 for all three semiconductors considered, so that the elements involved go into solution in the +3 oxidation state. As far as phosphorus is concerned, this is somewhat surprising in view of the low standard redox potential of the H_3PO_4/H_3PO_3 couple ($E^o = -0.276$ V). Based on the fact that during anodic oxidation of GaP, PO_4^{3-}, and PH_3 have been detected in solution [23, 28], it has been suggested that the H_3PO_3 or HPO_3^{2-} formed anodically reacts further in solution through chemical disproportionation to H_3PO_4 and PH_3.

The i-V behavior demonstrates that holes are involved in the anodic dissolution reactions; the question arises, however, whether charge transfer occurs exclusively over the valence band. A straightforward way to investigate this problem is by comparing the number of photons absorbed in an n-type photoanode to the number of electrons flowing through the external circuit. This procedure has been used by Kohl et al. [33], and its results indicate a non-negligible contribution of the conduction band in the oxidation of (100) and $(\bar{1}\bar{1}\bar{1})$ InP. This conclusion has been recently confirmed by other investigators using the same method [35]. An alternative and elegant procedure to study the participation of conduction band electrons to anodic dissolution, which has originally been used on Ge [37], is based on hole injection by oxidizing agents into n-type electrodes in the dark. Under anodic bias, the injected holes are consumed in the oxidation of the semiconductor. If the latter reaction involves the valence band solely, the anodic blocking current will remain unchanged by adding the hole-injecting reactant. Any participation of conduction band electrons to the dissolution reaction will show up as an increase in the dark anodic limiting current. By this method it has been demonstrated that the conduction band contributes to a minor fraction (on the order of some ‰ to some %) to the anodic dissolution current of GaAs [38–40] and of GaP [23, 29, 39–41], whereas in the case of InP, this fraction appears to be considerably larger [42, 43]. The difference in surface state position and of the chemistry involved has been discussed recently [44]. It should be remarked that the conduction band contribution may depend on various factors, and that the quantitative study of these dependencies affords detailed information on the dissolution mechanism, as will be explained further. A third possible method of detecting the participation of conduction band electrons to anodic dissolution is by comparing the limiting anodic photocurrent at n-type electrodes in an indifferent electrolyte to the current in the presence of a reducing agent which is known to be oxidized by holes solely [29, 43]. This reactant thus competes for holes with the semiconductor itself, and the observed current decrease can be related to the decrease in electron injection due to decreased dissolution.

On the basis of the experimental data summarized above, and taking into account the chemistry of the elements involved in strongly acidic and alkaline media [15], the following overall reaction equations can be proposed for the anodic dissolution of the III–V semiconductors under consideration:

at a low pH:

$$\mathrm{GaAs} + 2\,\mathrm{H_2O} + (6-x)\mathrm{h^+} \rightarrow \mathrm{Ga^{3+}} + \mathrm{HAsO_2} + 3\,\mathrm{H^+} + x\mathrm{e^-} \tag{9}$$

$$\mathrm{GaP} + 3\,\mathrm{H_2O} + (6-x)\mathrm{h^+} \rightarrow \mathrm{Ga^{3+}} + \mathrm{H_3PO_3} + 3\,\mathrm{H^+} + x\mathrm{e^-} \tag{10}$$

$$\mathrm{InP} + 3\,\mathrm{H_2O} + (6-x)\mathrm{h^+} \rightarrow \mathrm{In^{3+}} + \mathrm{H_3PO_3} + 3\,\mathrm{H^+} + x\mathrm{e^-} \tag{11}$$

at a high pH:

$$\mathrm{GaAs} + 10\,\mathrm{OH^-} + (6-x)\mathrm{h^+} \rightarrow \mathrm{GaO_3^{3-}} + \mathrm{AsO_2^-} + 5\,\mathrm{H_2O} + x\mathrm{e^-} \tag{12}$$

$$\mathrm{GaP} + 11\,\mathrm{OH^-} + (6-x)\mathrm{h^+} \rightarrow \mathrm{GaO_3^{3-}} + \mathrm{HPO_3^{2-}} + 5\,\mathrm{H_2O} + x\mathrm{e^-} \tag{13}$$

$$\mathrm{InP} + 9\,\mathrm{OH^-} + (6-x)\mathrm{h^+} \rightarrow \mathrm{InO_2^-} + \mathrm{HPO_3^{2-}} + 4\,\mathrm{H_2O} + x\mathrm{e^-} \tag{14}$$

($x \ll 1$ for GaAs and GaP)

Reactions different from those listed above may simultaneously contribute to a minor extent. Thus, the characterization of the GaAs electrode by XPS has demonstrated a significant enrichment in As at the surface after mild anodization [45]. Also by in-situ ellipsometric measurements, combined with ex-situ surface analysis by SEM, Auger spectroscopy and X-ray diffraction, it has recently been shown [46] that a porous arsenic layer develops on the p-GaAs electrode surface in acid medium during anodic current flow. Due to its porosity, this layer does not affect the forward *i-V* characteristics of the electrode. Hence it can be concluded that three-equivalent oxidation of GaAs occurs to a small extent, parallel to the six-equivalent oxidation. In the intermediate pH range, the formation of an anodic oxide film on the electrode surface is often observed; i.e., on GaAs, film formation in a weekly alkaline medium (pH = 11.5) was reported and attributed to slow dissolution of the Ga_2O_3 and As_2O_3 formed anodically under these circumstances [21]. Thicker passivating layers on GaAs have been produced under various conditions (see, e.g., references in ref. [21]). As mentioned above, in view of the scope of this paper, the discussion will be primarily confined to circumstances (either low or high pH) in which layer formation can largely be prevented.

2.2 Competitive Reactivity Studies of Anodic Dissolution Mechanisms

2.2.1 n-Type Electrodes

It is clear from the discussion in the previous section that voltammetric studies at semiconductor electrodes in indifferent electrolyte solutions yield little information about the dissolution mechanisms. As already mentioned in the introduction, it appears that such information can be obtained by studying the competition between the (photo)anodic reaction of interest and the (photo)anodic oxidation of a competing reducing agent added to the solution. An appropriate technique of performing quantitative studies of this competition is the RRDE (rotating ring-disk electrode) technique, in which the total anodic photocurrent I_{tot} is measured at the semiconductor disk electrode, whereas the partial current I_{redox}, which is associated with the oxidation of the dissolved reducing agent (the stabilization reaction), is determined from the current measured at the concentric metallic ring, taking into account the collection efficiency of the RRDE (see, e.g., ref. [47]). The results are expressed as the stabilization ratio *s*, i.e., the fraction of the total photocurrent corresponding to the stabilization reaction: $s = I_{redox}/I_{tot}$. Typical kinetic studies involve investigation of the dependence of *s* on the concentration of the reducing agent y and on the light intensity, hence on the total photocurrent density. In this section (2.2.1), the symbol *i* denotes the total photocurrent density, whereas in all other sections, *i* simply represents the current density.

When performing a study of this type on the system n-GaP/$Fe(CN)_6^{4-}$, the research group to which the present authors belong found that *s* decreases with increasing light intensity, hence photocurrent density [48]. This dependence was subsequently also observed for most other systems involving III-V semiconductor electrodes [49-51] (some exceptions are discussed in ref. [52]). In all of these cases, the values of *s* were found to be independent of the rotation speed of the electrode, i.e., they are kinetically controlled. The *i*-dependence of *s* hence indicates that the competition between the six-equivalent photoanodic oxidation of the III-V semiconductor to dissolution products and that of the (usually one-equivalent) dissolved reducing agent Y to the oxidizing agent Z does not occur through the simple mechanism denoted by DH-SH and represented by the reaction steps

$$\mathbf{DH}:\left\{\begin{array}{lll} \mathrm{X_0 + h^+} \xrightarrow{k_1} & \mathrm{X_1} & \qquad (4)\\ \mathrm{X_1 + h^+} \xrightarrow{k_2} & \mathrm{X_2} & \qquad (15)\\ \mathrm{X}_i \mathrm{+ h^+} \xrightarrow{k_{i+1}} & \mathrm{X}_{i+1}\ (i = 2,\ 3,\ 4) & \qquad (16)\\ \mathrm{X_5 + h^+} \xrightarrow{k_6} & \mathrm{X_0} + \text{dissolution products} & \qquad (17) \end{array}\right.$$

$$\mathbf{SH}:\quad \mathrm{Y + h^+} \xrightarrow{k_s^h} \mathrm{Z} \tag{18}$$

which would involve dissolution of the semiconductor by subsequent irreversible hole capture steps, leading to decomposition intermediates of subsequently higher oxidation states, parallel to the oxidation of Y by holes. Indeed, according to this mechanism, the stabilization and dissolution partial currents are described by the following expressions:

$$s i = e k_s^h y p_s \tag{19}$$

$$(1-s)\, i = 6 e k_1 p_s \tag{20}$$

(for the latter expression, see Eqs. (3) and (5))
so that by dividing Eq. (19) by Eq. (20) and rearranging, one obtains the i-independent Eq. (21):

$$s = \frac{(k_s^h/6k_1)\, y}{1 + (k_s^h/6k_1)\, y} \tag{21}$$

which is obviously in conflict with most experimental observations.

In a 1980 paper [49], our group discussed several possible competition mechanisms leading to kinetics in which the stabilization ratio decreases with increasing photocurrent density. Four out of the resulting kinetic equations have been found to describe the experimental cases. These $s(y,\ i)$ relations, the cases in which they were observed, and the corresponding mechanisms are described here (cases **(i)** to **(iv)**).

(i) $[s^2/(1-s) + s/6] = k(y/i)$ (22)

Cases in which Eq. (22) was found to hold are GaP, stabilized be $\mathrm{Fe^{2+}}$ in strongly acidic aqueous medium [53], and GaAs, stabilized by TMPD (tetramethyl-p-phenylenediamine) in mixed solvents consisting either of 48 mol% $\mathrm{CH_3OH}$–52 mol% $\mathrm{H_2O}$ [54] (see Fig. 3) or of 13 mol% $\mathrm{CH_3CN}$–87 mol% $\mathrm{H_2O}$ [55].

A mechanism leading to these kinetics, denoted by DH-$\mathrm{SX_1}$, consists of the dissolution sequence according to Eqs. (4) + (15) to (17), combined with a stabilization reaction SX_1 in which a partially broken surface bond X_1 is restored by an electron from the reducing agent

$$SX_1\text{: } Y + X_1 \xrightarrow{k_s^{X_1}} Z + X_0 \tag{23}$$

As an empty surface state may be associated with X_1 (see also further), reaction (23) electronically amounts to the filling of such a state by Y. A slightly modified form of this mechanism has been proposed by Gerischer and Lübke [51] to account for light-intensity-dependent stabilization kinetics.

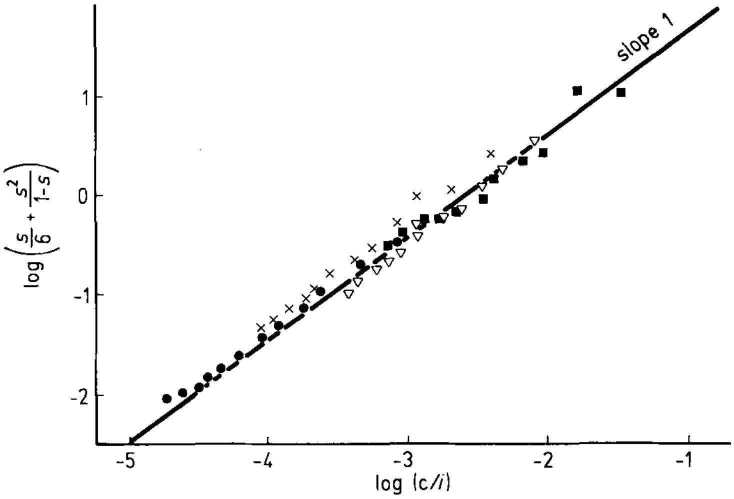

Fig. 3. Plot of log $[s^2/(1-s)+s/6]$ vs. log (c/i) (c is proportional to y). n-GaAs/TMPD electrode, $(\bar{1}\bar{1}\bar{1})$-face, illuminated.
Electrolyte composition: 0.25 mol · l^{-1} $LiClO_4$ + c mol · l^{-1} TMPD in a $H_2O + CH_3OH$ mixture (48 mol% CH_3OH), pH = 1.6. c: ● 0.01, x 0.05, ▽ 0.20, ■ 0.39.
(From ref. (54), by permission of Elsevier Sequoia).

The stabilization current density corresponding to reaction (23) is

$$si = ek_s^{X_1}yx_1 \tag{24}$$

x_1 representing the concentration of X_1 surface intermediates. As each hole used up in reaction (15) leads to dissolution of the semiconductor, the dissolution current density is given by

$$(1-s)i = 6ek_2x_1p_s \tag{25}$$

Dividing Eq. (24) by Eq. (25) and combining with the steady-state expression for X_1

$$dx_1/dt = 0 = k_1p_s - k_2x_1p_s - k_s^{X_1}yx_1 = k_1p_s - (1-s)i/6e - si/e \tag{26}$$

one indeed finds Eq. (22), with

$$k = ek_1 k_s^{X_1}/6k_2 \tag{27}$$

$$\textbf{(ii)}\quad s = k\,(y/i) \tag{28}$$

This kinetic law was found to be valid within a limited s range for the InP/Fe^{2+} electrode in strong acid [56]. It can be accounted for by a mechanism that is analogous to the preceding one, but in which the stabilization reaction is written:

$$\mathbf{SX_2}\text{: } Y + X_2 \xrightarrow{k_s^{X_2}} Z + X_1 \tag{29}$$

as can be easily demonstrated by expressing the partial current densities

$$si = ek_s^{X_2} y x_2 \tag{30}$$

$$(1-s)\,i = 6ek_3 x_2 p_s \tag{31}$$

(x_2 is the X_2 concentration), and by combinig these with the steady-state expressions for x_1 and x_2. It turns out that

$$k = ek_1 k_s^{X_2}/k_3 \tag{32}$$

$$\textbf{(iii)}\quad s^2/(1-s) = k(y^2/i) \tag{33}$$

This rate law has been observed for GaAs/Fe^{2+} in strongly acidic aqueous medium [57], see Fig. 4 as an example, for GaAs/Fe(II)-EDTA in the intermediate pH range [50], and for GaAs/TMPD in acidic aqueous medium at high LiCl concentrations [58], as well as in 42 mol% CH_3CN–58 mol% H_2O [55].

A simple mechanism accounting for this law, denoted by DH′-SH, is a modification of the mechanism DH-SH, in that the reaction step (4) is assumed to be reversible and at equilibrium:

$$X_0 + h^+ \underset{k_{-1}}{\overset{k_1}{\rightleftharpoons}} X_1 \tag{4′}$$

In this case, Eqs. (19) and (25) describe the rates of the competing reactions, so that by combining both equations and inserting the equilibrium condition

$$k_1/k_{-1} = x_1/p_s \tag{34}$$

Eq. (33) is obtained, with

$$k = ek_{-1}(k_s^{h})^2/6k_1 k_2 \tag{35}$$

This mechanism has been proposed independently by Frese et al. [50] and by our group [49], and has subsequently been adopted in models describing charge-transfer processes at GaAs electrodes [59, 60]. It leads, however, to the following incon-

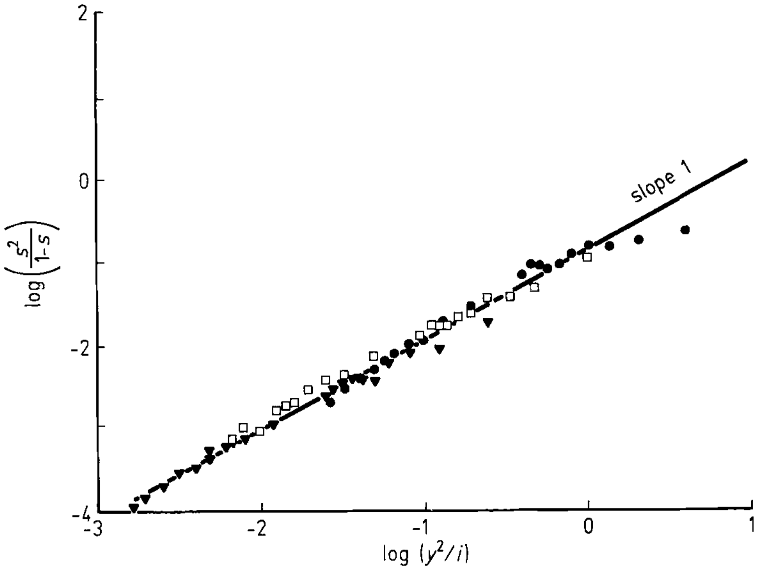

Fig. 4. Plot of log $[s^2/(1-s)]$ v. log (y^2/i). n-GaAs/Fe^{2+} electrode, $(\bar{1}\bar{1}\bar{1})$-face, illuminated; $V = +0.5$ V vs. SSE.
Electrolyte composition: 0.25 mol · l^{-1} K_2SO_4 + y mol · l^{-1} $FeSO_4$ + H_2SO_4, pH = 1.
y: ▼ 0.5, □ 1, ● 2. (From ref. (57), by permission of VCH).

sistency. Anticipating a point which will be developed in Sec. 2.2.2., we should mention here that the same competition kinetics are observed, for a given electrolyte composition, with dark p-type anodes as with illuminated n-type anodes of a given semiconductor. Consider now the expression for the anodic current density in indifferent electrolyte solution ($s = 0$), as it would follow from the model presented here. By writing $s = 0$ in Eq. (25) and inserting Eq. (34), one obtains:

$$i = (6ek_1k_2/k_{-1}) \cdot p_s^2 \tag{36}$$

This equation, which has, e.g., been proposed in ref. [59], predicts a Tafel slope of 0.03 V for p-type electrodes in indifferent electrolyte (see Sec. 2.1). In reality, to our knowledge Tafel slopes below 0.06 V have not been observed. Actually, in the case of GaAs in an acidic medium, in which the kinetic law (33) has been found to hold, the Tafel slope is found to be almost exactly 0.06 V (see Sec. 2.1).

In order to account for the kinetic equation (33), an alternative competition mechanism, denoted by DX-SX_1, can be constructed:

$$\textbf{DX:}\left\{\begin{array}{llll} X_0 + h^+ & \xrightarrow{k_1} & X_1 & (4) \\ X_1 + X_1 & \xrightarrow{k_2'} & X_2 + X_0 & (37) \\ X_i + X_1 & \xrightarrow{k_{i+1}'} & X_{i+1} + X_0 \quad (i = 2, 3, 4) & (38) \\ X_5 + X_1 & \xrightarrow{k_6'} & 2X_0 + \text{dissolution products} & (39) \end{array}\right.$$

$$\textbf{SX}_1\textbf{:}\quad Y + X_1 \xrightarrow{k_s^{X_1}} Z + X_0 \tag{23}$$

Indeed, taking the square of Eq. (24), which in this case describes the stabilization current density, and dividing it by the appropriate expression for the dissolution current density,

$$(1-s)i = 6ek_2' x_1^2 \tag{40}$$

affords Eq. (33), with k equal to:

$$k = e(k_s^{X_1})^2/6k_2' \tag{41}$$

The underlying assumption of reactions (37) to (39) is that the first decomposition intermediate X_1 and not the free hole h^+ constitutes the mobile species involved in the consecutive steps of the dissolution reaction, and hence that the decomposition intermediate X_1 is mobile within a two-dimensional surface layer. In other words, a bonding electron can jump from an unbroken surface bond to a neighboring electron-deficient surface bond. Note that here, the only step consuming holes is step (4), so that in an indifferent electrolyte, Eqs. (3) and (5) are expected to hold, with $n = 1$.

(iv) In certain cases, such as GaAs/TMPD in acidic aqueous medium at not too high ionic strength [54] and GaP/$Fe(CN)_6^{4-}$ at pH = 9 [30], a different relationship between s and the variable y^2/i is observed, i.e.,

$$s^3/(1-s)^2 + s^2/6\,(1-s) = k(y^2/i) \tag{42}$$

Examples are shown in Fig. 5 for the illuminated n-type as well as for the dark p-type GaP anode in $Fe(CN)_6^{4-}$ solution. The corresponding mechanism can be described as DX-SX$_2$, i.e., as a combination of the DX dissolution mechanism (Eqs. (4), (37) to (39)) and the stabilization step (29). Combining the rate Eq. (30) for si to

$$(1-s)i = 6ek_3' x_2 x_1 \tag{43}$$

and to the steady-state condition for X_2:

$$\mathrm{d}x_2/\mathrm{d}t = 0 = k_2' x_1^2 - k_3' x_2 x_1 - k_s^{X_2} y x_2 = k_2' x_1^2 - (1-s)i/6e - si/e \tag{44}$$

one easily finds Eqn. (42) with

$$k = ek_2'(k_s^{X_2})^2/(6k_3')^2 \tag{45}$$

It should be mentioned here that in general, the kinetic laws expressed by Eqs. (22), (28), (33), and (42) are rather easily distinguishable experimentally, as can be judged from the comparative plots in ref. [52]. It might actually seem somewhat surprising that these laws hold over a wide range of y^2/i values, although it is known that the band edges may shift with increasing concentration and/or current density (see also further), which should influence the stabilization rate constant. However, recent experiments on the GaP/Fe^{2+} electrode at different pH values have shown that for this system, the influence of the semiconductor level position upon reactivity is weak, which might, at least in the given case, explain the observed simple kinetic behavior [61]. Since this influence in general depends on the relative position of the semiconductor levels with respect to the redox level Gauss curves, one should nevertheless not extrapolate this conclusion beyond cases which have actually been studied.

Several conclusions may be drawn from the results discussed in this section. Firstly, it appears that in almost all cases studied, the stabilization reaction involves decomposition intermediates instead of free holes. We will not comment on this point here (for a discussion, see ref. [52]). Similarly, we will not enlarge on the observation that in certain cases, X_1 and in other cases X_2 intermediates are involved, as these problems are beyond the scope of the present paper, which essentially pertains to anodic dissolution and etching. As far as this subject is concerned, two important points emerge, i.e., the fact that, due to the interconnection between stabilization and dissolution, the latter reaction tends to dominate at sufficiently high current densities, and the fact that, depending on the semiconductor and on the circumstances, dissolution either occurs by the DH or by the DX mechanism. In what follows, independent information on the latter point will be gathered, and the factors which determine the dissolution mechanism will be investigated.

2.2.2 p-Type Electrodes

In several of the cases mentioned above, stabilization experiments were also conducted on the corresponding p-type electrodes in the dark under the same circumstances in terms of anodic current density and electrolyte composition as those used on n-type photoanodes [25, 30, 62]. In p-type electrodes, holes constitute the majority carriers and may be assumed to be at quasi-equilibrium at the surface (see Sec. 2.1), so that their concentration p_s at the surface and hence the anodic current density can be monitored via the electrode potential. It was found that the same kinetic law holds for a given p-type electrode/electrolyte combination (here, i is the dark anodic current density) as for the corresponding n-type electrode (see Fig. 5 for an example), and that hence the same competition mechanism holds. This fact suggests a criterium for distinguishing between the DH and the DX dissolution mechanisms, based on the observation of the influence of the stabilizing agent upon the current density at given band-bending (the latter being determined from the flatband potential V_{fb}) and resulting p_s. Consider, e.g., the DH-SX_1 competition mechanism (Eqs. (4) and (15) to (17) vs. Eq. (23)). In indifferent electrolyte ($s = 0$), the capture of one hole by X_0 eventually leads to dissolution, i.e., to the consumption of five more holes (consider the fact that at the p-type surface, an unlimited supply of holes is available). With perfect stabilization ($s = 1$), the capture of one hole by X_0 leads to no further hole consumption (see reactions (4) and (23)). Hence the expectation is that, by adding Y at a given p_s, i will decrease by a factor of up to 6. By a more detailed analysis, one can also show that linear Tafel behavior with

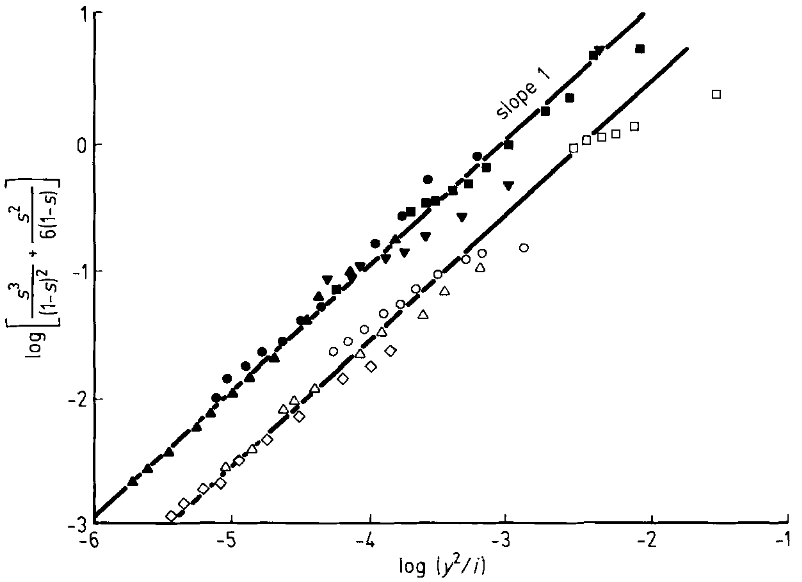

Fig. 5. Plot of log $[s^3/(1-s)^2+s^2/6(1-s)]$ vs. log (y^2/i). GaP/Fe$(CN)_6^{4-}$ electrodes, $(\bar{1}\bar{1}\bar{1})$-face. Open symbols: n-type, illuminated; closed symbols: p-type, dark.
Electrolyte composition: 0.25 mol · l^{-1} K_2SO_4 + 0.1 mol · l^{-1} $Na_2B_4O_7$ + y mol · $l^{-1}K_4Fe(CN)_6$ in H_2O (pH = 9.0). y: ◇ 0.027, △ ▲ 0.05, ○ ● 0.1, ▼ 0.25, □ 0.4, ■ 0.5.
(After ref. (30), by permission of Elsevier Sequoia).

a 0.06 V slope is only to be expected if *s* is 0 or 1 [62]. These predictions have been found to be fulfilled in cases where the DH-SX_1 mechanism was found to hold [25, 68]. In contrast, in the case of the DX dissolution mechanism, the only step in which holes are consumed is reaction (4). Hence the current density at a given p_s is predicted to be independent of the addition of Y, and simple Tafel behavior is expected. This has indeed been experimentally confirmed in cases where, as deduced from stabilization kinetics, the DX mechanism is valid [25, 30]. The study of the *i*-*V* behavior at dark p-type electrodes hence supports the distinction which has been made between both dissolution mechanisms. Note further that, if all electrochemical reaction steps involved holes (mechanisms DH-SH or DH'-SH), addition of Y to an indifferent electrolyte solution would lead to an increase of i for dark p-type electrodes at a given p_s.

2.2.3 Chemical Steps in the Dissolution Reaction

It was pointed out many years ago [3, 27] that the anodic dissolution of III-V semiconductors in aqueous media not only consists of electrochemical steps, but must also involve chemical steps in which H_2O molecules or OH^- ions participate. This follows from mere consideration of the overall reaction Eqs. (9) to (14) and, as far as alkaline media are concerned, from the fact that under certain circumstances, diffusion limitation by OH^- ions is observed (see Sec. 2.1). More detailed information on one of these chemical steps first emerged from a study [54] on the pH dependence of the stabilization kinetics at the GaAs/TMPD electrode in an aqueous medium, which, as mentioned above, obeys Eq. (42). A careful analysis of the results revealed that the observed very pronounced pH dependence can be understood on the basis of a combination of two assumptions, i. e.:

- the electroactive reducing agent Y in solution is $TMPDH^+$,
- the rate constant k in Eq. (42) obeys $k \sim (c_{H^+})^{-1}$.

The latter conclusion appeared in turn to be interpretable by adopting the following modified version of the DX dissolution mechanism, including a chemical step and therefore symbolized by DXC:

$$\mathbf{DXC}: \left\{ \begin{array}{lllll} X_0 & + h^+ & \xrightarrow{k_1} & X_1 & \qquad (4) \\ X_1 & + H_2O & \underset{k_{-c}}{\overset{k_c}{\rightleftharpoons}} & X_1 - OH + H^+ & \qquad (46) \\ X_1 - OH + X_1 & & \xrightarrow{k_2''} & X_2 + X_0 & \qquad (47) \\ & & \text{- - - -} & & \end{array} \right.$$

The steady-state condition for X_2 now becomes with x_1' the surface concentration of X_1-OH:

$$\mathrm{d}x_2/\mathrm{d}t = k_2'' x_1' x_1 - (1-s)i/6e - si/e \tag{48}$$

(see also Eqs. (38), (29), (43), and (30)).

Combining Eqs. (30), (43), and (48) and assuming a quasi-equilibrium in Eq. (46), i. e.,

$$\mathrm{K}_c = k_c/k_{-c} \simeq x_1' \cdot c_{H^+}/x_1 \cdot c_{H_2O} \, , \tag{49}$$

Eqn. (42) is indeed obtained, with k equal to the following expression:

$$k = \frac{e k_2'' (k_s^{X_2})^2 k_c}{(6k_3')^2 k_{-c}} \cdot \frac{c_{H_2O}}{c_{H^+}} \tag{50}$$

which accounts for the observed pH dependence. It should be remarked that again in this interpretation, the influence of the pH-induced band shift upon $k_s^{X_2}$ is assumed to be negligible.

Remembering that X_1 actually represents a positively charged surface intermediate, Eq (46) may be considered to represent the neutralization of this positive charge by reaction with H_2O. It is reasonable to assume that further electrochemical reaction will, for electrostatic reasons, rather occur between the neutral entity X_1-OH and the positively charged intermediate X_1 than between two positive X_1 intermediates (note that the stabilization kinetics yield no information on chemical steps which may also occur in between further electrochemical steps). It is equally reasonable to assume that, in contrast to X_1, the neutralized surface intermediate X_1-OH will be immobile, since an -OH group is attached to it. Little information is available about the chemical and electronic properties of X_1 and X_1-OH. A simplified representation of the non-oxidized GaAs ($\bar{1}\bar{1}\bar{1}$) surface is shown in Fig. 6 (a). The unpaired electron of X_1 is likely to be located on the more electronegative atom, i.e., on As in the case of GaAs, leaving a positive charge on the Ga atom, see Fig. 6 (b). The presumed structure of X_1-OH is represented in Fig. 6 (c).

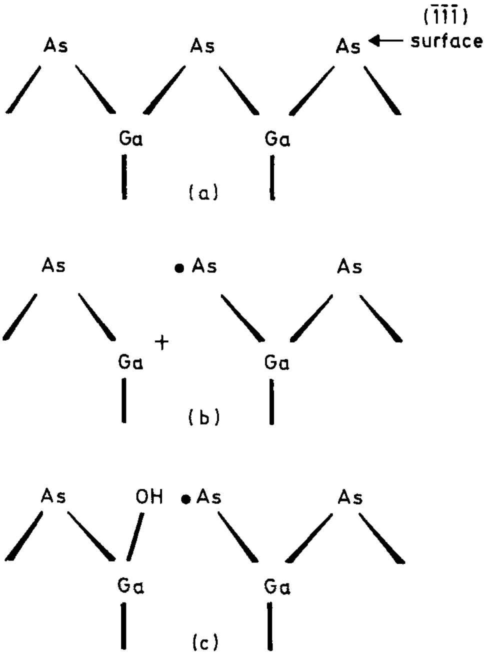

Fig. 6. Schematic representation of the GaAs ($\bar{1}\bar{1}\bar{1}$) surface; (a) before hole capture, (b) X_1 (c) X_1-OH. (For simplicity, only parts of the bonds are shown; e.g., the dangling bonds of the normal surface As atoms or the possible groups saturating them are omitted).

Accepting the existence of the equilibrium (46) and its kinetic consequences as expressed in Eq. (50), it is expected that the competitive rates will also be altered by lowering the water concentration or, more precisely, the water activity. This can be achieved, for instance, by adding a large concentration of a salt that is highly hydrated in solution, such as LiCl. Experiments in this medium ($\simeq 4 \text{ mol} \cdot l^{-1}$) show a more drastic change in behavior than expected, i.e., a transition to the DX dissolution mechanism, as appears from the absence of a pH dependence in this medium [58]. Apparently, the shift to the left in equilibrium (46) is so pronounced that now step (47) is substituted by step (37). The same effect is observed when substituting about half of the aqueous solvent by acetonitrile [55]. Considering the rather restricted reduction of the water activity in both cases, it is concluded [63] that equilibrium (46) should actually be rewritten as

$$X_1 + nH_2O \rightleftharpoons X_1 - OH + H^+(H_2O)_{n-1} \quad (n \simeq 10) \tag{46'}$$

Surprisingly, when using mixed solvents, such as 13 mol% CH_3CN-87 mol% H_2O [55] or 48 mol% CH_3OH-52 mol% H_2O [54], the competition kinetics at the GaAs/TMPD electrode indicate that not X_1 intermediates, but holes constitute the mobile species involved in the consecutive steps of the decomposition reaction (see Sec. 2.2.1 (i)), and hence that equilibrium (46) must be shifted far to the **right**, so that there is a lack of mobile X_1 intermediates. This unexpected behavior has been interpreted on a thermodynamic basis: the change in standard free enthalpy for proton transfer from pure water to the mixed solvents of the given composition has been reported to be considerably negative, providing a negative contribution to the ΔG^0-value of reaction (46), so that the corresponding equilibrium constant K_c (see Eq. (49)) can be concluded to be much larger in these mixed solvents than in water.

The main conclusion to be drawn from these investigations concerning media effects on the stabilization kinetics at GaAs electrodes is that the position of the equilibrium between mobile and immobile dissolution intermediates determines whether under given circumstances either X_1 intermediates or holes participate in the consecutive electrochemical dissolution steps. Since at GaP in acidic aqueous media, the latter is apparently the case (see the results on GaP/Fe^{2+}, case (i) in Sec. 2.2.1), it must be concluded that for this electrode, equilibrium (46′) is shifted much more to the right than for GaAs in the same electrolyte. It has been recently shown [61] that in aqueous 4 mol · l^{-1} LiCl, the stabilization ratio at the GaP/Fe^{2+} electrode depends on the Fe^{2+} concentration, according to $s^2/(1-s) \sim y^2$ which, as we have seen before, is typical of a dissolution mechanism involving mobile X_1 intermediates. The change in the dissolution mechanism of the GaP electrode, caused by reducing the water activity, is again in agreement with the general picture outlined for GaAs and GaP in acidic solution. Since the necessary experimental information is lacking, no analogous model involving chemical steps can presently be proposed for InP, nor for alkaline media.

A general remark concerns the fact that from competitive reactivity studies, very few indications emerge on the role of specific reactions sites, which might be anticipated to be important, especially in anodic dissolution. A possible reason may be that the experiments have been mostly performed on the $(\bar{1}\bar{1}\bar{1})$ face and to a lesser extent on the (100) face, whereas the role of specific sites is primarily important at the (111) face, as shown in Sec. 3.

2.3 Electron Excitation Studies of Anodic Dissolution Mechanisms

In the above section, various dissolution mechanisms for III-V compound electrodes were proposed on the basis of stabilization studies. There is evidently a need for confirmation of these mechanisms from independent data. Such confirmation can be obtained by quantitatively studying the enhancement of the anodic dark current at n-type electrodes, caused by hole injection. Although, as mentioned in Sec. 2.1, this effect has been known for many years, only recently was it realized [41] that the relationship between the additional anodic current density i_a and the cathodic hole injection current density i_c constitutes a powerful probe for investigating the dissolution mechanism. The theoretical relationship between i_a and i_c has been derived for various dissolution mechanisms. The basic assumption of all these derivations is that the anodic current increase is due to injection of an electron by the decomposition intermediate X_1 into the conduction band:

$$X_1 \xrightarrow{k_2^{ex}} X_2 + e^- \tag{51}$$

As i_a was found to increase with temperature [40,41], step (51) is believed to be an activated process, in which the electron must first be thermally excited from the X_1 surface state to the conduction band edge before injection can occur. The corresponding current density i_a is therefore usually referred to as the electron excitation current density. The reaction step with which reaction (51) is assumed to compete is then step (15) in the DH dissolution mechanism, step (37) in the DX mechanism, step (46) (or (46′)) in the DXC mechanism, and equally step (46) or (46′) in the DHC mechanism, which we have hitherto not considered, and which comprises the following steps:

$$X_0 + h^+ \xrightarrow{k_1} X_1 \tag{4}$$

$$\left\{\begin{array}{lll} X_1 + H_2O & \underset{k_{-c}}{\overset{k_c}{\rightleftharpoons}} & X_1\text{-}OH + H^+ \qquad (46) \\ X_1 & \xrightarrow{k_2^{ex}} & X_2 + e^- \qquad (51) \end{array}\right.$$

$$X_1\text{-}OH + h^+ \xrightarrow{k_2'''} X_2 \tag{52}$$

$$\text{----}$$

(the species X_2 formed according to Eq. (51) is evidently different from the one formed in Eq. (52) and must hence undergo further chemical changes, but these are irrelevant to the present discussion).

Table 1. i_a vs. i_c relationships for different decomposition mechanisms [summarized from ref. (64)].

Mechanism		Relationship*	Experimental case	Fig.
DH		$\frac{\lvert i_c \rvert}{i_a} = 5 + C_1 \cdot \lvert i_c \rvert$		
DHC	DHC(R)	$\frac{\lvert i_c \rvert}{i_a} = 5 + \frac{C_2}{a_{H^+}} \lvert i_c \rvert$	GaP/aq. H_2SO_4	8(b)
	DHC(I)	$i_a = C_3 \cdot \lvert i_c \rvert$		
DX		$i_a = -C_4 + C_5 \cdot \sqrt{\lvert i_c \rvert}$	GaAs/aq. H_2SO_4 + LiCl	7(b)
DXC	DXC(R)	$i_a = -C_6 \cdot a_{H^+} + C_7 \cdot \sqrt{a_{H^+}} \cdot \sqrt{\lvert i_c \rvert}$	GaP/aq. H_2SO_4 + LiCl	8(c)
	DXC(I)	$i_a = C_8 \cdot a_{H^+} + C_9 \cdot \lvert i_c \rvert$	GaAs/aq. H_2SO_4	7(a)

* The coefficients C_1 through C_9 are positive pH-independent combinations of rate constants.

The described and similar reaction schemes have been worked out according to the usual steady-state treatment in order to obtain the corresponding i_a vs. i_c relationships. The results of these calculations, for which we refer to the literature [40, 41, 64], are summarized in Table 1. It should be noted that for both mechanisms,

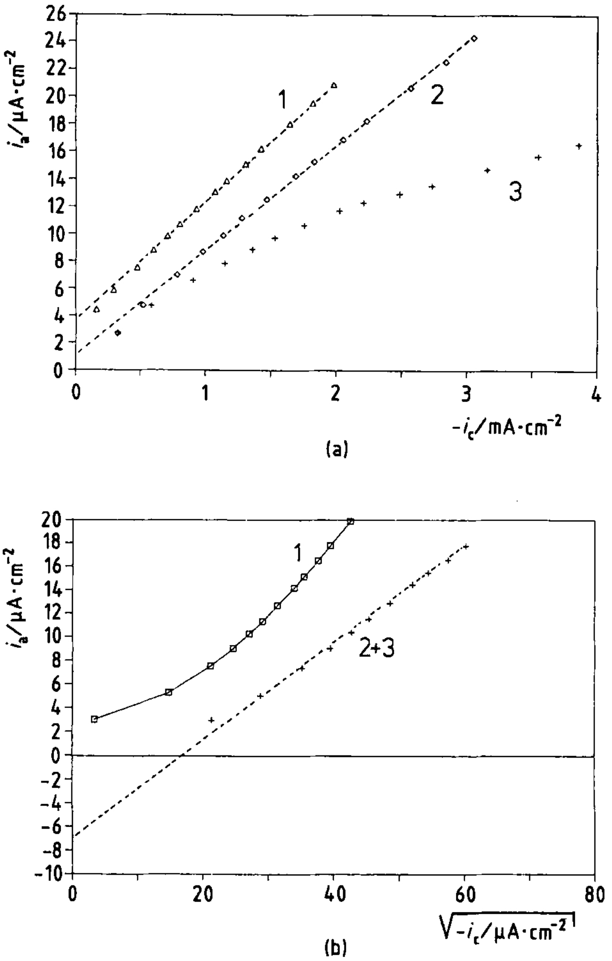

Fig. 7. (a) The limiting anodic excitation current density i_a as a function of the hole injection current density i_c measured at an n-GaAs/Ce^{4+} electrode in different aqueous electrolytes.
(1) 0.01 mol · l^{-1} $Ce(SO_4)_2$ + 4 mol · l^{-1} H_2SO_4.
(2) 0.01 mol · l^{-1} $Ce(SO_4)_2$ + 0.5 mol · l^{-1} H_2SO_4.
(3) 0.025 mol · l^{-1} $Ce(SO_4)_2$ + 2 mol · l^{-1} H_2SO_4 + 4.5 mol · l^{-1} LiCl.
(b) The limiting anodic excitation current density i_a as a function of a square root of the hole injection current density i_c measured at an n-GaAs/Ce^{4+} electrode in different aqueous electrolytes.
(1) 0.01 mol · l^{-1} $Ce(SO_4)_2$ + 2 mol · l^{-1} H_2SO_4.
(2) 0.025 mol · l^{-1} $Ce(SO_4)_2$ + 2 mol · l^{-1} H_2SO_4 + 4.5 mol · l^{-1} LiCl.
(3) 0.025 mol · l^{-1} $Ce(SO_4)_2$ + 0.5 mol · l^{-1} H_2SO_4 + 4.5 mol · l^{-1} LiCl.
(From ref. (64), by permission of Elsevier Sequoia).

which include the chemical reaction step (46) or (46′), Vanmaekelbergh et al. [64] have considered two cases, in which this step is either reversible (R) or irreversible (I). Hence a total of six cases has been treated, i.e., DH, DHC(R), DHC(I), DX, DXC(R), and DXC(I). It turns out that in each case either the relationship between i_a and i_c or the pH dependence is different, so that electron excitation experiments, including the pH dependence, make it possible to decide which dissolution mechanism applies.

This method has been applied to n-GaAs as well as to n-GaP in various electrolytes. The data in strongly acidic aqueous media without and with 4.5 mol · l^{-1} LiCl added are illustrated in Figs. 7 and 8 for GaAs and GaP, respectively. The results are included in Table 1 with reference to Figs. 7 and 8. These data appear to be in excellent agreement with those obtained from stabilization measurements. In the case of GaAs, the transition from the DXC to the DX mechanism through addition of LiCl is confirmed. The fact that electron excitation experiments demonstrate that the neutralization reaction of X_1 in the presence of water is irreversible does not contradict the stabilization results, which are based on the assumption of reversibility, since the dissolution rates are one to two orders of magnitude higher in the former case than in the latter. In fact, recent measurements at lower hole injection current densities point to a $\sqrt{|i_c|}$ dependence of i_a [43]. In the case of GaP, the observed transition from holes to X_1 intermediates as mobile species in the electrochemical steps upon addition of LiCl is confirmed and identified more precisely as a transition from the DHC to the DXC mechanism.

Some electron excitation experiments have also been performed on GaAs and GaP electrodes in alkaline media. Whereas the results on GaAs agree with the general concept of the role of neutralization equilibrium (46′) as outlined above, those on GaP do not seem to fit into the model, so that further investigation will be necessary.

Fig. 8. (a) The limiting anodic current density i_a as a function of the hole injection current density i_c measured at an n-GaP/Ce^{4+} electrode in different aqueous electrolytes.
(1) 0.01 mol · l^{-1} $Ce(SO_4)_2$ + 0.5 mol · l^{-1} H_2SO_4.
(2) 0.01 mol · l^{-1} $Ce(SO_4)_2$ + 2 mol · l^{-1} H_2SO_4.
(3) 0.01 mol · l^{-1} $Ce(SO_4)_2$ + 4 mol · l^{-1} H_2SO_4.
(4) 0.025 mol · l^{-1} $Ce(SO_4)_2$ + 2 mol · l^{-1} H_2SO_4 + 4.5 mol · l^{-1} LiCl.
(b) $(-i_c/i_a)$ as a function of $-i_c$ at an n-GaP/Ce^{4+}electrode. Same data and notation as in Fig. 8(a).
(c) i_a as a function of $\sqrt{-i_c}$ at an n-GaP/Ce^{4+} electrode in different aqueous electrolytes.
(1) 0.025 mol · l^{-1} $Ce(SO_4)_2$ + 2 mol · l^{-1} H_2SO_4 + 4.5 mol · l^{-1} LiCl.
(2) 0.025 mol · l^{-1} $Ce(SO_4)_2$ + 1 mol · l^{-1} H_2SO_4 + 4.5 mol · l^{-1} LiCl.
(From ref.(64), by permission of Elsevier Sequoia).

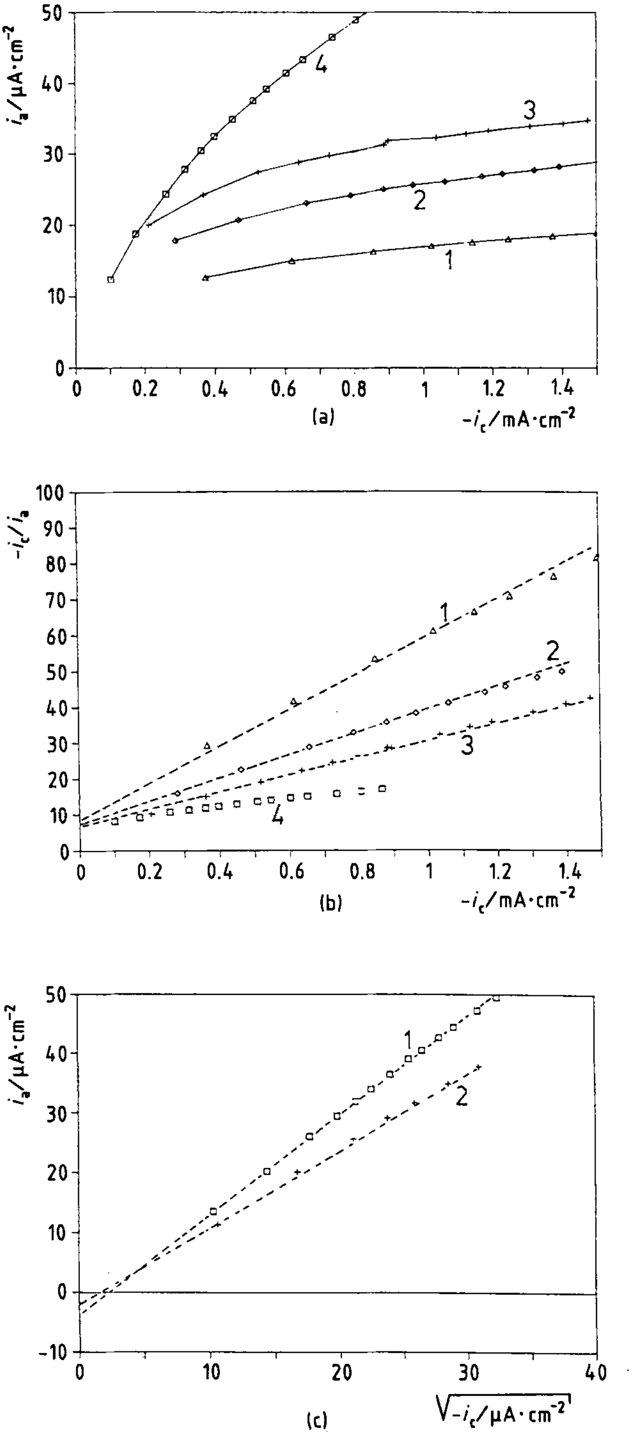
$i_a/\mu A\cdot cm^{-2}$
50
40
30
20
10
0
0
0.2
0.4
0.6
0.8
1
1.2
1.4
1
2
3
4
(a)
$-i_c/mA\cdot cm^{-2}$
$-i_c/i_a$
100
90
80
70
60
50
40
30
20
10
0
0
0.2
0.4
0.6
0.8
1
1.2
1.4
1
2
3
4
(b)
$-i_c/mA\cdot cm^{-2}$
$i_a/\mu A\cdot cm^{-2}$
50
40
30
20
10
0
-10
0
10
20
30
40
1
2
(c)
$\sqrt{-i_c/\mu A\cdot cm^{-2}}$

2.4 Other Approaches to the Investigation of Anodic Dissolution Kinetics and Mechanisms

An interesting theoretical analysis has recently been performed [65] on the relationship between the rest potential of n-type semiconductors and the hole injection rate, leading to the conclusion that the experimental study of this relationship may yield information on the dissolution mechanism of the semiconductor, similar to that obtained from electron excitation studies.

Another method of investigating the kinetics and mechanisms of the anodic oxidation of semiconductors and of stabilization reaction has recently been proposed [43, 44, 66, 67]. The band edge position of illuminated n-type electrodes is determined by impedance measurements in the photocurrent saturation region under various reaction conditions. The underlying idea is that band shifts originate from the accumulation at the surface of positive charges, due to holes and to decomposition intermediates. Since the steady-state concentrations of these charges are governed by the interfacial kinetics, the analysis of the band shifts as a function of the current density may in principle yield kinetic and hence mechanistic information. In the case of III-V electrodes, this method has been applied to GaAs and InP[43, 44, 67]. Current vs. band-shift plots for illuminated n- and dark p-type electrodes, as well as current vs. potential plots for dark p-type electrodes, have been simulated on the basis of various anodic dissolution models involving up to 8 parameters, the best fit being considered to constitute a proof for the dissolution mechanism. The conclusions from this work differ from those mentioned previously in that the DH′-SH mechanism including the reversible hole capture step (4′) is accepted, but they agree with other sources as far as inclusion of the chemical step (46) is concerned.

3 Etching of III-V Compound Semiconductors

3.1 General

As stated in the introduction, wet etching processes may proceed either with or without external current flow. In the former case, the semiconductor crystal is incorporated as an electrode in an electrochemical cell and polarized anodically under illumination or in darkness for n- and p-type samples, respectively, leading to dissolution of the sample (see Sec. 2). This is referred to as the **(photo)anodic etching** process.

In the case of open-circuit etching processes, no electrical contacts are required at the back of the sample, which is more attractive from a technological point of view: the semiconductor crystal is simply immersed in the etchant solution and in some cases illuminated with light of an appropriate wavelength. Depending on the mechanism, three types of open-circuit etching processes can be distinguished, i.e., electroless, chemical, and photoetching processes. The first two proceed in the dark, the third under illumination.

It was probably Gerischer who, as early as in the 1960s, first recognized the value of semiconductor electrochemistry for investigating the mechanisms of these open-circuit etching processes [27, 38, 68–70].

In the case of an **electroless etching** process, an oxidizing agent in solution injects holes into the valence band of a semiconductor, which are then consumed in the semiconductor decomposition reaction. Hence, the mechanism is an electrochemical one, in which the anodic oxidation of the semiconductor by holes is electrically compensated for by the cathodic reduction of a dissolved oxidizing agent over the valence band (i. e., through injection of holes). Electroless etching mechanisms can easily be identified by combining investigations on the etching and electrochemical kinetics. Firstly, the ability of the oxidizing agent to inject holes into the valence band can be checked by measuring the dark cathodic current at a p-type electrode, as this current is markedly increased when holes are injected. Secondly, as under cathodic polarization the injected holes migrate into the interior of the semiconductor crystal, they cannot be consumed at the surface in the semiconductor oxidation reaction, so that electroless etching stops when the crystal is sufficiently cathodically polarized. Thirdly, as the electroless process essentially consists of two partial processes or currents, the open-circuit etch rate, expressed as a current density, must correlate with the hole injection rate. The latter can be measured cathodically, provided that the hole injection rate is independent of the semiconductor polarization, which can be checked by means of rotating ring–disk experiments.

In the case of a **chemical etching** mechanism, the semiconductor is dissolved via a chemical reaction between a reactive species in solution and surface atoms of the solid, in which bonds are broken between atoms of the solid and between atoms of the reactant, respectively, and new bonds are formed between atoms of the solid and atoms of the reactant. In this case, no free electronic charge carriers are exchanged at the interface during etching. No holes are injected, which can be checked by measuring the dark cathodic current at a p-type electrode (see above). As a consequence, chemical etching may still proceed under cathodic polarization of the semiconductor. It has to be mentioned that the latter distinction between chemical and electroless etching is best observed with p-type samples. Not only is it hard to unambiguously identify a cathodic process as being a hole injection one at n-type electrodes, but it is furthermore often found at n-type electrodes that the chemical attack by an oxidizing agent is suppressed by cathodic reduction of this reactant over the conduction band, i. e., when the latter is diffusion-limited. The absence of etching at the n-type electrode might then erroneously be attributed to an electroless mechanism, if not checked at p-type samples.

In the case of **photoetching**, the mechanism is again electrochemical, with two partial currents cancelling each other electrically but not chemically [5, 71]. Under illumination, electron-hole pairs are created; the conduction band electrons reduce a dissolved oxidizing agent, whereas the holes oxidize the semiconductor. This model implies that at rest potential V_r, the photoetch rate (i. e., the etch rate under illumination minus the etch rate in the dark, both at a potential corresponding to V_r under illumination) should correlate with the net photocurrent density at V_r under illumination. Such a simple photoetching mechanism can hence easily be identified by combining photoetching and photoelectrochemical data.

It is worth-while mentioning that most open-circuit etching processes involve oxidation of the semiconductor to dissolution products. Indeed, most chemical etchants are oxidizing agents. The etching process is therefore essentially a transition of electrons from semiconductor surface bonds to the oxidizing agent. Three different ways of transition may be distinguished:

(a) The electrons first pass to the valence band (Fig. 9a, step (1)) before being transferred to the solution (Fig. 9a, step (2)). This is the electroless mechanism. Note that step (1) corresponds to the capture of a hole by X_0 (see Sec. 2.1, reaction (4)), whereas step (2) corresponds to the injection of a hole by the oxidizing agent. (Note that the division into steps (1) and (2) has no chronological meaning).

(b) The electrons are donated directly via a chemical reaction at the surface (Fig. 9b). No charge carrier exchange between the surface bond levels and the semiconductor bands occurs, hence no free electronic charge carriers and thus no partial currents are involved. This is the chemical mechanism, at least in the case of an oxidative chemical etch.

(c) The electrons pass to the valence band (Fig. 9c, step (1)), are excited to the conduction band (Fig. 9c, step (2)), and are transferred to the solution (Fig. 9c, step (3)). This is the photoetching mechanism.

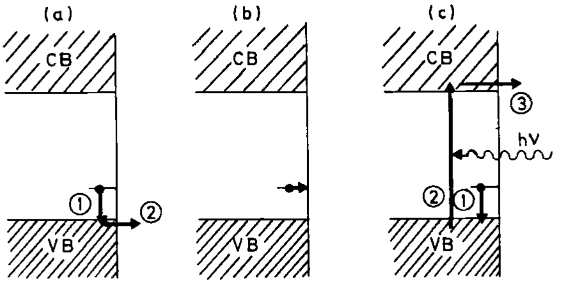

Fig. 9. Schematic representation of the electron transfer process from a surface bond towards an oxidizing agent in solution. (a) Electroless etching, (b) chemical etching, (c) photoetching.

In our further discussion, we will first treat the new insights into the kinetics and mechanisms of wet etching processes obtained during the last decade (Sec. 3.2). This is exemplified by the etching behavior of the semiconductor GaP, which has been extensively studied by our research group [20, 24, 31, 72, 73]. It is our aim to show how, by combining etching data with electrochemical data, it is possible to unravel the etching mechanism. Since the kinetics and mechanisms of the (photo)anodic oxidation of III–V semiconductors are treated in Sec. 2, this discussion is restricted to the three types of open-circuit etching processes.

In the next part (Sec. 3.3), the morphology of the etched surfaces is discussed. It is shown that a strategy of combining kinetic, morphological, and electrochemical studies affords fundamental insight into the origin of the surface morphology after etching. Similarly, this discussion mainly focuses on GaP single crystals, and the key role of (photo)anodic studies in elucidating open-circuit processes is demonstrated.

3.2 Etching Kinetics and Mechanisms

3.2.1 Electroless Etching

As mentioned above, this discussion focuses on the semiconductor GaP. Alkaline $K_3Fe(CN)_6$ solutions are known to be good etchants for this material and are often used to differentiate between the two polar faces, i.e., the (111)- and the $(\bar{1}\bar{1}\bar{1})$-face [74] (see also Sec. 3.3.2). Memming [23] showed that the $Fe(CN)_6^{3-}$ ion in alkaline solution is able to inject a hole into GaP, so that an electroless etching mechanism is expected. From etching experiments carried out at different electrode potentials, it was demonstrated that neither n- nor p-GaP crystals are etched by $Fe(CN)_6^{3-}$ ions when the electrode is polarized cathodically, so that any possible contribution of a chemical etching process can be excluded [73]. The open-circuit etching of GaP single crystals in alkaline $Fe(CN)_6^{3-}$ solutions in the dark hence consists of two partial reactions: injection of holes by $Fe(CN)_6^{3-}$ ions (cathodic partial reaction), and consumption of holes by GaP (anodic partial reaction). Hence, under open-circuit conditions, two partial currents are flowing, which cancel each other electrically but not chemically:

$$
\begin{array}{llr}
6\,[Fe(CN)_6^{3-} & \longrightarrow Fe(CN)_6^{4-} + h^+] & (53) \\
GaP + 6h^+ + 11\,OH^- & \longrightarrow GaO_3^{3-} + HPO_3^{2-} + 5\,H_2O & (13') \\
\hline
\end{array}
$$

$$GaP + 6\,Fe(CN)_6^{3-} + 11\,OH^- \longrightarrow GaO_3^{3-} + HPO_3^{2-} + 6\,Fe(CN)_6^{4-} + 5\,H_2O \qquad (54)$$

The anodic partial reaction (the oxidation of GaP) is discussed in Sec. 2. Note that in reaction (13′), the contribution of the conduction band is neglected (compare to reaction (13)). (In fact, the few electrons injected during the anodic oxidation of GaP will recombine with the holes injected by $Fe(CN)_6^{3-}$). The cathodic reduction of $Fe(CN)_6^{3-}$ at [111] oriented GaP single crystals shows some interesting features [73]. According to Gerischer's model of direct electron transfer across the semiconductor/redox electrolyte interface [2], the injection rate depends upon the energetic position E_V^s of the valence band edge at the surface with respect to the unoccupied redox energy levels. This explains the difference in hole injection kinetics observed in alkaline $Fe(CN)_6^{3-}$ solutions (pH = 13) between the two polar faces (i.e., (111) and $(\bar{1}\bar{1}\bar{1})$-faces) (see Fig. 10) [73]. Whereas the hole injection rate at the $(\bar{1}\bar{1}\bar{1})$-face is limited by the diffusion rate of $Fe(CN)_6^{3-}$ ions toward the GaP surface, the injection rate at the (111)-face is under mixed kinetic–diffusion control. This difference can be attributed to the difference in the valence band edge position between the two faces, as derived from impedance measurements. The different band edge position in turn was attributed to the different orientation of the Ga–P surface dipole.

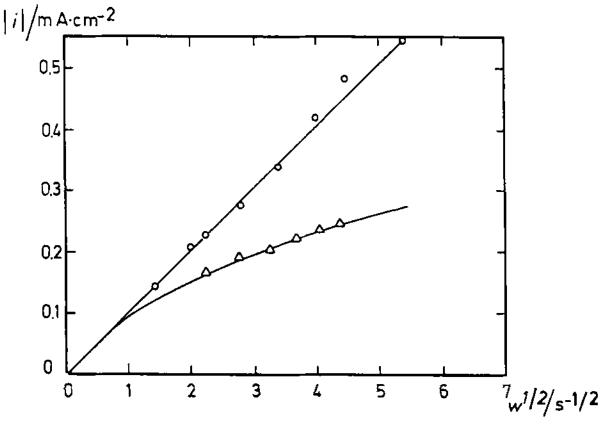

Fig. 10. The cathodic current density i as a function of the square root of the rotation speed w at p-GaP in aqueous 10^{-3} mol · l^{-1} $K_3Fe(CN)_6$ + KOH (pH = 13); $V = -1.5$ V vs. SCE. ○ ($\bar{1}\bar{1}\bar{1}$)-face, △ (111)-face. (From ref. (73), by permisson of Pergamon Press).

Whereas at the ($\bar{1}\bar{1}\bar{1}$)-face, the surface dipole is oriented with its negative end toward the surface, it is oriented oppositely at the (111)-face, which results in a lower position of E_V^s at the (111)-face and hence in less extensive overlap with the $Fe(CN)_6^{3-}$ levels (i.e., a lower hole injection rate). It is interesting to note that the difference in electron density around group III and group V atoms in the zincblende lattice has been directly visualized by recording STM-images of the (110) GaAs surface [75]. The influence of the valence band edge position E_V^s on the injection kinetics is additionally confirmed by the fact that the kinetics at both faces can be changed (if not limited by the diffusion rate of $Fe(CN)_6^{3-}$ ions) by changing the pH, causing a rise of E_V^s over 60 meV per pH unit.

A shift in the band edge position also explains the observed dependence of the hole injection rate on the electrode polarization. Fig. 11 exemplifies this by the total current-potential behavior of a (111) n-GaP electrode in alkaline $Fe(CN)_6^{3-}$ solutions (pH = 13), together with the partial current due to the injection of holes (revealed by rotating ring-disk experiments, see ref. [73]). Also at p-GaP, it was shown that the hole injection rate is lower with anodic polarization than with cathodic polarization. The potential-dependent position of the band edges is ascribed to a potential-dependent accumulation of positive charges (holes, surface decomposition intermediates, ...) at the semiconductor surface [62, 73].

The above cited factors influencing the hole injection kinetics have important consequences on the dark open-circuit etching behavior of GaP single crystals in alkaline $Fe(CN)_6^{3-}$ solutions. At the (111)-face, the open-circuit etching rate is always found to be controlled by the rate of the charge transfer reaction (so-called kinetic control). At the ($\bar{1}\bar{1}\bar{1}$)-face, on the other hand, the etching rate is always found to be limited by ion diffusion towards the semiconductor surface, either of $Fe(CN)_6^{3-}$ (for $Fe(CN)_6^{3-}$ concentrations lower than 0.3 mol · l^{-1} or of OH^- (for $Fe(CN)_6^{3-}$ concentrations higher than 0.3 mol · l^{-1}). This difference between the two polar

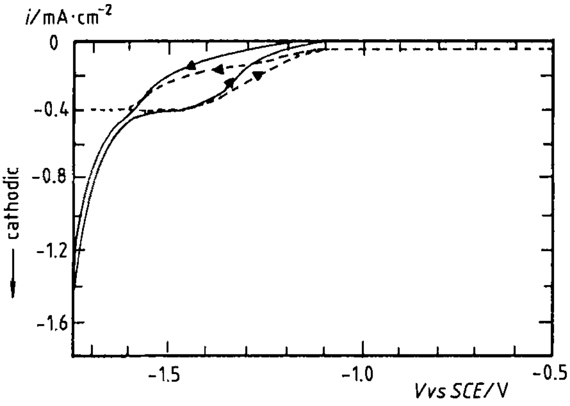

Fig. 11. Current density-potential curve at (111) n-GaP in aqueous 10^{-3} mol · l^{-1} $K_3Fe(CN)_6$ + KOH (pH = 13); rotation speed $w = 20\ s^{-1}$; scan rate = 10 mV · s^{-1}. ——— net current density, ----- partial current density due to reduction of $Fe(CN)_6^{3-}$. (From ref. (73), by permission of Pergamon Press).

faces is illustrated in Fig. 12, showing the etch rate r (measured by the flow-cell technique, in which the amount of dissolved Ga^{3+} in the collected electrolyte was determined spectrophotometrically [73]) as a function of the square root of the flow rate u. The etching rate at the (111)-face appears to be independent of the flow rate, which is characteristic for a reaction under kinetic control, whereas the etch rate at the $(\bar{1}\bar{1}\bar{1})$-face depends linearly on $u^{1/2}$, indicating a diffusion-limited process (although theory actually predicts a $u^{1/3}$ rate law for diffusion control, it is mentioned in the literature that a $u^{1/2}$ dependence may be found when the electrolyte flow deviates from ideal laminar streaming [76]).

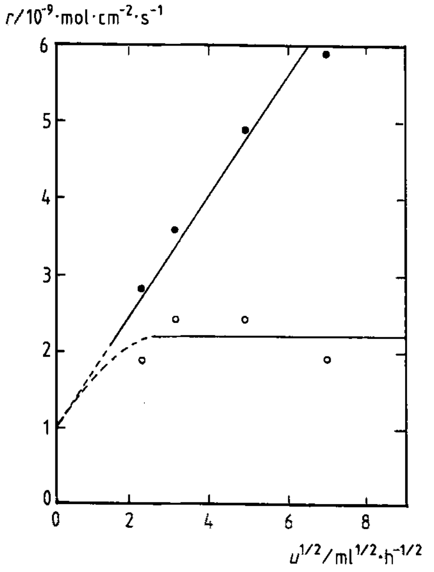

Fig. 12. The open-circuit etching rate r as a function of the square root of the flow rate u at p-GaP in aqueous 0.5 mol · l^{-1} $K_3Fe(CN)_6$ + KOH (pH = 13). ○ (111)-face, ● $(\bar{1}\bar{1}\bar{1})$-face. (From ref. (73), by permission of Pergamon Press).

Figure 13 shows schematically the current- and partial current-potential behavior of p-GaP ((a) and (b)) and n-GaP ((c) and (d)) in alkaline $Fe(CN)_6^{3-}$ solutions. In Fig. 13 (a) and (c), the partial current density at rest-potential or under open-circuit, and hence the etch rate, is limited by the cathodic partial reaction rate. This is the case for (111) GaP (for which the cathodic reaction is under kinetic control) and for $(\bar{1}\bar{1}\bar{1})$ GaP at low $Fe(CN)_6^{3-}$ concentrations (for which the cathodic reaction is under diffusion control). In Fig. 13 (b) and (d), the partial current density at rest-potential or under open-circuit is limited by the anodic partial reaction rate, which is limited by the OH^- diffusion rate (see Sec. 2.1); this is the case for $(\bar{1}\bar{1}\bar{1})$ GaP at

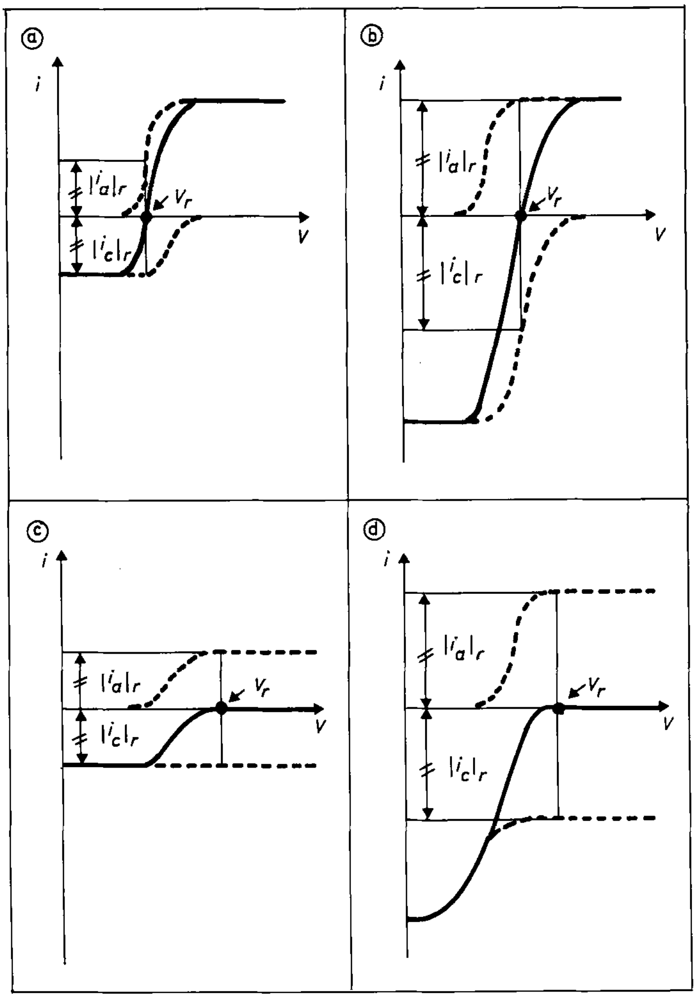

Fig. 13. Schematic representation of the i–V behavior of GaP in alkaline $Fe(CN)_6^{3-}$ solutions. (a, b) p-GaP, (c, d) n-GaP. ——— overall current density, - - - - - partial current densities. (From ref. (20), by permission of Pergamon Press).

high $\mathrm{Fe(CN)_6^{3-}}$ concentrations. For a more detailed treatment of these current-potential curves and for actual experimental curves, we refer to ref. [73].

It is worth-while mentioning that in the case of the diffusion-limited electroless etching of GaAs in alkaline $\mathrm{Fe(CN)_6^{3-}}$ solutions, a similar distinction was observed between etching controlled by the cathodic partial reaction (i. e. diffusion limitation by $\mathrm{Fe(CN)_6^{3-}}$ ions) and by the anodic partial reaction (i.e., diffusion limitation by $\mathrm{OH^-}$ ions) [22]. Other electroless etchants for GaP and GaAs include acidic $\mathrm{Fe^{3+}}$ [23, 77, 78] and $\mathrm{Ce^{4+}}$ [23, 38, 77, 78] solutions. In the case of GaAs/$\mathrm{Fe^{3+}}$, it was shown by means of rotating ring-disk experiments that the reduction rate of $\mathrm{Fe^{3+}}$ in the anodic potential region is drastically decreased in comparison to that in the cathodic potential region. In the case of GaAs/$\mathrm{Ce^{4+}}$, on the contrary, holes are injected at a diffusion-limited rate over the whole potential region [34, 78]. This different behavior is explained on the basis of the positions of the redox levels concerned. Whereas the $\mathrm{Ce^{4+}/Ce^{3+}}$ standard Fermi level lies well below the valence band edge, the $\mathrm{Fe^{3+}/Fe^{2+}}$ standard Fermi level is located close to the valence bend edge, so that the overlap of the unoccupied ($\mathrm{Fe^{3+}}$) levels with the valence band, and hence the $\mathrm{Fe^{3+}}$ reduction rate, is very sensitive to the downward displacement of the valence band edge under anodic polarization, caused by the accumulation of holes at the surface.

3.2.2 Photoetching

As stated in Sec. 3.1, in the simple photoetching model the photoetching rate should correlate with the net photocurrent density at V_r. Fig. 14 schematically shows the i-V behavior for a photoetching system at an n- and a p-type semiconductor, which demonstrates that the value of the photocurrent density at V_r can be obtained by measuring the dark current density $|i_d|_r$ at V_r. In order to measure $|i_d|_r$, the illuminated electrode is held at the potential at which the net current is zero ($V = V_r$). The illumination is then abruptly interrupted; the value of the current immediately

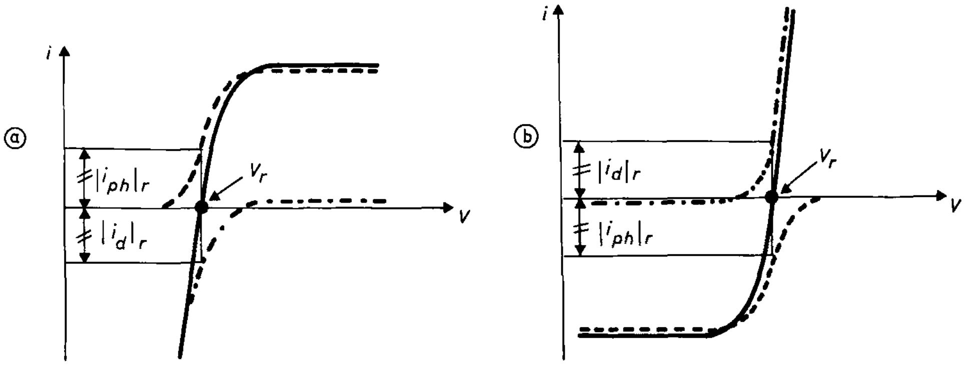

Fig. 14. Schematic representation of the i-V behavior of illuminated GaP in alkaline $\mathrm{OBr^-}$ solutions. (a) n-GaP, (b) p-GaP. ——— total current density under illumination, - · - · - dark current density, ----- photocurrent density. (From ref. (20), by permission of Pergamon Press).

after interruption of the light yields the value of $|i_d|_r$. A detailed description of such an experiment is given in ref. [34]. In order to quantitatively compare photocurrent densities to photoetching rates, the latter have to be expressed as current densities, taking into account the six-equivalency of the anodic oxidation reaction (see Sec. 2.1). A good quantitative correlation between the photocurrent density and the photoetching rate was indeed found for the photoetching of GaP in alkaline OBr^- solutions [24] and for the photoetching of InP in acidic Fe^{3+} solutions [34] (Fig. 15), demonstrating that at least in those cases the simple model of two compensating partial currents is valid. Moreover, according to this model, the photoetching rate is expected to increase when the onset of the anodic dissolution curve shifts towards more negative potentials, or when the onset of the cathodic reduction curve shifts towards more positive potentials. A striking illustration of this model is the high photoetching rate of InP by Fe^{3+} in an HCl medium in comparison to that in H_2SO_4 or $HClO_4$ media; voltammetric results indeed show that in an HCl medium, both currents are shifted in the favorable direction in comparison to H_2SO_4 or $HClO_4$ media.

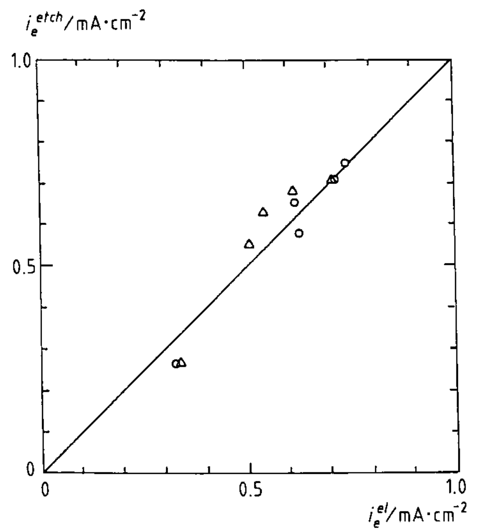

Fig. 15. The photoetch current density obtained from etch rate measurements, i_e^{etch}, vs. the current density obtained electrochemically, i_e^{el}, in aqueous 0.02 mol · l^{-1} $FeCl_3 + HCl$ (pH = 0). Flow rate u = 10 $cm^3 \cdot h^{-1}$; $V = V_r$. ○ n-InP, △ p-InP. (From ref. (34), by permission of Elsevier Sequoia).

At this point, it is important to mention that for GaAs, bisymmetrical molecules such as Br_2 and H_2O_2, which etch the semiconductor chemically in the dark, are found to be effective photoetchants as well [71]. This may be understood in terms of the simple model, since it is known that these chemical etchants tend to shift the onset of the anodic partial current density curve towards more negative potentials. Recently, a model was proposed for the processes involving these reactants at the GaAs surface (cathodic reduction, chemical etching). This model assumes that a surface intermediate involving the oxidizing agent acts as a common precursor for both the electrochemical reduction (via current-doubling at p-GaAs), and hence also for photoetching, and chemical etching [79, 80]. This model thus yields a more chemical interpretation of the fact that effective chemical etchants for GaAs are also suitable photoetchants for this material (see also Sec. 3.2.3).

It is interesting to note here that for the reduction of electroactive oxidizing agents by conduction band electrons, the onset of the reduction current is found to be more positive than for the H^+ reduction. In contrast, as mentioned in Sec. 2.2.2, in the case of hole-capture currents at p-type electrodes, a corresponding negative shift (i. e., an anodic current increase at given potentia) is usually not observed when adding an electroactive reducing agent to the indifferent electrolyte; this fact has been explained in terms of the linkage between competing hole-capture reactions by decomposition intermediates. Apparently, in the cathodic case, the competing reactions occur simply in parallel.

Photoetching processes do not always consist of a simple superposition of an anodic and a cathodic partial process and may exhibit various types of complications. Firstly, even in the "simple" case of the photoetching of GaP single crystals in alkaline OBr^- solutions, the situation is actually more complex than depicted above, since at n-type crystals, it appears that the photoetching process itself induces a hole injection reaction and hence and electroless etching effect [24]. Initially, OBr^- is reduced at the GaP surface via the current-doubling mechanism (as is concluded from photocurrent measurements at p-type samples):

$$OBr^- + e^- + H_2O \longrightarrow Br^{\cdot} + 2OH^- \qquad (55)$$

$$Br^{\cdot} \longrightarrow Br^- + h^+ \qquad (56)$$

At the rest potential V_r, this reaction is electrically compensated for by the anodic oxidation of GaP (reaction (13')), so that the overall reaction can be written as:

$$GaP + 5OH^- + 3OBr^- \xrightarrow{h\nu} GaO_3^{3-} + HPO_3^{2-} + 3Br^- + 2H_2O \qquad (57)$$

The role of illumination consists in creating electron-hole pairs, which are necessary for the partial reactions. During the reduction of OBr^- ions, $Br^{\cdot}$ radicals are formed as intermediates (cfr. reaction (55)), which appear to initiate an autocatalytic reaction mechanism: surface states are formed, through which holes are injected into the valence band (at least at not too high OBr^- concentrations). These surface states, which are experimentally detected as a peak in the capacitance-potential plot [24, 81], are believed to be associated with adsorbed OBr^-. Furthermore, voltammetric experiments demonstrate that these surface states can be annihilated by a sufficiently large concentration of holes at the surface. The latter explains why this induced electroless etching effect is not observed at p-GaP, since in this case the holes are present at the surface in a quasi-equilibrium cloud of majority carriers, in contrast to the case of n-GaP.

Another more complex case is that of the etching of GaAs in CrO_3-HF solutions, studied both in the dark and under illumination by Kelly et al. [82, 83]. The etching kinetics depend upon the CrO_3/HF concentration ratio; at a low ratio, the etching rate is limited by diffusion of Cr(VI) from solution, while at high values, the etching is kinetically controlled and depends only on the HF concentration. Illumination considerably enhances the dissolution rate of n-GaAs but has no effect on that of p-GaAs. The authors present quite a complex etching model to account for these facts, in which the oxidative dissolution of GaAs and the reduction of the oxidizing agent Cr(VI) are not totally independent partial reactions, but are linked to each other through the GaAs decomposition intermediate X_1 (see Sec. 2.2). Specifically, the following reaction scheme has been proposed. Injection of six holes by the hexavalent chromium yields an adsorbed mixed-valence complex that blocks the surface:

$$\{\mathrm{Cr(VI)-Cr(VI)-Cr(VI)}\} \longrightarrow \{\mathrm{Cr(III)-Cr(VI)-Cr(III)}\}_{\mathrm{ads}} + 6\,\mathrm{h}^+ \qquad (58)$$

This passivating surface complex can be reduced either by electrons (reaction (59)) or by X_1 (reaction (60)) and subsequently removed by HF (reaction (61)):

$$\{\mathrm{Cr(III)-Cr(VI)-Cr(III)}\}_{\mathrm{ads}} + \mathrm{e}^- \longrightarrow \{\mathrm{Cr(II)-Cr(VI)-Cr(III)}\}_{\mathrm{ads}} \qquad (59)$$

$$\{\mathrm{Cr(III)-Cr(VI)-Cr(III)}\}_{\mathrm{ads}} + X_1 \longrightarrow \{\mathrm{Cr(II)-Cr(VI)-Cr(III)}\}_{\mathrm{ads}} + X_2 \qquad (60)$$

$$\{\mathrm{Cr(II)-Cr(VI)-Cr(III)}\}_{\mathrm{ads}} \xrightarrow{\mathrm{HF}} \mathrm{Cr(II)} + 2\,\mathrm{Cr(III)} + 3\,\mathrm{h}^+ \qquad (61)$$

The photoetching effect at n-GaAs is thus explained on the basis of a recombination mechanism involving the surface decomposition intermediates, influencing the concentration of the adsorbed complex that is responsible for blocking the surface. Since one intermediate X_1, and hence one photogenerated hole (see reaction (4)) is capable of freeing a blocked site at which multiple hole injection can subsequently take place, the apparent quantum efficiency is very high (higher than 1). A similar etching mechanism appears to hold in the case of the (photo)etching of GaAs in CrO_3-HCl solutions [84].

In the case of a non-uniformly illuminated surface, finally, the anodic and cathodic partial reactions of the photoetching process take place at macroscopially distinguishable sites. At an n-type semiconductor, the illuminated area plays the role of a local anode, at which the semiconductor is dissolved, whereas the non-illuminated area acts as a local cathode, at which reduction of the oxidizing agent occurs; the opposite holds for p-type samples [85, 86]. Hence, on the whole, the sample behaves as a corroding short-circuited galvanic cell [5]. The effect of this galvanic element formation is the most interesting in the case of laser-etching of n-type semiconductors: due to the large ratio of cathodic (dark) vs. anodic (illuminated) surface area, a high etching rate at the illuminated spot can be obtained [87, 88]. Van de Ven et al. [88] showed experimentally that the anodic dissolution proceeds at the illuminated area, whereas the electron consumption that is necessary to maintain charge neutrality proceeds at the same rate everywhere (see Fig 16). In a first experiment, a two-compartment cell was used in which an n-type crystal formed the partition between the compartments; one side of the crystal was partly masked, leaving a small spot for illumination, whereas the back side was kept in the dark. A high photoetching rate resulted when the large dark surface was in contact with an appropriate oxidizing agent (e.g., H_2O_2). In another, so-called two-spot experiment, the authors showed experimentally that the photoetching rate increases with increas-

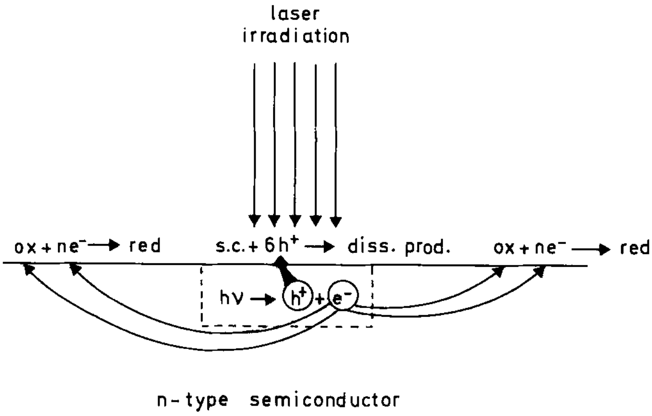

Fig. 16. Schematic representation of galvanic element formation due to laser etching.

ing ratio of dark vs. illuminated spot area. The formation of such a photogalvanic element also implies that the majority of carriers are at (quasi-)equilibrium throughout the crystal and that they can travel relatively long distances [87]. The same authors also showed that limitation of the overall photoetching rate by the cathodic partial reaction only occurs at low ratios of dark to illuminated surface area with poorly conducting crystals and with strongly inhibited reduction kinetics, so that it can be ruled out in the case of laser-etching of n-type crystals in an appropriate oxidizing medium. In most cases, the kinetics are determined by the light intensity, and quantum efficiencies close to one are obtained [88]. At relatively high etching rates or in the intermediate pH range, the removal of photo-oxidation products may become rate-determining, but as the resulting etched structures have generally poor morphologies, photoetching in this kinetic regime has no practical applications.

Results on laser-etching obtained by other investigators confirm the model of a corroding galvanic cell (see, e.g., ref. [89]). This model also explains the large discrepancies in the photoetching rates that are often observed between different experiments; these rates are indeed dependent on experimental parameters, such as the ratio of dark to illuminated surface area, coverage or exposure of the rear surface, etc. [87].

3.2.3 Chemical Etching

As stated in Sec. 3.1, valuable information on the mechanism of chemical etching processes can similarly be obtained by studying the electrochemical behavior of the interface. In the particular case of GaP, the conclusion that open-circuit etching of GaP single crystals in acidic Br_2 solutions proceeds via a chemical mechanism arises from two experimental observations. Firstly, current-potential measurements at p-GaP show that Br_2 cannot inject holes into the valence band of GaP, so that electroless etching can be excluded. Secondly, from etching rate measurements performed under different conditions of electrode polarization, it follows that cathodic polarization does not impede the etching of p-GaP, which is in agreement with a chemical mechanism.

The electrochemical reduction of Br_2 occurs via reactions (62) and (56) (photocurrent doubling at p-GaP [72]):

$$Br_2 + e^- \longrightarrow Br^{\cdot} + Br^- \qquad (62)$$

$$Br^{\cdot} \longrightarrow Br^- + h^+ \qquad (56)$$

and competes with the etching of GaP by Br_2 when sufficient electrons are available at the surface. Fig. 17 shows that under cathodic polarization, the chemical etching of $(\bar{1}\bar{1}\bar{1})$ n-GaP is almost completely suppressed by the cathodic reduction of Br_2. Rotating ring-disk experiments indicate that the consumption rate of Br_2 at $(\bar{1}\bar{1}\bar{1})$ n-GaP is limited by the Br_2 diffusion rate over the whole potential range, so that the constancy of the sum of the etching rate (expressed in $mA \cdot cm^{-2}$, assuming six-equivalent oxidation of GaP) and the absolute value of the reduction current density over the whole potential range in Fig. 17 leads us to conclude that the oxidation of the GaP surface by Br_2 indeed proceeds to Ga(III) and P(III). The stoichiometry of the chemical etching reaction may hence be written as:

$$GaP + 3Br_2 + 3H_2O \longrightarrow Ga^{3+} + H_3PO_3 + 3H^+ + 6Br^- \qquad (63)$$

At the n-GaP anode, the reverse dark current increases upon addition of Br_2 to indifferent H_2SO_4 solution [72], analogously to the increase of the reverse current in the presence of an electroless etching agent, i.e., a hole injector (see Sec. 2.3). Since

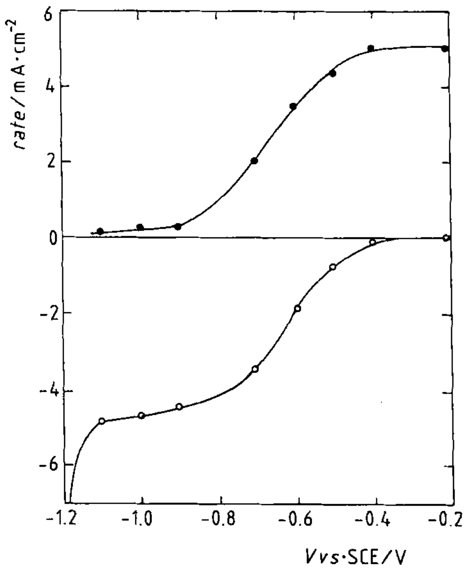

Fig. 17. Combined etching rate and current density vs. potential plots at $(\bar{1}\bar{1}\bar{1})$ n-GaP in aqueous 0.05 mol $\cdot$ l^{-1} Br_2 + 0.2 mol $\cdot$ l^{-1} KBr + H_2SO_4 (pH = 0). Flow rate u = 50 $cm^3 \cdot h^{-1}$. ● etching rate (expressed in $mA \cdot cm^{-2}$), ○ current density. (From ref. (72), by permission of Elsevier Sequoia).

none of the species in solution can possibly inject electrons into the conduction band of GaP, the electron injection current in the presence of Br_2 is attributed to the presence of decomposition intermediates of GaP, which are formed in reaction (63) and which can inject electrons into GaP, similarly to the intermediates formed by anodic decomposition (see Sec. 2.3). This indication of the presence of such intermediates contradicts the concerted etching mechanism formerly proposed for the GaAs etching by symmetrical bifunctional molecules, such as Br_2, H_2O_2, and I_2 [38]. Instead, one has to consider a mechanism involving consecutive steps and radical intermediates. On the basis of the experimental relationship between the electron injection current density and the chemical etching rate, a mechanism was proposed for the chemical etching of GaP in acidic Br_2 solutions [72]. In the first step, a GaP surface bond is assumed to be broken by a Br_2 molecule, leaving an electron-deficient bond X_1 (for meaning of the symbols X_0, X_1, X_1-OH and X_2, we refer to Sec. 2):

$$X_0 + Br_2 \longrightarrow X_1 + Br^{\cdot} + Br^- \tag{64}$$

The X_1 intermediate is assumed to be the same as the first intermediate of the anodic decomposition reaction (see reaction (4)). Similarly, the positive intermediate X_1 is first neutralized by water through reaction (46); the neutral species X_1-OH is subsequently oxidized by a $Br^{\cdot}$ radical:

$$X_1\text{-OH} + Br^{\cdot} \longrightarrow X_2 + Br^- \tag{65}$$

As in the case of anodic etching, electron injection by X_1 (reaction (51)) is considered to occur parallel to reaction (46). Further oxidation of X_2 to the final products proceeds analogously. The fact that the decomposition intermediates of the chemical etching process are essentially the same as those of the anodic etching process leads to mixed chemical-anodic etching of the p-GaP anode in acidic Br_2 solutions; the competitive chemical and anodic reactions are linked via the radical intermediates. This explains why at sufficiently high anodic polarization, the etching of p-GaP consumes neither 3 Br_2 molecules per GaP surface entity nor 6 holes, but 1 Br_2 molecule and 4 holes.

Similarly to the kinetics of the electroless etching of GaP in alkaline $Fe(CN)_6^{3-}$ solutions, the kinetics of the chemical etching of [111]-oriented GaP depend upon the crystal orientation: whereas the etching rate at the (111)-face is kinetically controlled, the etching rate at the $(\bar{1}\bar{1}\bar{1})$-face is diffusion-limited. This difference in reactivity of the GaP-face towards the electron acceptor Br_2 is explained by the difference in the Ga-P surface dipole orientation [72].

Kelly et al., in their study on the behavior of bisymmetrical molecules, such as Br_2 and H_2O_2, at the GaAs surface, observed an interdependence between the rates of chemical etching and of cathodic reduction, as well as an enhanced anodic dark current at n-type electrodes [79, 80] (see also Sec. 3.2.2). They concluded that hole injection, electron capture, and chemical etching reactions are coupled through a biradical-type common precursor, part of which is X_1, as defined in Sec. 2. The proposed reaction scheme is shown in Fig. 18. Such a mechanism, moreover, ac-

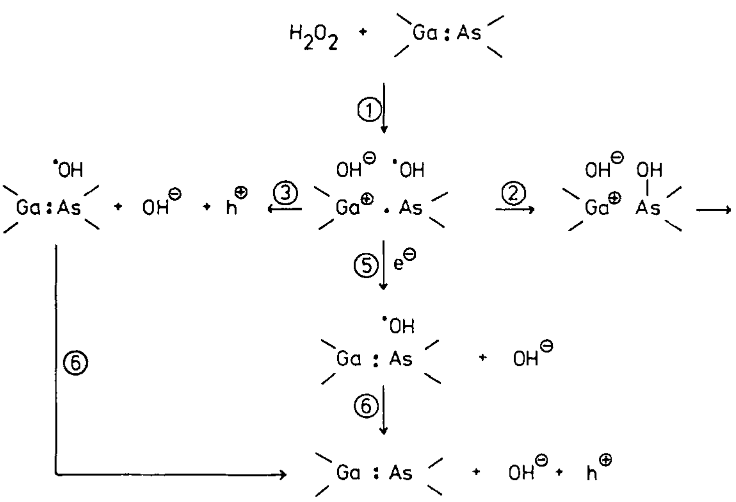

Fig. 18. Unified model for cathodic reduction and chemical etching at the GaAs/H_2O_2 interface. (From ref. (80), by permission of Elsevier Sequoia).

counts for the low hole injection rate observed at p-GaAs in these etchants, and it combines the observations of photocurrent doubling effect at p-GaAs with that of two recombination steps observed during impedance measurements at n-GaAs. Also in the case of GaAs etching by the asymmetrical hypohalite ions OBr^- and OCl^-, a similar reaction scheme seems to hold [90]. Combined kinetic and impedance results suggest the same reaction scheme for the GaAs/I_2 interface [91].

Etching of InP in iodic acid solutions also proceeds via a chemical mechanism involving consecutive steps [92]. By analogy with the case of GaP/Br_2, the stoichiometry of the etching reaction was identified as:

$$InP + HIO_3 + 2H^+ \longrightarrow In^{3+} + H_3PO_3 + I^- \qquad (66)$$

An enhanced anodic dark current was also observed at n-InP in the presence of HIO_3. On the basis of the kinetic results, an etching mechanism analogous to that of GaP/Br_2 was proposed, which can compete with the anodic etching of p-InP, resulting in a mixed chemical-anodic mechanism. The chemical etching rate was furthermore found to be diffusion-limited at the (111)-, $(\bar{1}\bar{1}\bar{1})$- as well as at the (100)-face. Other chemical etchants for InP include HCl, HBr, and Br_2 [93, 94]; in the case of HCl and HBr, it was demonstrated that etching involves undissociated molecules only. It is important to note that etching of InP by HCl or HBr is non-oxidative. Accordingly, in the case of etching of n-InP by HCl, anodic electron injection by decomposition intermediates is not observed [92], so that a concerted bond-exchange mechanism seems more likely for these reactions.

3.3 Etching Morphology

3.3.1 (Photo)anodic Etching

In order to discuss the correlation between etching kinetics and etching morphology, let us first reconsider the current-potential characteristics of III-V semiconductors, as depicted in Fig. 1. For the sake of clarity, the behavior in alkaline solutions (Fig. 1 (b)) is treated first. As announced, the discussion is mainly based on experimental results obtained from GaP single crystals.

For p-GaP, a distinction has to be made between the exponential region I of the i-V curve, in which the current densitiy is determined by the hole capture rate, and the plateau region II, in which the anodic current density and hence the etching rate is determined by diffusion of OH^- ions towards the surface. For n-GaP, a distinction has to be made between the photocurrent onset region I, in which surface recombination of the charge carriers is important, and the photocurrent plateau region, in which the current density is controlled either by OH^- diffussion (region II; high light intensities) or by the light-intensity dependent creation of electron-hole pairs (region III; low light intensities). The morphological results for the (photo)anodic etching of p- and n-GaP under different circumstances are summarized in Table 2.

This table clearly shows that for all three crystal faces studied, etching at a diffusion-limited rate leads to a flat surface (Table 2, cases A, B, C, and G, H, I). This is explained by the fact that for a diffusion-limited process, the etching rate is the same over the entire surface and is hence unaffected by solid-state factors.

As a result of etching at a rate below the diffusion limit, specific etch patterns develop at the surface, due to local differences in the rate of the surface reaction. As a consequence of etching p-GaP in the rising part of the i-V curve (Table 2, cases D, E, F), etch pits develop at the surface with a density of 10^5-10^6 cm^{-2} and with a geometry depending on the crystal orientation (Fig. 19): the pits at the $(\bar{1}\bar{1}\bar{1})$- and (111)-faces exhibit a more or less equilateral-triangular shape, whereas those at the (100)-face are roughly rectangular. Furthermore, it is important to note that at the (111)-face, the etch pits are more easily developed than at the $(\bar{1}\bar{1}\bar{1})$- and (100)-face. The etch pit formation and the difference in selectivity is explained as follows. As stated in Sec 2.1, in a p-type semiconductor holes are the majority carriers, constituting a quasi-equilibrium cloud at the surface. Surface bonds at dislocations and impurity sites may be assumed to be weaker than those at intact sites [31], resulting in an enhanced hole capture rate and hence in the formation of etch pits at these sites. Assuming that the reactivity at these defect sites is not or hardly affected by the crystal orientation, the observed difference in selectivity can be attributed to differences in the hole capture rate between the three crystal faces at intact sites, the higher selectivity at the (111)-face corresponding to a lower "normal" rate. The difference in the hole capture rates between the (111)- and the $(\bar{1}\bar{1}\bar{1})$-face can thus be associated with the Ga-P surface dipole orientation, which in the case of the $(\bar{1}\bar{1}\bar{1})$-face is in an energetically favorable direction for holes to reach the surface, in contrast to the (111)- face [31]. As to the similar reactivity of the (100)-face in comparison to the $(\bar{1}\bar{1}\bar{1})$-face, the assumption has been made, based upon experimental results, that the etching of the (100)-face actually proceeds perpendicularly to the {111}-faces, so that for the (100)-face the opportunity always exists to etch the {111}-face pairs from the P-side and hence to obtain an etch reactivity similar to that of the $(\bar{1}\bar{1}\bar{1})$-face [20].

Table 2. Survey of results on (photo)anodic etching of GaP in aqueous 0.1 mol · l^{-1} KOH solutions.

Identification letter	Type	Face	Etching conditions	Rate-determining step	Surface morphology
A	p	$(\bar{1}\bar{1}\bar{1})$	anodic current plateau (fig. 1 (p) (b) region II)	OH^- diffusion	homogeneously flat
B	p	(111)	see A	see A	see A
C	p	(100)	see A	see A	see A
D	p	$(\bar{1}\bar{1}\bar{1})$	rising part of *i*, *V*-curve (fig.1 (p) (b) region I)	surface reaction (kinetically controlled)	equilateral triangular etch pits, see fig. 19
E	p	(111)	see D	see D	see D, but more selective (fig. 19)
F	p	(100)	see D	see D	rectangular pits (fig. 19)
G	n	$(\bar{1}\bar{1}\bar{1})$	photocurrent plateau, high light intensity (fig. 1 (n) (b) region II)	OH^- diffusion	homogeneously flat
H	n	(111)	see G	see G	see G
I	n	(100)	see G	see G	see G
J	n	$(\bar{1}\bar{1}\bar{1})$	photocurrent plateau, low light intensity (fig. 1 (n) (b) region III)	hole supply, controlled by $e^- - h^+$ photogeneration	microrough
K	n	(111)	see J	see J	starlike etch pits (fig. 21 b)
L	n	(100)	see J	see J	microrough (fig.21 a)
M	n	$(\bar{1}\bar{1}\bar{1})$	photocurrent onset (fig. 1 (n) (b) region I)	hole supply, controlled by $e^- - h^+$ photogeneration and recombination	etch hillocks and ridges
N	n	(111)	see M	see M	see M (fig. 20)
O	n	(100)	see M	see M	see M

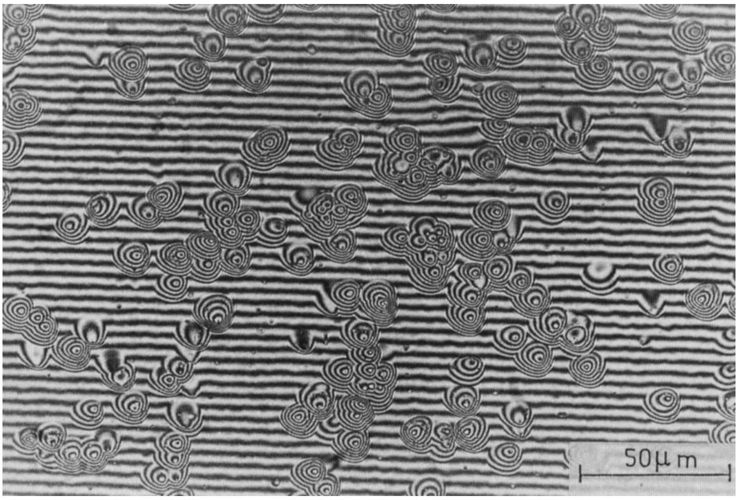

Fig. 19. Interference photomicrograph of the (111) p-GaP surface after etching for 30 min. at $i = 4.5$ mA · cm^{-2} in aqueous KOH (pH = 13). (From ref. (31), reprinted by permission of the publisher, The Electrochemical Society, Inc.).

When etching n-GaP photoanodically in the onset region I of the photocurrent-potential curve (Table 2, cases M, N, O), etch hillocks and ridges are observed at the surface after removal of only a small amount of material (see, e.g., Fig. 20). In this region of the i-V curve, recombination of the photogenerated charge carriers

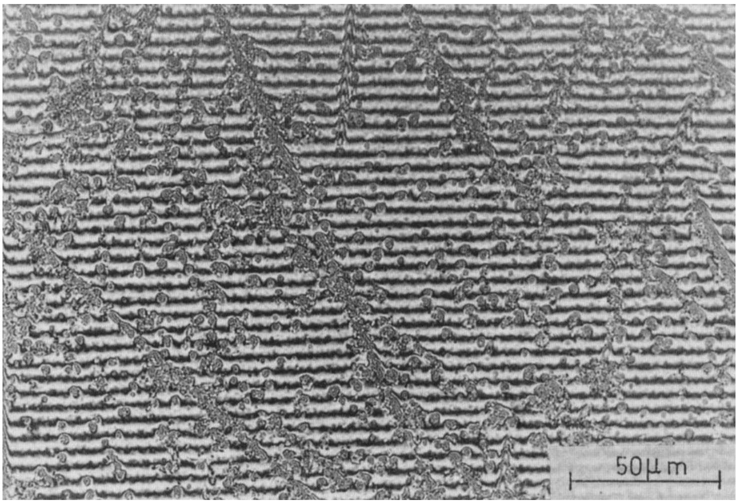

Fig. 20. Interference photomicrograph of the (111) n-GaP surface after etching during 10 min. at $i = 0.3$ mA · cm^{-2} in aqueous KOH (pH = 13); full light intensity. (From ref. (31), reprinted by permission of the publisher, The Electrochemical Society, Inc.).

predominates. As dislocations and damaged sites locally enhance the recombination rate, the local surface concentration of holes will be lower than that of the surroundings, resulting in the formation of etch hillocks. This interpretation of the occurence of elevations has been evidenced directly in the case of n-GaAs anodes by laser scanning of the electrode surface after photoanodic etching, which demonstrated that at elevated lines, apparently associated with mechanical damage, the local photocurrent is indeed lower than elsewhere on the surface [95]. The fact that the etch rate is controlled by the supply of holes, not by their reactivity, explains the similarity in the results obtained at the three faces [20].

In the photocurrent plateau region III, in which the photocurrent density is determined by the light intensity, etching of n-GaP ($\bar{1}\bar{1}\bar{1}$) and (100) crystal faces leads to a microrough surface, with a few scratches developed as ridges (Table 2, cases J and L), whereas at the (111)-face, isosceles triangular pits are formed in three orientations at 120° angles, often forming starlike configurations (see Table 2, case K), see Fig. 21. The interpretation of these cases is based on the assumption that, in contrast to p-GaP, the holes at the n-GaP surface do not constitute a quasi-equilibrium cloud [31]. Instead, they are created in the semiconductor by light and move through the space-charge region to the surface, where they can be assumed to react almost immediately. The microroughness of the ($\bar{1}\bar{1}\bar{1}$)- and (100)-face is thus interpreted by assuming an inhomogeneous flow of holes through the space-charge layer, a concept introduced by Tenne et al. [96–98] in their work on II–VI semiconductors. The few ridges observed are attributed to mechanical damage (resulting from pretreatment) extending deeper than the width of the space-charge region, and hence leading to recombination in the diffusion layer [20]. The different morphology of the (111)-face

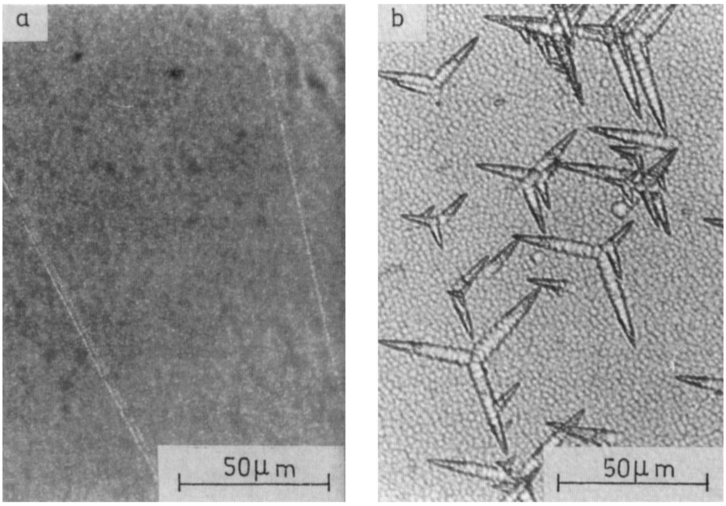

Fig. 21. Photomicrograph of the n-GaP surface after etching at $V = +1.6$ V (vs. SCE) in aqueous KOH (pH = 13). (a) (100)-face, light intensity = 10% of full value, etching time = 15 min. (b) (111)-face, light intensity = 15% of full value, etching time = 1 h. (From ref. (20), by permission of Pergamon Press).

can likewise be attributed to a lower hole capture reactivity, so that holes at the (111)-face have more chance to move parallelly to the surface and hence to react selectively at reactive sites [31]. The typical morphology of the starlike pits is not fully understood yet, but the fact that this morphology only develops at photoanodically etched n-type surfaces indicates a possible effect of non-uniform hole flow towards the surface. Similar etch pits have been reported for n-GaAs [99-101], also without a satisfactory explanation.

In acidic solutions, surface morphologies analogous to the corresponding cases in alkaline solutions are obtained, although etching in acidic media seems to proceed less selectively than in alkaline media [20]. In contrast to alkaline solutions, a steady-state condition in which the anodic current density is diffusion-limited does not exist. Instead, in acidic solutions at sufficiently high anodic current densities, passivation of the GaP surface occurs (see Fig. 1 (n) (a), region II and Fig. 1 (p) (a), region II). Etching in this region does not lead to homogeneously flat surfaces; scratches are observed on p-GaP, whereas large-sized etch pits as well as a few scratches form on n-GaP. The development of these etch figures must obviously be related to the physical and chemical properties of the passivation layer, such as the adherence of the layer, the rates of electron and ion transport through this layer, the optical absorption, etc., which are still unknown.

Although there is no systematic comparative study of the kinetics of the anodic dissolution reaction and the morphology of the etched surface of GaAs and InP, it seems that several of the conclusions drawn for GaP also hold for these materials. It was, e.g., found that photoanodic etching of n-GaAs and n-InP in the photocurrent onset region leads to very selective etching and formation of etch hillocks, whereas photoanodic etching in the photocurrent plateau region is often found to be hardly selective, and may lead to the development of sporadic etch pits [101-105].

To summarize the described results, we may conclude that a marked difference exists between p- and n-type crystals. With p-type crystals, the holes are spread out over the surface in a quasi-equilibrium cloud, so that local differences in anodic reaction rate are due to differences in the hole capture rate. With n-type crystals, the holes are minority carriers, and their reaction rate at the surface is mainly determined by their availability. They are created by light in the semiconductor and transported through the space-charge layer towards the surface, where they may diffuse laterally to a certain extent, depending on their rate of capture. The latter effect also occurs during fabrication of diffraction gratings by a photoanodic etching process. A very attractive method is direct holographic recording of submicron gratings on III-V materials [5, 105-109]. Such gratings find applications in the fabrication of distributed feedback (DFB) lasers, as well as in input and output couplers in integrated optics. The great advantage of such a photoelectrochemical etching process is that no masking is required, since the spatial distribution of the light intensity is created by interference of two coherent laser beams. The quality of the recorded interference patterns, however, is reduced by any lateral spread in the photogenerated charge carriers. Two theoretical models have been developed to describe the resolution of the etching process [5, 108]. In both models, the same conclusion is reached, i.e., the resolution can largely be improved by using reactants with a high reaction rate, so that the photogenerated holes have little opportunity to spread out over the surface. An alternative procedure for fabricating gratings involves using a photoresist mask to create the spatial distribution of the light intensity [110-112]. It is interesting to note that in these cases, too, poor resolution (i. e., undercutting of the mask) is associated with the presence of lateral diffusion of holes, due to slow kinetics of consumption by the interfacial reaction [111].

3.3.2 Electroless Etching

The GaP/$Fe(CN)_6^{3-}$ system is used to illustrate the factors determining the morphology in electroless etching.

As mentioned in Sec. 3.2.1, alkaline $K_3Fe(CN)_6$ solutions are often used to differentiate between the two polar faces of GaP, i. e., the (111)- and $(\bar{1}\bar{1}\bar{1})$-face [74]. In fact, in most cases more or less equilateral triangular etch pits develop at the (111)-face (see, e. g., Fig. 22), whereas the $(\bar{1}\bar{1}\bar{1})$-face is etched homogeneously. The situation, however, is slightly more complex, since equilateral triangular etch pits were also observed at $(\bar{1}\bar{1}\bar{1})$ p-GaP, but only at $Fe(CN)_6^{3-}$ concentrations below 0.3 mol · l^{-1} and after a very long etching time (>48 h). In order to facilitate the discussion of these observations, the morphological results on electroless etching by $Fe(CN)_6^{3-}$ are summarized in Table 3.

The morphology of etched surfaces can be understood on the basis of the electroless mechanism and hence according to electrochemical principles. To this end, it is assumed that the two partial electrochemical reactions constituting the electroless process do not necessarily take place at the same sites, a concept which is currently used in metallic corrosion. Furthermore, since only the anodic partial current

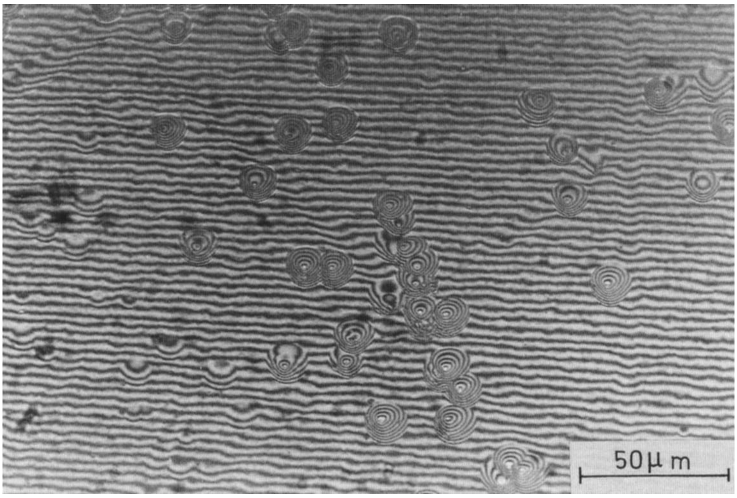

Fig. 22. Interference photomicrograph of the (111) n-GaP surface after etching for 1 h. in aqueous 0.75 mol · l^{-1} $K_3Fe(CN)_6$ + KOH (pH = 13); $V = V_r$; flow rate u = 10 cm^3 · h^{-1}. (From ref. (73), by permission of Pergamon Press).

Table 3. Survey of results on electroless etching of GaP in alkaline $Fe(CN)_6^{3-}$ solutions [from ref. (20)].

Face	Type	$Fe(CN)_6^{3-}$ concentration	Schematic i-V behavior	Rate-determining step	Surface morphology
(111)	p	$c \leq 1 \text{ mol} \cdot l^{-1}$	fig. 13a	injection of h^+, kinetically controlled	equilateral triangular pits
	n	$c \leq 1 \text{ mol} \cdot l^{-1}$	fig. 13c	injection of h^+, kinetically controlled	equilateral triangular pits
$(\bar{1}\bar{1}\bar{1})$	p	$c < 0.3 \text{ mol} \cdot l^{-1}$	fig. 13a	diffusion of $Fe(CN)_6^{3-}$	equilateral triangular pits, only observed after a long etching time
		$0.3 \leq c \leq 1 \text{ mol} \cdot l^{-1}$	fig. 13b	diffusion of OH^-	homogeneously flat
	n	$c < 0.3 \text{ mol} \cdot l^{-1}$	fig. 13c	diffusion of $Fe(CN)_6^{3-}$	homogeneously flat
		$0.3 \leq c \leq 1 \text{ mol} \cdot l^{-1}$	fig. 13d	diffusion of OH^-	homogeneously flat

involves dissolution of the semiconductor, it is important to realize that the surface morphology reflects only local differences in the anodic partial current density. In p-GaP, the holes, being the majority carriers, are at quasi-equilibrium at the surface. The anodic partial reaction rate at a given site is thus determined by the local hole capture reactivity, which hence determines the surface morphology, except when the anodic partial reaction rate is limited by OH^- diffusion. In the latter case, the anodic partial reaction rate is the same over the entire surface. The case of n-GaP, however, is quite different. Here, holes are the minority carriers, and since they can be assumed to be very rapidly captured in surface bonds (see Sec. 3.3.1 and ref. [31]), it is now the availability of holes at the surface that determines the anodic partial reaction rate and hence the surface morphology. In electroless etching, holes are supplied by injection from solution (reaction (53)), so that for n-GaP, the anodic partial reaction (13') is expected to take place near the sites where the holes are injected by $Fe(CN)_6^{3-}$. The morphology thus reflects local differences in the hole injection rate. If either the injection rate is limited by $Fe(CN)_6^{3-}$ diffusion or the anodic partial reaction rate is limited by OH^- diffusion, the anodic partial current density is constant over the entire surface.

If we keep these reflections in mind, interpretation of the morphology of the GaP surface etched in alkaline $K_3Fe(CN)_6$ solutions is straightforward. At the (111)-face, the overall etch rate is kinetically controlled. The i-V curves for the p-type (111) GaP-face are schematically shown in Fig. 13a, which demonstrates that the situation at the rest potential V_r corresponds to the rising part of the anodic partial current density. Etch pits are formed due to local differences in hole capture reactivity, analogously to the anodic etching of p-GaP in the rising part of the i-V curve (Fig. 1

(p) (b), region I). The i–V behavior of the n-type (111) GaP-face is schematically represented in Fig. 13c. Etch pits are formed at sites with a locally enhanced hole injection rate, due to a locally higher position of the valence band edge (dislocation sites). In this case, the situation is analogous to the photoanodic etching of n-GaP in the photocurrent plateau (Fig. 1 (n) (b), region III) in that the morphology is determined by local differences in the availability of holes at the surface. An important difference, however, is the fact that in this case the holes are not created by photons inside the semiconductor, but are injected from the solution. This explains why in the case of electroless etching, no etch pits in starlike configurations are observed, since – as assumed in Sec. 3.3.1 – this specific geometry is a consequence of the inhomogeneous flow of holes through the space–charge layer.

Let us now consider the $(\bar{1}\bar{1}\bar{1})$-face. For the p-type $(\bar{1}\bar{1}\bar{1})$ GaP-face and at low $Fe(CN)_6^{3-}$ concentrations (< 0.3 mol · l^{-1}) the overall etching rate is determined by diffusion of $Fe(CN)_6^{3-}$. The rest potential V_r is thus found in the rising part of the anodic partial current density curve (Fig. 13a), and etch pits are similarly formed as a result of local differences in the hole capture reactivity. The fact that these pits are only visible after a long etching time may, on the one hand, be ascribed to the low etching rate at these low concentrations and, on the other hand, be attributed to the low selectivity of the $(\bar{1}\bar{1}\bar{1})$-face, as discussed in Sec. 3.3.1. At high $Fe(CN)_6^{3-}$ concentrations, the overall etching rate at p-GaP is determined by the diffusion rate of OH^-. The rest potential V_r thus corresponds to the plateau region of the anodic partial current density curve (Fig. 13b), so that etching leads to a homogeneously flat surface, as in the case of anodic etching of p-GaP in the diffusion-limited regime (Fig. 1 (p) (b), region II). For the n-type $(\bar{1}\bar{1}\bar{1})$ GaP-face at low $Fe(CN)_6^{3-}$ concentrations (<0.3 mol · l^{-1}), the overall etching rate is determined by $Fe(CN)_6^{3-}$ diffusion. The i–V behavior is shown schematically in Fig. 13c; the etched surface is homogeneously flat, since the hole supply, i.e., the hole injection rate, is the same over the entire surface. At high $Fe(CN)_6^{3-}$ concentrations (>0.3 mol · l^{-1}), the overall etching rate at n-type $(\bar{1}\bar{1}\bar{1})$ GaP is limited by the OH^- diffusion rate. Schematic i–V curves are shown in Fig. 13d, in which the anodic partial current density reaches its OH^- diffusion limit. A flat surface is formed, analogously to the diffusion-limited, photoanodically etched surfaces (Fig. 1 (n) (b), region II).

In summary, the interpretation of the morphology of electroless etching processes at GaP is analogous to the proposed interpretation of (photo)anodic etching. In electroless etching, though, the potential is not applied by an external source, but it is imposed as a rest potential through addition of $Fe(CN)_6^{3-}$ to the solution.

In the case of open-circuit etching of GaAs in $K_3Fe(CN)_6$ solutions, it was found that etch pits develop at both n- and p-GaAs when etching is diffusion-limited through the cathodic partial reaction [13]. In the profile etching of GaAs in alkaline $K_3Fe(CN)_6$ solutions, a difference in profile shape is observed, depending on whether the process is diffusion-limited by $Fe(CN)_6^{3-}$ or by OH^-, independently of the semiconductor type. Whereas a round profile, typical of diffusion-limited etching, is observed at the resist edge when OH^- diffusion is rate-limiting, a faceted (anisotropic) profile develops when $Fe(CN)_6^{3-}$ diffusion determines the etching rate. This observation has been interpreted in terms of galvanic element formation between different crystal planes, which is in some way analogous to the interpretation of etch pit formation at p-GaP during etching at a $Fe(CN)_6^{3-}$ diffusion-limited rate, since in both cases a spatial seperation into anodic and cathodic regions is assumed. The fact that with GaAs, in contrast to GaP, a distinction between diffusion limitation by the cathodic and by the anodic partial reaction is also observed at n-type crystals may be due to the higher hole mobility in GaAs, which might enable the holes, injected at a diffusion-limited rate, to move along the surface before being captured selectively.

3.3.3 Photoetching

Photoetched (111)- and $(\bar{1}\bar{1}\bar{1})$-faces of GaP in alkaline OBr^- solutions show a remarkable difference in terms of morphology: etch hillocks develop on n-GaP (similar to those formed by photoanodic etching of n-GaP in the onset region of the photocurrent-potential curve), whereas etch pits are formed on p-GaP (similar to those formed by anodic etching of p-GaP in the rising part of the i-V curve) [31].

By analogy with electroless etching, it is assumed that on the microscale, the two partial reactions under consideration do not necessarily take place at the same sites. The morphology thus reflects local differences in the hole supply rate for n-GaP and local differences in the hole capture reactivity for p-GaP. At n-GaP, the anodic partial reaction proceeds by the minority carriers. The situation at the rest potential corresponds to the onset of the photocurrent-potential curve (see Fig. 14), in which recombination processes determine the availability of holes and hence the value of the current density. The hillocks formed by photoetching thus correspond to sites where the recombination rate is high (dislocation sites, damaged areas). In the case of p-GaP, however, the holes being the majority carriers, locally enhanced recombination leads to a local decrease of the cathodic partial current density (and hence to a decrease of the overall etching rate), but does not significantly influence the local anodic partial current density. The situation in this case is analogous to the anodic etching of p-GaP in the rising part of the i-V curve (see also Fig. 20): the holes are at quasi-equilibrium at the surface, so that etch pits develop at sites with an enhanced reactivity for hole capture.

In the case of GaAs photoetching in CrO_3-HF solutions, etch hillocks are formed both on n- and p-type crystals [113-114]. Hillocks, however, are also observed in the dark, and their occurrence has been explained on the basis of the complex reaction scheme described by Eqs. (58)-(61). The CrO_3-HF etch has been found to be very sensitive to defects at GaAs and even more so at InP crystals [115].

3.3.4 Chemical Etching

In the case of the chemical etching of n- and p-GaP in acidic Br_2 solutions, it was found that the $(\bar{1}\bar{1}\bar{1})$-face is always etched homogeneously flat, whereas more or less equilateral triangular etch pits are formed at the (111)-face [73]. No difference is observed between n- and p-type crystals. This may be explained as follows. Since etching does not involve holes, considerations pertaining to free charge carriers of the semiconductor are irrelevant. At the $(\bar{1}\bar{1}\bar{1})$-face, the etching rate is determined by diffusion of Br_2 and is hence equal at all sites (homogeneous etching). At the (111)-face, where the etching rate is determined by the surface reaction (63) itself, sites with a higher reactivity (defect sites) will be etched faster and will hence form etch pits.

The morphology of chemical etching, however, is not always this simple; a more complicated case, for instance, is InP etching by HIO_3 [92]. In this case, it was found that, although the etching rate is under diffusion control at all three crystal faces considered ((111), $(\bar{1}\bar{1}\bar{1})$ and (100)), triangular etch pits are developed at the (111)-face, whereas the $(\bar{1}\bar{1}\bar{1})$- and (100)-faces are etched more or less homogeneously. The following explanation has been offered. As mentioned in Sec. 3.2.3, the etching mechanism consists of different consecutive steps, involving the formation of decomposition intermediates and of intermediates of the I(V) reduction. The rate of the first step in the decomposition reaction, in which an In–P bond is broken by an HIO_3 molecule (leading to the formation of a first intermediate X_1) may be assumed to be determined by the supply of HIO_3 at the surface. Hence, at all surface sites, X_1 is formed at the same rate. If, however, one of the subsequent steps is sensitive to local variations in the reaction rate, then the reaction between an intermediate of the I(V) reduction and a decomposition intermediate will be slow at sites with a low intrinsic reaction rate, so that the I(V)-reduction intermediates have the opportunity to move along the surface and hence to react selectively at sites with a higher intrinsic rate. At these sites, etch pits will hence develop. The fact that no pits are observed at the $(\bar{1}\bar{1}\bar{1})$- and (100)-faces can be explained by assuming a higher reactivity at these faces, analogously to the etching of GaP (see Sec. 3.3.1), so that at these faces, the I(V)-reduction intermediates are less likely to move along the surface.

4 Conclusions and Prospects

This discussion shows that the insights concerning the mechanisms of anodic decomposition reactions of III–V semiconductors, obtained from electrochemical measurements, significantly contribute to the unraveling of the mechanisms of etching processes without external current flow. Combined electrochemical and etching experiments, for instance, indicate that the dark etching of GaAs and GaP by Br_2 proceeds via a non-concerted chemical mechanism, and that the photoetching of GaP by OBr^- and that of InP by Fe^{3+} involves simple superposition of anodic and cathodic partial currents. In addition, it appears that also the surface morphology obtained after anodic as well as after open-circuit etching can to a large extent be understood on the basis of electrochemical experiments and concepts. Thus, the observed difference in the surface morphology between n- and p-type GaP after dark etching in $Fe(CN)_6^{3-}$ or after photoetching in OBr^-, for instance, has been rationalized.

This electrochemical approach hence appears to provide a fundamental scientific basis for the understanding of existing as well as for the development of new etching procedures, which hitherto were established mainly by trial and error. This is particularly important in view of the ever increasing complexity and degree of miniaturization in semiconductor device technology. In the specific case of III-V semiconductors, the need for wet etching processes with well-controlled rates, selectivity, and resulting profiles is especially obvious in the field of optoelectronics. The fabrication of devices such as LEDs and laser diodes requires a pattern definition on the microscale in multilayer structures involving binary, ternary, and quaternary III-V semiconductors. It therefore seems particularly important to extend the present line of research to mixed III-V semiconductors. Some of the studies that have been published on this subject point to many interesting features caused by the influence of the chemical and physical properties of the materials involved upon the etching characteristics [13, 116].

An important future objective in the present field of research evidently concerns surface characterization during and after the anodic and open-circuit processes under consideration, not only as far as the surface composition is concerned, but also from the viewpoint of the surface microstructure and defect structure. Recently developed in-situ techniques such as FTIR, photocurrent imaging by laser scanning and STM may constitute excellent tools for this purpose.

Acknowledgements. The financial support from the I.I.K.W. (Inter-University Institute for Nuclear Sciences, Belgium) is gratefully acknowledged.

5 References

1. W.H. Brattain and C. G. B. Garrett, Bell. Syst. Tech. J. 34, 129-176 (1955).
2. H. Gerischer, in: Adv. Electrochemistry and Electrochem. Eng., P. Delahay (ed.), Interscience, New York (1961), Vol. I, pp. 139-232.
3. H. Gerischer, in: Physical Chemistry, An Advanced Treatise, H. Eyring (ed.), Academic Press, New York (1970), Vol. IX A, pp. 436-542.
4. S. R. Morrison, Electrochemistry at Semiconductor and Oxidized Metal Electrodes, Plenum Press, New York (1980).
5. Yu. V. Pleskov and Yu. Ya. Gurevich, Semiconductor Photoelectrochemistry, Consultants Bureau, New York (1986).
6. A. Fujishima and K. Honda, Nature 238, 37-38 (1972).
7. H. Gerischer, J. Electroanal. Chem. 58, 263-274 (1975).
8. R. Hill and M. D. Archer, J. Photochem. and Photobiol. A 51, 45-54 (1990).
9. M. Datta and L. T. Romankiw, J. Electrochem. Soc. 136, 285C-292C, (1989).
10. H. Beneking, J. Electrochem. Soc. 136, 2680-2686 (1989).
11. S. J. Moss and A. Ledwith, The Chemistry of the Semiconductor Industry, Blackie & Son, London (1987).
12. D. V. Morgan and K. Board, An Introduction to Semiconductor Microtechnology, J. Wiley & Son, Chichester (1990), p. 34.
13. P. H. L. Notten, J. E. A. M. van den Meerakker, and J. J. Kelly, Etching of III-V Semiconductors: An Electrochemical Approach, Elsevier Advanced Technology, Oxford (1991).
14. J. Li and L. M. Peter, J. Electroanal. Chem. 199, 1-26 (1986).
15. M. Pourbaix, Atlas d'Equilibres Electrochimiques, Gauthier-Villars, Paris (1963), pp. 436-442.

16. A. Gagnaire, J. Joseph and A. Etcheberry, J. Electrochem. Soc. 134, 2475-2478 (1987).
17. D. S. Ginley and M. A. Butler, in: Semiconductor Electrodes, H. O. Finklea (ed.), Elsevier, Amsterdam (1988), Chap. 7.
18. F. W. Ostermayer, Jr. and P. A. Kohl, Appl. Phys. Lett. 39, 76-78 (1981).
19. W. J. Plieth, G. Pfuhl, A. Felske, and W. Badawy, Electrochim Acta 34, 1133-1140 (1989).
20. H. H. Goossens and W. P. Gomes, Electrochim. Acta 37, 811-826 (1992).
21. F. Decker, Electrochim. Acta 30, 301-304 (1985).
22. P. H. L. Notten, Electrochim. Acta 32, 575-581 (1987).
23. R. Memming and G. Schwandt, Electrochim. Acta 13, 1299-1310 (1968).
24. H. H. Goossens, F. Van den Kerchove, and W. P. Gomes, J. Electroanal. Chem. 261, 89-103 (1989).
25. S. Lingier, W. P. Gomes, and F. Cardon, Ber. Bunsenges. Phys. Chem. 93, 2-7 (1989).
26. W. P. Gomes and F. Cardon, Progr. Surf. Sci. 12, 155-216 (1982).
27. H. Gerischer, Ber. Bunsenges. Phys. Chem. 69, 578-583 (1965).
28. R. L. Meek and N. E. Schumaker, J. Electrochem. Soc. 119, 1148-1152 (1972).
29. M. J. Madou, F. Cardon, and W. P. Gomes, Ber. Bunsenges. Phys. Chem. 81, 1186-1190 (1977).
30. D. Vanmaekelbergh, Lu Shou yun, W. P. Gomes, and F. Cardon J. Electroanal. Chem. 221, 187-196 (1987).
31. H. H. Goossens and W. P. Gomes J. Electrochem. Soc. 138, 1696-1701 (1991).
32. E. A. Efimov and I. G. Erusalimchik, Elektrokhimiya 1, 818-821 (1965).
33. P. A. Kohl, C. Wolowodiuk, and F. W. Ostermayer, Jr., J. Electrochem. Soc. 130, 2288-2293 (1983).
34. I. E. Vermeir, F. Van den Kerchove, and W. P. Gomes, J. Electroanal. Chem. 313, 141-159 (1991).
35. S. Preusser, M. Herlem, A. Etcheberry, and J. Jaume, Electrochim. Acta 37, 289-295 (1992).
36. A. B. Ellis, J. M. Bolts, and M. S. Wrighton, J. Electrochem. Soc. 124, 1603-1607 (1977).
37. H. Gerischer and F. Beck, Z. Phys. Chem. NF 13, 389-395 (1957).
38. H. Gerischer and I. Wiallem-Mattes, Z. Phys. Chem. NF 64, 187-198 (1969).
39. P. Janietz, R. Weiche, J. Westfahl, and R. Landsberg, J. Electroanal. Chem. 112, 63-70 (1980).
40. D. Vanmaekelbergh, J. J. Kelly, S. Lingier, and W. P. Gomes, Ber. Bunsenges. Phys. Chem. 92, 1068-1072 (1988).
41. D. Vanmaekelbergh and J. J. Kelly, J. Electrochem. Soc. 136, 108-113 (1989).
42. A. Etcheberry, J. Gautron, E. M. Khoumri, and J. L. Sculfort, J. Electroanal. Chem. 283, 177-186 (1990).
43. P. Allongue and S. Blonkowksi, J. Electroanal. Chem. 316, 57-77 (1991).
44. P. Allongue and S. Blonkowksi, J. Electroanal. Chem. 317, 77-79 (1991).
45. T. Solomun, R. McIntyre, W. Richtering, and H. Gerischer, Surface Sci. 169, 414-424 (1986).
46. S. Lingier and W. P. Gomes, Ber. Bunsenges. Phys. Chem. 95, 170-176 (1991).
47. W. J. Albery and M. L. Hitchmann, Ring-Disc Electrodes, Clarendon Press, Oxford (1971).
48. F. Van Overmeire, F. Van den Kerchove, W. P. Gomes, and F. Cardon, Bull. Soc. Chim. Belg. 89, 181-186 (1980).
49. F. Cardon, W. P. Gomes, F. Van den Kerchove, D. Vanmaekelbergh, and F. Van Overmeire, Disc. Faraday Soc. 70, 153-164 (1980).
50. K. W. Frese Jr., M. J. Madou, and S. R. Morrison, J. Phys. Chem. 84, 3172-3178 (1980).
51. H. Gerischer and M. Lübke, Ber. Bunsenges. Phys. Chem. 87, 123-128 (1983).
52. W. P. Gomes, S. Lingier, and D. Vanmaekelbergh, J. Electroanal. Chem. 269, 237-249 (1989).
53. D. Vanmaekelbergh, W. P. Gomes, and F. Cardon, J. Electrochem. Soc. 129, 546-550 (1982).
54. S. Lingier, D. Vanmaekelbergh, and W. P. Gomes, J. Electroanal. Chem. 228, 77-88 (1987).
55. S. Lingier and W. P. Gomes, Port. Electrochim. Acta 6, 85-104 (1988).
56. D. Vanmaekelbergh, Ph. D. Thesis, University of Gent (1984).
57. D. Vanmaekelbergh, W. P. Gomes, and F. Cardon, Ber. Bunsenges. Phys. Chem. 89, 987-994 (1985).

58. S. Lingier, D. Vanmaekelbergh, and W. P. Gomes, in: Photocatalytic Production of Energy-Rich Compounds, D. O. Hall and G. Grassi (eds.), Elsevier Applied Science Publishers, London (1988), pp. 127-137.
59. P. Allongue and H. Cachet, J. Electrochem. Soc. 131, 2861-2868 (1984).
60. P. Allongue and H. Cachet, Electrochim. Acta 33, 79-87 (1988).
61. K. Strubbe, H. H. Goossens, and W. P. Gomes, Electrochim. Acta, 37, 1343-1350 (1992).
62. Lu Shou yun, D. Vanmaekelbergh, W. P. Gomes, and F. Cardon, Ber. Bunsenges. Phys. Chem. 91, 390-394 (1987).
63. D. Vanmaekelbergh and W. P. Gomes, J. Phys. Chem. 94, 1571-1575 (1990).
64. D. Vanmaekelbergh, C. W. Hoogendam, and J. J. Kelly, J. Electroanal. Chem. 270, 175-189 (1989).
65. D. Vanmaekelbergh and J. J. Kelly, J. Phys. Chem. 94, 5406-5412 (1990).
66. D. Lincot and J. Vedel, J. Phys. Chem. 92, 4103-4110 (1988).
67. P. Allongue, S. Blonkowski, and D. Lincot, J. Electroanal. Chem. 300, 261-281 (1991).
68. H. Gerischer and I. Mattes, Z. Phys. Chemie NF 49, 112-126 (1966).
69. H. Gerischer and W. Mindt, Electrochim. Acta 13, 1329-1341 (1968).
70. H. Gerischer, Surf. Sci. 18, 97-122 (1969).
71. J. J. Kelly, J. E. A. M. van den Meerakker, and P. H. L. Notten, in: „Grundlagen von Elektrodenreaktionen", J. W. Schultze (ed.), Dechema Monographien Band 102, VCH, Frankfurt (1986), p.p. 453-464.
72. H. H. Goossens, K. Strubbe, and W. P. Gomes, J. Electroanal. Chem. 286, 133-149 (1990).
73. H. H. Goossens, I. E. Vermeir, F. Van den Kerchove, and W. P. Gomes, Electrochim. Acta 35, 1351-1358 (1990).
74. L. R. Plauger, J. Electrochem. Soc. 121, 455-457 (1974).
75. R. M. Feenstra, J. A. Stroscio, J. Tersoff, and A. P. Fein, Phys. Rev. Letters 58, 1192-1195 (1987).
76. H. Gerischer, I. Mattes, and R. Braun, J. Electroanal. Chem. 10, 553-567 (1965).
77. F. Decker, B. Pettinger, and H. Gerischer, J. Electrochem. Soc. 130, 1335-1339 (1983).
78. J. J. Kelly and P. H. L. Notten, Electrochim. Acta 29, 589-596 (1984).
79. B. P. Minks, G. Oskam, D. Vanmaekelbergh, and J. J. Kelly, J. Electroanal. Chem. 273, 119-131 (1989).
80. B. P. Minks, D. Vanmaekelbergh, and J. J. Kelly, J. Electroanal. Chem. 273, 133-145 (1989).
81. H. H. Goossens, W. P. Gomes, and F. Cardon, J. Electroanal. Chem. 278, 335-349 (1990).
82. J. van de Ven, J. E. A. M. van den Meerakker, and J. J. Kelly, J. Electrochem. Soc. 132,3020-3026 (1985).
83. J. J. Kelly, J. van de Ven, and J. E. A. M. van den Meerakker, J. Electrochem. Soc. 132, 3026-3033 (1985).
84. J. van de Ven, A. F. Lourens, J. L. Weyher, and L. J. Gilling, Chemotronics 1, 19-26 (1986).
85. F. Kuhn-Kuhnenfeld, J. Electrochem. Soc. 119, 1063-1068 (1972).
86. R. W. Haisty, J. Electrochem. Soc. 108, 790-794 (1961).
87. J. van de Ven and H. J. P. Nabben, J. Electrochem. Soc. 137, 1603-1610 (1990).
88. J. van de Ven and H. J. P. Nabben, J. Electrochem. Soc. 138, 144-152 (1991).
89. M. N. Ruberto, X. Zhang, R. Scarmozzino, A. E. Willner, D. V. Podlesnik, and R. M. Osgood, Jr., J. Electrochem. Soc. 138,1174-1185 (1991).
90. B. P. Minks, M. Wiegel, and J. J. Kelly, Electrochim. Acta 36, 695-701 (1991).
91. J. E. A. M. van den Meerakker, Electrochim. Acta 30, 435-440 (1985).
92. I. E. Vermeir, H. H. Goossens, F. Van den Kerchove, and W. P. Gomes, J. Electrochem. Soc. 139,1389-1396 (1992).
93. P. H. L. Notten and A. A. J. M. Damen, Appl. Surf. Sci. 28, 331-344 (1987).
94. P. H. L. Notten, J. Electrochem. Soc. 131, 2641-2644 (1984).
95. R. Peat, A. Riley, D. E. Williams, and L. M. Peter, J. Electrochem. Soc. 136, 3352-3355 (1989).
96. R. Tenne, V. Marcu, and N. Yellin, Appl. Phys. Lett. 45, 1219-1221 (1984).
97. R. Tenne and M. Schatkay, Appl. Phys. B 35, 243-247 (1984).

98. R. Tenne, V. Marcu, and Y. Prior, Appl. Phys. A37, 205-209 (1985).
99. J.-P. Krumme and M. E. Straumanis Trans. AIME 239, 395-402 (1967).
100. M. E. Straumanis, J.-P. Krumme, and W. J. James, J. Electrochem. Soc. 115, 1050-1053 (1968).
101. A. Yamamoto and S. Yano, J. Electrochem. Soc. 122, 260-267 (1975).
102. M. M. Faktor and J. L. Stevenson J. Electrochem. Soc. 125, 621-629 (1978).
103. A. Yamamoto, S. Tohno, and C. Uemura, J. Electrochem. Soc. 128, 1095-1100 (1981).
104. C. R. Elliott and J. C. Regnault, J. Electrochem. Soc. 128, 113-116 (1981).
105. R. Bhat, J. Electrochem. Soc. 132, 2284-2285 (1985).
106. R. M. Lum, A. M. Glass, F. W. Ostermayer, Jr., P. A. Kohl, A. A. Ballman, and R. A. Logan, J. Appl. Phys. 57, 39-44 (1985).
107. R. M. Lum, F. W. Ostermayer, Jr., P. A. Kohl, A. M. Glass, and A. A. Ballman, Appl. Phys. Lett. 47, 269-271 (1985).
108. F. W. Ostermayer, Jr., P. A. Kohl, and R. M. Lum, J. Appl. Phys. 58, 4390-4396 (1985).
109. R. Matz and J. Zirrgiebel, J. Appl. Phys. 64, 3402-3406 (1988).
110. M. M. Carrabba, N. W. Nguyen, and R. D. Rauh, Appl. Optics 25, 4516-4518 (1986).
111. M. M. Carrabba, N. M. Nguyen, and R. D. Rauh, J. Electrochem. Soc. 134, 1855-1859 (1987).
112. J. Li, M. M. Carrabba, J. P. Hachey, S. Mathew, and R. D. Rauh, J. Electrochem. Soc. 135, 3170-3171 (1988).
113. J. L. Weyher and J. van de Ven, J. Physique 43, C5-313-C5-319 (1982).
114. J. L. Weyher and J. van de Ven, J. Cryst. Growth 63, 285-291 (1983).
115. J. L. Weyher and L. J. Gilling, J. Appl. Phys. 58, 219-222 (1985).
116. L. Hollan, J. C. Tranchant, and R. Memming, J. Electrochem. Soc. 126, 855-859 (1979).
117. F. Ozanam and J.-N. Chazalviel, J. Electroanal. Chem. 269, 251-266 (1989).
118. L. M. Peter, D. J. Blackwood, and S. Pons, J. Electroanal. Chem. 294, 111-121 (1990).
119. G. Vercruysse, W. Rigole, and W. P. Gomes, Solar Energy Mat. 12, 157-167 (1985).
120. A. R. Kucernak, R. Peat, and D. E. Williams, J. Electrochem. Soc. 138, 1645-1653. (1991).
121. P. Carlsson, B. Holmström, H. Kita, and K. Uosaki, Surface Sci. 237, 280-290 (1990).
122. P. Carlsson, B. Holmström, H. Kita, and K. Uosaki, J. Electroanal. Chem. 283, 425-433 (1990).
123. S. Eriksson, P. Carlsson, B. Holmström, and K. Uosaki, J. Electroanal. Chem. 313, 121-128 (1991).

Advances in Electrochemical Science and Engineering
Edited by Heinz Gerischer and Charles W. Tobias

Electroless Deposition Processes: Fundamentals and Applications

Yutaka Okinaka[1] **and Tetsuya Osaka**[2]

[1] AT&T Bell Laboratories (Retired), Murray Hill, New Jersey, U.S.A.

[2] Department of Applied Chemistry, School of Science and Engineering, Kagami Memorial Lab. for Materials Science and Technology, Waseda University, Tokyo, Japan

Contents

List of Symbols

a, b, c, d	reaction orders (dimensionless)
A	Arrhenius factor
B_S	saturation magnetic flux density (tesla)
C	concentration
C_d	double layer capacitance
C_{ext}	capacity of the external capacitor
E	electrode potential (V)
E	activation energy
E_m	mixed potential
E_{mix}	mixed potential
E_{pl}	electroless plating potential (V)
$E_{t=0}$	initial potential (V)
E_{RED}	zero-current potential
ΔE^*	activation energy (kJ/mol)
H_d	demagnetizing field
i_a	partial anodic current density
i_c	partial cathodic current density
i_m	deposition rate (µm/h)
i_m	current
i_{pl}	rate of electroless plating
i	net current caused by polarization
K	proportionality constant, see Eq. (24)
k_1, k_2	rate constants (s^{-1})
pK_a	dissociation constant
Δq	electrical charge
r	radius
r^*	critical radius
R_c	charge transfer resistance of the cathodic partial reaction
R_a	charge transfer resistance of the anodic partial reaction
R_p	polarization resistance at the electroless plating potential
R_s	solution resistance between the mixed potential electrode and the counterelectrode
R_t	overall charge transfer restistance
T	temperature
v	molar volume
$Z_{(j)}$	total cell impedance
η_0	intercept of log η_t against t
η_t	overvoltage at the time t
μ	permeability
σ	surface tension
ω	frequency of the AC signal

Abbreviations

DMAB	dimethylamine borane
SPT	single-pole type head
SEM	scanning electron microscopy
TCR	temperature coefficient of resistance
TEM	transmission electron microscopy

1 Introduction

"Eletroless" metal deposition (or plating) is a term coined by Brenner and Riddell [1], inventors of the electroless nickel deposition process, to describe an autocatalytic process of depositing a metal in the absence of an external source of electric current. In this process, the deposited metal itself acts as a catalyst for further deposition of the metal. Thus, by definition, the thickness of the depositing metal layer should continue to increase even after the substrate is completely covered by deposited metal. However, a literature survey shows that the term "electroless plating" has been used to describe not only autocatalytic processes, but also two other, fundamentally different processes of metal deposition, which are performed in the absence of an external electric current, i.e., galvanic displacement and substrate-catalyzed processes. In the latter two processes, the deposition should cease once the substrate is covered completely with a thin layer of deposited metal. It should be mentioned that such processes have their own merit and find applications, but from the mechanistic viewpoint they should be clearly distinguished from the autocatalytic electroless process. To produce a thick non-porous layer of the deposit, an autocatalytic process is naturally preferred. In this chapter, only autocatalytic processes are discussed, and the two terms "autocatalytic" and "electroless" are used interchangeably.

As indicated in the periodic table of elements shown in Fig. 1, the following single metals are currently known to be platable by autocatalytic means: Ni, Co, Cu, Ag, Au, Pt, Pd, Rh, Ru, and Sn. In addition, a large number of alloys can be deposited. For example, Ni can be codeposited with the following elements: P, B, V, Mo, W, Mn, Re, Fe, Zn, and Tl. Other alloys which are known to be autocatalytically depositable, include CuNi, CuCo, CuCd, CuAu, PdNiP, PdCoP, PdZnP, AuAg, AuSn, and AuIn. Among the large number of metals and alloys listed above, electroless Ni and Co (and their alloys), Cu, and Au are currently the most important ones for industrial applications. In this chapter, the deposition process of only the latter metals and alloys are treated individually in separate sections, following a discussion of fundamental aspects of autocatalytic metal deposition processes in general from an electrochemical standpoint. It is beyond the scope of this chapter to review the large number of individual plating processes and physical and metallurgical properties of the produced deposits. For an extensive review of these aspects of electroless plating, the reader is referred to a monograph recently published by the American Electroplaters and Surface Finishers Society [2].

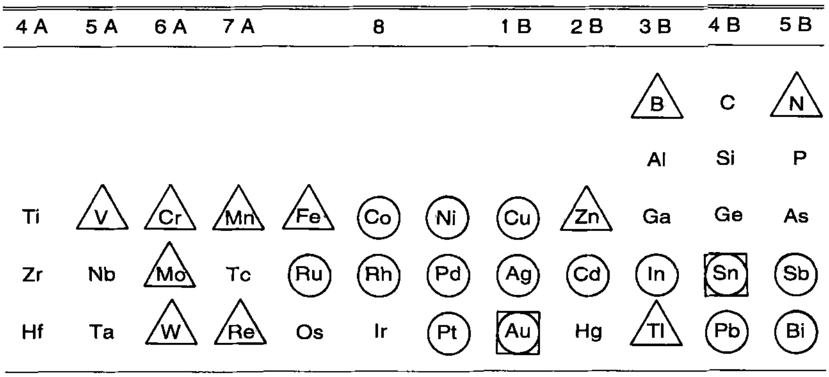

Fig. 1. Periodic table of the elements, showing metals and alloys which are known (or claimed) to be depositable in the absence of an external source of electric current.
○ autocatalytic deposition, △ codeposition with Ni or Co, □ galvanic displacement.

2 General Reaction Mechanism

2.1 Mixed Potential Concept

Quite generally, electroless plating solutions contain the components listed in Table 1. Small amounts of additives are usually employed to improve the solution stability and to impart the desired physical properties on the deposit. The functions of such additives are discussed later. Here, we shall consider reactions of major constituents only.

It is well established that the overall electroless deposition reactions are basically electrochemical in nature, consisting of cathodic and anodic partial reactions occurring simultaneously on the same substrate surface:

Overall reaction:

$$\mathrm{ML}_m^{n+} + \mathrm{Red} \rightarrow \mathrm{M} + m\mathrm{L} + \mathrm{Ox}^{n+} \tag{1}$$

Cathodic partial reaction:

$$\mathrm{ML}_m^{n+} + ne^- \rightarrow \mathrm{M} + m\mathrm{L} \tag{2}$$

Anodic partial reaction:

$$\mathrm{Red} \rightarrow \mathrm{Ox}^{n+} + ne^- \tag{3}$$

The two partial reactions (2) and (3) determine the potential of electroless deposition, called mixed potential. The concept presented above is called the "mixed potential theory", a term derived from a concept proposed for interpreting corrosion

Table 1. Composition of an electroless plating bath.

Component	Purpose
Metal salt	Source of metal deposit
Reducing agent	Reduction of metal ion
pH adjuster	pH adjustment
Complexing agent	To form metal complex
Additives	To improve bath stability or deposit properties

phenomena. A schematic representation of the plot for the mixed potential concept used to describe the principle of an electroless deposition reaction is shown in Fig. 2. Historically, the mixed potential concept was first applied to the analysis of electroless metal deposition processes by Saito [3] and Paunovic [4].

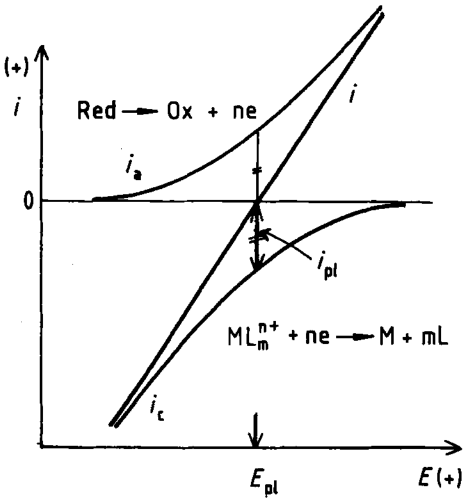

Fig. 2. Schematic diagram of mixed potential electrode. i: net current, i_a: partial anodic current, i_c: partial cathodic current, i_{pl}: electroless plating current at mixed potential E_{pl}.

According to the mixed potential theory, the overall reaction should be interpretable simply by superimposing the respective electrochemical behavior of the two partial reactions, determined independently. More recent studies, however, show that electroless deposition processes are much more complicated than represented by the simple mixed potential theory described above. Interdependence of partial reactions and participation of a third reaction are among the complications which limit the significance of simple combination of independently studied partial reactions. Examples of such complications are discussed in the subsequent sections.

In spite of such limitations associated with the application of the mixed potential concept, results of electrochemical investigation of the partial reactions are highly useful to understand the characteristics of electroless deposition processes.

2.2 Catalytic Activity of Various Metals for the Anodic Oxidation of Reducing Agents

The electrochemical mechanism described above demonstrates that the catalytic activity of the metal to be deposited in the cathodic partial reaction (2) for the anodic oxidation of the reducing agent (3) determines the capability of the given electroless deposition system in terms of deposition rate. Ohno et al. [5] compared catalytic activities of different metals for the anodic oxidation of various reducing agents that are commonly used in electroless deposition systems. The comparison was based on determining current-potential (polarization) curves and observing potential at a fixed current density, corresponding to a typical deposition rate of the electroless process under consideration. For example, polarization curves for the anodic oxidation of hypophosphite, a common reducing agent used for the electroless deposition of Ni, Co, and their alloys, on various metal electrodes are reproduced in Fig. 3. These curves were obtained with a citrate-based solution at pH 9.0 and at 70 °C (for the exact composition, see legend). Similar sets of curves were obtained for formaldehyde, sodium borohydride, dimethylamine borane (DMAB), and hydrazine. Different solution compositions and temperatures were used for the different reducing agents to simulate the conditions used in practical

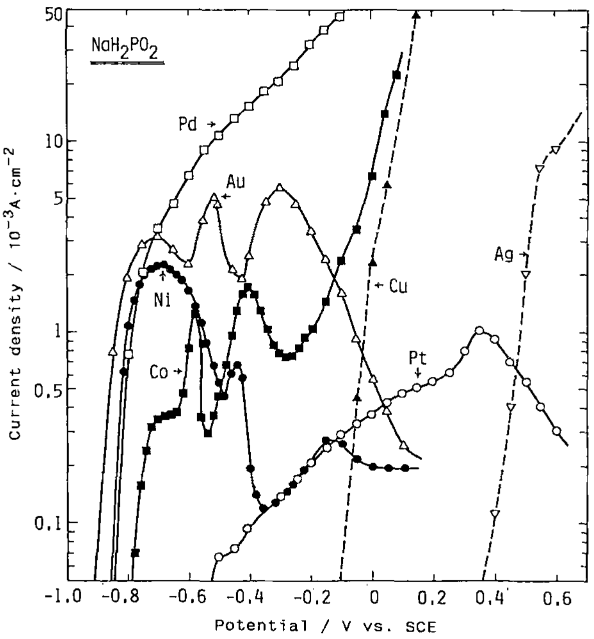

Fig. 3. Polarization curves for anodic oxidation of hypophosphite on different metals (bath composition: 0.2 mol · dm^{-3} NaH_2PO_2, 0.2 mol · dm^{-3} sodium citrate, 0.5 mol · dm^{-3} H_3BO_3, pH 9, 70 °C). Dashed lines: current density attributed to anodic dissolution of silver or copper (I. Ohno et al., 1985 [5]).

plating processes. (The reader is referred to the original paper [5] for detailed compositions and conditions). As illustrated by the examples shown in Fig. 3, the polarization curves do not exhibit linear Tafel regions, and it was not possible to find the exchange current densities by the usual extrapolation method. This was the reason why the alternative method of comparing potentials was adopted. The result of the comparison at 0.1 mA/cm^2 is summarized in Fig. 4. Based on this comparison, the metals can be listed in decreasing order of catalytic activity for the anodic oxidation of each reducing agent:

NaH_2PO_2: Au > Ni > Pd > Co > Pt
HCHO: Cu > Au > Ag > Pt > Pd > Ni > Co
$NaBH_4$: Ni > Co > Pd > Pt > Au > Ag > Cu
DMAB: Ni > Co > Pd > Au > Pt > Ag
NH_2NH_2: Co > Ni > Pt > Pd > Cu > Ag > Au

It should be emphasized that these sequences are valid only for the specific solution compositions and the specific temperatures used in the experiments.

An electrochemical method of evaluating the substrate surface activity in electroless nickel plating has been proposed by Osaka et al., who used mixed potential measurements [6-8]. After activating a copper wire substrate with a mixed $PdCl_2/SnCl_2$ catalyst, the mixed potential of the Cu wire in the plating bath is

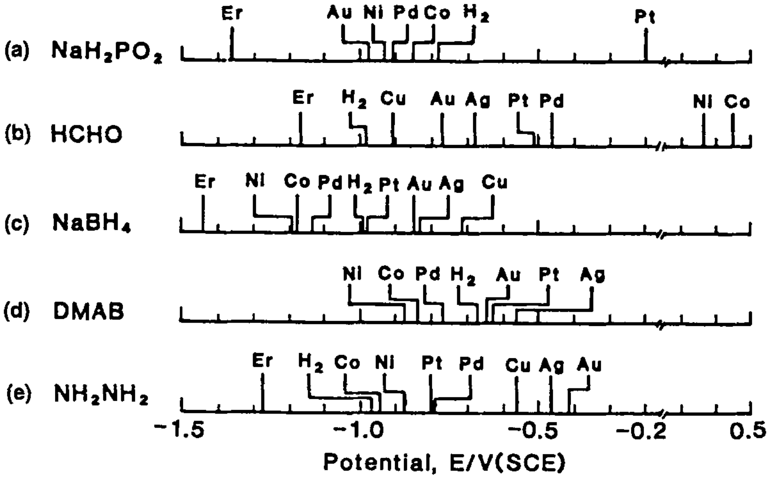

Fig. 4. Catalytic activities of metals (potentials at 10^{-4} A · cm^{-2}) during anodic oxidation of different reducing agents. E_r is the oxidation-reduction potential of the reducing agent and H_2 is the reversible hydrogen potential. Bath compositions: (a): 0.2 mol · dm^{-3} NaH_2PO_2, 0.2 mol · dm^{-3} sodium citrate, 0.5 mol · dm^{-3} H_3BO_3, pH 9, 70 °C, (b): 0.1 mol · dm^{-3} HCHO, 0.175 mol · dm^{-3} EDTA · 2 Na, pH 12.5, 25 °C, (c): 0.03 mol · dm^{-3} $NaBH_4$, 0.175 mol · dm^{-3} EDTA · 2 Na, pH 12.5, 25 °C, (d): 0.2 g · dm^{-3} DMAB, 0.2 mol · dm^{-3} sodium citrate, 0.5 mol · dm^{-3} H_3BO_3, pH 7, 25 °C, (e): 2.0 g · dm^{-3} DMAB, 0.2 mol · dm^{-3} sodium citrate, 0.5 mol · dm^{-3} H_3BO_3, pH 7, 25 °C, (f): 1.0 mol · dm^{-3} N_2H_4, 0.175 mol · dm^{-3} EDTA · 2 Na, pH 12.0, 25 °C (I. Ohno et al., 1985 [5]).

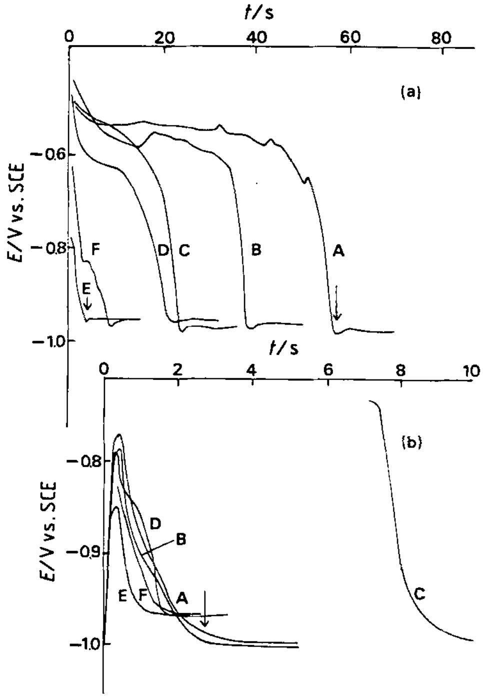

Fig. 5. Functionality test for electroless nickel plating. (a) Time dependence of mixed potential after activation, (b) time dependence of mixed potential after acceleration: A–F indicate various catalyst solutions (T. Osaka et al., 1980 [6, 7]).

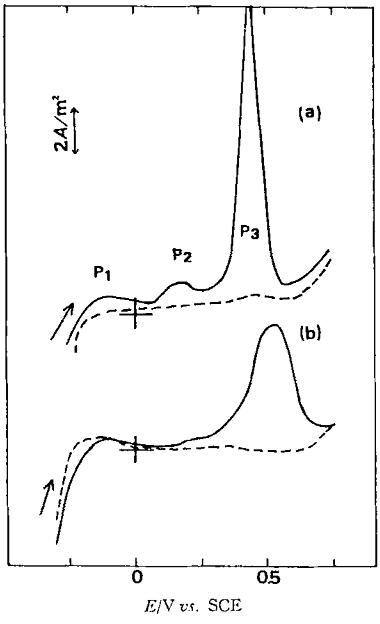

Fig. 6. Voltammograms at 0.1 V · s^{-1} on Au electrode in 1 mol · dm^{-3} HCl after activation with a catalyst solution (a) and after acceleration with 6 mol · dm^{-3} HCl (b). Solid lines: anodic scan after activation or acceleration, dashed lines: anodic scan without immersion step (T. Osaka et al., 1982 [8]).

measured as a function of the immersion time. The potential-time curves A-E shown in Fig. 5 were obtained with catalysts of different activities. Since the mixed potential changes drastically at the time when the Cu substrate surface is completely covered with a nickel layer, the initiation of electroless plating after Cu immersion can easily be determined, as shown in Fig. 5 (a) (see arrows in the figure). The reciprocal order of the induction time corresponds to the order of the catalyst activity. Osaka et al. [6-8] also proposed the activity comparison method based on an anodic sweep of an Au electrode in HCl solution. This method is illustrated in Fig. 6. The Au electrode after immersion into a mixed $PdCl_2/SnCl_2$ catalyst solution is rinsed with water and placed in an HCl solution. The potential of the Au electrode is then scanned in the anodic direction. The P1 and P2 peaks shown in Fig. 6 are due to desorption of adsorbed Sn(II) or adsorbed Sn(O) and oxidation of Sn(II) to Sn(IV), respectively. The P3 peak is caused by dissolution of Pd. Observation of the magnitude of the anodic peaks affords a rapid diagnosis of catalyst activity on a substrate surface. For example, the results shown in Fig. 6 demonstrate that the acceleration process effectively strips the Sn surface and exposes the Pd nuclei on the surface.

2.3 Unified Mechanism

Several fundamentally different mechanisms have been proposed for various electroless deposition reactions with different reducing agents. On the other hand, researchers realize that there are certain distinct features which are common to many different electroless systems. Van den Meerakker [9] noted that (1) electroless plating processes are always accompanied by evolution of hydrogen gas, (2) metals which are known to be platable by an electroless process are always effective hydrogenation-dehydrogenation catalysts, (3) poisons for hydrogenation-dehydrogenation reactions, such as thiourea and mercaptobenzothiazole, act as stabilizers in practically all electroless processes (for a discussion of the stabilization mechanism of electroless systems, see Sec. 3.), and that (4) electroless deposition reactions are generally accelerated when the pH is increased. To accomodate these common features, van den Meerakker proposed a unified mechanism which is valid for all electroless systems:

Anodic:

Dehydrogenation: $RH \rightarrow R + H$ (4)
Oxidation: $R + OH \rightarrow ROH + e^-$ (5)
Recombination: $H + H \rightarrow H_2$ (6)
Oxidation: $H + OH^- \rightarrow H_2O + e^-$ (7)

Cathodic:

Metal deposition: $M^{n+} + n\, e^- \rightarrow M$ (8)
Hydrogen evolution: $2\, H_2O + 2\, e^- \rightarrow H_2 + 2\, OH^-$ (9)

In this mechanism, RH represents the reducing agent, which, upon adsorption at the surface of the deposited metal, dissociates to form the radical R and atomic hydrogen H, according to the first reaction step (4). The electrons that are necessary to reduce the metal ions to the metal are supplied by R (reaction (5)) and/or H (reaction (7)). The relative contribution of each of these two reactions determines the utilization efficiency of the reducing agent. The gaseous hydrogen results from recombination of adsorbed atomic hydrogen produced by the reducing agent (reaction (6)). It is also possible to form gaseous hydrogen cathodically, according to reaction (9).

It is well known that when hypophosphite is the reducing agent, phosphorus codeposits with the metal. Similarly, boron codeposits when borohydride or DMAB is used as a reducing agent for certain metals (Ni, Co, Pd, etc., but not Au). Codeposition of these elements is known to result from a cathodic process, which should be added to the above reaction scheme to completely describe the entire process. This reaction mechanism is discussed further in the sections on the deposition of individual metals.

3 Stability of Electroless Systems

Thermodynamic aspects of the stability of electroless plating solutions have been discussed by Vashkyalis [10]. Electroless plating solutions are thermodynamically unstable and subject to spontaneous decomposition, resulting in precipitation of metal throughout the solution. For the plating solution to be practically useful, the actual occurrence of spontaneous decomposition must be prevented. Thermodynamic conditions which must be met to prevent decomposition can be discussed on the basis of the Gibbs-Thomson equation, which relates the chemical potential of a substance to the curvature of its surface. It follows that the equilibrium potential E_r of a metal particle with the radius r shifts in negative direction as the value of r is reduced:

$$E_r = E_\infty - \left(\frac{2\sigma v}{nF}\right)\left(\frac{1}{r}\right), \tag{10}$$

where E_∞ is the equilibrium potential of a flat surface of the same metal, σ is the surface tension, and v is the molar volume of the metal. In an electroless system, this means that E_r approaches the zero-current potential E_{RED} for the redox reaction of the reducing agent as the radius r is decreased, and that when E_r becomes more negative than E_{RED}, the electroless reaction can no longer proceed and hence the system becomes permanently stable. This situation is illustrated schematically in Fig. 7. The particle radius which affords $\Delta E = |E_{\mathrm{RED}}| - |E_r| = 0$ is called the critical radius r^*. If $r < r^*$, the electroless reaction does not proceed, and the system is stable. Vashkyalis calculated numerical values of r^* for various electroless systems (Table 2). Fig. 8 illustrates how the deposition rate on a particle increases once the radius of the particle increases beyond the critical radius r^*.

Based on the above considerations, a general principle governing the stabilization of electroless systems can be derived. Namely, metal particles which are formed in solution upon mixing metal ions and reducing agent must be either (1) dissolved again by

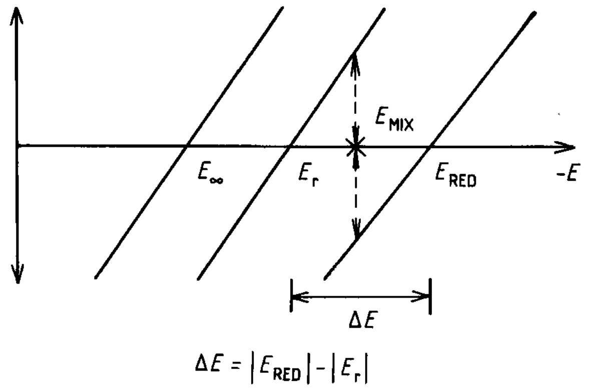

Fig. 7. Schematic representation of the effect of particle radius (r) on the current vs. potential relationship. Conditions: $\Delta E > 0$ particle grows, $\Delta E \leq 0$ particle does not grow, and $\Delta E = |E_{RED}| - |E_r|$ (A. Vashkyalis, 1978 [10]).

Table. 2. Critical radii in autocatalytic metal deposition (Vashkyalis, 1978 [10]).

System	r^* (nm)
Cu-HCHO	0.3
Ni-$H_2PO_2^-$	0.8
Ni-BH_4^-	1.1
Au-BH_4^-	1.5

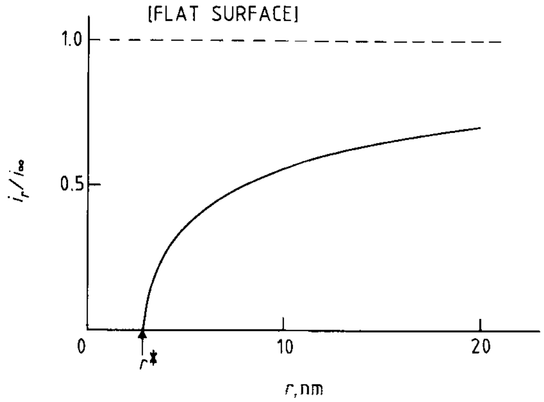

Fig. 8. Effect of the particle radius r on the electroless deposition rate. r^* and i_∞ are the critical radius at $\Delta E = 0$ and the current at E_∞ (equilibrium potential), respectively (A. Vashkyalis, 1978 [10]).

the solution to keep the radius of the particles r smaller than r^*, or (2) made catalytically inactive by, for example, adsorption of a catalytic poison before r exceeds r^*.

Electroless copper deposition is discussed briefly below to exemplify the application of the above principle. In electroless copper deposition, cyanide and mercaptobenzothiazole are known to stabilize the bath. It is well known that dissolved oxygen also serves as a stabilizer and should be considered a major bath component.

Mercaptobenzothiazole is believed to function as a catalytic poison by adsorption. Cyanide converts Cu_2O particles, predecessors of Cu particles, into an inactive cuprous cyanide complex. Dissolved oxygen oxidizes Cu_2O particles to form the original Cu(II) complex. It is important to note that, according to the above stabilization principle, these stabilizers function by acting on the particles before their radii exceed the critical value of r^*.

4 Deposition Kinetics

4.1 Empirical Rate Laws

Shippey and Donahue [11] were the first to show how to derive an empirical expression for the overall rate law for electroless deposition reactions. They studied an electroless copper system with tartrate as a complexing agent. Later, Molenaar et al. [12] performed similar kinetic studies concerning an electroless copper deposition reaction with EDTA as a complexing agent. The kinetics of electroless nickel deposition was investigated by Mallory and Lloyd [13].

As an example, the case of electroless copper deposition is described briefly below. For the overall electroless copper deposition reaction

$$\mathrm{Cu(II)} + 2\mathrm{HCHO} + 4\mathrm{OH}^- \rightarrow \mathrm{Cu} + \mathrm{H_2} + 2\mathrm{HCOO}^- + 2\mathrm{H_2O}, \tag{11}$$

the following general equation describes the deposition rate as a function of various variables:

$$r = k\,[\mathrm{Cu(II)}]^{a}\,[\mathrm{OH}^-]^{b}\,[\mathrm{HCHO}]^{c}\,[\mathrm{L}]^{d}\exp\left(-\frac{E}{T}\right), \tag{12}$$

where k is the rate constant, L represents the ligand of the copper ions, a, b, c, and d are the respective reaction orders, E is the activation energy, and T is the temperature. From Eq. (12) it follows that

$$\begin{aligned}\log r &= \log k + a\log[\mathrm{Cu(II)}] + b\log[\mathrm{OH}^-]\\ &\quad + c\log[\mathrm{HCHO}] + d\log[\mathrm{L}] - \frac{E}{2.3\,T}\end{aligned} \tag{13}$$

This equation shows that the reaction orders can be determined by the slope of the logarithmic plot of the deposition rate r against the concentration of each reactant. The activation energy can be calculated from the slope of the plot of log r against the reciprocal temperature.

Shippey and Donahue [11], analyzed rate data according to Eq. (13) for the case where L = tartrate, while Molenaar et al. [12] investigated the case where L = EDTA. The rate parameters reported by the above authors are summarized in Table 3. Molenaar et al. [12] noted that the empirical data for the EDTA system are valid only

Table 3. Empirical reaction orders for electroless copper deposition (Shippey et al., 1973 [11], Molenaar et al., 1974 [12]).

	L = TARTRATE	L = EDTA [HCHO] > 0.05 [OH$^-$] > 0.07	 [HCHO] > 0.04 [OH$^-$] > 0.05
a	0.47	0.78	0
b	0.18	< 0.02	4
c	0.07	0.13	1.7
d	$k[L]^d = 18.5$ (40 °C)	< 0.02	–
k		82	–
E	11.7 kcal/mol	11 kcal/mol	–

$Cu(II) + 2\ HCHO + 4\ OH^- \rightarrow Cu + H_2 + 2\ HCOO^- + 2\ H_2O$
$r = k[Cu(II)]^a\ [OH^-]^b\ [HCHO]^c\ [L]^d \exp(-E/T)$.

in limited concentration ranges, where the logarithmic plot of the rate against the concentration is linear. It is interesting to note that in the EDTA system, the dependence of the rate on the concentration is very different in different ranges of formaldehyde and hydroxide concentrations. Based on the study of the rate law, Molenaar et al. concluded that at high OH$^-$ (> 0.07 M) and high HCHO (> 0.05 M) concentrations, the deposition rate of electroless copper from the EDTA system is controlled by the Cu(II) concentration in the range from 0.02 M to 0.08 M. At lower OH$^-$ and HCHO concentrations, the deposition rate is controlled by the concentrations of these species, and it is independent of the Cu(II) concentration.

Overall rate laws such as those discussed above are useful for obtaining information on which variables must be controlled more closely in order to maintain a constant deposition rate in practical electroless plating. However, overall rate laws do not provide any mechanistic information. Donahue and Shippey [14] proposed a method of deriving rate laws for partial anodic and cathodic processes in order to gain insight into the mechanism of electroless deposition reactions. If it is assumed that the anodic and cathodic partial processes may interact with each other, then the general rate laws for the partial reactions can be written as follows:

$$r_a = k_a\ [HCHO]^{\gamma}\ [OH^-]^{\varepsilon}\ [Cu(II)]^{\delta'} \tag{14}$$

$$r_c = k_c\ [Cu(II)]^{\delta}\ [HCHO]^{\gamma'}\ [OH^-]^{\varepsilon'} \tag{15}$$

The reaction orders were determined by measuring the mixed potential E_m and the deposition rate (in terms of current i_m at E_m) at various concentrations of the reactants, determining the slopes of the graphs obtained by plotting E_m vs. log [HCHO], log i_m vs. log [HCHO], E_m vs. log i_m, etc., and solving Donahue's general equations [15], relating the slopes to reaction orders and Tafel slopes for partial cathodic and anodic reactions of a mixed potential system. Donahue and Shippey [14] reported the following rate laws for the respective partial reactions of the particular electroless copper deposition system they studied:

$$r_a = k_a\,[\mathrm{HCHO}]^{0.18}\,[\mathrm{OH}^-]^{0.18} \tag{16}$$

$$r_c = k_c\,\frac{[\mathrm{Cu(II)}]^{1.7}\,[\mathrm{OH}^-]^{0.18}}{[\mathrm{HCHO}]^{0.23}} \tag{17}$$

These rate laws demonstrate that Cu(II) is not involved in the anodic partial reaction, whereas both HCHO and OH^- are involved in the cathodic copper deposition reaction. It is interesting to note that HCHO acts as an inhibitor of the partial cathodic reaction. The above rate laws suggest that the mechanisms are more complex than indicated by simple combination of two independent partial reactions.

4.2 Electrochemical Methods of Rate Measurement

The rate of electroless plating can be measured by several different methods, including nonelectrochemical techniques, such as those based on weight gain determination, electrical resistance measurement, and optical transmission measurement. The latter methods have been adopted to continuously determine plating rates for the purpose of process control. Electrochemical methods described below have also proven to be useful for automatic control of various electroless processes.

4.2.1 Polarization Resistance Method

Ohno and Haruyama [16] have shown that the instantaneous deposition rate of electroless plating is inversely proportional to the polarization resistance of complete plating solutions. The following generalized derivation of this relation was developed by the above authors. The partial anodic and cathodic current densities i_a and i_c are first written in the following generalized form:

$$i_a = \mathrm{f}(E) \tag{18}$$

$$i_c = \mathrm{g}(E) \tag{19}$$

where E is the electrode potential. In the stationary state, the electrode exhibits a mixed potential E_{mix} (or an electroless plating potential E_{pl}), where i_a is equal to i_c:

$$\mathrm{f}(E_{\mathrm{pl}}) = \mathrm{g}(E_{\mathrm{pl}}) = i_{\mathrm{pl}} \tag{20}$$

in which i_{pl} is the rate of electroless plating. If the electrode is polarized externally, the net current is given by

$$i = i_a - i_c = \mathrm{f}(E) - \mathrm{g}(E) \tag{21}$$

Expansion of Eq. (21) for a small perturbation of the potential ΔE near E_{pl} yields

$$\begin{aligned}\Delta i = {} & \{\mathrm{f}(E_{\mathrm{pl}}) + (\Delta E)\,\mathrm{f}'(E_{\mathrm{pl}}) + (1/2)(\Delta E)^2\mathrm{f}''(E_{\mathrm{pl}}) + \ldots\} \\ & -\{\mathrm{g}(E_{\mathrm{pl}}) + (\Delta E)\,\mathrm{g}'(E_{\mathrm{pl}}) + (1/2)(\Delta E)^2\mathrm{g}''(E_{\mathrm{pl}}) + \ldots\}\end{aligned} \tag{22}$$

where prime and double prime indicate the first and second derivatives of the functions, respectively, and Δi is the net current caused by polarization by ΔE. If all terms higher than second order are neglected, Eq. (22) reduces to

$$\begin{aligned}\Delta i &= f(E_{pl})[1 + \Delta E\{f'(E_{pl})/f(E_{pl})\}]\\ &\quad - g(E_{pl})[\{1 + \Delta E\{g'(E_{pl})/g(E_{pl})\}]\\ &= \Delta E\{f'(E_{pl}) - g'(E_{pl})\}\end{aligned} \tag{23}$$

Therefore,

$$\frac{1}{R_p} = \left(\frac{\Delta i}{\Delta E}\right)_{E=E_{pl}} = i_{pl}\left[\left\{\frac{\partial \ln f(E)}{\partial E}\right\}_{E=E_{pl}} - \left\{\frac{\partial \ln g(E)}{\partial E}\right\}_{E=E_{pl}}\right] \tag{24}$$

which can be written as

$$\frac{1}{R_p} = \frac{i_{pl}}{K} \tag{25}$$

where R_p is the polarization resistance at the electroless plating potential, and K is a constant which equals the reciprocal of the term in brackets in Eq. (24). The terms in braces { } in Eq. (24) quantify the slopes of the partial polarization curves on a semilogarithmic scale at the plating potential. Eqs. (24) and (25) describe the general relation between the polarization resistance and the rate of electroless plating. Partial polarization curves are not generally obtained from simple polarization experiments carried out in solution in the absence of either metallic ions or reducing agents. This is because complications may result from interdependence of partial reactions. Therefore, the numerical value of K must be derived from the empirical relationship between the polarization resistance and the plating rate.

Ohno and Haruyama [16] experimentally determined the polarization resistance of various electroless plating baths and compared the results with the deposition rates measured by the weight gain method. As an example, current density-potential relations for moderately polarized electroless cobalt plating solutions containing diethylamine borane (DEAB) as a reducing agent are reproduced in Fig. 9. Good linearity is seen within ±8 mV on both the positive and the negative sides of E_{pl}. The slope, which is the polarization resistance, decreases with increasing DEAB concentration. Fig. 10 shows the relation between log $(1/R_p)$ and log i_{pl}, including R_t values obtained by the ac impedance method. As expected according to Eq. (25), all plating baths give rise to linear plots with a slope of one. The values of the proportionality constant K are shown in Fig. 10. The K values vary greatly, depending on the nature of the plating bath, because K is related to the kinetic parameters of the partial reactions which are characteristic of the respective bath.

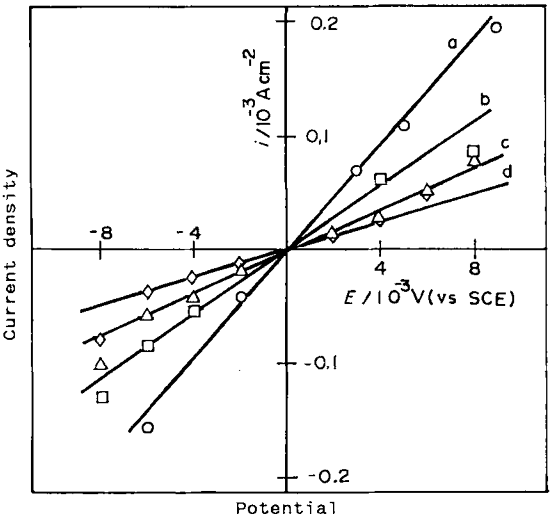

Fig. 9. Current density vs. potential relations at low polarization in electroless cobalt plating baths (Bath composition: 0.10 mol · dm^{-3} $CoSO_4$, 0.20 mol · dm^{-3} citrate, 0.50 mol · dm^{-3} H_3BO_3, at various DEAB concentrations; pH 7.0, 80 °C. a: 0.005 mol · dm^{-3} DEAB, $E_{pl} = -0.834$ V (SCE), b: 0.025 mol · dm^{-3} DEAB, $E_{pl} = -0.790$ V (SCE), c: 0.013 mol · dm^{-3} DEAB, $E_{pl} = -0.754$ V (SCE), d: 0.063 mol · dm^{-3} DEAB, $E_{pl} = -0.714$ V (SCE) (I. Ohno et al., 1981 [16]).

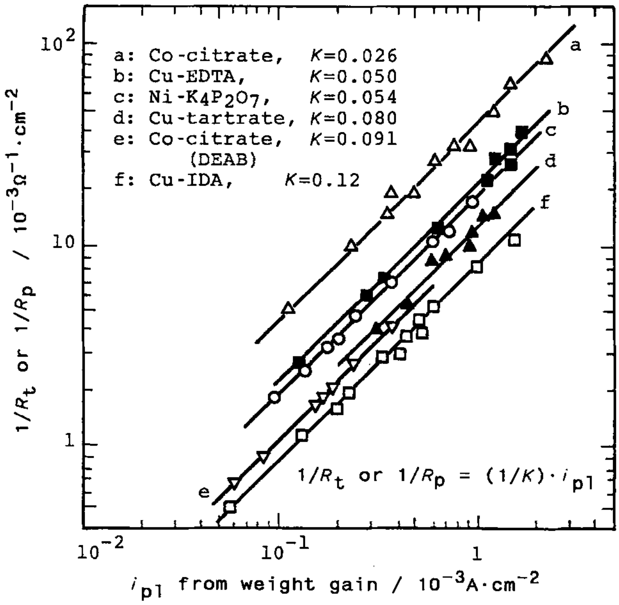

Fig. 10. Plots of R_p^{-1} and R_t^{-1} against i_{pl} in various electroless plating baths. Hollow symbols: polarization resistance R_p, solid symbols: transfer resistance R_t (I. Ohno, 1985 [5]).

4.2.2 AC Impedance Method

The interfacial impedance of mixed potential electrode systems, such as metals undergoing corrosion, was investigated by Haruyama [18] and Epelboin et al. [19]. They showed that the impedance characteristics of such systems can be represented by the equivalent circuit illustrated in Fig. 11, where C_d represents the double layer capacitance, R_c and R_a are the charge transfer resistances of the cathodic and the anodic partial reaction, respectively, and R_s is the solution resistance between the mixed potential electrode and the counterelectrode. The total cell impedance is given by

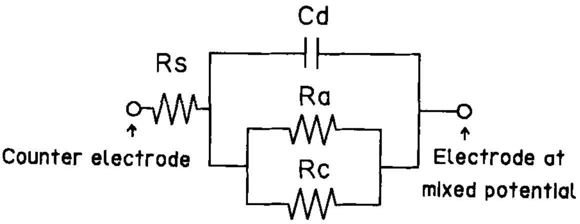

Fig. 11. Schematic representation of an equivalent circuit for a mixed potential system. C_d: double layer capacitance, R_S: solution resistance, R_a: anodic charge transfer resistance, R_c: cathodic charge transfer resistance.

$$Z\,(\mathrm{j}\omega) = R_s + \frac{R_t}{1 + \mathrm{j}\omega C_d R_t} \tag{26}$$

where ω is the frequency of the AC signal, j equals $\sqrt{-1}$, and R_t is the overall charge transfer resistance, which is related to R_c and R_a by

$$\frac{1}{R_t} = \frac{1}{R_c} + \frac{1}{R_a} \tag{27}$$

The dependence of the impedance on the frequency is outlined in Fig. 12. It demonstrates that the following relations hold at extreme frequencies:

$$\omega \to \infty;\ Z \to R_s \tag{28}$$

$$\omega \to 0;\ Z \to R_s + R_t \tag{29}$$

Thus, R_t can be calculated by subtracting an impedance value measured at a very high frequency from a value measured at a very low frequency. Ohno et al. [20] applied the above principle to the measurement of the rate of electroless copper deposition and demonstrated that R_t is inversely proportional to the plating rate determined by weight gain measurement. This is exemplified by the relationship between polarization resistance R_p and the plating rate i_{pl} (Eq. (25)). The experimental results are shown in Fig. 10.

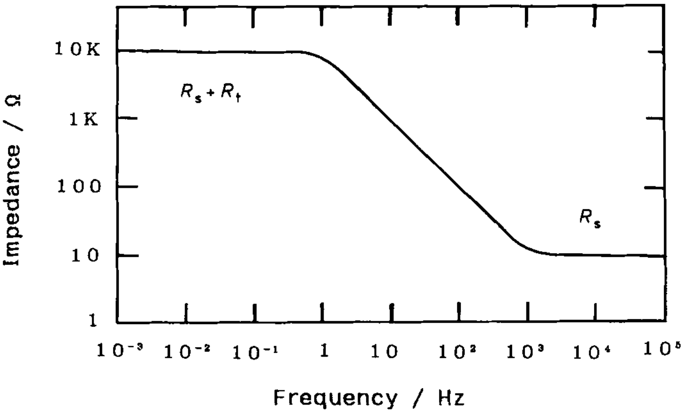

Fig. 12. Frequency dependence of interfacial impedance.

It should be noted that if one or both of the partial reactions are at least partially controlled by the diffusion of reacting species, then the expression describing the impedance becomes more complex because of participation of the component called "Warburg impedance" at low frequencies. Under such circumstances, selection of an optimum frequency becomes critical for the impedance measurement at low frequencies.

4.2.3 Coulostatic Method

The coulostatic method was applied to *in situ* measurement of the polarization resistance R_p (Eq. (25)). Thus, the rate of electroless plating was determined by Suzuki et al. [21-23]. Two advantages of this technique have been cited by the inventors: (1) measured R_p values are not influenced by the solution resistance, and (2) measurements can be finished very rapidly, within a few tens of milliseconds. The principle is briefly explained below.

A schematic diagram of the circuitry for performing a coulostatic analysis is shown in Fig. 13. In this example, two identical electrodes C and W are placed in a cell containing an electroless plating solution, and a reference electrode R is inserted into the cell to monitor the change in potential of W (or C). A power supply and an external capacitor with the capacity C_{ext} are connected to the cell, as illustrated. The external capacitor is first charged with a small amount of electrical charge Δq. This charge is supplied to the cell by flipping a switch S. If C_{ext} is much smaller than the double layer capacity C_d, essentially all of the charge in the external capacitor flows into the cell to charge the double layer. The charge supplied to the cell in this manner causes the plating (mixed) potential E_{pl} to rise to an initial potential $E_{t=0}$. The initial amount of potential shift is related to Δq and C_d by the equation:

$$E_{t=0} - E_{pl} = \eta_0 = -\frac{\Delta q}{C_d} \tag{30}$$

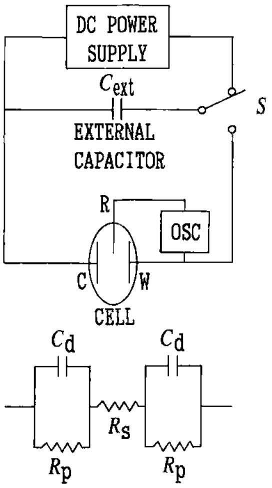

Fig. 13. Diagram of a coulostatic circuitry with two identical electrodes C and W. C_d: double layer capacitance, R_s: solution resistance, R_p: polarization resistance, R: reference electrode.

It is assumed that the double layer capacity is constant within a small potential interval (< 10 mV). After completion of the charging of the double layer, the charge is consumed gradually by the plating reaction: in other words, the double layer capacitor discharges through the polarization resistance. The decay of overvoltage with time during discharge can be expressed by:

$$\eta_t = \eta_0 \exp\left(-\frac{t}{C_d R_p}\right) \tag{31}$$

where η_t is the overvoltage at the time t. This equation can be rewritten in logarithmic form:

$$\log \eta_t = \log \eta_0 - \frac{t}{2.3 C_d R_p} \tag{32}$$

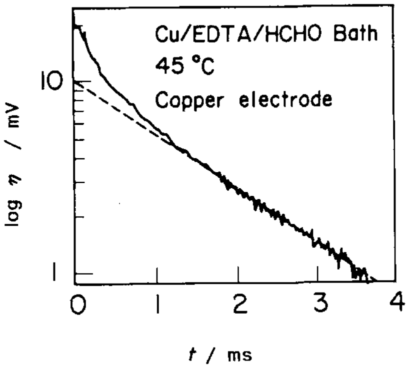

Fig. 14. Coulostatic potential decay curve for a copper electrode in an electroless copper plating bath (M. Suzuki et al., 1982 [22]).

Eq. (32) shows that plotting log η_t against t should yield a straight line with a slope of $-1/2.3\ C_d R_p$ and a 0 intercept of log η_0. Since C_d can be calculated according to $C_d = \Delta q/\eta_0$, it should be possible to determine R_p from the slope.

Suzuki et al. [22] demonstrated that this method may be used to measure the plating rate of electroless nickel and copper plating processes. An example of a potential decay curve is shown in Fig. 14. The authors also demonstrated the validity of Eq. (25) and determined the K values of various plating systems.

5 Electroless Nickel and Its Alloys

5.1 Electroless Nickel

Since electroless plating was invented by Brenner and Riddell [1], electroless NiP plating has been investigated by many researchers. The main reason why electroless NiP plating has been studied so extensively and has been applied in many different areas is that the properties of NiP film are easily controlled by changing the bath composition, and that codeposition of other metals in the NiP film is also easy. It is possible, for example to change the structure and properties of NiP film, e. g., its electric resistivity [24], its magnetic properties [24], and its corrosion resistance [25] by simply varying the phosphorus content. An amorphous film with a high specific resistance and a low temperature coefficient of resistance (TCR) in particular is easily obtained by optimizing the phosphorus content.

Fig. 15 shows representative properties of NiP films which are obtained by varying the pH of the plating bath from 4 to 10. A typical NiP bath with the composition listed in Table 4 [24] was used. The film properties change drastically in the pH range between 8 and 9. The film structure changes from amorphous to crystalline, as shown in Table 5 [26]; the main factor controling the film structure is the codeposited phosphorus content. If borohydride or dimethylamine borane is used as a reducing agent, NiB films are obtained instead of NiP. In the case of NiB films, relatively pure Ni films with only 0.7 wt% B [27] are easily obtained; such films possess higher ductility, better bonding properties, and better etching properties than NiP films. Amorphous NiB films can be obtained at a higher B content (>6 wt%) [28].

Table 4. Standard bath composition and operating conditions for electroless NiP plating (T. Osaka et al., 1983 [24]).

Chemicals	Concentration [mol · dm^{-3}]
$NaH_2PO_2 \cdot H_2O$	0.15
$(NH_4)_2SO_4$	0.50
$Na_3C_6H_5O_7 \cdot 2\ H_2O$	0.20
$NiSO_4 \cdot 6\ H_2O$	0.10

Bath temperature 90 °C
Bath pH 9.0 (adjusted with NaOH)

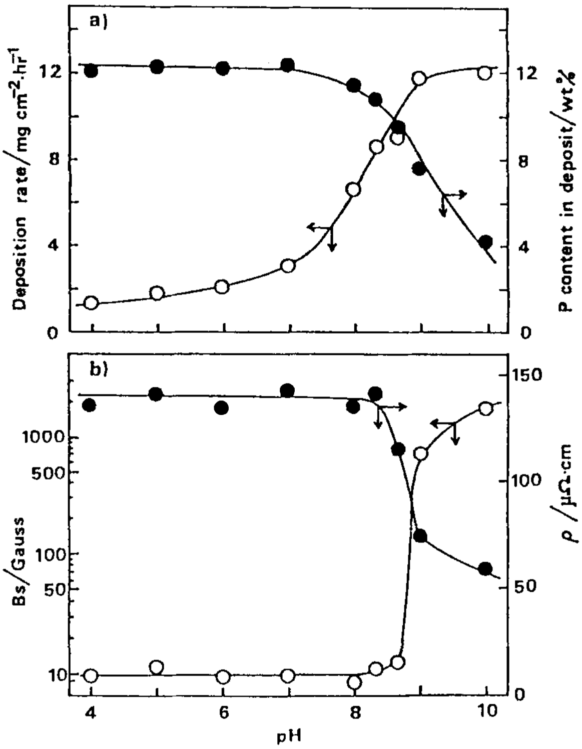

Fig. 15. Effect of the pH of the bath on the deposition rate, phosphorus content, saturation magnetic flux density (B_s), and specific resistance (ρ) of NiP deposits (T. Osaka et al., 1983 [24]).

Table 5. Bath pH, phosphorus content, and properties of electroless NiP films (T. Osaka et al., 1988 [26]).

Bath pH	P cont. [at%]	ρ [μΩcm]	Ms [emu · g^{-1}]	Structure
10.0	4.6	60.4	15.5	Cryst.
9.5	5.3	73.5	9.5	Cryst.
9.2	6.6	82.7	4.0	Cryst.
9.0	8.0	95.2	1.4	Cryst.
8.6	10.4	117.6	0.0	Amor.
8.3	12.3	127.8	0.0	Amor.
8.0	12.8	132.2	0.0	Amor.
6.0	14.0	140.2	0.0	Amor.

5.2 Electroless Nickel Alloys

As mentioned above, metals which are difficult to deposit electrolessly by themselves, e.g., W, Mo, or V, can be codeposited with electroless nickel (NiP or NiB). Some researchers attempted to codeposit metals into NiP or NiB film for basic scientific research and/or to improve, or develop film properties for specific applications. For example, the following alloy films have been deposited: NiCuP, NiFeP, NiWP, NiMoP, NiMoB, NiReP, NiReMP (M: Zn, Sn, W), NiZnP, NiVP, NiMnP, NiPdP, NiCrP. In this review, CoNi alloys are classified as cobalt alloys. On the basis of the research performed by T. Osaka and his colleagues, nickel alloys with refractory metals are introduced in this section as a representative group of nickel-based ternary alloys.

Electroless NiP films are sometimes used in their amorphous condition as highly corrosion-resistant coatings, thin film resistors, and nonmagnetic underlayers of a magnetic rigid disk. However, amorphous materials are generally unstable against exposure to high temperature, because they are in a thermodynamically metastable state. Excellent properties of the amorphous electroless NiP alloy film, e.g., high resistivity at a low TCR (temperature coefficient of resistance), are lost after heat treatment because of the resulting structural change. The resistivity of electroless NiP at an optimum composition is not maintained at temperatures above 300 °C [26]. In a systematic approach to an investigation of nickel-based ternary alloys, codeposition of refractory metals in electroless NiP films was studied. This is one of the effective methods of improving the thermal stability. Electroless Ni-based ternary alloys of NiWP [29-35], NiReP [29, 36-38], and NiMoP [39-48] were investigated by many workers, but there is no systematic study on the thermal stability of the resistivity and structure of films containing the refractory metals W, Mo, and Re. The film resistivity attracts special attention because of its dependence on the thermal stability and because it has a certain impact on thin film resistor applications.

Fig. 16 shows the effect of adding Na_2WO_4, NH_4ReO_4, or Na_2MoO_4 to an electroless nickel plating bath (a) on the refractory metal content and (b) on the phosphorus content of electroless NiWP, NiReP, and NiMoP alloy films. The used electroless plating bath compositions and conditions are listed in Table 6 [26, 35-38, 44]. In all systems, the content of refractory metal increases, while the phosphorus content decreases with increasing metal oxide salt concentration in the bath. Codeposition of W with NiP is usually easy, but the maximum content of W in this case is less than 10 at% (a W content of 20 at% has also been reported [35]). In an NiReP film, the rhenium content can be controlled over a wide range, reaching a maximum value of 44 at%. A NiMoP alloy film was first described by Mallory [39, 41], but codeposition of Mo was possible only with a special, separately prepared Mo complex. We have recently developed a new bath containing glycolic acid as a complexing agent, to which Na_2MoO_4 can be added directly without forming its own molybdenum complex. The molybdenum content of NiMoP alloy film plated from this bath can be varied over a wider range than the molybdenum content in a film plated from the bath proposed by Mallory.

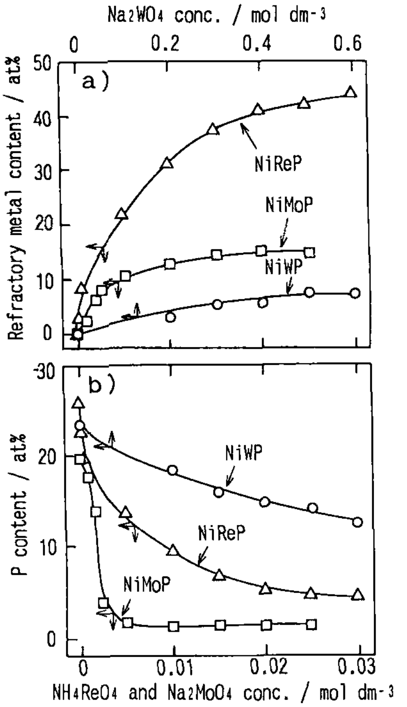

Fig. 16. Effect of Na_2WO_4, NH_4ReO_4, and Na_2MoO_4 concentrations on the refractory metal (a) and phosphorus (b) content of electroless NiWP, NiReP, and NiMoP alloy films (T. Osaka et al., 1992 [38]).

It had previously been reported that the structure of electroless NiP alloy films containing less than 15 at% phosphorus is crystalline, while the structure of films containing more than 15 at% is amorphous [26]. The structure of NiWP and NiMoP depends on the phosphorus content. NiP, NiWP, and NiReP, for instance, become amorphous if their phosphorus content exceeds a certain value. NiReP and NiWP, as shown in Table 6 and 7, are amorphous over the entire range of compositions. The structure of NiReP film plated from a bath containing 0.03 mol · dm^{-3} of NH_4ReO_4 in particular is peculiarly amorphous, in spite of the fact that its phosphorus content is only 5 at%. This film contains as much as 44 at% of rhenium.

The specific resistance of NiWP film with any composition is very high (160 μΩ · cm), due to its amorphous structure. The resistivity of NiMoP in the crystalline state is lower, while in the amorphous state it is as high as that of amorphous electroless-plated NiP [36]. On the other hand, the resistivity of NiReP with any film composition is considerably higher than that of conventional electroless-plated Ni alloy films, with a maximum value of 3000 μΩ · cm if the film is plated from a bath containing 0.03 mol · dm^{-3} of NH_4ReO_4. Such a high value is not always due to its microstructure, but it is assumed to be caused by weak adsorption of water molecules or hydroxyl groups [36].

The thermal effect was investigated to clarify the effect of codeposited refractory metals on the thermal stability. The effect of the heat treatment temperature on the

Table 6. Bath compositions and operating conditions for electroless Ni alloy plating (T. Osaka et al., 1992 [38]).

Chemicals Operating conditions	Concentrations / mol · dm^{-3} NiP	 NiWP	 NiReP	 NiMoP
$NaH_2PO_2 \cdot H_2O$	0.15	0.10	0.10	0.20
$(NH_4)_2SO_4$	0.50	–	–	–
$C_3H_4(OH)(COONa)_3 \cdot 2\ H_2O$	0.20	0.60	0.40	0.10
$CH_2(OH)(COOH)$	–	–	–	–
$NiSO_4 \cdot 6\ H_2O$	0.10	0.075	0.075	0.10
$Na_2WO_4 \cdot 2\ H_2O$	–	0–0.60	–	–
NH_4ReO_4	–	–	0–0.030	–
$Na_2MoO_4 \cdot 2\ H_2O$	–	–	–	0–0.020
Bath pH (adjusted with NaOH and NH_4OH)	6.0	9.0	9.0	9.0
Bath temperature / °C	90	90	90	90

Table 7. Specific resistance ρ and temperature coefficient of resistance TCR of electroless-plated Ni-based alloy films (T. Osaka et al., 1992 [38]).

Samples	ρ/µΩ cm	TCR/ppm K^{-1}	Temperature range of TCR / °C
$Ni_{80}P_{20}$			
300 °C	144	118	−60 – +70
as-plated	149	−15	
$Ni_{81}W_7P_{12}$			
400 °C	190	56	−10 – +70
as-plated	178	−18	
$Ni_{51}Re_{44}P_5$			
500 °C	195	18	−60 – +70
as-plated	3000	−151	
$Ni_{86}Mo_{13}P_1$			
500 °C	147	134	−60 – +70
as-plated	113	254	−60 – +70

Subscript numbers denote atomic % of the films.

specific resistance of representative alloy films is shown in Fig. 17. For comparison, this figure also includes data obtained with an electroless NiP film plated from the bath whose composition is shown in Table 6. Electroless NiWP, NiReP, and NiMoP alloy films were plated from baths containing 0.6 mol · dm^{-3} of Na_2WO_4, 0.01 mol · dm^{-3} of Na_2MoO_4, and 0.03 mol · dm^{-3} of NH_4ReO_4, respectively. The resulting data are considered to be representative of each system. The specific resistance of electroless NiP remains constant at temperatures below 300 °C, and it

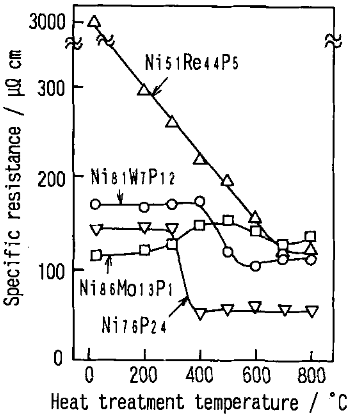

Fig. 17. Effect of the annealing temperature on the specific resistance of electroless $Ni_{81}W_7P_{12}$, $Ni_{51}Re_{44}P_5$, $Ni_{86}Mo_{13}P_1$, and $Ni_{76}P_{24}$ alloy films (T. Osaka et al., 1992 [38]).

begins to decrease upon heat treatment at 400 °C. The behavior of electroless NiWP is almost the same as that of amorphous NiP, and the specific resistance value remains constant up to 400 °C. These results indicate that NiWP is thermally more stable than NiP. The very high specific resistance of as-plated NiReP abruptly decreases as a result of heat treatment at 200 °C, and it decreases further with increasing temperature. The specific resistance of crystalline as-plated NiMoP is lower than that of amorphous Ni, but it unexpectedly increases and reaches its maximum after heat treatment at 400 °C. This peculiar behavior is induced by the nonuniformity of the Mo content, which is found along grain boundaries in the NiMo film [45].

The TCR value of an amorphous alloy strongly correlates with its specific resistance [49]. It also corresponds to the thermal effect on the specific resistance, i.e., the TCR increases at the temperature where the specific resistance abruptly decreases. The TCR values of alloys containing refractory metals exceed those of NiP; NiReP alloy film annealed at 500 °C in particular has an excellent TCR of 18 ppm $\cdot$ K^{-1} [36]. Although the TCR of as-plated crystalline NiMoP is lower than TCR values of amorphous alloys, heat treatment at 500 °C slightly decreases the TCR to 134 ppm $\cdot$ K^{-1}, which is a relatively high value, while the value measured after annealing at 700 °C is the lowest of all Ni alloys.

Finally, the thermal stability of the specific resistance of various films is demonstrated in Fig. 18, which shows the behavior of NiWP annealed at 400 °C for 1 h, NiReP annealed at 500 °C for 1 h, and NiMoP annealed at 500 °C for 1 h. The resistance of crystalline NiMoP heat-treated at 500 °C increases with rising temperature, which indicates that the thermal stability of NiMoP with a specific resistance of 147 μΩ cm is inferior to that of the other materials. While the resistance of NiWP and NiReP films remains almost constant until about 500 °C, the resistance of NiReP is maintained at a more constant level than that of NiWP. The results shown in Fig. 18 indicate that NiReP containing a large amount of refractory metal (44 at% rhenium) is most suitable for a thin film resistor for use at temperatures below 500 °C. Specific resistance and TCR values of the respective films are listed in Table 7.

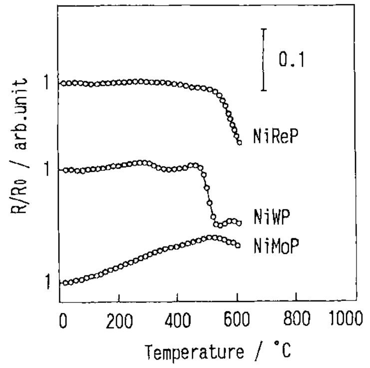

Fig. 18. Change in resistance of electroless $Ni_{81}W_7P_{12}$ (annealed at 400 °C for 1 h), $Ni_{51}Re_{44}P_5$ (annealed at 500 °C for 1 h), and $Ni_{86}Mo_{13}P_1$ (annealed at 500 °C for 1 h) alloy films during heating at a rate of 10 °C min^{-1} and 2.0×10^{-3} Pa (T. Osaka et al., 1992 [37]).

6 Electroless Cobalt and Its Alloys

Cobalt-phosphorus deposition was first described by Brenner and Riddell [1], who used alkaline baths at pH 8 to 10. The high coercivity of CoP films deposited by means of electroless plating was first observed in 1962 by Fisher and Chilton, who pointed to the possibility of exploiting this property for high-density magnetic recording [50]. Since their discovery, electroless cobalt plating has been developed further because of its value for magnetic recording devices. Ranson and Zentner [51] obtained deposits of low coercivity and suggested that these might be applicable as computer storage elements for high-speed switching devices. In the 1960s, a number of studies were carried out that showed that a wide variety of magnetic properties can be induced by changing the plating conditions, such as the concentration of the bath constituents, the pH, and the concentration of additives [51–64]. Pearlstein and Weightman [64] in 1974 developed a plating bath that contained dimethylamine borane as a reducing agent; this bath, unlike its phosphinate counterpart, was found to deposit CoB at a low pH. Such cobalt deposits containing boron usually possess soft magnetic properties, in contrast to those deposited from phosphinate baths. The following materials have been deposited by electroless methods: Co (with N_2H_4 as a reducing agent), CoP, CoB, CoNi, CoNiP, CoNiB, CoWP, CoNiWP, CoReP, CoNiReP, CoZnP, CoMnP, CoNiMnP, etc. Electrodeposited Co films were also studied extensively [65–72].

6.1 Electroless Cobalt Alloys for Longitudinal Magnetic Recording Media

High saturation magnetization and rather high coercivity are required for magnetic recording media. Cobalt film, due to its high saturation magnetization of about 1400 emu · cc^{-1}, has the potential of satisfying these requirements, but pure cobalt ones have a lower coercivity. Other elements must therefore be codeposited in order to produce a highly coercive film. Codeposition of a sparingly soluble second element with cobalt is usually attempted to induce segregation.

The first commercial usage of cobalt films involved electroplated Co films, which in the 1970s were applied to magnetic drums and analogue disks. In the late 1970s, an electroless Co alloy film was attempted in practical use, and in 1981 electroless CoNiP film as well as sputtered γ-Fe_2O_3 media were utilized by NTT as standard materials for the PATTY high density storage system [73, 74]. A CoNiP plating bath was developed for highly reliable production of electrolessly plated media [75]. Successively, various plated disk systems were developed, and a precision production technology was established. Magnetic properties are very sensitive to the structure, crystallinity, particle size, crystal orientation, etc. of a material, and magnetic materials must be investigated with regard to many factors to find out how to control these properties. The presence of very small amounts of metallic impurities in plating baths for longitudinal CoNiP media can affect the magnetic properties of the products, as shown in Fig. 19. Thus, high reproducibility is obtained only by closely controlling such impurities in the baths [75].

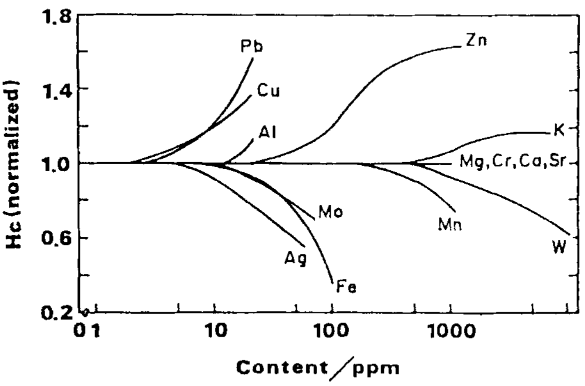

Fig. 19. Effect of the concentration of metal ion impurities in the plating bath on the coercivity of disk media. Elements in the figure show their metal ions. Bath composition (0.06 mol · dm^{-3} $CoSO_4 \cdot 7\,H_2O$, 0.04 mol · dm^{-3} $NiSO_4 \cdot 6\,H_2O$, 0.2 mol · dm^{-3} $NaH_2PO_2 \cdot H_2O$, 0.1 mol · dm^{-3} $(NH_4)_2SO_4$, 0.3 mol · dm^{-3} sodium malonate, 0.4 mol · dm^{-3} sodium malate, 0.5 mol · dm^{-3} sodium succinate, 80 °C, pH 9.0) (F. Goto et al., 1982 [75]).

Recent research on more coercive media with a low noise ratio involved addition of Zn to the Co alloy system [76–79]. Addition of Zn to the cobalt alloy very effectively produces a film with a fine particle structure, which results from codeposition of elements which are hardly soluble in the matrix. Such codeposition causes segregation and hence produces a film microstructure consisting of fine particles. The fine particulate structure lowers the noise ratio and increases the coercivity of the medium.

In practice, the thickness of most media is typically 50 nm, which is why the substrate surface and the conditions of initial deposition are extremely important [80–83]. The effect of changing the substrate surface conditions on the deposited media was investigated, and an attempt of controlling the medium properties involved varying the pretreatment of the substrate surface [82].

6.2 Electroless Cobalt Alloys for Perpendicular Magnetic Recording Media

The recording density of a longitudinal recording system can be increased by decreasing the medium thickness and by increasing the coercivity. However, decreasing the medium thickness also decreases the total magnetization of the medium, while increased coercivity causes saturation of the recording head.

Iwasaki et al. [84] proposed that perpendicular recording is independent of the effect of the demagnetizing field H_d, which forms the transition area in longitudinal media. Thus, the recording method is essentially suitable for achieving ultra high recording density, as has been confirmed both by theory and by experiment [85]. A disadvantage of the system is the requirement for very narrow spacing and lower output voltage. However, the latter can be avoided by applying a soft magnetic underlayer, because of the formation of horseshoe mode magnetization in combination with a single-pole type (SPT) head [86, 87].

Before the proposal of perpendicular recording, efforts were made to use the vertical magnetization mode for magnetic recording on the basis of electrochemically deposited media, such as electrodeposited CoNiP [88] and Co-electrodeposited alumite films [89–91]. Chen and Cavalotti [92, 93] was the first to use an electrochemically deposited medium for perpendicular recording. They used electrodeposited Co film with a "cellular-like" columnar structure. Horkans et al. [93] employed electrodeposited CoMnP as a medium. Electroless-plated media were introduced by Osaka and Kasai et al. [94,95], who used CoWP films. Their group investigated CoMnP, CoNiMnP, and CoNiReP [96–105]. Takano et al. also investigated the suitability of electroless-plated media for perpendicular recording [106, 107]. Fig. 20 shows a typical example of X-ray patterns of CoNiMnP films, which illustrate that addition of $MnSO_4$ makes the c-axis orientation of the hcp crystal perpendicular. In this system, addition of $MnSO_4$ effectively controls the perpendicular orientation of the c-axis of the hcp crystal. Elementary rhenium was then added to lower the M_s and hence to lower the demagnetizing field. Research on

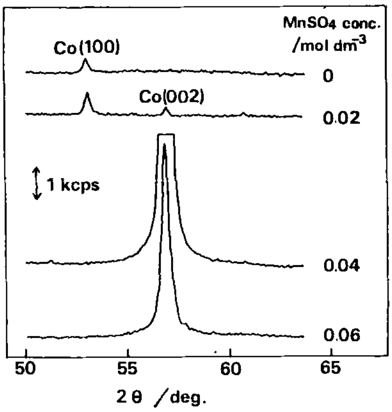

Fig. 20. X-ray diffraction patterns of CoNiMnP films with various $MnSO_4$ concentrations on a Cu substrate (T. Osaka et al., 1983 [98]).

CoNiReMnP showed that addition of certain complexing agents as well as addition of $MnSO_4$ controls the c-axis orientation. Table 8 lists typical bath compositions and conditions of electroless cobalt alloy plating for perpendicular magnetic recording media.

Based on CoNiReP, further studies were carried out to simplify the bath and alloy systems. In this approach, various perpendicular anisotropic films were obtained [96-105, 108-114], finally affording CoNiP ternary alloy films for perpendicular magnetic recording media. It was confirmed that CoNiP media possess excellent perpendicular recording characteristics [96], and the coercivity of CoNiP films can be controlled over a wide range up to 1500 Oe by simply adjusting certain plating bath factors [115]. Representative magnetic properties and compositions of films are listed in Table 9 [116].

Table 8. Bath compositions and operating conditions for electroless-plated perpendicular magnetic recording media (T. Osaka et al., 1991 [116]).

Chemicals	Concentrations / mol · dm^{-3}			
	Bath 1	Bath 2	Bath 3	Bath 4
$NaH_2PO_2 \cdot H_2O$	0.20	0.20	0.20	0.20
$(NH_4)_2SO_4$	0.50	0.50	0.50	0.50
$CH_2(COONa)_2 \cdot H_2O$	0.75	0.50	0.75	0.75
$C_2H_2(OH)_2(COONa)_2 \cdot 2\ H_2O$	0.20	–	0.20	0.20
$CH(OH)(COOH)_2$	0.05	–	–	–
$CH_2(OH)\ COOH$	–	–	1.00	1.10
$C_2H_3OH(COONa)_2$	–	–	–	0.01
$CoSO_4 \cdot 7\ H_2O$	0.06	0.01	0.13	0.06
$NiSO_4 \cdot 6\ H_2O$	0.08	0.05	0.16	0.16
NH_4ReO_4	0.003	0.003	0.003	–
pH (adjusted with NH_4OH)	8.7	9.6	8.0	8.7
Bath temperature / °C	80	80	80	80

Table 9. Magnetic profiles of CoNiReP films (T. Osaka et al., 1991 [116]).

		Film A	Film B	Film C	Film D
Composition	Co	32	24	38	35
[at%]	Ni	55	62	49	57
	Re	6	6	6	–
	P	7	8	7	8
M_s	[emu cc^{-1}]	250	80	400	600
H_c (//)	[Oe]	600	200	600	500
H_c ($\perp$)	[Oe]	1200	500	1200	1200
K_u	[x10^5 erg cc^{-1}]	+2.9	+0.8	+2.3	−8.0
$K_\perp$	[x10^5 erg cc^{-1}]	+6.8	+1.2	+12.3	+14.6

6.3 Electroless Cobalt Alloys as Soft Magnetic Materials

Soft magnetic thin films have been investigated for their suitability for use with sensor devices and as head core materials for magnetic recording systems. In 1979, the first commercial thin film was mounted on the IBM 3370 disk drive, which contained electrodeposited NiFe film with 80 wt% Ni as a head core material [117–119]. Recently, materials with a higher B_s (saturation magnetic flux density) have been claimed to improve the head properties, and an electrodeposited CoFe film with a high B_s (1.9 tesla), which is almost twice as high as that of permalloy, has been described [120]. Electroless plating can also afford such high B_s soft magnetic materials if DMAB (dimethylamine borane) is used as a reducing agent. We have attempted to produce soft magnetic CoB and CoFeB materials with a high B_s value, as listed in Table 10 [121, 122]. The moderately coercive as-deposited state, e.g., 0.64 and 0.72 Oe for CoB and CoFeB, respectively, is obtained by applying an external magnetic field during electroless deposition. Codeposition of Fe into CoB film increases the permeability μ from 580 to 800 in the as-deposited state. The μ values of CoFeB are not as high as those of permalloy, but annealing raises μ by more than 1500 to 2000 [123].

Table 10. Magnetic properties of electroless $Co_{94}B_6$ films deposited without (a) or with (b) an applied external field (560 G), and electroless $Co_{92}Fe_2B_6$ film deposited with an applied external field (560 G). (T. Osaka et al., 1992 [121, 122]).

		(a)	(b)	(c)
M_s	[emu cc^{-1}]	1140	1140	1180
H_c (easy axis)	[Oe]	1.20	0.64	0.72
H_c (hard axis)	[Oe]	3.26	1.83	1.13
H_k	[Oe]	40	40	25
μ (5 MHz)	[–]	370	580	800
λ_s	[–]	–	–	-4.4×10^{-7}

Subscript numbers denote atomic % of the films.

7 Electroless Copper Deposition

Electroless copper plating is indispensable for providing electric conduction paths to through-holes in printed wiring boards. It is used either to plate the first thin layer of copper, followed by electroplating to build up the desired thickness, or to plate the entire layer by the electroless method. The latter is called the "full-build" process, and it is in principle attractive because it can be used not only to deposit copper in through-holes, but also to produce an entire circuit on the surface of a circuit board without using etching and electrolytic plating processes. Full-build electroless copper must meet certain requirements in terms of physical and mechanical properties in order to withstand the stress resulting from processes such as soldering, which are used to fabricate circuit boards, and to maintain integrity during usage of the circuit board. It is thus important to scientifically explain the factors which affect the deposit properties. In this section, both chemical and physical aspects of electroless copper deposition are discussed.

7.1 Mechanism of Electroless Copper Deposition

A typical electroless copper plating bath contains divalent copper, EDTA as a complexing agent, NaOH, formaldehyde as a reducing agent, and (a) small amount(s) of additive(s) to stabilize the bath and to impart desired physical properties to the deposit. For thin metallization purposes, the bath may remain at room temperature, but the full-build bath is operated at elevated temperature. The composition and operation conditions of a typical full-build bath are shown in Table 11 [124]. It is well known that the two partial reactions are [3, 4]:

$$\text{Cathodic:}\quad Cu(II) + 2\,e^- \rightarrow Cu \tag{33}$$

$$\text{Anodic:}\quad 2\,HCHO + 4\,OH^- \rightarrow 2\,HCOO^- + 2\,H_2O + H_2 + 2\,e^- \tag{34}$$

where Cu(II) represents divalent Cu-EDTA complex ions (perhaps a mixture of CuY^{2-} and $Cu(OH)Y^{3-}$ in which the ratio of the two species is dependent on the pH [125]).

Table 11. Composition and operating conditions of a typical full-build electroless copper bath (H. Akahoshi et al., 1986 [124]).

$CuSO_4$	0.04 mol dm^{-3}
EDTA	0.08 mol dm^{-3}
HCHO	0.04 mol dm^{-3}
pH(NaOH)	12-13
Additives	NaCN, $K_4Fe(CN)_6$, 2,2'-Bipyridyl, Polyethyleneglycol, etc.
Temperature	65-67 °C
Agitation	Air

7.1.1 Mechanism of Partial Reactions

The cathodic process (33) appears to proceed in a single step involving simultaneous transfer of two electrons. No Cu(I) formation was detected in the course of an investigation involving a rotating ring-disk electrode [126]. Formation of Cu(I) as an intermediate was clearly demonstrated by using tartrate instead of EDTA as a complexing agent. However, Bindra et al. [127], who determined the kinetic parameters of the reduction of the Cu-EDTA complex, concluded that the reduction proceeds in two steps, and that the first step (CU (II) to Cu (I)) is rate-determining. They argue that a two-electron transfer would require a very high activation energy.

The anodic reaction (34) is a catalytic process, and it proceeds in several distinct steps. Formaldehyde in aqueous solution is known to exist almost entirely in the form of methylene glycol [128]:

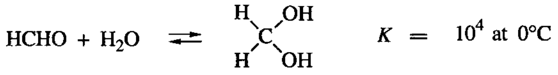

$$\mathrm{HCHO + H_2O} \rightleftharpoons \begin{matrix} \mathrm{H} & & \mathrm{OH} \\ & \mathrm{C} & \\ \mathrm{H} & & \mathrm{OH} \end{matrix} \qquad K = 10^4 \text{ at } 0\,^\circ\mathrm{C} \tag{35}$$

Methylene glycol is a weak acid and dissociates as follows:

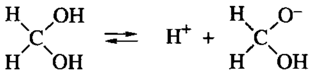

$$\begin{matrix} \mathrm{H} & & \mathrm{OH} \\ & \mathrm{C} & \\ \mathrm{H} & & \mathrm{OH} \end{matrix} \rightleftharpoons \mathrm{H^+} + \begin{matrix} \mathrm{H} & & \mathrm{O^-} \\ & \mathrm{C} & \\ \mathrm{H} & & \mathrm{OH} \end{matrix} \tag{36}$$

The dissociation constant determined most recently by Schumacher et al. [129] by NMR spectroscopy in 0.5 M Na_2SO_4 is $pK_a = 13.10$ at 25 °C. The kinetic analysis performed by these authors shows that under conditions where the overall reaction is kinetically controlled by the surface reaction, the deposition rate R is directly proportional to the concentration of the methylene glycolate anion MG^-:

$$R = A \exp\left(\frac{-\Delta E^*}{RT}\right) [\mathrm{MG^-}] \tag{37}$$

where A is the Arrhenius pre-exponential factor, $[MG^-]$ is the concentration of MG^- near the surface (surface concentration), and ΔE^* is the activation energy. The surface concentration of MG^- is assumed to be equal to the bulk concentration under conditions where mass transport is not rate-limiting. In terms of the formal concentration of formaldehyde C_{HCHO}, Eq. (37) can be rewritten as follows:

$$R = A \exp\left(\frac{-\Delta E^*}{RT}\right) \frac{K_a[\mathrm{OH^-}]}{K_w + K_a[\mathrm{OH^-}]} C_{\mathrm{HCHO}} \tag{38}$$

As this equation indicates, the deposition rate was found to depend on the following experimentally determined factors: (1) At high concentrations (>10 mmol/dm^3), R is independent of the Cu(II) concentration, whereas at low concentrations (<5 mmol/dm^3) it is limited by mass transport; (2) The dependence of R on the OH^- concentration is based exclusively on its effect on the dissociation of MG (Eq. (36)); (3) The dependence of R on the formaldehyde concentration is first order with respect to MG^-. The dependence of R on the temperature afforded a activation energy ΔE^* of 46 kJ/mol.

Furthermore, Schumacher et al. [129] found that in the case of deuterated formaldehyde, in which protium is substituted with deuterium, the rate decreases by a factor of five. This indicates that hydrogen is a primary reactant in the rate-determining step, and these authors proposed that cleavage of the C–H bond of MG^- must be the rate-determining step. Okinaka [126] analyzed gases produced by substituting formaldehyde in an electroless copper bath with deuterated formaldehyde. He found that the gaseous product essentially consists of D_2 with minor amounts of HD and H_2.

The mode of adsorption and dissociation of MG^- has been discussed in detail by Gottesfeld et al. [130]. These authors argued that MG^- is likely to be adsorbed on copper not through an oxygen atom, but rather with the C–H bonds being adjacent to the copper surface. This is for two reasons: (1) the negative charge on copper expected at the high pH of the electroless copper bath and the potential difference at the metal–solution interface tend to orient the negatively charged oxygen atom of MG^- away from the surface, and (2) the C–H side of the MG^- ion shows hydrophobic interactions, in contrast to the hydrophilic interactions of the C–O bonds.

The experimental results and discussions presented by the various authors cited above, in combination with the unified mechanism proposed by van der Meerakker and described in Sec. 3, make it possible to write the following reaction equations to formulate the mechanism of the partial anodic process:

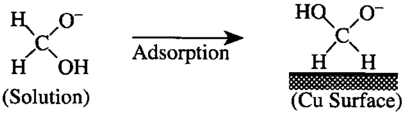

(39)

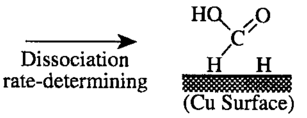

(40)

$$\xrightarrow{+OH^-} HCOO^- + H_{ads} + H_2O + e^- \quad (41)$$

$$H_{ads} + H_{ads} \rightarrow H_2 \quad (42)$$

7.1.2 Interaction between Anodic and Cathodic Partial Reactions

As mentioned in Sec. 2.1, simple superposition of the respective current–potential curves for the two partial reactions does not always yield the curve obtained with a complete electroless bath. This is illustrated in Fig. 21 [126], in which the current–potential curve obtained with a complete electroless copper bath containing EDTA (curve 1) is compared with the curve obtained in solution in the absence of formaldehyde (curve 2) and with that obtained in solution in the absence of Cu(II) (curve 3). All three curves were recorded at room temperature with a copper disk electrode rotating at 2100 rpm, while scanning the potential in the positive direction

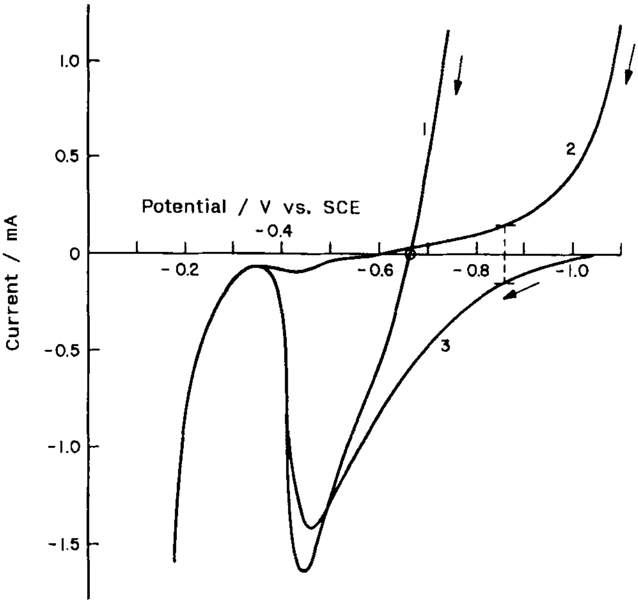

Fig. 21. Current vs. potential curves of a rotating Cu disk electrode in a solution of 0.12 mol · dm^{-3} EDTA and 0.5 mol · dm^{-3} NaOH containing 0.1 mol · dm^{-3} Cu(II) + 0.39 mol · dm^{-3} HCHO (curve 1), 0.1 mol · dm^{-3} Cu(II) (curve 2), and HCHO only (curve 3), respectively. (Y. Okinaka, 1969 [126]).

at a speed of 1 V/min. Fig. 21 demonstrates that the plating potential of − 0.67 V, which is the zero-current potential of curve (1), is entirely different from the potential where the anodic and cathodic currents of curves (2) and (3) are equal (− 0.86 V). Evidently, the reduction of the Cu(II)-EDTA complex is greatly accelerated by the presence of formaldehyde. This acceleration effect is seen clearly, even at very small concentrations of formaldehyde, as shown in Fig. 22.

Recently, Feldmann and Melroy [131] utilized a quartz microbalance technique to simultaneously determine the net current and the partial anodic and cathodic currents in a single complete electroless copper bath. The cathodic current is calculated by converting the deposition rate measured with the microbalance into the unit of current, while the anodic current is computed by subtracting the cathodic current from the net current measured directly on the microbalance electrode. Using this technique, Feldmann and Melroy showed that the potential at which the reduction of the Cu-EDTA complex begins at 70 °C shifts by as much as 0.3 V in positive direction upon addition of formaldehyde. It was also shown that at a given potential, the rate of copper deposition increases with increasing formaldehyde concentration (Fig. 23). The observed catalytic effect of formaldehyde is attributed to an interaction between formaldehyde and the Cu-EDTA complex, possibly to the formation of Cu(EDTA)/formaldehyde complex. However, the detailed mechanism of this catalytic effect has not been clarified.

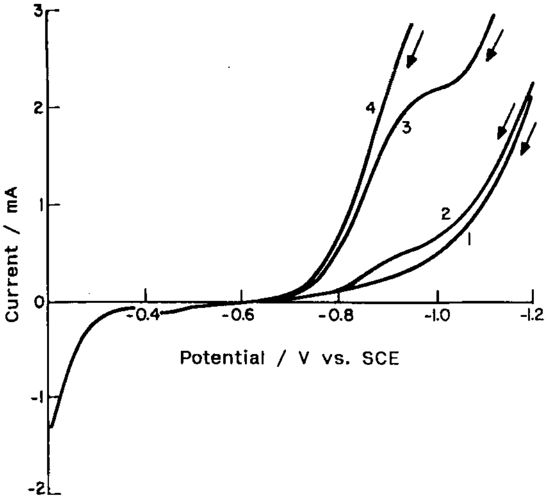

Fig. 22. Effect of formaldehyde on the cathodic reduction of 0.1 mol · dm^{-3} Cu(II) in 0.5 mol · dm^{-3} NaOH containing 0.12 mol · dm^{-3} EDTA at a rotating Cu disk electrode [(1) no HCHO; (2) 1.3 × 10^{-4} mol · dm^{-3}; (3) 2.6 × 10^{-4} mol · dm^{-3}; (4) 3.9 × 10^{-4} mol · dm^{-3} HCHO] (Y. Okinaka, 1969 [126]).

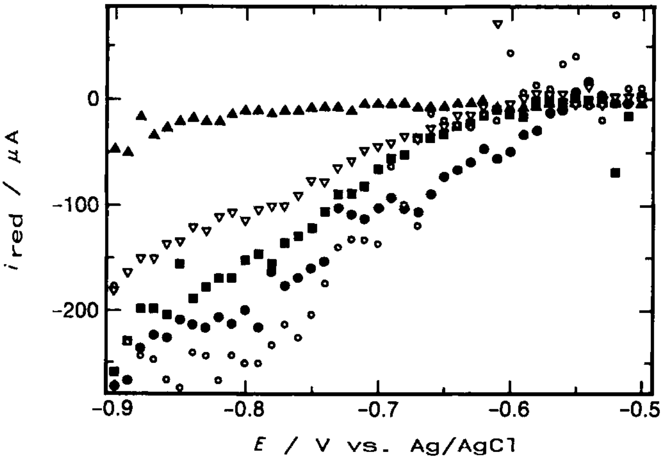

Fig. 23. Rate of copper deposition, determined with a quartz crystal microbalance, vs. potential in an electroless copper plating bath at various formaldehyde concentrations. ▲ 0 mmol · dm^{-3} HCHO, ▼ 15 mmol · dm^{-3}, ■ 30 mmol · dm^{-3}, ● 45 mmol · dm^{-3}, ○ 60 mmol · dm^{-3} (B. J. Feldmann et al., 1989 [131]).

Wiese and Weil [132], who used the same technique combined with fast solution exchange, confirmed the catalytic effect of formaldehyde on the reduction of the Cu-EDTA complex. They also observed that the anodic oxidation of formaldehyde proceeds at a steady rate during electroless copper deposition, because the latter steadily activates the copper surface for formaldehyde oxidation. Without simultaneous copper reduction, the oxidation of formaldehyde on the copper surface is increasingly inhibited as the experiment proceeds.

The experimental evidence described above clearly shows that the cathodic and anodic partial reactions interact with each other, and that such interactions are an essential part of the mechanism of electroless copper deposition. It should be noted that the interdependence of partial reactions has also been demonstrated by Bindra et al. [127], based on their results of kinetic and mechanistic analysis.

7.2 Properties of Electroless Copper Deposits

Full-build electroless copper plated on printed circuit boards must maintain its structural integrity under thermal stress, i.e., no cracking should occur when it is heated or cooled. Tests conducted to ascertain the thermal reliability of printed circuit boards typically include a thermal shock test, consisting of floating on molten solder at 260 °C for 10 seconds, and a thermal cycle test consisting of repetitive temperature excursions, such as room temp. → −65 °C → room temp. → +125 °C → room temp. Cracking under thermal stress is believed to occur because of a mismatch in the thermal expansion coefficients of copper and the material of the board, which is typically epoxy resin. The thermal expansion of copper is much less (0.3% at 200 °C) than that of epoxy resin (2.1%). Materials with a lower expansion coefficient, such as polyimide are preferred, but its expansion coefficient of 0.8% is still significantly higher than that of copper. To avoid the formation of cracks in copper, copper must therefore be capable of elongating with the expanding board, i.e., it must have sufficient ductility. It must also be capable of resisting the force resulting from thermal expansion of the board material; i.e., it must have sufficient tensile strength. Of the two important metallurgical properties of electroless copper, ductility and factors affecting this property have been investigated more extensively. The rest of this section deals with the ductility of electroless copper.

7.2.1 Effect of Inclusions on the Ductility

The effect of included impurities, especially molecular hydrogen, has been studied extensively [133–140]. Table 12 lists the concentration ranges of impurity elements found in deposits formed under various conditions. Comparison of the atomic ppm values of the various elements clearly shows that the hydrogen content can be disproportionately high compared to the other elements.

It has long been known that the ductility of electroless copper can be increased by annealing at relatively low temperatures, and that the hydrogen content of the deposit decreases upon annealing. The existence of a close correlation between the two annealing effects has been demonstrated [141]. Fig. 24 shows an example of the variation of the ductility (% elongation determined by a mechanical bulge tester)

Table 12. Inclusions in electroless copper (Y. Okinaka et al., 1976 [133]).

	ppm, weight	ppm, atomic
H	4–200	250–12700
C	20–500	105–2650
O	50–450	200–1800
N	20–170	90–770
Na	20–70	55–190

and the hydrogen content (determined by an inert gas fusion technique) with the annealing time at 150 °C in a nitrogen atmosphere. The electroless copper deposit used to obtain this set of data was grown epitaxially on a large-grained (10–40 μm) copper foil to prevent the result from being affected by the grain growth (see Sec. 7.2.2). Fig. 24 shows that the ductility improves with the annealing time and that it reaches a nearly constant level after approximately 24 hours. Correspondingly, the hydrogen content decreases initially and becomes constant after the same length of time. The hydrogen curve clearly shows that two kinds of hydrogen are present in the deposit: "diffusible hydrogen", which escapes upon annealing, and "residual hydrogen", which is not liberated by annealing.

Graebner and Okinaka [136], using low temperature calorimetry, demonstrated that the portion of diffusible hydrogen consists entirely of molecular hydrogen H_2. This calorimetric method is based on measuring the heat that is produced by quenching a copper sample from room temperature to 4.2 K (liquid helium) as a function of time. At equilibrium at 300 K, molecular hydrogen consists of 75% ortho-H_2

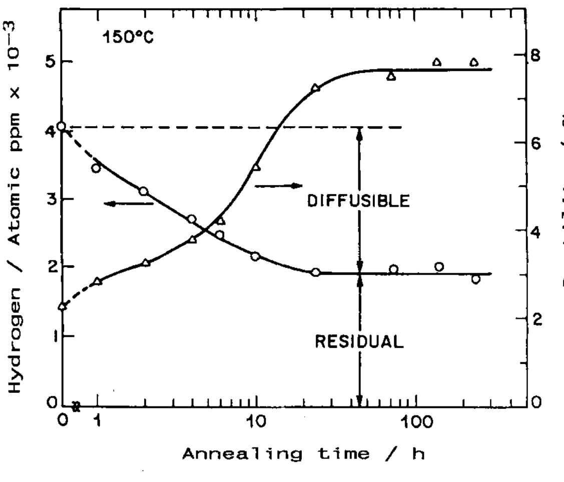

Fig. 24. An example of the variation of the hydrogen content and the ductility with the annealing time at 150 °C (deposit plated epitaxially on large-grained copper foil) (Y. Okinaka et al., 1986 [135]).

isomer and 25% para-H_2, whereas at 0 K it contains 100% para-H_2. The conversion of ortho- to para-H_2 is known to be a bimolecular exothermic reaction, and kinetic analysis based on thermal measurements yields the molecular hydrogen content of the copper deposit. Analytical results obtained by this method compared favorably with those found by the inert gas fusion technique for diffusible hydrogen. For example, for an as-deposited sample the calorimetric method yielded 1860 atomic ppm of H, while the fusion method afforded a diffusible hydrogen content of 2046 ± 155 ppm. The difference between these two values is considered insignificant in view of the uncertainties associated with both methods. The sample annealed at 150 °C for 24 hours showed no heat generation upon cooling down to 4.2 K; in other words, there was no H_2 left in the annealed sample. By definition, there was no diffusible hydrogen in the annealed sample. Thus, the diffusible hydrogen content of as-deposited electroless copper is indentified as molecular hydrogen.

In a previous study by Okinaka and Nakahara [133] involving transmission electron microscopy (TEM), it was observed that electroless copper contains randomly distributed voids measuring 20–300 Å within grains and large faceted voids measuring 500–750 Å at low-angle grain boundaries. TEM micrographs showing such voids are reproduced in Fig. 25. The volume fraction occupied by such voids in the deposit can be calculated from the accurately determined mass density of the deposit. Careful measurements with a conventional specific gravity bottle afforded a value of 8.861 ± 0.012 g/cm^3 for the sample used in the calorimetric study, as compared to 8.92 g/cm^3 for ordinary bulk copper. From these density values the void fraction of this sample was calculated to be 0.66%. If it is assumed that the entire amount of molecular hydrogen is squeezed into the voids, the H_2 pressure in the voids is calculated to be 700 ± 150 atm at room temperature and 1200 atm at 260 °C (temperature of molten solder). These H_2 pressures exceed the yield stress of copper (680 atm), which indicates that the pressure of molecular hydrogen in electroless copper can generate dislocations in copper crystals, causing a loss of ductility. A TEM observation did reveal such dislocations around the voids [140].

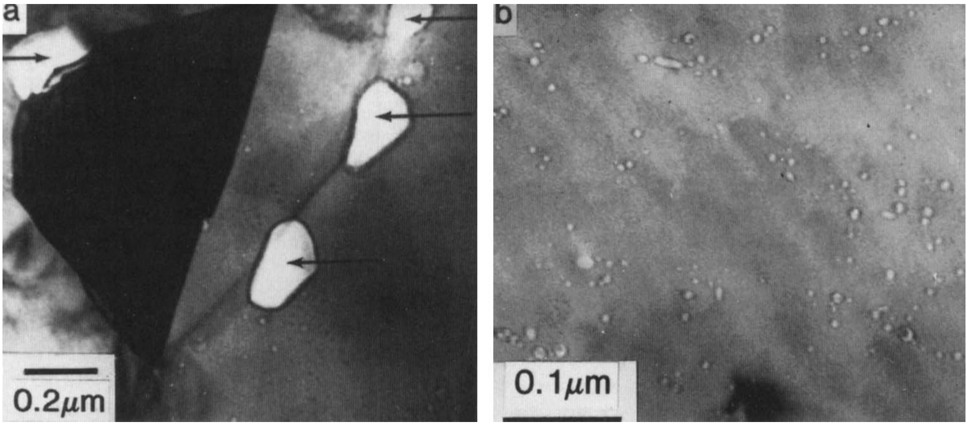

Fig. 25. TEM micrographs showing voids in electroless copper. (a) Grain boundaries, (b) inside the grains (Y. Okinaka et al., 1976 [133]).

7.2.2 Effect of Bath Additives on the Ductility

It is customary to add a small amount of a compound called "ductility promotor" to practical full-build electroless copper baths. Known ductility promotors are NaCN, $K_4Fe(CN)_6$, $K_2Ni(CN)_4$, and 2,2′-dipyridyl. The ductility-promoting effect of the latter two compounds is illustrated in Fig. 26. Fig. 27 shows how the content of diffusible (molecular) hydrogen varies with the concentrations of the additives. Both additives decrease but do not completely eliminate the inclusion of diffusible hydrogen. A comparison of Figs. 26 and 27 indicates qualitatively that the ductility-promoting effect of the additives can be correlated with their ability to decrease the inclusion of diffussible hydrogen. A more quantitative comparison shows that dipyridyl is a less effective ductility promotor than $K_2Ni(CN)_4$, in spite of the fact that both compounds are capable of reducing the inclusion of diffusible hydrogen to the same extent. The less ductility-promoting effect of dipyridyl is attributed to the occlusion of this compound in the copper deposit, which is confirmed by the fact that addition of dipyridyl sharply increases the carbon content of the deposit [135]. An SEM examination showed that dipyridyl promotes the formation of twins in the copper crystals [135]. The presence of twins is equivalent to decrease in the grain size, as far as their effect on mechanical properties is concerned. The grain size effect is discussed in the next section.

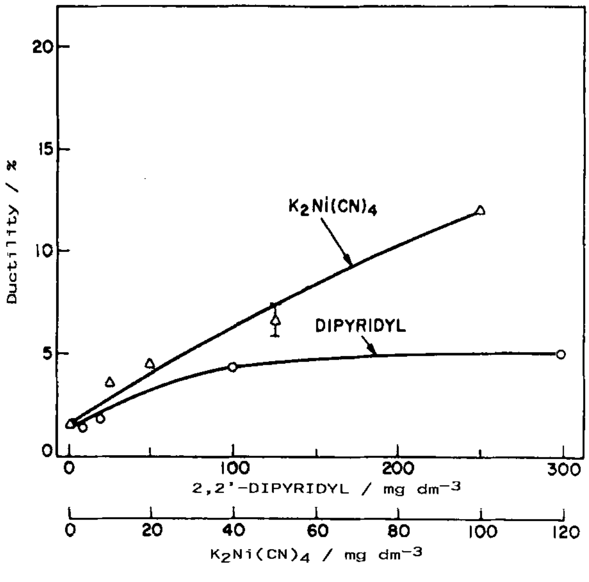

Fig. 26. Effects of 2,2′-dipyridyl and $K_2Ni(CN)_4$ on the ductility of an electroless copper deposit. Bath composition (0.04 mol · dm^{-3} $CuSO_4$, 0.08 mol · dm^{-3} EDTA, 0.04 mol · dm^{-3} HCHO, pH 12.5, 70 °C). Deposit plated epitaxially on large-grained copper foil (Y. Okinaka et al., 1986 [135]).

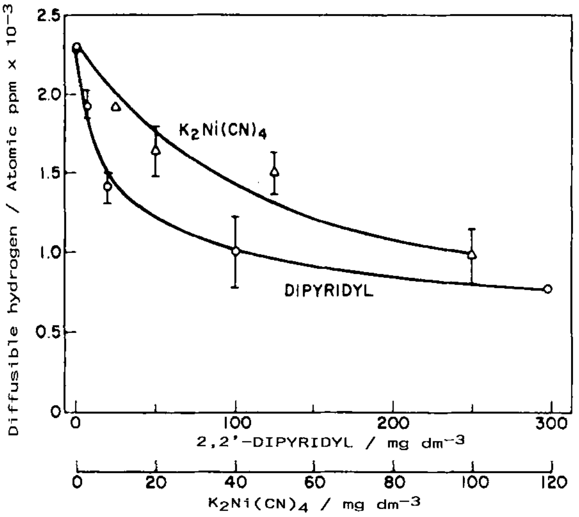

Fig. 27. Effect of 2,2'-dipyridyl and $K_2Ni(CN)_4$ on the diffusible (molecular) hydrogen content of an electroless copper deposit (Y. Okinaka et al., 1986 [135]).

7.2.3 Effect of the Grain Size on the Ductility

The grain size is generally considered an important factor affecting the physical properties of crystalline materials, such as yield stress and hardness. Although no general quantitative relationship is known between grain size and ductility, it is expected qualitatively that a decrease in the grain size lowers the ductility, in view of the known effect of grain boundaries inhibiting the slippage of crystal planes during plastic deformation. In additon to this "conventional" grain size effect, the effect of the grain size on the inclusion of hydrogen and hence on the resulting formation of voids has been shown to be an important factor to be considered in the case of electroless copper deposition [138].

A study was conducted to compare large-grained deposits (10–40 μm) with fine-grained deposits (0.2–2 μm) in terms of ductility and diffusible hydrogen content (and the content of other impurity elements) [138]. It was found that fine-grained deposits have much lower ductility values (0.8–6%) than large-grained ones (2–12%) produced in the same plating bath at the same time. (Different grain sizes were obtained on different substrates with different surface structures.) It was also found that fine-grained deposits contain larger amounts of diffusible hydrogen than large-grained ones obtained in the same bath. The ratio of the diffusible hydrogen content of fine-grained deposits to that of large-grained deposits plated in the same bath averaged at 2.5 ± 0.5 (18 baths with different compositions and at different plating conditions). This result indicates that fine grained deposits contain two to three times as many hydrogen-induced voids. Fig. 28 shows a plot of the ductility against the diffusible hydrogen content for all tested deposits, regardless of the grain size, before and after annealing at 150 °C for 24 hours. It is seen that the data for as-plated and annealed deposits form two separate smooth curves, regardless of the grain size. It should be noted that the data for annealed deposits show the extent of improvement in the ductility of corresponding as-plated samples. The annealed samples actually did not contain any diffusible hydrogen. Therefore, the curve representing annealed deposits should be interpreted as showing the effect of hydrogen-induced voids rather than that of the hydrogen pressure. Thus, the effect of diffusible hydrogen and the resulting voids on the ductility are clearly important, regardless of the grain size.

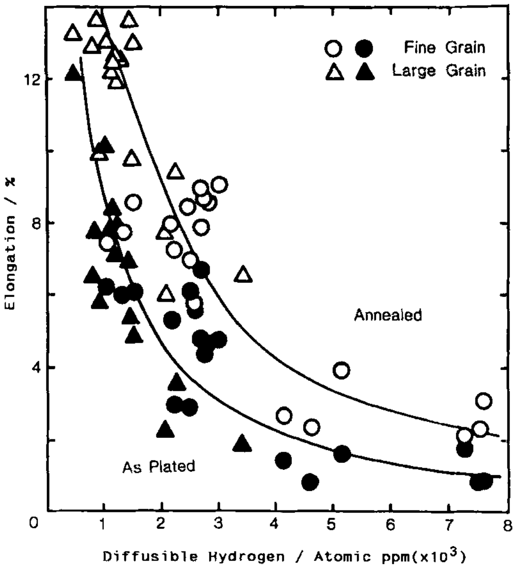

Fig. 28. Variation of the ductility of fine-grained and large-grained electroless copper deposits with diffusible hydrogen content (S. Nakahara et al., 1989 [138]).

7.2.4 Effect of Low Temperature Annealing on the Ductility

As discussed above, the ductility of electroless copper generally improves as a result of annealing at relatively low temperature (100–200 °C), and hydrogen loss by diffusion is clearly one of the factors that are responsible for this phenomenon. In addition, microstructural changes resulting from recrystallization and grain growth have been shown to be an important phenomenon influencing the annealing effect at low temperature. Honma and Mizushima [142] showed that ductility improvement resulting from recrystallization and grain growth may be observed after annealing at 140 °C for only one hour. Nakahara et al. [139] in studying fine-grained deposits observed that the extent of ductility improvement is higher if the deposit contains less diffusible hydrogen (and hence less voids) and less residual hydrogen. For example, deposits containing < 10 ppm (weight) of residual hydrogen and < 40 ppm of diffusible hydrogen showed a 5–6% ductility increase in terms of absolute % elongation as a result of annealing at 150 °C for 24 hours, whereas deposits containing

60–130 ppm of residual hydrogen and > 100 ppm of diffusible hydrogen gave a ductility improvement of only < 2% upon annealing. The residual hydrogen content may be considered a measure of the extent of non-volatile inclusions. These results can be visualized by assuming that deposits with larger amounts of hydrogen-containing voids or impurity molecules are hindered in their recrystallization and grain growth. The voids and impurity molecules at grain boundaries are believed to exert a pinning effect against the motion of grain boundaries, thus causing retardation of recrystallization and grain growth. A TEM examination of deposits with different purity levels actually showed that a large increase in grain size occurs upon annealing of relatively pure deposits, while little grain growth was observed in impure deposits [139].

7.2.5 Effects of Other Factors on the Ductility

Factors affecting the ductility of electroless copper which are considered in previous sections include inclusions such as molecular hydrogen and other impurities, voids created by inclusion of hydrogen, defects such as dislocations and twins, and grain size. Low temperature annealing has been shown to considerably affect the ductility through its effect on the removal of pressurized molecular hydrogen from voids and also through its promotion of recrystallization and grain growth. There are two other factors which should be mentioned here: (1) lattice strain, and (2) type of substrate. Matsuoka et al. [143] studied the effect of ductility-promoting additives, such as 2,2′-dipyridyl and $K_4Fe(CN)_6$, on the lattice strain, grain size, and ductility. The variation of the latter three parameters with the concentration of additives was found to be complex and dependent on the bath composition. It was observed that the ductility generally increases with increasing grain size and decreasing lattice strain. It was concluded that deposits with large grains and small lattice strain are obtained by using an additive which is not incorporated in the deposits.

Finally, Nakahara et al. [144] investigated the effect of the type of substrate on the ductility and microstructure of electroless copper deposits. They noted that under identical plating conditions, the ductility of electroless copper grown on activated plastic substrates was higher than that of a deposit grown epitaxially on a large-grained copper foil. TEM examinations showed that this substrate effect on the ductility originates from the difference in the size and numerical density of voids. The presence or absence of nodules in the deposit was also found to be an important factor influencing the ductility. For discussion of further details, the reader is referred to the original paper.

7.3 Recent Developments

Owing to the increasing technological interest of the electronics industry in electroless copper plating, a considerable amount of R&D is still in progress in this field, and many publications continue to appear in the literature. It is impossible to review all publications within the limited space of this chapter, and some important papers are not covered. In particular, contributions attempting to elucidate the relationship between physical properties and thermal reliability should be mentioned [145-147]. Furthermore, new additives have been found which improve the physical properties and the thermal reliability of electroless copper deposits; such developments are important for practical purposes. However, very few fundamental mechanistic investigations have been reported.

In view of the environmental concern about the use of formaldehyde, which is a known carcinogen, attempts have been made to develop new bath formulations using other reducing agents, e.g., hydrophosphite [148-152] or glyoxylic acid [153, 154]. The interested reader is referred to the original papers.

8 Electroless Gold

For more than 20 years, there has been sporadic interest in electroless gold plating as a simple and inexpensive method of depositing gold on semiconductors and circuit patterns. Recently, interest in this method has increased because of the need of depositing gold on small isolated areas of high density circuits fabricated on ceramic or plastic substrates.

8.1 Original Borohydride and Dimethylamine Borane (DMAB) Baths

Original autocatalytic gold plating baths [155-160] have quite simple compositions (Table 13), and they are stable even in the absence of stabilizing additives, provided that the chemicals and water used to prepare the bath are sufficiently pure. Gold deposits obtained from these baths are pure and soft and suitable for semiconductor bonding applications. A detailed mechanistic investigation by polarographic and voltammetric techniques [158] showed that one of the interesting characteristics of

Table 13. Examples of original borohydride and dimethylamine borane (DMAB) bath compositions (Y. Okinaka [155-156]).

	Borohydride Bath/mol · dm^{-3}	DMAB Bath mol · dm^{-3}
$KAu(CN)_2$	0.02	0.02
KCN	0.2	0.02
KOH	0.2	0.8
KBH_4	0.4	–
DMAB	–	0.4
Temperature	75 °C	85 °C

the borohydride system is the fact that the species which actually serves as a reducing agent is not the borohydride ion BH_4^- itself, but BH_3OH^- which is formed as an intermediate during hydrolysis of the BH_4^- ion:

$$BH_4^- + H_2O \rightarrow BH_3OH^- + H_2 \tag{43}$$

$$BH_3OH^- + H_2O \rightarrow BO_2^- + 3\ H_2 \tag{44}$$

The anodic current-potential curves shown in Fig. 29 support this mechanism. These curves were obtained by scanning the potential in positive direction; recording started approximately 10 minutes after the solution temperature reached the bath operating temperature of 75 °C. Curve (1) was obtained in a solution containing 0.1 M KBH_4 and 0.2 M KOH. The current rise at the negative end of the potential interval is due to cathodic hydrogen evolution. The first anodic wave, with the plateau appearing in the potential range of electroless deposition in the complete bath is attributed to anodic oxidation of BH_3OH^-. The final rise of anodic current in curve (1) is due to oxidation of BH_4^-, but the entire curve could not be recorded at this high KBH_4 concentration. A much lower KBH_4 concentration (2×10^{-4} M) afforded curve (2), in which the first rise of anodic current is clearly due to oxidation of BH_4^-. The current produced by anodic oxidation of BH_3OH^- is not visible in this curve, because its concentration is too low for the current to be observable on this scale. Comparison between the potential range of electroless deposition and that of anodic oxidation of each of the boron-containing species shows that BH_3OH^-

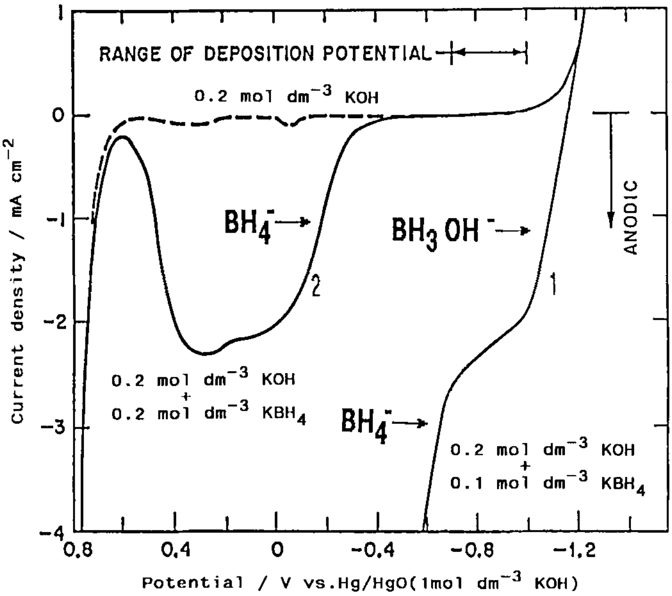

Fig. 29. Current vs. potential curves for the oxidation of borohydride at a gold electrode in various solutions at 75 °C. Potential scanned from negative to positive at 5.56 mV · s^{-1}.

is the species that serves as a reducing agent in the electroless deposition reaction. According to a polarographic investigation carried out by Gardiner and Collat [161], the anodic oxidation reaction of BH_3OH^- may be written as follows:

$$BH_3OH^- + 3\,OH^- \rightarrow BO_2^- + (3/2)\,H_2 + 2\,H_2O + 3\,e^- \tag{45}$$

Combining this reaction with the cathodic reaction

$$Au(CN)_2^- + e^- \rightarrow Au + 2\,CN^- \tag{46}$$

yields the overall reaction equation describing electroless gold deposition from a borohydride bath:

$$\begin{aligned} &BH_3OH^- + 3\,Au(CN)_2^- + 3\,OH^- \rightarrow \\ &\qquad BO_2^- + (3/2)\,H_2 + 2\,H_2O + 3\,Au + 6\,CN^- \end{aligned} \tag{47}$$

The kinetics of the hydrolysis reactions (43) and (44) was studied in detail by means of polarography [158], and the respective pseudo-first-order rate constants k_1 and k_2 were determined. In 0.2 M KOH at 75 °C, the rate constants were $k_1 = 3.2 \times 10^{-5}\,s^{-1}$ and $k_2 = 1.43 \times 10^{-3}\,s^{-1}$, indicating that the second step of hydrolysis (44) is nearly 500 times faster than the first step (43). For this reason, the efficiency of borohydride in enhancing the plating reaction is very low, typically on the order of a few %, and most borohydride is lost by hydrolysis. (The actual efficiency depends on the ratio of substrate area to bath volume, i.e., the loading factor.)

Since the hydrolysis reactions proceed more rapidly at a lower pH, the plating rate is faster at lower KOH concentrations. To avoid spontaneous decomposition of the bath, however, alkalinity of at least 0.1 M must be used. The effect of the KOH concentration on the deposition rate of a borohydride bath is illustrated in Fig. 30.

When DMAB instead of borohydride is used as a reducing agent, the deposition rate increases with the KOH concentration, a behavior which is exactly opposed to that found for the borohydride bath (Fig. 31). This can be explained by assuming that the reducing species in the DMAB bath is also BH_3OH^-:

$$(CH_3)_2NH \cdot BH_3 + OH^- \rightarrow (CH_3)_2NH + BH_3OH^- \tag{48}$$

This reaction indicates that DMAB must react directly with OH^- ions to form the reducing species BH_3OH^-, hence the deposition rate increases with increasing alkalinity. Experimentally, it was found that for the deposition rate to reach a practically useful level, the KOH concentration must be as high as 0.8 M [155].

The high alkalinity of both the borohydride and the DMAB bath seriously limits the scope of these baths. Photoresists which are commonly used to define circuit patterns are not stable at high pH values, especially at elevated operating temperatures. Substrate materials are often attacked by hot alkaline solutions, leading to undercutting of the metallized fine circuit lines.

Another shortcoming of these baths is their sensitivity to contamination by nickel ions. At concentrations as low as 10^{-5} M, nickel ions clearly decrease the

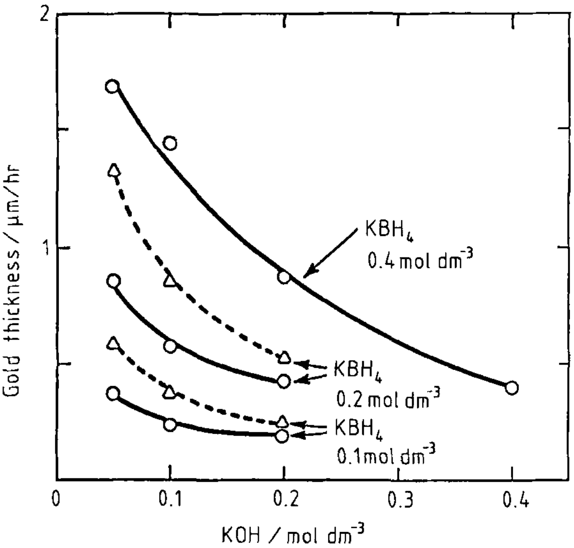

Fig. 30. Effect of the KOH concentration on the deposition rate of a borohydride bath. 0.02 · mol dm^{-3} $KAu(CN)_2$, 0.2 mol · dm^{-3} KCN (solid lines) and 0.1 mol · dm^{-3} KCN (dashed lines), 80 °C.

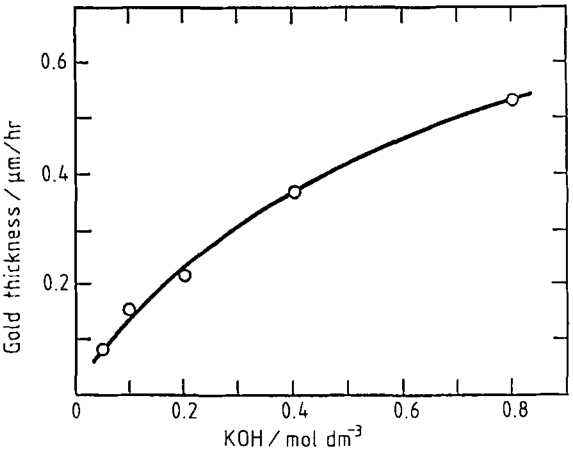

Fig. 31. Effect of the KOH concentration on the deposition rate of a DMAB bath. 0.02 mol · dm^{-3} $KAu(CN)_2$, 0.02 mol · dm^{-3} KCN, 0.4 mol · dm^{-3} DMAB, 75 °C.

plating rate, and the bath begins to decompose, accompanied by precipitation of gold in a solution of 10^{-3} mol dm^{-3}. Contamination with Cu^{2+} ions has no such effect. The effects of these contaminants on the plating rate are illustrated in Fig. 32. The adverse effect of such low nickel concentrations is serious from a practical viewpoint, because nickel as a metal is commonly used as a barrier layer to prevent diffusion of underlying copper through the top layer of gold in circuit metallization.

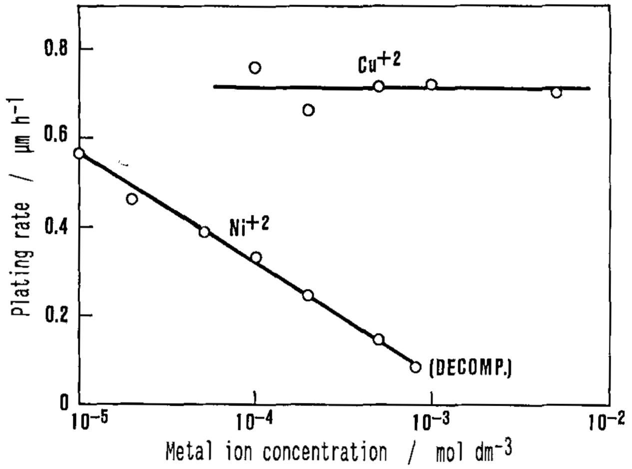

Fig. 32. Effect of copper and nickel contaminants on the plating rate of electroless gold.

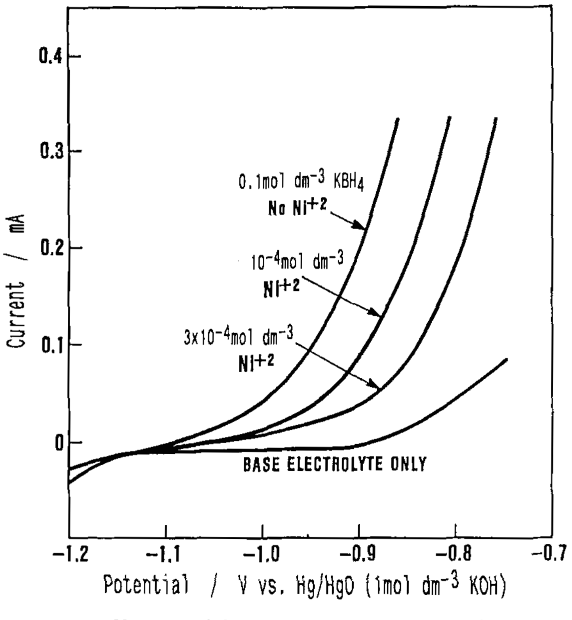

Fig. 33. Effect of nickel ions on the anodic oxidation of BH_3OH^- at a rotating gold disk electrode, 0.2 mol · dm^{-3} KOH + 0.1 mol · dm^{-3} KCN, 75 °C.

When nickel metal is placed in a borohydride or a DMAB bath, initial deposition of gold proceeds by galvanic displacement, as a result of which a small amount of nickel dissolves into the bath.

The cause of this effect of nickel ions was investigated voltammetrically with a gold-plated rotating platinum disk electrode [158]. The current-potential curves shown in Fig. 33 demonstrate that the anodic oxidation of the reducing agent

BH_3OH^- is greatly inhibited by addition of minute amounts of nickel ions. In the base electrolyte containing KOH and KCN, nickel ions are actually present in the form of $Ni(CN)_4^{2-}$. It is likely that this complex ion has a poisoning effect as a result of its preferential adsorption on the gold surface.

In addition, the deposition rate obtained with the original borohydride and DMAB baths (0.5–1.5 μm/h) is too slow for some applications. Thus, these baths have the following three disadvantages: (1) a slow plating rate, (2) a high pH, and (3) incompatibility with nickel. Among these three factors, the pH cannot be changed because it is an intrinsic property of the reducing agents. On the other hand, significant improvements have been made by different groups of investigators concerning the other two factors. These improvements are briefly described below.

8.2 Improved Borohydride or DMAB Baths

Two different approaches have been made to increase the maximum deposition rate which is reached under a given set of deposition conditions. The first approach involves addition of a depolarizer, such as lead or thallium ions [162–164]. These ions are known to adsorb strongly on gold and to bring about "underpotential deposition (UPD)" during electrodeposition of gold [165]. The depolarization effect amounts to as much as 0.2 V, as reported by Matsuoka et al. [164] and illustrated in Fig. 34. These authors show that addition of such depolarizers to a borohydride bath increases the deposition rate by a factor of as much as 8 to 10 (Fig. 35).

A second approach to increasing the plating rate was described recently by Iacovangelo [166]. This method involves addition of an oxidation promotor which accelerates the anodic oxidation of the reducing agent. It was shown that carbonate or triethanolamine serves as an oxidation promotor for DMAB. To the authors' knowledge, however, the mechanism of this effect has not yet been studied.

When electroless gold must be deposited on nickel metal, the common practice is to precoat the nickel with galvanic displacement gold prior to plating electroless

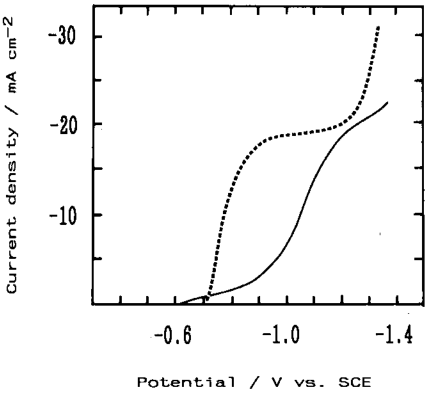

Fig. 34. Effect of $PbCl_2$ on the polarization curve for the reduction of $Au(CN)_2^-$ at a rotating Au electrode, 0.009 mol · dm^{-3} $KAu(CN)_2$, 0.2 mol · dm^{-3} KOH (M. Matsuoka et al., 1987 [164]).

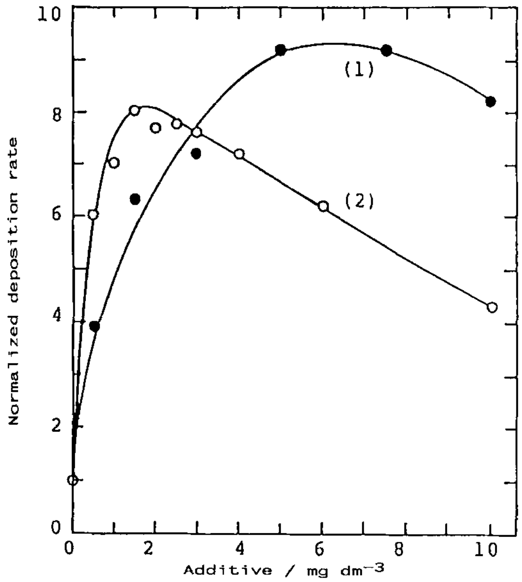

Fig. 35. Normalized deposition rate of Au from a borohydride bath as a function of the concentration of additives (1) TlCl, (2) $PbCl_2$ (M. Matsuoka et al., 1988 [164]).

gold to minimize the exposure of nickel to the electroless gold bath. Because of the extreme sensitivity of electroless gold baths to contamination with dissolved nickel, this approach has not been quite successful. Recently, Iacovangelo [166] explored an entirely new approach; he added hydrazine as a second reducing agent in addition to DMAB. The composition of the bath used by Iacovangelo is shown in Table 14. Note that lead acetate and K_2CO_3 are added to accelerate the cathodic and anodic partial reactions, thereby increasing the deposition rate. From anodic polarization curves of hydrazine and DMAB in basic electrolyte containing KCN, Iacovangelo concluded that (1) hydrazine is easily oxidized on Ni, but not on Au (Fig. 36), and that (2) DMAB is easily oxidized on Au, but only slowly on Ni (Fig. 37). These

Table 14. Bath composition with dual reducing agents (C. D. Iacovangelo, 1991 [166]).

$KAu(CN)_2$	0.005 mol dm^{-3}	
KCN	0.035 mol dm^{-3}	
KOH	0.8 mol dm^{-3}	
K_2CO_3	0.45 mol dm^{-3}	
Pb-acetate	15 ppm	
DMAB	0.05 mol dm^{-3}	
N_2H_4	0.25 mol dm^{-3}	
Temperature	80 °C	
Rate		
	Initial (on Ni)	2.6 μm/h
	On Au	7.8 μm/h

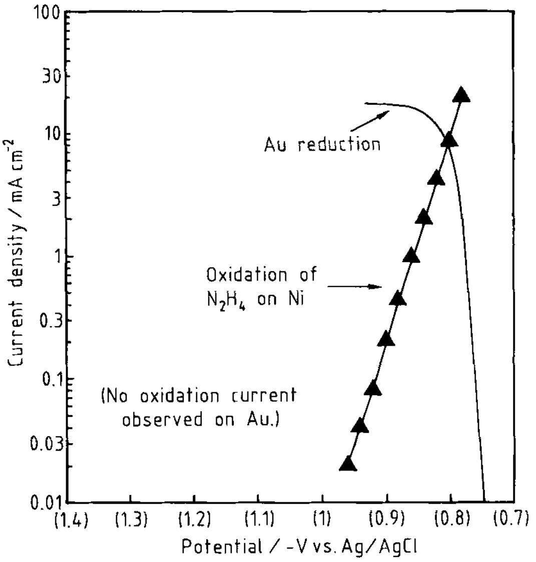

Fig. 36. Polarization curves for the oxidation of N_2H_4 and for the reduction of $Au(CN)_2^-$ on Ni. 0.8 mol · dm^{-3} KOH + 0.035 mol · dm^{-3} KCN + 0.05 mol · dm^{-3} N_2H_4, 80 °C (C. D. Iacovangelo, 1991 [166]).

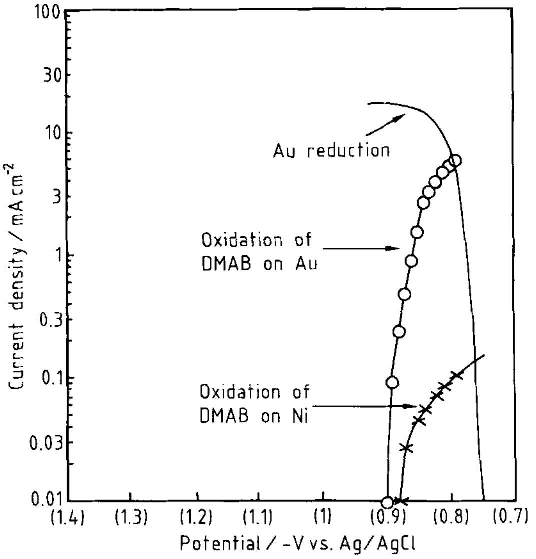

Fig. 37. Polarization curves for the oxidation of DMAB and for the reduction of $Au(CN)_2^-$ on Ni and Au. Bath composition (0.8 mol · dm^{-3} KOH, 0.035 mol · dm^{-3} KCN, 0.05 mol · dm^{-3} DMAB), 80 °C (C. D. Iacovangelo, 1991 [166]).

results show that in the initial stages after a nickel substrate is placed in the bath, gold deposition is primarily based on the catalytic action of the nickel substrate ("substrate-catalyzed" plating), whereas further deposition of gold on the gold produced by the substrate-catalyzed reaction proceeds via autocatalytic reaction with DMAB. It was shown that by selecting suitable concentrations of hydrazine and KCN, dissolution of nickel can be effectively prevented.

In passing, it should be mentioned that Iacovangelo et al., in a second paper [167], showed that if the bath is made only with hydrazine and without DMAB, deposition of gold occurs only by the catalytic action of nickel, and it continues until a thickness corresponding to complete coverage of the nickel substrate with gold is reached. This process involves purely substrate-catalyzed plating. It was shown that the maximum gold thickness obtainable with this bath depends on the free CN^- concentration (Fig. 38). This result indicates that the gold thickness can be controlled by adapting the solution composition rather than by changing the plating time. In spite of the rather small thicknesses, Iacovangelo reports that the gold deposit obtained by this process is essentially pore-free and suitable for bonding purposes encountered in electronics applications.

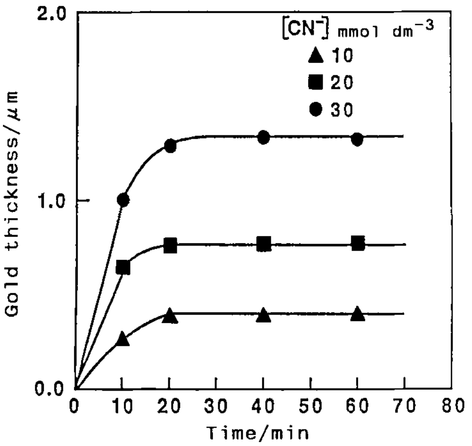

Fig. 38. Gold plating thickness vs. time curves at various cyanide concentrations for substrate-catalyzed gold deposition with hydrazine as reducing agent (C. D. Iacovangelo et al., 1991 [167]).

8.3 New Electroless Gold Plating Baths

The recent literature describes several autocatalytic gold bath formulations which are not based on the gold cyanide complex and which are operated at a near-neutral or acidic pH. These baths have been reviewed recently by one of the present authors [168]. Among these new baths, those based on the thiosulfate gold complex are believed to deserve special attention.

Two independent groups in Japan developed thiosulfate baths. The first group used thiourea as a reducing agent, whereas the second group used ascorbic acid.

Table 15. Composition of thiosulfate baths.

	Bath A*	Bath B*
$NaAuCl_4$	0.01 mol dm^{-3}	0.0125 mol dm^{-3}
$Na_2S_2O_3$	0.08 mol dm^{-3}	0.1 mol dm^{-3}
Na_2SO_3	0.4 mol dm^{-3}	0.1 mol dm^{-3}
$Na_2B_4O_7$	0.1 mol dm^{-3}	–
NH_4Cl	–	0.05 mol dm^{-3}
Thiourea	0.1 mol dm^{-3}	–
Sodium-L-ascorbate	–	0.25 mol dm^{-3}
pH	9.0	6.0
Temperature	80 °C	60 °C
Rate	1.9–2.3 µm/h	1.5–2.0 µm/h

* Ushio et al., 1989 [174].
** Kato et al., 1991 [176].

Typical bath compositions are shown in Table 15. Several basic questions on thiosulfate processes are addressed in a paper published by Kato et al. [176]; the results of their studies are briefly summarized below.

(1) The baths contain both sulfite and thiosulfate with trivalent gold chloride. What is the form of gold complex that is actually reduced to gold metal?

When trivalent gold is mixed with sulfite and thiosulfate, it is reduced to monovalent gold. Kato et al. studied the stoichiometry of the redox reaction and arrived at the conclusion that the predominant gold species in the system is $[Au(S_2O_3)_2]^{3-}$, a monovalent gold thiosulfate complex. If the solution contains only sulfite but no thiosulfate, the gold complex takes the form of $[Au(SO_3)_2]^{3-}$, a monovalent gold sulfite complex:

$$Au(III) + SO_3^{2-} + 2\,S_2O_3^{2-} + H_2O \rightleftharpoons [Au(S_2O_3)_2]^{3-} + SO_4^{2-} + 2\,H^+ \qquad (49)$$

$$Au(III) + 3\,SO_3^{2-} + H_2O \rightleftharpoons [Au(SO_3)_2]^{3-} + SO_4^{2-} + 2\,H^+ \qquad (50)$$

The cathodic polarization curves were determined for the reduction of gold ions in solutions containing, respectively, sulfite alone, thiosulfate alone, and a mixture of sulfite and thiosulfate. These curves are shown in Fig. 39. Addition of thiosulfate to the solution of gold sulfite complex shifts the polarization curve to the potential range where the thiosulfate complex is reduced. This result shows that the reduction of gold in the sulfite–thiosulfate mixture takes place from the thiosulfate complex. This conclusion is consistent with the difference between the stability constants of the two complexes:

$$Au^+ + 2\,SO_3^{2-} \rightleftharpoons Au(SO_3)_2^{3-} \qquad K = 10^{10} \qquad (51)$$

$$Au^+ + 2\,S_2O_3^{2-} \rightleftharpoons Au(S_2O_3)_2^{3-} \qquad K = 10^{26} \qquad (52)$$

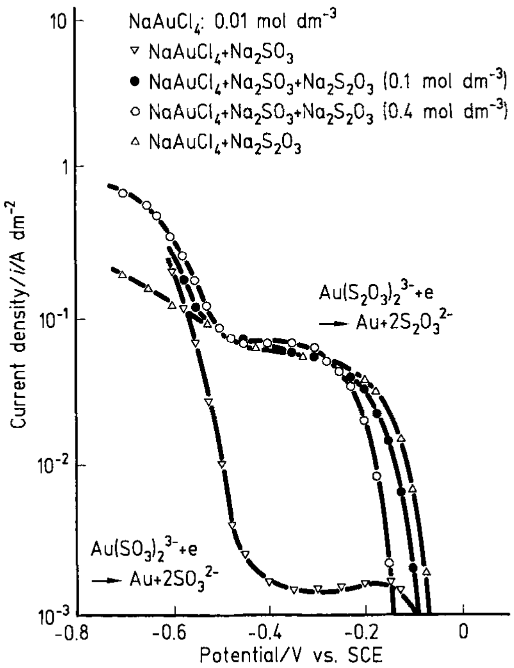

Fig. 39. Polarization curves for Au deposition from Au$(SO_3)_2^{3-}$ and from Au$(S_2O_3)_2^{3-}$ (Kato et al., 1991 [176]).

(2) The Au(I) sulfite complex is well known to be the source of gold in an electroplating bath. Will the Au(I) sulfite complex in the absence of thiosulfate work as a source of gold for electroless plating?

Fig. 40 shows polarization curves obtained from a system containing sulfite alone and one containing both sulfite and thiosulfate, respectively. It is seen that the deposition rate expected from the current at the mixed potential (indicated by arrows) is about ten times higher in the sulfite-thiosulfate mixture than in the solution containing sulfite alone.

(3) How does ascorbate compare with thiourea? Are there other reducing agents that may work as well in a thiosulfate bath?

A comparison of anodic polarization curves for various reducing agents shows that the reducing power in a base electrolyte containing sulfite, thiosulfate, and ammonium chloride at pH 6.0 and at 60 °C decreases in the order ascorbate > thiourea > hydrazine. These polarization curves are reproduced in Fig. 41, which demonstrates that hydroxylamine and formaldehyde are not useful as reducing agents in this system.

As far as the authors are aware, no detailed investigations have been performed to elucidate the overall mechanism of gold deposition from thiosulfate baths. Based

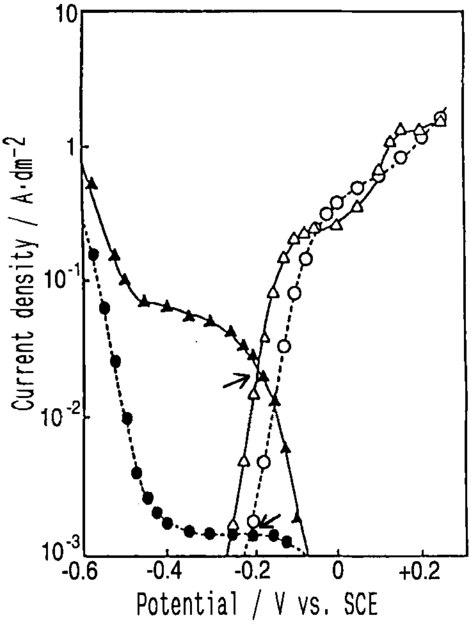

Fig. 40. Anodic and cathodic polarization curves of a gold electrode. ● 0.2 mol · dm^{-3} Na_2SO_3 + 0.1 mol · dm^{-3} NH_4Cl + 0.01 mol · dm^{-3} $NaAuCl_4$, ▲ 0.2 mol · dm^{-3} Na_2SO_3 + 0.1 mol · dm^{-3} NH_4Cl + 0.01 mol · dm^{-3} $Na_2S_2O_3$, ○ 0.2 mol · dm^{-3} Na_2SO_3 + 0.1 mol · dm^{-3} NH_4Cl + 0.1 mol · dm^{-3} Na-ascorbate, △ 0.2 mol · dm^{-3} Na_2SO_3 + 0.1 mol · dm^{-3} NH_4Cl + 0.1 mol · dm^{-3} Na-ascorbate + 0.1 mol · dm^{-3} $Na_2S_2O_3$, pH: 6.0, 60 °C (Kato et al., 1991 [176]).

on the available information on the oxidation reactions of the reducing agents employed, the following partial cathodic and anodic reactions can be proposed:

Cathodic partial reaction

$$Au(S_2O_3)_2^{3-} + e^- \rightarrow Au + 2\,S_2O_3^{2-} \quad (53)$$

Anodic partial reaction

thiourea bath

$$\underset{}{CS(NH_2)_2} + 5\,H_2O \rightarrow \underset{\text{(urea)}}{CO(NH_2)_2} + H_2SO_4 + 8\,H^+ + 8\,e^- \quad (54)$$

ascorbate bath

$$C_6H_8O_6 \rightarrow C_6H_6O_6 + 2\,H^+ + 2\,e^- \quad (55)$$

From a practical viewpoint, the significance of the thiosulfate bath lies in the fact that it is a noncyanide, near-neutral pH system, and that it is not sensitive to nickel contamination. Because of the very mild conditions used, this type of bath may find wide application in the future whenever the substrate to be plated is incompatible with borohydride of DMAB baths.

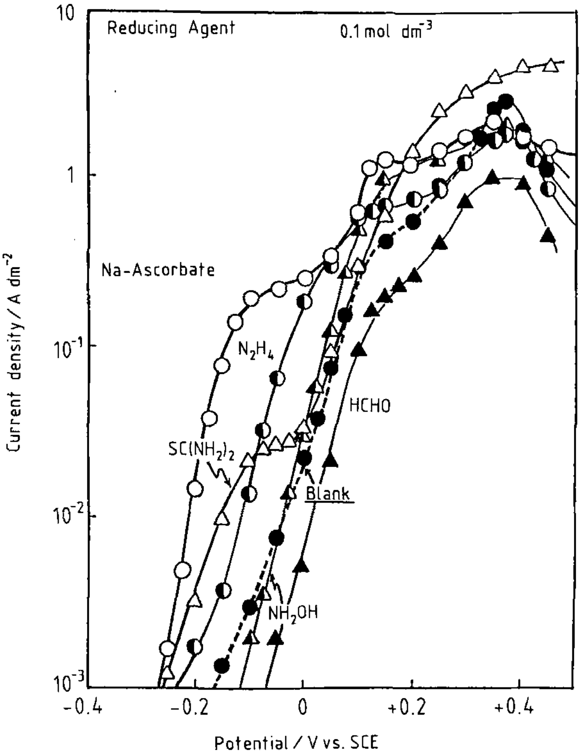

Fig. 41. Anodic polarization curves of various reducing agents at an Au electrode (Kato et al., 1991 [176]).

9 Electroless Deposition of Other Metals and Alloys

There are many metals and alloys that are known or have been reported to be autocatalytically platable, but which are not covered in the preceding sections. These metals and alloys are listed in Table 16, together with the respective reducing agents and corresponding references. Some references discuss fundamental aspects of the deposition reactions involved, but these are not reviewed here because of the limitation in space. In additon to the original references listed in Table 16, extensive reviews are available concerning electroless deposition of silver [198], gold and gold alloys [199], and platinum group metals and alloys [200]. These reviews and original references may be consulted for details.

Table 16. List of other metals and alloys known or reported to be autocatalytically platable.

Metal/Alloy	Reducing agent	Reference
Ag	Glucose	[177, 178]
	Rochelle Salt	
	Formaldehyde	
	Hydrazine	
AuAg	KBH_4	[179]
AuCu	Formaldehyde	[180]
AuSn	$SnCl_2$	[181]
AuIn	KBH_4	[182]
Pd	Hydrazine	[183, 184]
	Hypophosphite	[185]
	Tertiary Amineborane	[186]
PdNi	Hypophosphite	[185]
PdCo	Hydrophosphite	[185]
PdZn	Hydrophosphite	[185]
Pt	Hydrazine	[187]
PtRh	Hydrazine	[187]
PtIr	Hydrazine	[187]
PtPd	Hydrazine	[188]
Ru	Hydrazine	[189]
Rh	Hydrazine	[190]
In	$NaBH_4$	[191]
Sn	$TiCl_3$	[192]
	$TiCl_3$	[193]
	Hypophosphite	[194]
	Disproportionation reaction of Sn^{2+}	[195]
Pb	Thiourea	[196]
	$TiCl_3$	[197]
SnPb	Hypophosphite	[198]
	Thiourea	[199]
Bi	$TiCl_3$	[200]
	$SnCl_2$	[201]
Cd	$TiCl_3$	[202]
Sb	$TiCl_3$	[203]

10 Conclusion

The technique of electroless plating is in principle attractive for industrial applications because of its unique advantages over conventional electrolytic plating. These advantages include (1) the ability to deposit a metal on catalyzed nonconductive substrates, (2) the ability to plate substrates with complex shapes at a uniform metal thickness, and (3) the ability to selectively deposit a metal on catalyzed areas of the substrate surface only. Because of these advantages, industry has found a number of sophisticated applications, for example through-hole plating of electroless copper on multilayered printed wiring boards with an aspect ratio (ratio of the board thickness to the through-hole diameter) higher than 20, and the deposition of a very thin, uniform layer of cobalt alloy on magnetic memory disks.

Applications in such sophisticated areas of technology require process control with a high degree of accuracy and reliability, which stimulated investigations in recent years to gain fundamental understanding of the chemistry and physics involved in the process. Nevertheless, electroless plating is still considered by many to be "black magic", with some mysterious elements playing a critical role in ensuring successful operation of the process. Clearly, much more work is needed to advance solid, scientific understanding if the technique of electroless plating is to be accepted with greater confidence. It is the authors' belief that advancing fundamental understanding is the only approach which can be expected to lead to more reliable process control, wider acceptance of the technology, and the development of new or improved processes that are compatible with today's highly sophisticated industrial needs. We hope that this article will stimulate further progress to promote scientific understanding of electroless deposition processes.

11 References

1. A. Brenner, G. E. Riddell, J. Res. Nat'l Bur. Std. 37, 31 (1946); ibid., 39, 385 (1947).
2. Electroless Plating – Fundamentals and Applications, G. O. Mallory and J. B. Haydu (eds.), American Electroplaters and Surface Finishers Society, Orlando (1990).
3. M. Saito, J. Met. Finish. Soc. Jpn 16, 300 (1965); ibid., 17, 14 (1966); 17, 258 (1966); ibid., 17, 264 (1966).
4. M. Paunovic, Plating 55, 1161 (1968).
5. I. Ohno, O. Wakabayashi, S. Haruyama, J. Electrochem. Soc. 132, 2323 (1985).
6. T. Osaka, H. Takematsu, K. Nihei, J. Electrochem. Soc. 127, 1021 (1980).
7. T. Yoshida, T. Osaka, Memoirs Sch. Sci. Eng., Waseda Univ. 44, 41 (1980).
8. T. Osaka, K. Nihei, F. Goto, Denki Kagaku 50, 418 (1982).
9. J. E. A. M. van den Meerakker, J. Appl. Electrochem. 11, 395 (1981).
10. A. Vashkyalis, Elektrokhimiya 14, 1770 (1978).
11. F. L. Shippey, F. M. Donahue, Plating 60, 43 (1973).
12. A. Molenaar, M. F. E. Holdrinet, L. K. H. Van Beek, Plating 61, 238 (1974).
13. G. O. Mallory, V. Lloyd, Plating Surface Finish., 72 (9), 65 (1985).
14. F. M. Donahue, F. L. Shippey, Plating 60, 135 (1973).
15. F. M. Donahue, J. Electrochem. Soc. 119, 72 (1972).
16. I. Ohno, S. Haruyama, Surface Technol. 13, 1 (1981)
17. I. Ohno, Mat. Sci. Eng. A146, 33, (1991).
18. S. Haruyama, Proc. 5th Int. Congr. on Metallic Corrosion, Houston, Texas (1974), p. 82.
19. I. Epelboin, M. Keddam, H. Takenouchi, J. Appl. Electrochem. 2, 71 (1972).
20. I. Ohno, T. Tsuru, S. Haruyama, Proc. 10th International Congress of Metal Finishing (Interfinish '80), Kyoto, Jpn., 152 (1980).
21. M. Suzuki, K. Kanno, O. Sakai, Y. Sato, Proc. 10th International Congress of Metal Finishing (Interfinish '80), Kyoto, Jpn., 157 (1980).
22. M. Suzuki, N. Sato, K. Kanno, Y. Sato, J. Electrochem. Soc. 129, 2183 (1982).

23. N. Sato, M. Suzuki, Y. Sato, J. Electrochem. Soc. 130, 1485 (1983).
24. T. Osaka, I. Koiwa, J. Metal Finish. Soc. Jpn. 34, 330 (1983).
25. Y. Shimizu, S. Ishibashi, J. Metal Finish. Soc, Jpn. (Kinzoku Hyomen Gijutsu) 19, 418 (1968).
26. T. Osaka, M. Usuda, I. Koiwa, H. Sawai, Jpn. J. Appl. Phys. 27 (10), 1885 (1988).
27. K. Nihei, T. Osaka, H. Sawai, Denki Kagaku 44, 402 (1976).
28. T. Osaka, K. Arai, N. Masubuchi, J. Metal Finish. Soc. Jpn. 39, 778 (1988).
29. F. Pearlstein, R. F. Weightman, R. Wick, Metal Finish. 61 (11), 77 (1963).
30. F. Pearlstein, R. F. Weightman, Electrochem. Technol. 6, 427 (1968).
31. T. Osaka, H. Sawai, F. Otoi, K. Nihei, J. Metal Finish. Soc. Jpn. 31, 661 (1980).
32. T. Osaka, H. Sawai, N. Kasai, J. Metal Finish Soc. Jpn. 32, 615 (1981).
33. I. Koiwa, T. Osaka, H. Sawai, J. Metal Finish. Soc. Jpn. 34, 600 (1983).
34. H. Sawai, T. Kanamori, S. Shibata, K. Nihei, T. Osaka, I. Koiwa, M. Nishikawa, Proc. 11th International Congress of Metal finishing Interfinish '84), Jerusalem, Israel (1984), p. 323.
35. I. Koiwa, M. Usuda, T. Osaka, J. Electrochem. Soc. 135, 1222 (1988).
36. T. Osaka, M. Fukawa, J. Kawaguchi, Denki Kagaku 56, 60 (1988).
37. T. Osaka, M. Fukawa, J. Kawaguchi, Denki Kagaku 60, 523 (1992).
38. T. Osaka, M. Fukawa, S. Ueda, J. Kawaguchi, Proc. 13th International Congress of Metal Finishing (Interfinish '92), Sao Paulo, Brazil (1992).
39. G. O. Mallory, Plat. Surface Finish., 63 (6), 34 (1976).
40. M. Schwartz, G. O. Mallory, J. Electrochem. Soc. 123, 606 (1976).
41. G. O. Mallory, T. R. Hohn, Plating Surface Finish., 66 (4), 40 (1979).
42. I. Koiwa, M. Nishikawa, K. Yamada, T. Osaka, Bull. Chem. Soc. Jpn. 59, 133 (1986).
43. I. Koiwa, K. Yamada, M. Usuda, T. Osaka, Denki Kagaku 54, 514 (1986).
44. I. Koiwa, M. Usuda, K. Yamada, T. Osaka, J. Electrochem. Soc. 135, 718 (1988).
45. T. Osaka, K. Arai, Y. Yamazaki, T. Namikawa, Jpn. J. Appl. Phys. 28 (2), 229 (1989).
46. T. Osaka, H. Yamazaki, I. Saito, J. Electrochem. Soc. 136, 3418 (1989).
47. T. Osaka, K. Arai, N. Masubuchi, H. Sawai, J. Surface Finish. Soc. Jpn. (Hyomen Gijutsu) 41, 45 (1990).
48. T. Osaka, N. Masubuchi, K. Arai, Y. Okuno, J. Surface Finish. Soc. Jpn. 41, 49 (1990).
49. T. Matsuda, U. Mizutani, in: Proc. 4th Int. Conf. Rapidly Quenched Metals, T. Masumoto and K. Suzuki (ed.), Jpn. (1982), Vol. 2, p. 1315.
50. R. D. Fisher, W. H. Chilton, J. Electrochem. Soc. 109, 485 (1962).
51. L. D. Ranson, V. Zentner, J. Electrochem. Soc. 111, 1423 (1964).
52. Y. Moradzadeh, J. Electrochem. Soc. 112, 891 (1965).
53. D. E. Speriotis, J. R. Morrison, J. S. Judge, IEEE Trans. Magn., MAG-1, 348 (1965).
54. J. S. Judge, J. R. Morrison, D. E. Speriotis, G. Bate, J. Electrochem. Soc. 112, 681 (1965).
55. D. E. Speliotis, J. S. Judge, J. R. Morrison, J. Appl. Phys. 37, 1158 (1966).
56. M. G. Miksic, R. Travieso, A. Arcus, R. H. Wright, J. Electrochem. Soc. 113, 360 (1966).
57. J. S. Judge, J. R. Morrison, D. E. Speriotis, J. Electrochem. Soc. 113, 547 (1966).
58. J. R. DePew, J. Electrochem. Soc. 120, 1187 (1973).
59. R. D. Fisher, D. E. Koopman, J. Electrochem. Soc. 111, 263 (1964).
60. A. S. Frieze, R. Sard, R. Weil, J. Electrochem. Soc. 115, 586 (1968).
61. V. Morton, R. D. Fisher, J. Electrochem. Soc. 116, 188 (1969).
62. S. L. Chow, N. E. Hedgecock, M. Schlesinger, J. Electrochem. Soc. 119, 1614 (1972).
63. F. Pearlstein, R. F. Weightman, Plating 54, 714 (1967).
64. F. Pearlstein, R. F. Weightman, J. Electrochem. Soc. 121, 1023 (1974).
65. I. Tsu, Plating 48, 379 (1961); J. Electrochem. Soc. 48, 1207 (1961).
66. J. S. Sallo, J. M. Carr, J. Electrochem. Soc. 109, 1040 (1962).
67. G. V. Elmore, P. Bakos, J. Electrochem. Soc. 111, 1244 (1964).
68. G. Bate, D. E. Speliotis, J. Appl. Phys. 34, 1073 (1964).
69. S. Iwasaki, K. Yasuda, A. Senda, IECEJ Tech. Rep. MR65-17 (1965).
70. R. Sard, C. D. Schwartz, R. Weil, J. Electrochem. Soc. 113, 424 (1966).
71. S. Iwasaki, K. Ouchi, K. Yasuda, IECEJ Tech. Rep. MR66-18 (1966).

72. J. H. Kefalas, J. Appl. Phys. 37, 1160 (1966).
73. S. Hattori, A. Tago, Y. Ishii, A. Terada, O. Ishii, S. Ohta, Elec. Comm. Lab. Tech. J., 31, 277 (1982).
74. Y. Sato, A. Terada, S. Ohta, T. Miyamoto, NTT Elec. Comm. Lab. Tech. J. 36, 485 (1987).
75. F. Goto, Y. Suganuma, T. Osaka, J. Metal Finish. Soc. Jpn. 33, 414 (1982).
76. R. D. Fisher, IEEE Trans. Magn. MAG-2, 681 (1966).
77. H. Matsuda, O. Takano, J. Jpn. Inst. Met. 52, 414 (1988).
78. F. Goto, M. Kimura, N. Shiota, T. Yamamoto, M. Yanagisawa, Autmn Natl. Conv. Rec., IEICEJ, 5-164 (1989).
79. H. Nagasaka, T. Michimori, H. Takeno, J. Surface Finish. Soc. Jpn. 42, 58 (1991).
80. T. Osaka, H. Nagasaka, J. Electrochem. Soc. 128, 1686 (1981).
81. M. Mirzamaani, L. T. Romankiw, C. McGrath, J. Mahlke, N. C. Anderson, J. Electrochem. Soc. 135, 2813 (1988).
82. D. DiMilia, J. Horkans, C. McGrath, M. Mirzamaani, G. Scilla, J. Electrochem. Soc. 135, 2817 (1988).
83. H. Matsubara, M. Toda, T. Sakuma, T. Homma, T. Osaka, Y. Yamazaki, T. Namikawa, J. Electrochem. Soc. 136, 753 (1989).
84. S. Iwasaki, Y. Nakamura, IEEE Trans Magn. MAG.-13, 1272 (1977).
85. J. Hokkyo, F. Kugiya, J. Magn. Soc. Jpn. 13 (S1), 1 (1989).
86. Y. Nakamura, S. Iwasaki, IEEE Trans. Magn. MAG-20, 105 (1984).
87. S. Yamamoto, Y. Nakamura, S. Iwasaki, IEEE Trans. Magn. MAG-23, 2070 (1987).
88. M. Sato, Y Hoshino, Denki Kagaku 35, 111 (1967).
89. S. Kawai, R. Ueda J. Electrochem. Soc. 122, 32 (1975).
90. S. Kawai, J. Electrochem. Soc. 122, 1026 (1975).
91. S. Kawai, I. Ishiguro, J. Electrochem. Soc. 123, 1047 (1975).
92. T. Chen, P. Cavallotti, IEEE Trans. Magn. MAG-18, 1125 (1982).
93. J. Horkans, D. J. Seagle, I-C. H. Chang, J. Electrochem. Soc. 137, 2056 (1990).
94. T. Osaka, F. Goto, N. Kasai, Y. Suganuma, Denki Kagaku 49, 792 (1981).
95. T. Osaka, N. Kasai, J. Metal Finish. Soc. Jpn. 32, 309 (1981).
96. F. Goto, T. Osaka, N. Kasai, I. Koiwa, H. Tanaka, M. Aoyama, Y. Suganuma, Proc. Symp. on Inst. Elec. Comn., Tohoku Univ. 197 (1982).
97. T. Osaka, G. Goto, N. Kasai, I. Koiwa, Y. Suganuma, J. Electrochem. Soc. 130, 568 (1983).
98. T. Osaka, N. Kasai, I. Koiwa, F. Goto, J. Electrochem. Soc. 130, 790 (1983).
99. I. Koiwa, Y. Okabe, H. Matsubara, T. Osaka, F. Goto, J. Magn. Soc. Jpn. 9, 83 (1985); translated into English in IEEE Translation J. Magn. Jpn, TJMJ-1, 443 (1985).
100. I. Koiwa, M. Toda, T. Osaka, J. Electrochem. Soc. 133, 597 (1986).
101. I. Koiwa, H. Matsubara, T. Osaka, Y. Yamazaki, T. Namikawa, J. Electrochem. Soc. 133, 685 (1986).
102. T. Osaka, I. Koiwa, M. Toda, T. Sakuma, Y. Yamazaki, T. Namikawa, J. Magn. Soc. Jpn. 10, 5 (1986); translated into English in IEEE Translation J. Magn. Jpn. TJMJ-2, 208 (1987).
103. T. Osaka, I. Koiwa, M. Toda, T. Sakuma, Y. Yamazaki, T. Namikawa, F. Goto, IEEE Trans. Magn. MAG-22, 1149 (1986).
104. I. Koiwa, T. Osaka, Y. Yamazaki, T. Namikawa, IEEE Trans. Magn. MAG-23, 2800 (1987).
105. T. Osaka, H. Matsubara, T. Sakuma, T. Homma, S. Yokoyama, Y. Yamazaki, T. Namikawa, J. Magn. Soc. Jpn. 12, 77 (1988); translated into English in IEEE Translation J. Magn. Jpn TJMJ-4, 39 (1989).
106. O. Takano, H. Matsuda, H. Izumitani, K. Ito, J. Metal Finish. Soc. Jpn. 35, 440 (1984).
107. H. Matsuda, O. Takano, J. Metal Finish. Soc. Jpn. 37, 753 (1986).
108. T. Osaka, H. Matsubara, K. Yamanishi, H. Mizutani, F. Goto, IEEE Trans. Magn. MAG-23, 2356 (1987).
109. H. Matsubara, S. Mitamura, K. Noda, T. Osaka, F. Goto, J. Magn. Soc. Jpn. 13, 153 (1989); translated into English in IEEE Translation J. Magn. Jpn TJMJ-5, 276 (1990).
110. H. Matsubara, K. Yamanishi, H. Mizutani, T. Osaka, J. Metal Finish. Soc. Jpn. 37, 708 (1986).

111. T. Homma, K. Saito, T. Osaka, J. Surface Finish. Soc. Jpn. 40, 140 (1989).
112. T. Homma, K. Saito, T. Osaka, Jpn. J. Appl. Phys. 29, 1701 (1990).
113. T. Osaka, T. Homma, K. Saito, K. Noda, F. Goto, N. Shiota, T. Yamamoto, IEICEJ Techn. Rep. MR90-10 (1990).
114. T. Osaka, T. Homma, K. Inoue, K. Saga, Denki Kagaku 58, 661 (1990).
115. T. Homma, K. Inoue, H. Asai, K. Ohrui, T. Osaka, Y. Yamazaki, T. Namikawa, J. Magn. Soc. Jpn. 15 (2), 113 (1991).
116. T. Osaka, T. Homma, J. Surface Finish. Soc. Jpn. 42, 283 (1991).
117. L. T. Romankiw, I. M. Croll, N. Hatzakis, IEEE Trans. Mag. MAG-6, 597 (1970).
118. D. A. Thompson, L. T. Romankiw, IBM Disk Storage Technology (1980), p. 3.
119. J. M. Harker, D. W. Brede, R. E. Pattison, G. R. Santana, L. G. Taft, IBM J. Res. Develop. 25, 677 (1981).
120. S. H. Liao, IEEE Trans. Mag. MAG-23, 2981 (1987).
121. T. Osaka, T. Homma, N. Masubuchi, K. Saito, M. Yoshino, Y. Yamazaki, T. Namikawa, J. Mag. Soc. Jpn. 14 (2), 309 (1990).
122. T. Osaka, T. Homma, K. Saito, A. Takekoshi, J. Electrochem. Soc. 139, 1311 (1992).
123. T. Osaka, T. Homma, C. Tsai, Proc. 59th Spring Meeting of Electrochem. Soc. Jpn (1992), p. 88; T. Osaka, T. Homma, C. Tsai, M. Takai, K. Kageyama, Denki Kagaku 61, No. 8 (1993).
124. H. Akahoshi, K. Murakami, M. Wajima, S. Kawakubo, IEEE Trans. Comp. Hybrids Manuf. Tech. CHMT-9, No. 2, 181 (1986).
125. M. C. Bennett, N. O. Schmidt, Trans. Faraday Soc. 51, 1412 (1955).
126. Y. Okinaka, Extended Abstract, Electrochemical Soc. Fall Meeting, Detroit (1969).
127. P. Bindra, D. Light, D. Rath, IBM J. Res. Develop. 28, 668 (1984).
128. R. Bieber, G. Trumpler, Helv. Chim. Acta 30, 1860 (1947).
129. R. Schumacher, J. J. Pesek, O. R. Melroy, J. Phys. Chem. 89, 4338 (1985).
130. S. Gottesfeld, J. Beery, M. Paffett, M. Hollander, C. Maggiore, J. Electrochem. Soc, 133, 1344 (1986).
131. B. J. Feldmann, O. R. Melroy, J. Electrochem. Soc. 136, 640 (1989).
132. H. Wiese, K. G. Weil, Ber. Bunsenges. Phys. Chem. 91, 619 (1987).
133. Y. Okinaka, S. Nakahara, J. Electrochem. Soc. 123, 475 (1976).
134. S. Nakahara, Y. Okinaka, Acta Metall. 31, 713 (1983).
135. Y. Okinaka, H. K. Straschil, J. Electrochem. Soc. 133, 2608 (1986)
136. J. E. Graebner, Y. Okinaka, J. Appl. Phys. 60 (1), 36 (1986).
137. S. Nakahara, Acta Metall. 36, 1669 (1988).
138. S. Nakahara, Y. Okinaka, H. K. Straschil, J. Electrochem. Soc. 136, 1120 (1989).
139. S. Nakahara, C. Y. Mak, Y. Okinaka, J. Electrochem. Soc. 138, 1421 (1991).
140. S. Nakahara, Y. Okinaka, Annual Rev. Mater. Sci. 21, 93 (1991).
141. J. Grunwald, L. Smolinski, A. Landau, Proc. the Fourth Plating in the Electronics Industry Symp. 13, (1973).
142. H. Honma, S. Mizushima, J. Metal Finish. Soc. Jpn. 34, 290 (1983).
143. M. Matsuoka, T. Ito, T. Hayashi, ibid., 33, 385 (1982).
144. S. Nakahara, C. Y. Mak, Y. Okinaka, J. Electrochem. Soc. 110, 533 (1993).
145. S. Mizumoto, H. Nawafune, M. Kawasaki, A. Kinoshita, K. Araki, Plating Surface Finish. 73 (12), 48 (1986).
146. S. Mizumoto, H. Nawafune, M. Kawasaki, J. Surface Finish. Soc, Jpn. 39, 301 (1988).
147. S. Mizumoto, H. Nawafune, T. Sonoda, K. Araki, J. Surface Finish. Soc. Jpn. 41, 169 (1990).
148. J. G. Grunwald, D. E. Kukanskis, R. A. Letize, D. A. Sawoska, H. Rhodenizer, Proc. AES Second Electroless Plating Symp. F-1 (1984).
149. A. Hung, Plating Surface Finish. 75 (1), 62 (1988).
150. A. Hung, Plating Surface Finish. 75 (1), 74 (1988).
151. A. Hung, K.-M. Chen, J. Electrochem. Soc. 136, 72 (1989).
152. A. Hung, I. Ohno, Plating Surface Finish. 77 (3), 54 (1990).
153. J. Darken, Printed Circuit World Convention V, Glasgow (June 1990), p. 12.

154. H. Honma, M. Komatsu, T. Fujinami, J. Surface Finish. Soc. Jpn. 42, 913 (1991).
155. Y. Okinaka, Plating 57, 914 (1970).
156. Y. Okinaka, C. Wolowodiuk, Plating 58, 1080 (1971).
157. R. Sard, Y. Okinaka, J. R. Rushton, Plating 58, 893 (1971).
158. Y. Okinaka, J. Electrochem. Soc. 120, 739 (1973).
159. Y. Okinaka, R. Sard, C. Wolowodiuk, W. H. Craft, T. F. Retajczyk, J. Electrochem. Soc. 121, 56 (1974).
160. R. Sard, Y. Okinaka, H. A. Waggener, J. Electrochem. Soc. 121, 62 (1974).
161. J. A. Gardiner, J. W. Collat, J. Am. Chem. Soc. 86, 3165 (1964); ibid., 87, 1692 (1965); Inorg. Chem. 4, 1208 (1965).
162. A. Kasugai, Kokai Tokkyo Koho (Japanese Pat. Disc.) 80-24914 (1980).
163. Y. Takakura, Kokai Tokkyo Koho (Japanese Pat. Disc.) 81-152958 (1981).
164. M. Matsuoka, S. Imanishi, M. Sahara, T. Hayashi, J. Metal Finish. Soc. Jpn. 38, 55 (1987); Plating Surface Finish., 75 (5), 102, (1988).
165. J. D. E. McIntyre, W. F. Peck, J. Electrochem. Soc. 123, 1800 (1976).
166. C. D. Iacovangelo, J. Electrochem. Soc. 138, 976 (1991).
167. C. D. Iacovangelo, K. P. Zarnoch, J. Electrochem. Soc. 138, 983 (1991).
168. Y. Okinaka, in: Electroless Plating: Fundamentals and Applications, G. O. Mallory, J. B. Haydu, (eds.), American Electroplaters and Surface Finishers Society (1990), Chap. 15.
169. J. Ushio, O. Miyazawa, H. Yokono, A. Tomizawa, Kokai Tokkyo Koho (Japanese Pat. Disc.) 87-86171 (1987).
170. J. Ushio, O. Miyazawa, A. Tomizawa, N. Matsuura, H. Yokono, Kokai Tokkyo Koho (Japanese Pat. Disc.), 87-247081 (1987).
171. N. Matsuura, O. Miyazawa, A. Tomizawa, J. Ushio, H. Yokono, Kokai Tokkyo Koho (Japanese Pat. Disc.) 87-270779 (1987).
172. O. Miyazawa, J. Ushio, A. Tomizawa, N. Matsuura, H. Yokono, Kokai Tokkyo Koho (Japanese Pat. Disc.) 88-79976 (1988).
173. J. Ushio, O. Miyazawa, H. Yokono, A. Tomizawa, European Patent Application EP 021789 (April 29, 1987).
174. J. Ushio, O. Miyazawa, A. Tomizawa, H. Yokono, N. Kanda, N. Matsuura, S. Ando, H. Okuhira, K. Mori, Kokai Tokkyo Koho (Japanese Pat. Disc.) 89-268876 (1989).
175. M. Kato, S. Hoshino, I. Ohno, Kokai Tokkyo Koho (Japanese Pat. Disc.) 89-191782 (1989).
176. M. Kato, K. Niikura, S. Hoshino, I. Ohno, J. Surface Finish. Soc. Jpn. 42, 729 (1991).
177. N. Koura, A. Kubota, J. Metal Finish. Soc. Jpn. 36, 182 (1985).
178. F. Pearlstein, Plating 58, 1014 (1971).
179. J. Jostan, W. Mussinger, German Pat. DE 3132679 (1983).
180. A. Molenaar, J. Electrochem. Soc. 129, 1917 (1982).
181. V. P. Pilnikov, USSR Pat. SU985136 (1983).
182. D. Lamouche, P. Clechet, J. R. Martin, E. Haroutiounian, J. P. Sandino, J. Electrochem. Soc. 134, 692 (1987).
183. R. N. Rhoda, Trans. Inst. Metal Finish. 36, 82 (1959).
184. H. Laub, H. Januschkowetz, German Pat. DE2841584 (1980).
185. F. Pearlstein, R. F. Weightman, Plating 56, 10, 1158 (1969).
186. W. V. Hough, J. L. Little, K. V. Warheit, U. S. Patent 4, 255, 194 (1981); 4, 279, 951 (1981).
187. R. N. Roda, R. F. Vines, U. S. Pat. 3, 486, 928 (1969).
188. E. Torikai, K. Takenaka, Y. Kawami, Japanese Pat. 84-80764 (1984).
189. E. Torikai, Y. Kawami, K. Takenaka, Japanese Pat. 84-80766 (1984).
190. V. Strejcek, German Pat. DE2607988 (1977).
191. H. Nishikawa, S. Minami, J. Metal Finish. Soc. Jpn. 33, 114 (1982).
192. A. Senda, Y. Takano, T. Nakagawa, J. Surface Finish. Soc. Jpn. 43, 694 (1992).
193. K. Obata, T. Sanoda, N. Dohi, J. Metal Finish. Soc. Jpn. 33, 375 (1982).
194. A. Molenaar, J. J. C. Coumans, Surface Tech. 16, 265 (1982).
195. A. Molenaar, J. W. G. deBakker, J. Electrochem. Soc. 136, 378 (1989).

196. B. G. Slay, B. G. Carbajal, J. Electrochem. Soc. 113, 306 (1966).
197. A. Senda, T. Nakagawa, Y. Takano, T. Kasanami, J. Surface Finish. Soc. Jpn. 43, 324 (1992).
198. H. Koyano, Japanese Pat. 59-211566 (1984).
199. Y. Kouchi, M. Oyamada, T. Hosaka, H. Honma, Proc. 82nd Conference of Surface Finishing Soc. Jpn. 17B-10 (1990).
200. D. L. Rutkevich, G. P. Shevchenko, V. V. Svirido, N. P. Osipovich, J. Electrochem. Soc. 139, 429C (1992).
201. A. Senda, Y. Takano, T. Nakagawa, J. Surface Finish. Soc. Jpn. 44, 145 (1993).
202. A. Senda, Y. Takano, T. Nakagawa, J. Surface Finish. Soc. Jpn. 43, 967 (1992).
203. A. Senda, Y. Takano, T. Nakagawa, J. Surface Finish. Soc. Jpn. 43, 689 (1992).
204. N. Koura, Chap. 17 in Ref. 2 (1990).
205. Y. Okinaka, Chap. 15 in Ref. 2 (1990).
206. Y. Okinaka, C. Wolowodiuk, Chap. 16 in Ref. 2 (1990).

Advances in Electrochemical Science and Engineering
Edited by Heinz Gerischer and Charles W. Tobias

Current Distribution and Shape Change in Electrodeposition of Thin Films for Microelectronic Fabrication

John O. Dukovic

IBM Research Division, T. J. Watson Research Center,
Yorktown Heights, New York

Contents

List of Symbols

a	active-area density (dimensionless)
$\bar{a}$	active-area density, averaged over cathode surface (dimensionless)
b	resist thickness
c_A	concentration of the leveling agent (mol/cm^3)
c_M	concentration of the depositing metal ion (mol/cm^3)
c_A^∞	bulk concentration of the leveling agent (mol/cm^3)
c_M^∞	bulk concentration of the metal ion (mol/cm^3)
c_A^*	$\frac{c_A}{c_A^\infty}$ leveling agent concentration (dimensionless)
c_M^*	$\frac{c_M}{c_M^\infty}$ metal ion concentration (dimensionless)
D_A	leveling agent diffusivity (cm^2/s)
D_M	metal ion diffusivity (cm^2/s)
F	Faraday's constant ($9.648 \cdot 10^4$ C mol^{-1})
h	height of resist wall (cm)
i	component of current density normal to electrode surface (mA/cm^2)
i^*	$\frac{i}{\bar{i}}$ current density (dimensionless)
i_{ACT}	active current density (mA/cm^2)
i_{SUP}	superficial current density (mA/cm^2)
$\bar{i}_{SUP}$	average superficial current density (mA/cm^2)
$\bar{i}^{t=0}$	average initial current density to feature (mA/cm^2)
$\bar{i}_{lim}^{t=0}$	mass-transfer-limited value of $\bar{i}^{t=0}$ (mA/cm^2)
i_0	exchange current density (mA/cm^2)
i_0^∞	exchange current density at $c_M = c_M^\infty$ (mA/cm^2)
$i_{0c_A=0}^\infty$	exchange current density at $c_M = c_M^\infty$ and $c_A^\infty = 0$ (mA/cm^2)
k_{LEV}	constant in inhibition model (mA · s/mol)
K_{LEV}	leveling parameter $\frac{nFc_A^\infty D_A}{w\bar{i}} k_{LEV}$ (dimensionless)
L	characteristic length of resist pattern (cm)
l	distance
n	number of electrons transferred
$\mathbf{n}$	unit vector normal to surface (cm)
N	magnitude of nonuniformity of current distribution (dimensionless)
N_A	flux of leveling-agent at the cathode surface (mol/cm^2 · s)
N_M	flux of metal ion at the cathode surface (mol/cm^2 · s)
N_A^*	leveling-agent flux $\frac{N_A w}{D_A c_A^\infty}$ (dimensionless)
N_M^*	metal-ion flux $\frac{N_M w}{D_M c_M^\infty}$ (dimensionless)
p	pitch (inter-cavity spacing) (cm)
Pe	Peclet number (dimensionless)
r	radial coordinate (cm)
R	universal gas constant (8.314 J/mol · K)
s	height of constant-i plane (cm)
Sh	Sherwood number $\frac{\bar{i}w}{nFD_M c_M^\infty}$, (dimensionless)
T	absolute temperature (K)
w	initial width of base of cavity (cm)

Wa_L	Wagner number for linear kinetics (dimensionless)
Wa_T	Wagner number for Tafel kinetics (dimensionless)
α_a, α_c	transfer coefficients (dimensionless)
γ	exponent in i_0-c_M relation
Γ_A	boundary corresponding to anode surface
Γ_B	boundary corresponding to boundary-layer edge
Γ_C	boundary corresponding to cathode surface
Γ_I	boundary corresponding to insulator surface
δ	thickness of diffusion boundary layer (cm)
η_s	surface overpotential (V)
η_c	concentration overpotential (V)
η_{tot}	total overpotential (V)
κ	electrolyte conductivity ($\Omega^{-1}\,cm^{-1}$)
λ	fractional extent of zone of $a = a_l$
Λ	fractional extent of deposition (dimensionless)
ξ	polarization parameter (dimensionless)
φ	potential within the electrolyte (V)
φ^*	dimensionless potential $\frac{\Phi\kappa}{\bar{i}w}$
φ_c	potential of the metal electrode phase
θ	resist wall angle (°)
Ω_c	domain of the concentration-field problems
Ω, Ω_Φ	domain of the potential-field problems
∇	gradient operator
∇^*	gradient operator (dimensionless)
∇^2	Laplace operator
∇^{2*}	Laplace operator (dimensionless)
ΔY	index of nonuniformity

Abbreviations

ADI	alternating-direction implicit
CAD	computer-aided design
TAB	tape automated bonding

1 Introduction

1.1 Patterned Electrodeposition in the Electronics Industry

Computers, microprocessors, and other microelectronic devices could not exist as we know them today without the technology of depositing thin metal or alloy films with fine lithographic patterns. For example, in a computer, the individual transistors that make up an integrated circuit must be electrically interconnected by a complex network of conducting lines and vias that are deposited above the semiconductor layers. Furthermore, the chips are joined to multi-chip packaging modules, a process in which many electrical connections are simultaneously established by solder balls.

This module or "first-level package" is a many-layered structure with multiple complex wiring patterns defined by lithography. This structure is mounted on a "second-level package" or a printed wiring board that consists of multiple layers of patterned conducting lines and through-holes. The technology of microelectronic packaging and the importance of patterned metal films are well described in two monographs [1, 2]. Another technology that is vital to modern computers, magnetic recording for information storage and retrieval, also depends critically on patterned thin metal films for the fabrication of read and write heads.

There are several key methods of depositing thin metal films. These include physical vapor deposition methods of evaporation and sputter deposition, chemical vapor deposition, electrodeposition, and electroless plating. All five methods possess characteristics befitting specific applications in the electronics industry. Electrodeposition, although for practical purposes still limited to those metals that can be plated from aqueous solution, and although it requires a supply of current through a conductive seed layer, has numerous advantages that make it very suitable for electronic microfabrication. Romankiw has demonstrated the capabilities of resist-patterned electroplating for two decades [3–5]. Fig. 1 shows a typical sequence of process steps used in fabricating small metallic features by patterned electrodeposition. A partial list of the attributes of this technology is given below.

Firstly, electrodeposition makes it possible to fill lithographically defined cavities with nanometer-scale fidelity. This pattern replication capability has been vividly demonstrated in numerous cases [6], even where the cavity depth significantly exceeds its width. Secondly, higher rates of metal deposition can typically be achieved

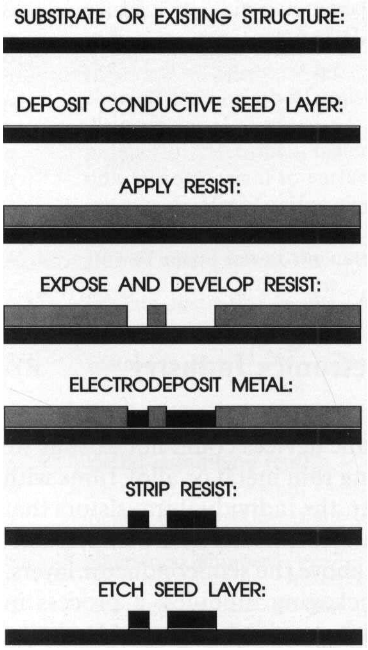

Fig. 1. Sequence of process steps used in fabricating small features by patterned electrodeposition.

by electrodeposition than by vapor-deposition techniques. Thirdly, the capital equipment for electroplating is simpler and less expensive than the high-vacuum equipment required for the vapor-deposition methods. Other advantages of electrodeposition include the avoidance of high-stress deposits, the general ability to cover irregularly shaped surfaces, and the avoidance of subtractive patterning steps.

Industrial applications of resist-patterned electrodeposition have been enumerated on several occasions by Romankiw and co-workers [4, 5]. Some key examples follow. Inductive heads for magnetic recording contain permalloy pole pieces, copper coils, and gold studs, all formed by through-mask electroplating [7, 8]; feature sizes below 10 micron are now routine [9]. In integrated-circuit technology, through-mask plating has been shown to be applicable to wafer-level interconnections [10, 11]. Gold bumps, used in attaching chips to first-level packages such as tape-automated-bonding (TAB) structures, are formed by through-mask electrodeposition directly on integrated-circuit wafers [12]. Patterned plating is also used to fabricate TAB tapes themselves [13], as well as other flexible circuits [14]. Thin-film packaging technology makes extensive use of patterned electroplating to form dense wiring structures [15]. Printed circuit boards and other second-level packages are often made by semi-additive or fully additive circuitization methods [16] based on patterned electrodeposition. Masks for X-ray lithography are made from gold absorber elements that are deposited by through-mask plating [17]. X-ray gratings, Fresnel zoneplates, and resolution targets are also fabricated this way [18]. The LIGA process, developed by Becker et al. [19], employs through-mask electrodeposition in conjunction with synchrotron radiation lithography and plastic molding to build extremly high aspect-ratio microstructures for a variety of purposes. Recently, microscopic motors have been fabricated on silicon wafers by patterned electrodeposition techniques [20, 21].

While the preceding paragraph attests to the present commercial importance of and varied growth opportunities for patterned electrodeposition, there are three current trends that appear to be propelling this technology into a phase of major expansion. Firstly, high-speed machines require the high conductivity of copper (the second most conductive element). Copper plating is a simple, well known, room temperature process, 100 percent efficient, and capable of reaching high rates. Secondly, the pattern replication powers of electrodeposition, which have gradually become widely recognized, are ideally suited to the level of miniaturization now required for wiring structures. Thirdly, the demand for cost reduction in electronic component manufacturing has increased the importance of reducing the capital and operating expenses associated with metal deposition processes. It is thus likely that electroplated copper thin-film wiring will play a central role in the coming decade.

1.2 Importance of Current Distribution and Shape Change

Unless the current efficiency varies strongly with the current density, the local rate of metal deposition by electroplating is proportional to the component of current density normal to the electrode surface. If all points on an electrode surface receive the same current density, all points will advance at the same rate. If a feature receives a higher current density at its periphery, it will grow thicker there than in the center. If two features receive different current densities, they will grow to different sizes.

Since an electrode with a lithographic pattern can be geometrically quite complicated, mathematical descriptions may be intractable if they attempt to embrace all length scales at once. It is often advantageous to focus on behavior on one length scale while temporarily disregarding (by way of approximation) effects acting on a larger and on a smaller scale. The dimensions and characteristics of lithographically patterned substrates suggest that it should be appropriate to study nonuniformity on three different length scales [22, 23]. These can be called the workpiece scale, the pattern scale, and the feature scale. Normally, one attempts to achieve a uniform current distribution on all three scales, and nonuniformity is regarded as a problem to be avoided.

1.2.1 Workpiece-Scale Nonuniformity

Most of the work on electrochemical current distribution that has been reported in the literature concerns the scale of the entire electrode or workpiece. Much of this work was reviewed in two articles [22, 24]. Primarily, workpiece-scale uniformity is affected by the cell geometry, the electrode configuration, and the Wagner number of the system (or a dimensionless group or combination of groups related to the Wagner number). A recent paper addressed the problem of achieving very high thickness uniformity on substrates such as wafers and packaging modules by the use of coplanar auxiliary electrodes [25]. As explained in Sec. 1.2.4 below, the present article is not primarily concerned with the workpiece scale.

1.2.2 Pattern Scale

The term pattern scale was introduced by Mehdizadeh et al. [23], who analyzed electrodeposit thickness nonuniformities that result from an uneven density of resist from one place to another within a lithographic pattern. (The name reflects the fact that wafers and multi-chip packaging modules often contain a regular array of identical patterns with characteristic lengths on the order of one centimeter.) This interesting effect is unique to patterned electrolysis and can cause profound thickness nonuniformity, even in cases where the cell design and operating conditions favor good workpiece-scale uniformity. This effect and its consequences are discussed in some detail. On both the pattern and the workpiece scale, one asks "are all features growing to the same height?" Thickness uniformity can be essential to the manufacturing yield and to product quality in the electronics industry. For example, gold bumps plated on the surface of a silicon wafer for flip-chip packaging must be of uniform height; otherwise not all of the bumps are in contact with the package upon joining. In nearly all applications, there are strong reasons for making sure that each feature on each portion of each substrate has the same dimensions within tight tolerances.

1.2.3 Feature Scale

The term "feature" is used to refer to an individual electrodeposited structure, such as a conducting line, a via, or a pole piece in a magnetic recording head. Here, we are primarily concerned with a scale of tens of microns or smaller. (We do not include through-holes in printed wiring boards, since these are larger and since there is abundant literature on this particular subject, for example reference [26], which describes much earlier work.) On the feature scale, we ask, "what shape is the feature acquiring?" Usually, one tries to achieve a flat profile. In a wiring line, for example, the aim is to obtain a conductor with largest possible cross section that does not exceed the maximum width or height. Obviously, such a structure should have a flat upper surface, if possible. Unless some kind of subtractive process is used after depositing a metal or alloy film, each electrodeposited feature will retain the shape imparted during electrodeposition. As such, each feature can be viewed as a cumulative record of the current distribution. As on the workpiece scale and on the pattern scale, one normally seeks uniform current distribution on the feature scale as well. The present article refers substantially to a recent paper by the author on the simulation of patterned electrodeposition on the feature scale.

1.2.4 Scope of this Chapter

This chapter is concerned with the technology of electrodeposition as applied in conjunction with lithographic patterning to fabricate microscopic structures for the electronics industry. In particular, we are focusing on the shape, size, and uniformity of features created by electrodeposition. The main motive for this work is to foster understanding of the effects that cause nonuniformity in patterned electrodeposition. Special attention is paid to identifying process conditions that produce flat-profiled features of uniform height, since these are normally sought in making electronic components. An important focus of this chapter is the use of mathematical models to simulate the behavior of electrodeposition systems. Predictive capability is viewed as being central to fundamental understanding and to technological progress. The emergence of computer-aided-design (CAD) tools for electrochemical microfabrication is also discussed.

Although thickness uniformity on the workpiece scale is often critical in microelectronic applications, the present article is not primarily concerned with the workpiece scale. One reason for this is that workpiece-scale effects are similar, whether or not the substrate is patterned (although there can be important differences, as discussed in [23]). Our present scope is restricted to the pattern and feature scales, which are more distinctly relevant to patterned electrodeposition.

Because of the very small scale of many lithographic features, radial and spherical diffusion enhancements can cause uneven growth. Leveling agents that act according to the diffusion theory can also exert a strong effect. Particular attention is paid to such geometric diffusion effects.

It would not be unreasonable to include through-holes in printed wiring boards in the scope of feature-scale current distribution problems. In through-hole plating, one must distribute current evenly along the barrel of a narrow cylinder (typically 0.5 mm wide and 5 mm long), a challenging feat that requires an understanding of the factors that influence uniformity. Many mathematical models of the through-hole problem have been reported; notable contributions include [26–36]. Despite the importance of the through-hole problem and its significance in electrochemical engineering, the present publication is primarily concerned with smaller features that are defined by lithography rather than by drilling.

2 Current Distribution on the Pattern Scale

2.1 Background and Literature, the "Active-Area-Density" Effect

Despite the numerous advantages of patterned electroplating as a metal-deposition process for electronic microfabrication, there is one disadvantage that requires attention. Under certain conditions, a nonuniform pattern of resist on the electrode surface can cause the current density to be nonuniform. This has been called the "active-area-density" effect and is explained below. Unlike "line of sight" processes, such as evaporation and sputtering, and unlike "surface-controlled" processes, such as chemical vapor deposition and electroless plating, electrodeposition is influenced by electric fields and current distribution. There is a voltage barrier at the electrode surface (the surface overpotential η_s) that increases with increasing current density. If one zone on the cathode surface is heavily blocked by resist, the current flowing to this zone will be partially diverted to other less occluded zones, where the surface-overpotential barrier (which rises with the current density) is lower. The resulting current distribution may be nonuniform, since the overall path of least resistance is followed (i.e., the lowest possible energy is liberated as heat).

In order for the deposition rate to be uniform, the local current density at all electroactive surfaces must be identical. If there are two adjacent zones of equal size on the cathode surface, the zone with the higher resist coverage will receive less current. We can say that the "superficial current density" at zone (1) is lower than at zone (2). If this is the case, there will be a lower ohmic potential drop associated with zone (1). Consequently, there will be a tendency for zone (1) to attract more current than zone (2). This would upset the uniformity in the electrodeposition rate distribution.

It is useful to define an "active-area density" a as the local fraction of the cathode area that is electroactive (i.e., the fraction that is not blocked by resist). This concept is illustrated in Fig. 2. In places where a large fraction of the electrode surface is blocked, a is low. Further, it is useful to define two different measures of current density. Let the "active current density" i_{ACT} represent the current per unit of electroactive area (remembering that some fraction of the electrode area is blocked by resist). Let the "superficial current density" i_{SUP} represent the current per unit superficial area (including both the resist-covered and the electroactive portions). The relationship between i_{ACT} and i_{SUP} is illustrated in Fig. 3. The physical basis for

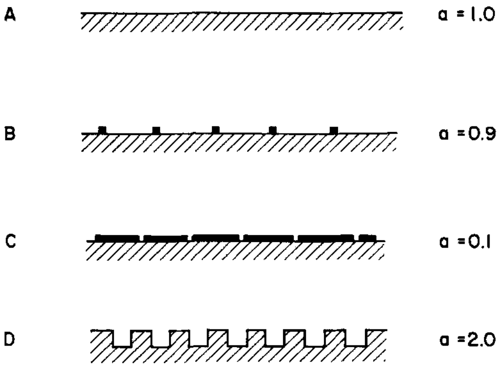

Fig. 2. Illustration of the concept of the active-area density used to describe patterned electrode surfaces; (A) bare, flat electrode, (B and C) flat electrodes covered by resist patterns of different density, (D) electrode with topographic pattern. (Reprinted by permission of the publisher, The Electrochemical Society, Inc. [25]).

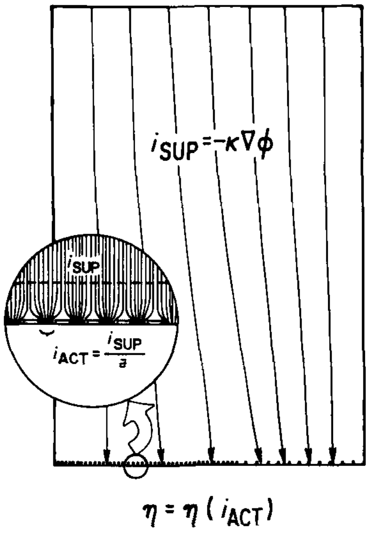

Fig. 3. Schematic illustration of the distinction between superficial current density i_{SUP} and active current density i_{ACT} in the case of through-mask plating. The enlarged view in the circle illustrates the crowding of the lines of current on the feature scale. The larger picture illustrates how, on the pattern scale, the lines of current bend in response to an uneven distribution of resist (black dots) on the electrode surface. (Reprinted by permission of the publisher, The Electrochemical Society, Inc. [25]).

pattern-driven nonuniformity can now be expressed as follows. Uniform thickness requires uniform i_{ACT}. However, if a is nonuniform, i_{SUP} must also be nonuniform. Since the sum of Ohmic drop and surface overpotential must be constant, we see that a uniform i_{ACT} cannot be reached. In practice, some current will be diverted from zone (2) to zone (1). This would raise both the surface overpotential and the Ohmic drop in zone (1) and would lower both in zone (2). This adjustment would allow the total potential drop to the cathode metal to be identical for zones (1) and (2). Zone (1) would receive a thicker electrodeposit. The only exception to the above argument occurs when the ohmic resistance is negligible with respect to the surface resistance (i.e., when $Wa_T \gg 1$). In this case, i_{ACT} could be equal in zones (1) and (2).

Relatively little attention has been paid to current-density nonuniformity caused by uneven pattern density. This effect has been discussed by Romankiw and coworkers [36–38]. A theoretical investigation of the "active-area-density effect" was presented by Mehdizadeh et al. [23]. This was followed by an experimental investigation [39, 40]. Some highlights from the above mentioned publications by Mehdizadeh et al. are presented in the next section. Further discussion of the active-area-density effect appears in a recent publication on electroplated thin-film wiring for high-performance packaging [41] and in a paper on the fabrication of flexible circuits [14].

2.2 An Analysis of Pattern-Scale Current Distribution

Reference [23] describes a treatment of the secondary current distribution on the pattern scale in a case with two adjacent zones with different active-area densities. The development shows that, in the Tafel kinetic regime, the current distribution should depend on the geometry, the Wagner number, and the ratio of the two active-area densities. The Wagner number is based on the length scale of the pattern nonuniformity (for example, the distance from the center of zone (1) to the center of zone (2)) and based on the superficial current density. There is a primary current distribution in the case of $Wa_T = 0$, in which i_{SUP} is uniform and i_{ACT} is inversely proportional to a. This represents the most extreme case of nonuniformity that pattern effects can produce. Fortunately, differences in active-area densities on patterned workpieces often exist across relatively short distances, and Wa_T is higher than 1. However, if there is a wide variation of the active-area density from place to place, the pattern-driven nonuniformity can still be severe, even across short distances.

One can describe the essence of current distributions resulting from uneven pattern density by the following approach. Firstly, the discrete pattern is viewed as a continuum. At any given location, the fractional area available for electrolysis (i.e., the fraction not covered by resist) is described by a, the active-area density. Thus, the active-area-density distribution is the only attribute of the resist pattern. This is to say that the sizes and shapes of individual features are ignored in this model. Secondly, one writes the boundary value problem that is normally solved to calculate the secondary current distribution. The problem domain, shown in Fig. 4 is the volume of electrolyte limited below by the electrode surface, at the sides by symmetry boundaries, and at the top by an iso-current-density plane. Within this domain, the potential is assumed to obey the Laplace equation,

$$\nabla^2 \varphi = 0 \text{ in } \Omega. \tag{1}$$

This is usually a good assumption in electroplating, where the bath conductivity κ is boosted by a supporting electrolyte and is nearly constant. No current is allowed to cross the symmetry boundaries, hence there can be no normal component of the potential gradient at these boundaries,

$$\nabla \Phi \cdot \boldsymbol{n} = 0 \text{ at } \Gamma_{\mathrm{I}}\,. \tag{2}$$

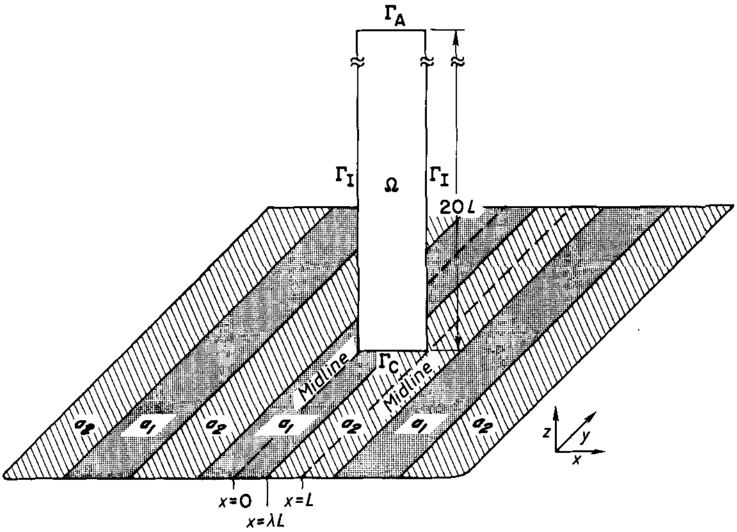

Fig. 4. Schematic representation of the problem geometry corresponding to a pattern involving a step distribution of the active-area density. The domain Ω can be viewed as a two-dimensional, symmetric section of a larger, three-dimensional configuration, as indicated. The relative dimensions are shown, and the boundary segments of the corresponding boundary-value problem are indicated. (Reprinted by permission of the publisher, The Electrochemical Society, Inc. [25]).

A uniform current density $\bar{i}$ is imposed at the top boundary, which is opposed to and far away from the cathode surface,

$$\nabla \Phi \cdot \boldsymbol{n} = -\bar{i}_{\mathrm{SUP}}/\kappa \quad \text{at } \Gamma_{\mathrm{A}} . \tag{3}$$

At the cathode surface, the active current density is related to the surface overpotential η_s by the Tafel kinetic expression,

$$i_{\mathrm{ACT}} = -i_0 \,\mathrm{e}^{-\alpha_c \frac{\eta_s F}{RT}} \quad \text{at } \Gamma_{\mathrm{C}} . \tag{4}$$

The surface overpotential can be regarded as the effective potential difference at the electrode surface, i.e., the potential of the metal electrode phase Φ_{C} minus the potential of the electrolyte phase at the electrode surface Φ.

$$\eta_s = \Phi_{\mathrm{C}} - \Phi \quad \text{at } \Gamma_{\mathrm{C}} \tag{5}$$

The active-area density a enters the problem as follows. It is assumed that, throughout most of the potential domain, the potential gradient is related to the *superficial* current density i_{SUP} by Ohm's law

$$i_{\mathrm{SUP}} = -\kappa \nabla \Phi . \tag{6}$$

In other words, we ignore the thin layer near the cathode surface where the lines of current are crowding toward those small electroactive sites on the surface. This is a fair assumption if the sizes of the lithographie features are much smaller than the scale of the problem. Since the active and superficial current densities are related directly by the local active-area density,

$$i_{\mathrm{ACT}} = i_{\mathrm{SUP}}/a\ , \tag{7}$$

one can now write the cathode boundary condition as

$$\frac{\kappa}{a}\nabla\Phi \cdot \boldsymbol{n} = i_0\, \mathrm{e}^{\alpha_c \frac{(\Phi-\Phi_{\mathrm{C}})F}{RT}} \text{ at } \Gamma_{\mathrm{C}}\ . \tag{8}$$

Since this boundary condition involves the active-area density a, the distribution of a on the cathode surface will influence the current distribution.

Dimensional analysis was performed to show that the current distribution should depend on the problem geometry, on the position of the boundary between zones (1) and (2) (denoted by λ, which may range from 0 to 1), and on two dimensionless groups, Wa_T and $\frac{a_2}{a_1}$. The Tafel form of the Wagner number is defined as

$$Wa_T = \frac{RT\kappa}{\alpha_c F \bar{i}_{\mathrm{SUP}} L} \tag{9}$$

where L is the characteristic length of the investigated pattern, e.g., in the present case L is the width of the problem domain. It should be noted that the characteristic current density appearing in Wa_T is the average superficial current density, which is not the same as the average active current density, which determines the average deposition rate. Ref. [23] also treats the more general case of Butler–Volmer kinetics, in which the solution also depends on $\frac{\alpha_a}{\alpha_c}$ and $\frac{Wa_L}{\bar{a}}$, the latter given by

$$\frac{Wa_L}{\bar{a}} = \frac{RT\kappa}{(\alpha_a + \alpha_c)F i_0 \bar{a} L} \tag{10}$$

where $\bar{a}$ is the average value of a over the area of interest.

The above model predicts the following behavior. If one initially considers two adjacent semi-infinite zones of equal width (i.e., $\lambda = 0.5$), zone (2) having nine times the active-area density of zone (1), the current distributions calculated for a range of Wagner numbers are shown in Fig. 5. When Wa_T is very high, the active current density is uniform. At the other extreme of $Wa_T = 0$, the primary current distribution, there is a step change in i_{ACT} at the inter-zone boundary. The resulting electrodeposit would be nine times thicker in zone (2) than in zone (1). For intermediate values of the Wagner number, the degree of nonuniformity lies between the two limiting cases, and there is a continuous variation in i_{ACT} with position. It is

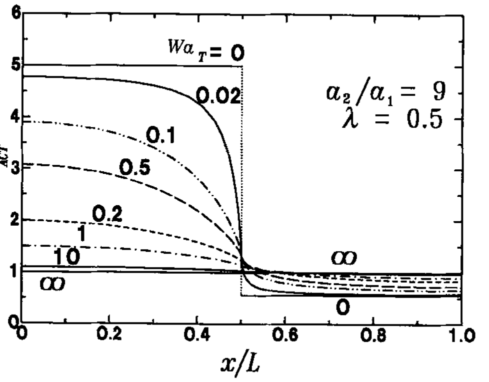

Fig. 5. Family of active-current-density distributions with Wa_T as a parameter for the adjacent-zone problem with $\frac{a_2}{a_1} = 9$. (Reprinted by permission of the publisher, The Electrochemical Society, Inc. [25]).

noteworthy that even with a Wa_T as high as 10, there is a detectable thickness nonuniformity that could be problematic in fabricating an electronic device.

If one adopts as a measure of nonuniformity the normalized difference N between the highest and lowest current densities in the distribution, one can show how nonuniformity depends on $\frac{a_2}{a_1}$ and Wa_T. Fig. 6 demonstrates that nonuniformity is always higher when the ratio of the active-area densities is high and when the Wagner number is low. Fig. 7, a different representation of the same data, shows that, as Wa_T approaches zero, nonuniformity reaches its maximum. In the high Wa_T range, N varies inversely with Wa_T. In this regime, one can halve the degree of pattern-driven thickness nonuniformity by halving the average current density. It should be remembered that $N = 1$ corresponds to a twofold variation in thickness across the pattern, a case that would be unacceptable in nearly any application of patterned electrodeposition. Although the above analysis corresponds to the simplest possible case of uneven resist coverage on an electrode surface (i.e., a step function), one can refer to Figs. 6 and 7 as approximate guides to the level of nonuniformity that could be expected in more complicated situations. (The reader is reminded that the Wagner number must be based on the length scale of the pattern in question.)

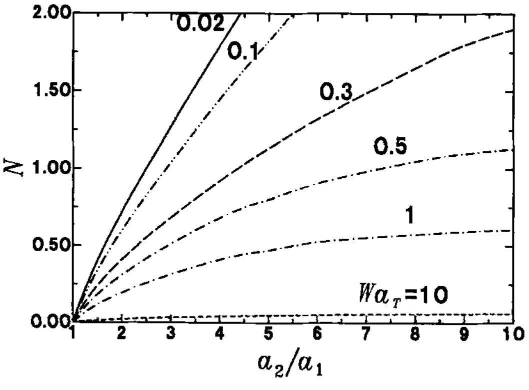

Fig. 6. Dependence of the nonumiformity N on the ratio of active-area densities a_1 and a_2 for different values of Wa_T. (Reprinted by permission of the publisher, The Electrochemical Society, Inc. [25]).

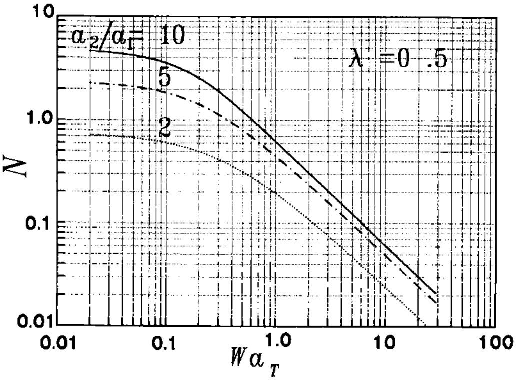

Fig. 7. Dependence of the nonuniformity N on Wa_T for different ratios of active-area densities a_1 and a_2 (Reprinted by permission of the publisher, The Electrochemical Society, Inc. [25]).

An experimental validation of the described model was carried out by Mehdizadeh et al. [39]. Copper was electrodeposited from an acid-sulfate bath onto a special patterned substrate. The substrate, a 5 × 5 cm square glass wafer, with a copper seed layer deposited by evaporation, was patterned with photoresist to create parallel bands, each 0.7 cm wide. This "zebra" pattern is shown in Fig. 8. Each band contained a very fine pattern of parallel lines. In the odd-numbered bands, the line widths and spacings were such that 10 percent of the electrode surface was masked by resist. In the even-numbered bands, the negative image of this pattern was used; thus, 90 percent of the area was masked by resist and only 10 percent of the area was available for electroplating. If one were to move from left to right across this "zebra" wafer, one would encounter alternating bands of respectively 10 and 90 percent ac-

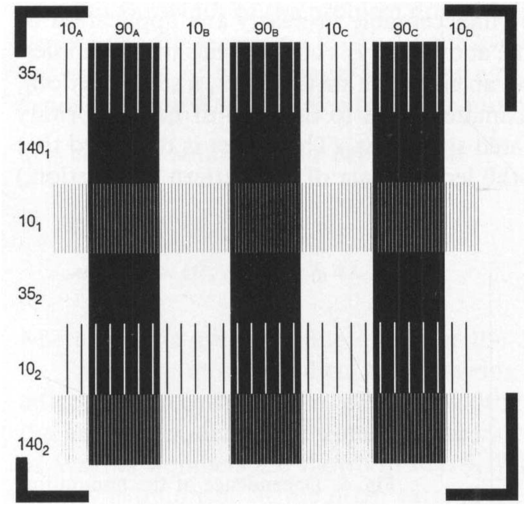

Fig. 8. Top view of a 4.7 × 4.7 cm wafer whose surface is coated by a thin seed layer of copper deposited by evaporation. Above the seed layer is a "zebra" pattern of photoresist: black indicates resist and white indicates exposed copper seed layer. (Originally presented at the Fall 1991 Meeting of the Electrochemical Society, Inc. [39]).

tive area density. The individual lines (i. e., the features) that made up the fine resist pattern in each band had different sizes in different locations on the wafer (10, 35, and 140 μm).

Identical "zebra" wafers were electrodeposited under different conditions in a paddle cell with a coplanar auxiliary electrode, so that agitation would be strong and nearly uniform, and so that the workpiece-scale current distribution would be nearly uniform. Deposits with an average thickness of approximately 2 micron were produced, and the feature heights were measured by profilometry at different positions. Fig. 9 shows normalized thickness measurements between the center of an $a = 10\%$ band and the center of an adjacent $a = 90\%$ band. The three different symbols correspond to the three different line widths, as marked. The continuous curve represents the prediction of the numerical model presented above. The close agreement between model and experiment confirms that the potential theory model based on a continuum description of a fine pattern is valid under the test conditions. The experiment also clearly illustrates that lithographic patterns can give rise to significant thickness nonuniformities in electroplated films.

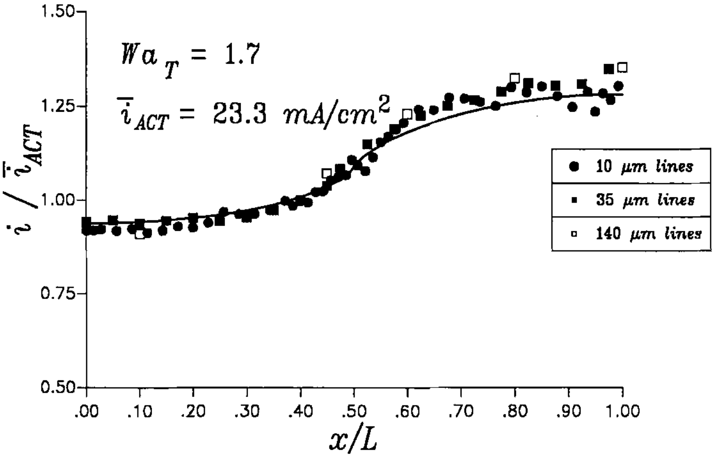

Fig. 9. Comparison between the current distribution across a symmetry element predicted by the active-area-density model (continuous curve) and experimentally measured thickness distributions (individual points). The normalized thickness or current density is plotted versus the position for three different line widths; $a = 0.9$ for $x/L < 0.5$, and $a = 0.1$ for $x/L > 0.5$. (Originally presented at the Fall 1991 Meeting of the Electrochemical Society, Inc. [39]).

2.3 Behavior on the Scale of Several Features

The continuum model of resist-driven nonuniformity by Mehdizadeh et al. [23, 39] cannot describe individual features or small clusters of discrete features that may influence each other during electrodeposition. Although detailed treatment of multiple features can require excessive computational resources, such problems are very im-

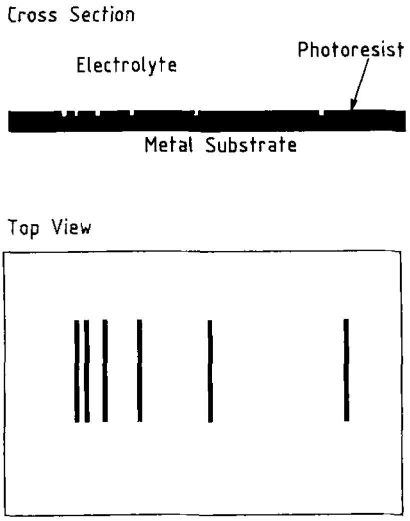

Fig. 10. A schematic (not drawn to scale) of the unevenly spaced pattern investigated by Rosset et al. [44, 45]. The counterelectrode (not shown) is placed at a distance very far from the pattern. (Figure and caption reprinted from West et al. [43] by permission of the publisher, The Electrochemical Society, Inc.).

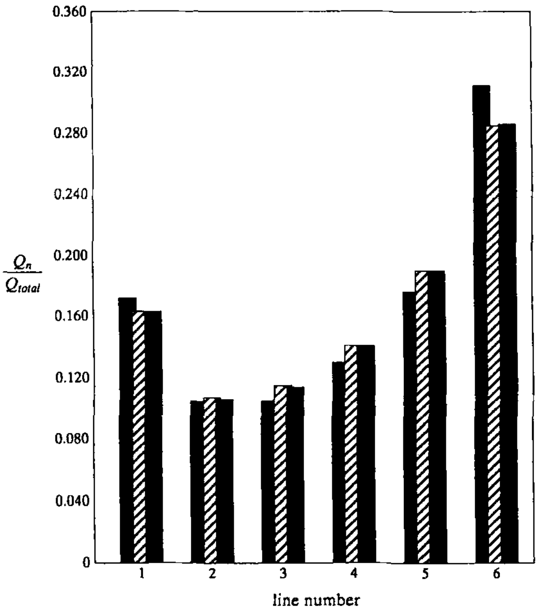

Fig. 11. A comparison of calculated and experimentally measured current distributions for the pattern shown in Fig. 10. The six resist-defined features are numbered from left to right. For each feature, three bars are shown: the left bar shows the experimental data obtained by Rosset et al. [44, 45], while the center and right bars correspond to current distributions calculated by two different methods. (Figure reprinted and caption paraphrased from West et al. [43] by permission of the publisher, The Electrochemical Society, Inc.).

portant. For example, a single feature that is relatively isolated from the others and might escape attention in a continuum-theory model can actually have the highest impact on the thickness distribution, since this feature may be affected by geometrically enhanced diffusion and conduction. The important question of current distribution within a cluster of unevenly spaced features was raised by Landau et al. [42]. Isolated features and clustered features were compared by analytical and numerical solutions of the primary, secondary, and tertiary current distributions in systems containing several nonuniformly spaced lines. Another analysis of small clusters of microscopic features was presented by West et al. [43], who calculated the primary current dustribution among unevenly spaced features. Both the current distribution within a single feature (as influenced by nearest-neighbor features) and the current distribution among a group of features were described, and reasonable agreement with an experiment was reported. Fig. 10 shows an uneven pattern of openings in a resist mask on an electrode surface. Fig. 11 shows the current distribution for this pattern, calculated by two different methods and compared to experimental data from Rosset [44, 45].

3 Feature-Scale Current Distribution and Shape Change

3.1 Background and Literature

On the very small scale of individual lines, vias, pole pieces, etc., current-distribution behavior is dominated by three characteristics. Firstly, ohmic potential drop becomes nearly insignificant because the distances are so short. Secondly, since small features can be smaller than or at least comparable in size to diffusion boundary layers, geometric concentration-field effects, such as radially and spherically enhanced diffusion, can play an important role. Thirdly, since the lateral dimensions of the feature are often comparable to the final thickness of the deposit, the geometry of the problem (which is responsible for mass-transfer nonuniformity) constantly evolves during deposition. Hence it may be necessary to include cumulative shape-change effects in studies on the feature scale.

3.1.1 Models of Resist-Patterned Electrodeposition

Perhaps the first numerical investigation of lithographically patterned electrodeposition was published by Alkire et al. [46]. In this work, the finite-element method was used to calculate the secondary current distribution at an electrode patterned with negligibly thin insulating stripes. (This is classified as a secondary current distribution problem because surface overpotential effects are included but concentration effects are not.) Growth of the electrodeposit was simulated in a series of pseudo-steady time steps, where each node on the electrode boundary was moved at each time step in proportion to the local current density. Lateral overgrowth over the insulating stripes was predicted to approach the rate of vertical growth as the length scale of the problem was reduced. Fig. 12, an example of the results of this investigation, shows the shape of an electrodeposit at different extents of deposition Λ, predicted under the following conditions: initial insulating and conducting stripes, both of width l, anode parallel to cathode at distance 10 l, applied voltage of 3.87 RT/nF, polarization parameter, defined as

$$\xi = \frac{i_0 l n F}{\kappa R T} \tag{11}$$

equal to 1.0. Alkire and Reiser [47] conducted an experiment to validate the findings of the above study.

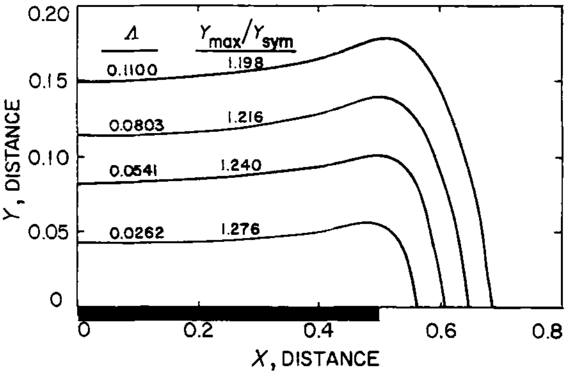

Fig. 12. Dependence of the cathode shape with number of coulombs depsited; original distance shown along abscissa. ($\Phi_A = 3.87$, $\xi = 1.0$, $\Lambda = 2.0$). (Figure and caption reprinted from Alkire, Bergh, and Sani [46] by permission of the publisher, The Electrochemical Society, Inc.).

An important contribution of feature-scale modeling was made by Hume et al. [48]. This team investigated electrodeposition into rectangular cavities defined in resist layers that were thin compared to the thickness of the concentration boundary layer. The geometry of the problem is shown in Fig. 13. The overpotential expression, based on Tafel kinetics, includes a dependence of the exchange current density on the surface concentration and includes the concentration overpotential. (Since concentration effects are included, this can be classified as a tertiary current distribution problem.) The transport of metal ion was assumed to obey Fick's second law of diffusion within a stagnant boundary layer extending above the height of the resist. Since the problem involved a conductive electrolyte and short length scales, potential variations were ignored in order to afford a simplified approximation. In other words, the total overpotential was assumed to be constant over the cathode surface. The boundary-element method with quadratic elements was used to calculate the concentration field at each time step. The boundary was moved assuming pseudo-steady behavior, according to Faraday's law at each node, using Euler-predictor, trapezoid-corrector time integration. It was found that faster-than-average growth at the sides of the feature occured when the current exceeded 40 percent of the diffusion-limited current. The magnitude of the nonuniformity increased as the deposit neared the top of the cavity where the influence of radial diffusion was strongest. Fig. 14 shows feature shape profiles at two different extents of deposition for each of two values of a polarization parameter, ξ, which is defined as

$$\xi = \frac{L i_0^{\infty}}{n F D_M c_M^{\infty}} \, e^{-\alpha_c F(\eta_s + \eta_c)/RT} \, . \tag{12}$$

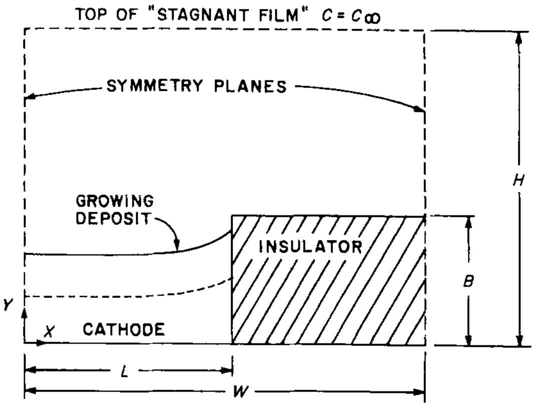

Fig. 13. Two-dimensional problem geometry. (Figure and caption reprinted from Hume et al. [48] by permission of the publisher, The Electrochemical Society, Inc.).

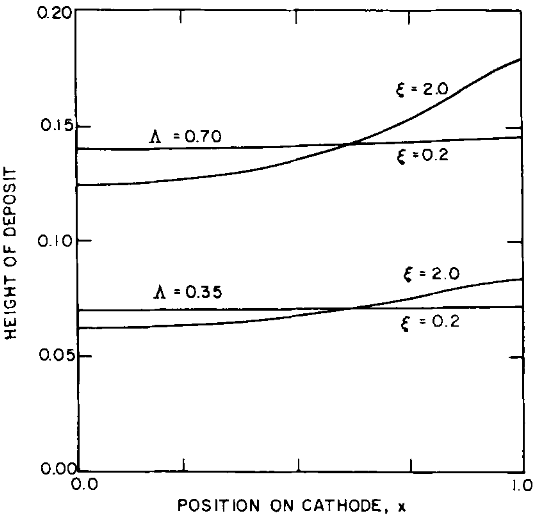

Fig. 14. Deposit profiles for two values of the polarization parameter when the trench area is 35% or 70% full, and $h = 5$, $b = 0.2$, and $w = 2$. (Figure and caption reprinted from Hume et al. [48] by permission of the publisher, The Electrochemical Society, Inc.).

The dependence on geometric and polarization parameters was investigated. Fig. 15 shows how the index of nonuniformity, $\Delta Y = (Y_{max} - Y_{min})/Y_{max}$, depends on the dimensionless extent of deposition Λ for different resist thicknesses $b = B/L$ and different values of ζ. (In this figure, $H/L = 5$, and $W/L = 2$.)

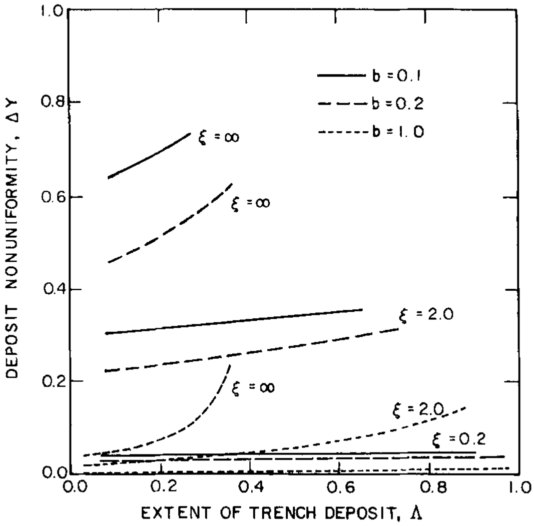

Fig. 15. Effect of the trench depth on the development of deposit nonuniformity for $h = 5$ and $w = 2$. (Figure and caption reprinted from Hume et al. [48] by permission of the publisher, The Electrochemical Society, Inc.).

Peskin [49] used the Galerkin finite-element method to compute current distribution and shape change for electrodeposition into rectangular cavities. A concentration-dependent overpotential expression including both forward and reserve rate terms was used, and a stagnant diffusion layer was assumed. An adaptive finite-element meshing scheme was used to redefine the problem geometry after each time step.

Maslanik [50] extended the above model to include convection produced by laminar flow parallel to the cathode surface and by perpendicular flow from an impinging jet. FIDAP[1] (a commercial finite-element package) was used to solve the Navier-Stokes equation for the velocity field at each time step. The steady-state electrochemical transport equations were solved by a Galerkin finite-element code. The results showed higher deposition rates along the side walls of the cavity under certain conditions. This nonuniformity was more severe for shallower cavities (in agreement with the findings of Hume et al. [48]). Interestingly, it was found that, at a given applied potential, the deposition rate is generally higher under low-Reynolds-number flow than under stagnant conditions. It was also predicted that, by comparison to

---

[1] FIDAP is a registered Trademark of Fluid Dynamics Inc., Evanston, Illinois.

the stagnant case, flow parallel to the electrode surface generally aggravates nonuniformity, and that impinging-jet flow can improve uniformity under certain conditions.

3.1.2 Related Work in Patterned Electrochemical Etching

West et al. [51] simulated shape changes in through-mask electrochemical micromachining. The degree of undercut was predicted for vertically-walled cavities of different aspect ratios, assuming primary current distribution. The boundary-element method was used.

3.1.3 Related Work Involving Stagnant Boundary Layers

Menon and Landau [52] developed a model to describe transient diffusion and migration in stagnant binary electrolytes. Nonuniformity at a partially masked cathode was found to increase during electrolysis as the diffusion resistance develops. The calculations were done using an alternating-direction implicit (ADI) finite difference method.

A variable transformation for treating coupled diffusion and migration of multiple ionic species in stagnant solution was recently described by Baker et al. [53]. The problem is redefined in terms of a "pseudo-potential" which obeys the Laplace equation, enabling solution by a number of available methods. Although it has not yet been applied to electrochemical microfabrication problems, this transformation could be useful to treat cases that do not involve an excess of supporting electrolyte.

3.1.4 Related Work Involving Convection

Two systems that bear close physical resemblance to electrodeposition on the microscale are electrochemical microetching and pitting corrosion. The following modeling investigations of shape change in such systems have been conducted using the FIDAP package or custom derivatives therefrom. Alkire et al. [54] adapted FIDAP to model dissolution in small cavities with rigorous treatment of convective diffusion, particularly the influence of recirculating eddies on shape change. Alkire and Deligianni [55] explored undercutting in through-mask electrochemical etching. They predicted and experimentally confirmed that, under certain conditions, eddies in corners contribute to beneficial anisotropic etching. Two examples of velocity profiles calculated by this team for the flow in small rectangular cavities are shown in Fig. 16. Fig. 17 shows a contour plot of the active-ion concentration computed for a case of through-mask electroetching and the reaction rate distribution across the bottom of the cavity for two different Peclet numbers *Pe*. Harb and Alkire [56] simulated the growth phase of pitting corrosion, accounting for convection, diffusion, and migration of multiple species, as well as reaction equilibrium by adapting the FIDAP code.

Jordan and Tobias [57] studied the influence of convection on mass transfer in a "V" groove under Couette and Poiseuille flow conditions. Flow fields were calculated using the POLYFLOW[2)] packaged program; these were then used in a finite-element code to calculate concentration fields. The latter were compared to concentration fields calculated for stagnant diffusion layers. Some intricate flow patterns were predicted, some involving multiple recirculating eddies. However, it was concluded that for Peclet numbers below 100 (as in the case of small features under common electroplating conditions) the convective effects are negligible. Fig. 18 shows the geometric configuration of the convective-diffusion problem. Fig. 19 compares computed concentration distributions based on pure diffusion and on rigorous treatment of convective diffusion (for a Peclet number of 100). Fig. 20 shows how, at three different Peclet numbers, the mass-transfer-limited flux distribution calculated by the convective model deviates from that calculated assuming pure diffusion.

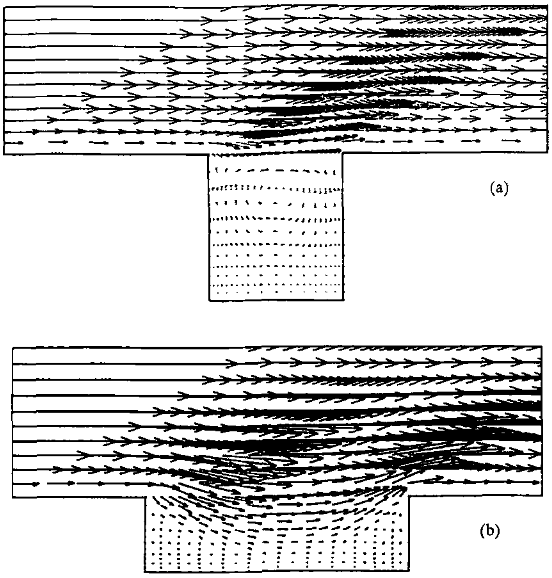

Fig. 16. Finite element results for the velocity vector flow field within rectangular cavities. (a) Aspect ratio 1:1. (b) Aspect ratio 4:1. The arrow length is proportional to the velocity. (Figure and caption reprinted from Alkire and Deligianni [55] by permission of the publisher, The Electrochemical Society, Inc.).

[2)] POLYFLOW is a commercial fluid-flow simulation program from Unite de Mecanique Appliquee, Universite Catholique De Louvain, Batiment Stevin 2, Place Du Levant, B-1348 Louvain-La-Neuve, Belgium.

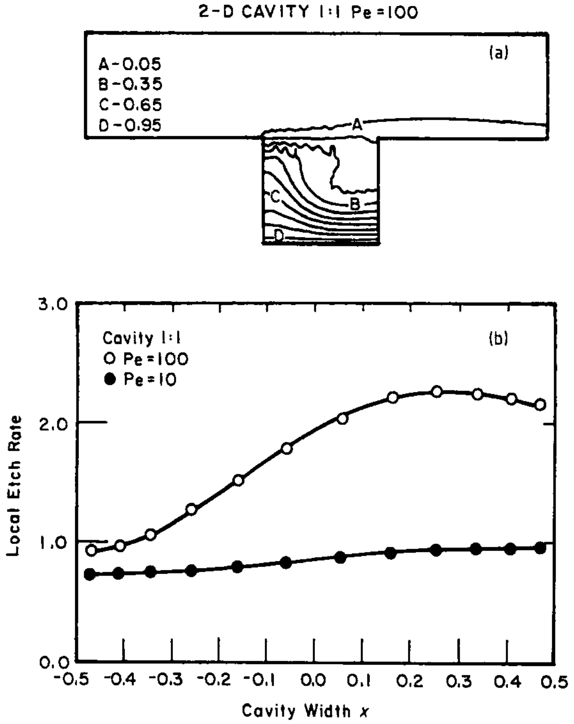

Fig. 17. (a) Equiconcentration contours are shown for various fractions of the saturation value as given in the key. Cavity aspect ratio is 1 : 1, *Pe* = 100. (b) ... provides the variation of local dissolution rate along the bottom surface for two values of Peclet number. (Figure, caption, and additional description reprinted from Alkire and Deligianni [55] by permission of the publisher, The Electrochemical Society, Inc.).

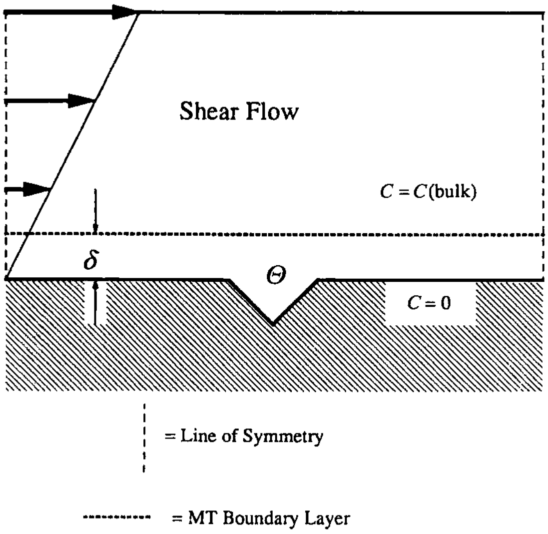

Fig. 18. Convective diffusion problem geometry and boundary conditions. (Figure and caption reprinted from Jordan and Tobias [57] by permission of the publisher, The Electrochmical Society, Inc.).

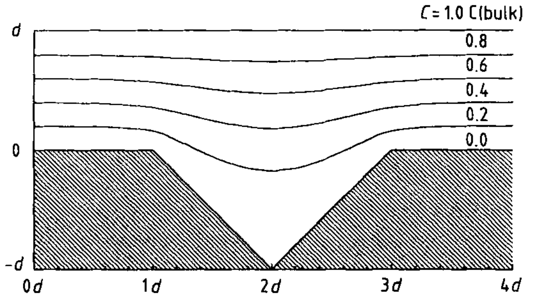

(a) Pure Diffusion

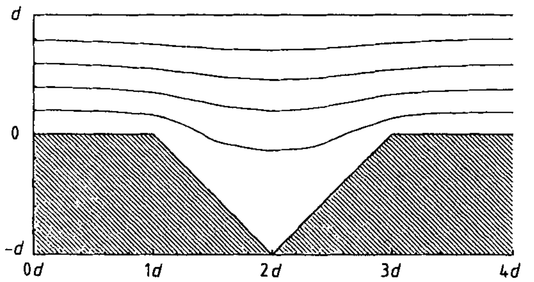

(b) Convective Diffusion, *Pe* = 100

Fig. 19. Isoconcentration contours for a mass transfer boundary layer thickness equivalent to the notch depth *d*. (Figure and caption reprinted from Jordan and Tobias [57] by permission of the publisher, The Electrochemical Society, Inc.).

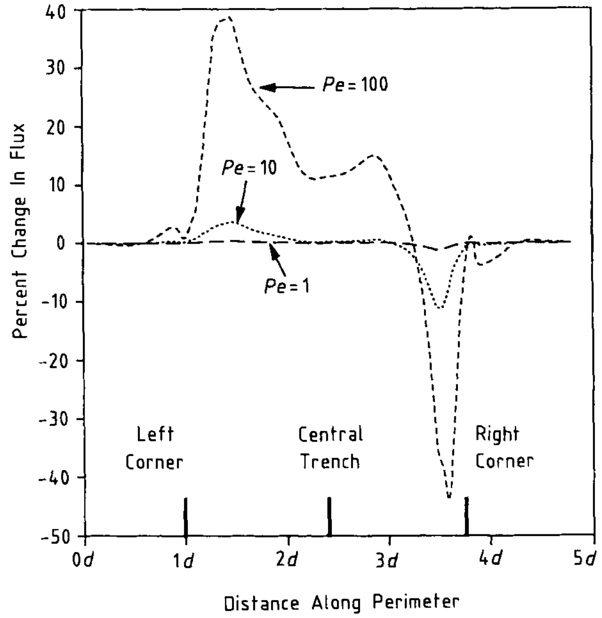

Fig. 20. Increase in flux as a function of distance along the perimeter for a mass transfer boundary layer thickness equivalent to the notch depth *d*. Note that the perimeter is longer than the distance in the *x* direction, hence the locations on the perimeter of the left corner, central trench, and right corner are also shown. (Figure and caption reprinted from Jordan and Tobias [57] by permission of the publisher, The Electrochemical Society, Inc.).

3.1.5 Related Work Involving Leveling

Many commercially used electroplating baths contain additives that promote brightness, ducitility, low stress, desirable mechanical properties, and/or leveling. Leveling agents in particular exert a strong effect on the shape evolution of topographic features (such as protrusions, pits, and scratches) on the 1 to 10 micron scale; such features are rapidly attenuated in amplitude as the deposit grows. It is quite reasonable to suspect that leveling agents should exert strong effects in resist-patterned electrodeposition on the feature scale.

Many papers were written in the 1950s, 1960s, and 1970s to explain leveling, to characterize the leveling performance of different baths either empirically or semi-quantitatively, or to develop approximate capability to predict how the amplitude of a notch or a groove would decay during plating. These developments benefitted the surface finishing industry, for which they were largely intended. However, a more exact and geometrically descriptive treatment of leveling has since become both appropriate, because of the importance of precision and uniformity in electronic microfabrication, and feasible, because of the availability of numerical methods and computing power. To this end, several attmepts have recently been made to incorporate leveling phenomena into numerical simulations of electrode shape change.

Dukovic and Tobias [58] performed a simulation of leveling in a "V" groove profiles for Watts nickel plating with added coumarin, as investigated experimentally by Kruglikov et al. [59]. It was reasoned that inhibitors described by the diffusion theory of leveling [60, 61] could be assumed to operate under diffusion control and that the overpotential should be a function of current density and inhibitor flux. A

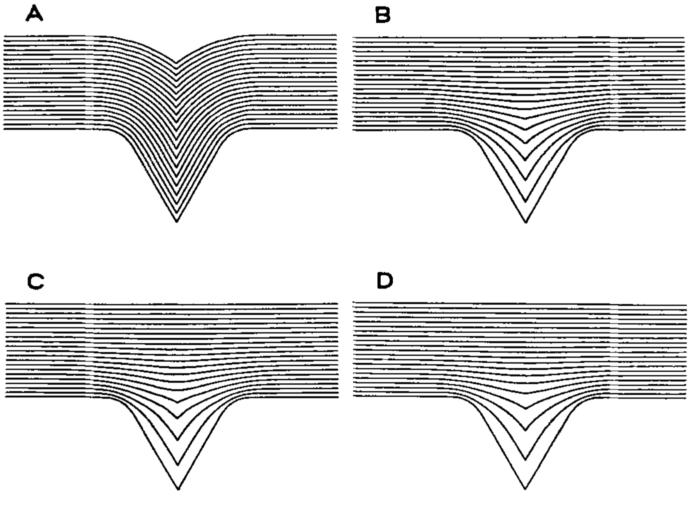

Fig. 21. Four simulated shape histories for nickel electrodeposition into a 50 μ "V" groove on a ratating disk electrode with coumarin as a leveling agent. (A) No coumarin present; (C–D) 0.68 mM coumarin at 150, 360, and 900 r. p. m. (Reprinted by permission of the publisher, The Electrochemical Society, Inc. [58]).

curve fitting of polarization data measured at different leveling agent fluxes by Kruglikov et al. was used as the overpotential expression. The boundary element method was used to solve the coupled boundary-value problem corresponding to ohmic conduction throughout the electrolyte and Fickian diffusion of the leveling agent within a flat-topped stagnant boundary layer. Four simulated shape histories produced by this model are shown in Fig. 21. The predicted leveling rates exceeded those measured by Kruglikov et al.

Jordan and Tobias [62] took a different approach to describing leveling in the "V" groove geometry and tested their model by comparison to the same published experimental data [59]. They considered diffusion layers that conformed to a varying extent to the groove profile, as could result from flow in different orientations with respect to the groove, as illustrated in Fig. 22. They also treated the inhibited kinetics differently. They showed that the polarization data published by Kruglikov et al.

(a) TRANSVERSE FLOW

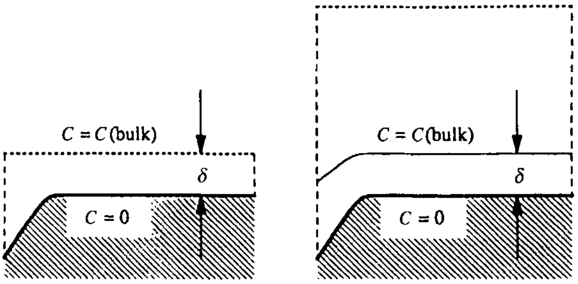

Flat Boundary Layer

2-D Nernstian Boundary Layer

(b) PARALLEL FLOW

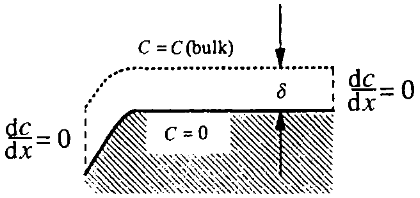

Profile Following Boundary Layer

Fig. 22. Concentration problem geometries and boundary conditions. (Figure and caption reprinted from Jordan and Tobias [62] by permission of the publisher, The Electrochemical Society, Inc.). Only the right-hand half of the V notch id depicted.

agree well with an area-blockage model. They used a one-parameter expression to relate inhibition to the ratio of leveling agent and metal ion fluxes. The resulting simulations, examples of which are shown in Fig. 23, matched the experimental data slightly better than did the simulations of Dukovic and Tobias [58]. Results corresponding to transverse flow across the notch are summarized in Fig. 24. Further improvement in the agreement with experiment resulted from the "profile following" boundary layer assumed for flow parallel to the groove. Jordan and Tobias also investigated the dependence of shape-change behavior on average inhibitor flux and other effects.

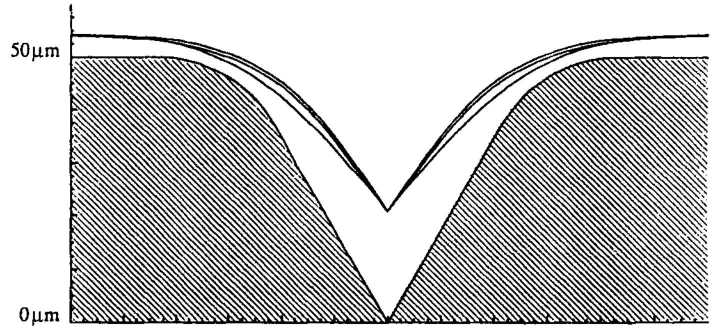

(a) Boundary Layer Thickness = 25μm

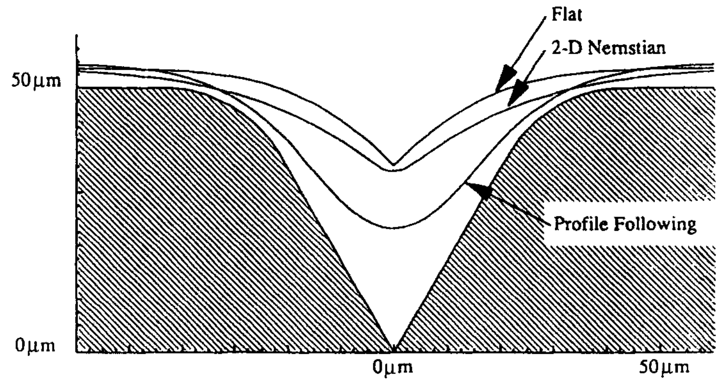

(b) Boundary Layer Thickness = 10μm

Fig. 23. Comparison between final deposit profiles predicted for three boundary layer shapes at two different boundary layer thicknesses after plating 5 μm far from trench. (Figure and caption reprinted from Jordan and Tobias [62] by permission of the publisher, The Electrochemical Society, Inc.). The three curves in each frame correspond to the three boundary-layer configurations shown in Fig. 22.

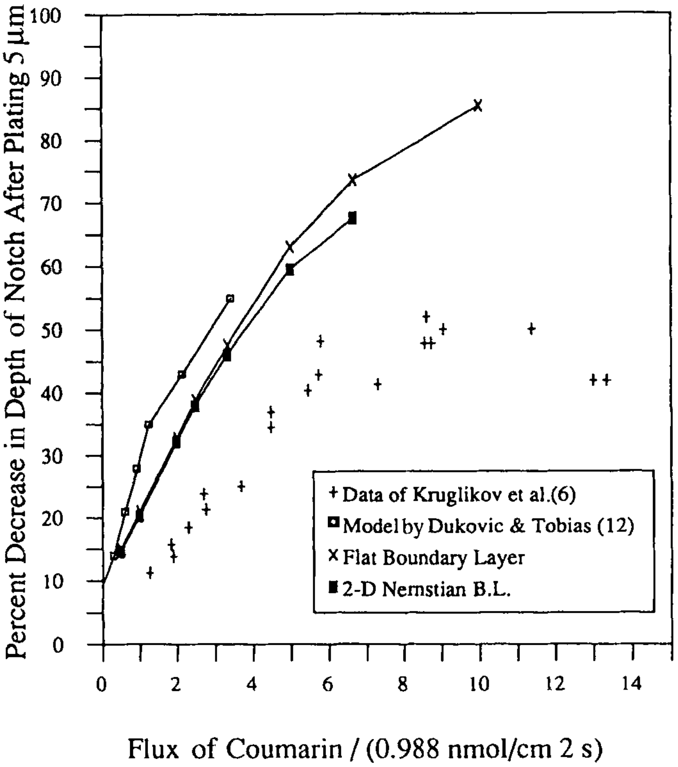

Fig. 24. Comparison between transverse flow simulation and experiment. (Figure and caption reprinted from Jordan and Tobias [62] by permission of the publisher, The Electrochemical Society, Inc.). "The data of Kruglikov et al." are from ref. [59]. The "model of Dukovic & Tobias" refers to ref. [58].

3.2 An Analysis of Feature-Scale Simulation of Patterned Electrodeposition

A numerical investigation of current distribution and shape change in resist-patterned electrodeposition was recently conducted [63]. This study focused on the effects of geometrically influenced diffusion both of the depositing metal ion and of an inhibitor described by the diffusion theory of leveling. This work disregarded convection within the concentration boundary layer. As reported above, several other teams have developed models that do include convection to treat microscale electrochemical systems [29, 50, 54–57, 64]. These publications have revealed some intricate and unusual effects caused by fluid flow under certain conditions, but they also support the view that, if the Peclet number is small, treatment as a stagnant system can be correct. The stagnant model is most likely to be valid for very small features, such as those on the micron and submicron scale.

The numerical investigation by Dukovic [63] centered on a base case of copper electrodeposition into a 10-micron cavity defined in a 5-micron resist wall. The following conditions were assumed: a current density of 50 mA/cm^2, a diffusion boundary layer extending 40 microns beyond the resist layer, a Cu^{2+} concentration of 100 mM in the plating bath, a Cu^{2+} diffusion coefficient of 5.2×10^{-6} cm^2/s, an exchange current density of 1 mA/cm^2, transfer coefficients of $\alpha_c = 0.5$ and $\alpha_a = 1.5$, and a bath conductivity of 0.5 Ω^{-1} cm^{-1}.

The geometry of the problem is shown in Fig. 25. The following geometric parameters are indicated in the figure: the cavity width *w*, the cavity-to-cavity spacing *p*, the boundary layer thickness δ, the resist wall height *h*, the distance between the cathode and the opposing iso-flux plane *s*, and the resist wall angle θ.

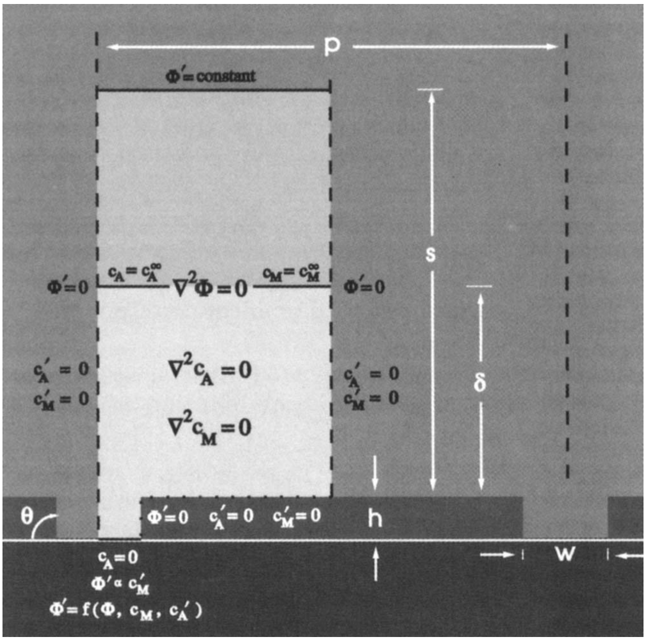

Fig. 25. The coupled boundary-value problem involving the potential, the metal-ion concentration, and the leveling-agent concentration. The geometry of the problem is schematically shown, and the base-case dimensions are given. (Copyright 1992 by International Business Machines Corporation; reprinted with permission [63]).

The mathematical model describing this problem was developed as follows. The potential obeys the Laplace equation in a domain limited by the cavity and the surrounding resist structure at the bottom, by lateral symmetry planes, and by an iso-flux boundary far above the electrode surface:

$$\nabla^2 \varphi = 0 \text{ in } \Omega_\varphi \, . \tag{13}$$

The concentrations of the cupric ion and the leveling agent obey the Laplace equation within a smaller domain, which corresponds to a concentration boundary layer where the two species are assumed to move only by diffusion:

$$\nabla^2 c_M = 0 \text{ in } \Omega_c \tag{14}$$

and

$$\nabla^2 c_\mathrm{A} = 0 \text{ in } \Omega_c\,. \tag{15}$$

The following boundary conditions and matching conditions apply. At the lateral symmetry boundaries and the exposed surfaces of the resist, none of the three field variables is allowed to have a nonzero normal derivative:

$$\nabla\Phi \cdot \boldsymbol{n} = 0 \text{ at } \Gamma_\mathrm{I} \tag{16}$$

$$\nabla c_\mathrm{M} \cdot \boldsymbol{n} = 0 \text{ at } \Gamma_\mathrm{I} \tag{17}$$

and

$$\nabla c_\mathrm{A} \cdot \boldsymbol{n} = 0 \text{ at } \Gamma_\mathrm{I}\,. \tag{18}$$

At the top of the potential domain, a uniform potential gradient corresponding to the average superficial current density is imposed:

$$\nabla\Phi \cdot \boldsymbol{n} = -\frac{w}{p}\,\frac{\bar{i}^{t=0}}{\kappa} \text{ at } \Gamma_\mathrm{A} \tag{19}$$

where $\bar{i}^{t=0}$ is the average current density at the active surface of the feature at the beginning of electrodeposition. (Once the deposit begins to grow, the electro-active area inside the cavity can change. It is the current density imposed far from the electrode rather than $\bar{i}$ within the feature that is kept constant during growth.) At the top of the concentration domain (the outer edge of the boundary layer), the concentrations of both species are kept at their bulk values:

$$c_\mathrm{M} = c_\mathrm{M}^\infty \text{ at } \Gamma_\mathrm{B} \tag{20}$$

and

$$c_\mathrm{A} = c_\mathrm{A}^\infty \text{ at } \Gamma_\mathrm{B}\,. \tag{21}$$

At the electrode surface, three conditions are imposed. Firstly, the leveling agent concentration is kept at zero,

$$c_\mathrm{A} = 0 \text{ at } \Gamma_\mathrm{C}\,. \tag{22}$$

This corresponds to the assumption that the leveling agent is consumed at its mass-transfer-limited rate, an assumption that leads to a maximum degree of nonuniformity in leveling agent flux. The second equation relates the normal derivatives of the metal ion concentration and the potential, since the current carried to the electrode surface by the diffusion of metal ions must match the current described by Ohm's law,

$$nFD_M \nabla c_M \cdot \boldsymbol{n} = \kappa \nabla \Phi \cdot \boldsymbol{n} \text{ at } \Gamma_C \,. \tag{23}$$

The third equation that applies at the cathode surface is the electrochemical rate expression, which relates the current density to the overpotential,

$$\kappa \nabla \varphi \cdot \boldsymbol{n} = i^{\infty}_{0c_A=0} \left(\frac{1}{1 + k_{\mathrm{LEV}} \dfrac{D_A \nabla c_A \cdot \boldsymbol{n}}{\kappa \nabla \varphi \cdot \boldsymbol{n}}} \right) \left(\frac{c_M}{c_M^{\infty}} \right)^{\gamma}$$

$$\left[\mathrm{e}^{-\alpha_\alpha \left(\frac{(\varphi - \varphi_C)F}{RT} + \frac{1}{n} \ln \frac{c_M}{c_M^{\infty}} \right)} - \mathrm{e}^{\alpha_c \left(\frac{(\varphi - \varphi_C)F}{RT} + \frac{1}{n} \ln \frac{c_M}{c_M^{\infty}} \right)} \right] \tag{25}$$

This rather complicated equation is based on the Butler–Volmer kinetic expression,

$$i = i_0 \left(\mathrm{e}^{\alpha_a \frac{\eta_s F}{RT}} - \mathrm{e}^{-\alpha_c \frac{\eta_s F}{RT}} \right) \tag{25}$$

where the surface overpotential η_s is one component of the total overpotential η_{tot}, which is the potential drop at the surface of the electrode,

$$\eta_{\mathrm{tot}} = \eta_s + \eta_c = \varphi_C - \varphi \,. \tag{26}$$

The other component, the concentration overpotential, arises from depletion of the metal ion at the electrode surface,

$$\eta_c = \frac{RT}{nF} \ln \frac{c_M}{c_M^{\infty}} \,. \tag{27}$$

The exchange current density i_0 is assumed to depend on the surface concentration of metal ion, according to

$$i_0 = i_0^{\infty} \left(\frac{c_M}{c_M^{\infty}} \right)^{\gamma} . \tag{28}$$

The rate constant i_0^{∞} is further assumed to be influenced by the inhibiting action of the leveling agent. It is assumed that the inbibiting power of the adsorbed leveling agent depends on the ratio of the leveling-agent flux to the metal-ion flux, since the surface concentration of adsorbate is assumed to be determined by the competition between the arrival of fresh inhibitor and the renewal of the electrode surface by fresh metal atoms. The following simple equation is assumed to apply:

$$i_0^\infty = i_{0c_A=0}^\infty \left(\frac{1}{1 + k_{\mathrm{LEV}} \dfrac{N_A}{i}} \right), \tag{29}$$

where N_A represents the local diffusive flux of leveling agent to the cathode surface and k_{LEV} is a constant characterizing the leveling power.

The above equations were made dimensionless by using the feature width w as the characteristic length, $\bar{i}^{t=0}$ as the characteristic current density, $\bar{i}^{t=0} w/\kappa$ as the characteristic potential, bulk values as characteristic concentrations, and $D_M c_M^\infty / w$ and $D_A c_A^\infty / w$ as characteristic fluxes. The resulting dimensionless equations are

$$\nabla^{*2} \varphi^* = 0 \quad \text{in} \quad \Omega_\varphi \tag{30}$$

$$\nabla^{*2} c_M^* = 0 \ \text{in} \ \Omega_c \tag{31}$$

$$\nabla^{*2} c_A^* = 0 \ \text{in} \ \Omega_c \tag{32}$$

$$\nabla^* \varphi^* \cdot \boldsymbol{n}^* = -w/p \ \text{at} \ \Gamma_A \tag{33}$$

$$c_M^* = 1 \ \text{at} \ \Gamma_B \tag{34}$$

$$c_A^* = 1 \ \text{at} \ \Gamma_B \tag{35}$$

$$\nabla^* \Phi^* \cdot \boldsymbol{n}^* = 0 \ \text{at} \ \Gamma_I \tag{36}$$

$$\nabla^* c_M^* \cdot \boldsymbol{n}^* = 0 \ \text{at} \ \Gamma_I \tag{37}$$

$$\nabla^* c_A^* \cdot \boldsymbol{n}^* = 0 \ \text{at} \ \Gamma_I \tag{38}$$

$$c_A^* = 0 \ \text{at} \ \Gamma_c \tag{39}$$

$$\nabla^* c_M^* \cdot \boldsymbol{n}^* = Sh \nabla^* \Phi^* \cdot \boldsymbol{n}^* \ \text{at} \ \Gamma_c \tag{40}$$

and

$$\frac{Wa_L}{Wa_T} \left(1 + \frac{\alpha_a}{\alpha_c}\right) \left(1 + K_{\mathrm{LEV}} \frac{\nabla^* c_A^* \cdot \boldsymbol{n}^*}{\nabla^* \varphi^* \cdot \boldsymbol{n}^*}\right) \frac{1}{c_M^{*\gamma}} \nabla^* \Phi^* \cdot \boldsymbol{n}^*$$

$$= \mathrm{e}^{\left(\frac{\varphi^*}{Wa_T} + \frac{\alpha_c}{n} \ln c_M^*\right)} - \mathrm{e}^{-\frac{\alpha_a}{\alpha_c}\left(\frac{\Phi^*}{Wa_T} + \frac{\alpha_c}{n} \ln c_M^*\right)} \ \text{at} \ \Gamma_c \, . \tag{41}$$

Dimensional analysis leads to the conclusion that for a given geometry the solution to the coupled boundary value problem depends on seven dimensionless groups. Three of these are $\dfrac{\alpha_a}{\alpha_c}$, $\dfrac{\alpha_c}{n}$, and γ. The other four are

$$Wa_T = \frac{RT\kappa}{\alpha_c F \bar{i}^{t=0} w} \tag{42}$$

$$Wa_L = \frac{RT\kappa}{(\alpha_a + \alpha_c)Fi^{\infty}_{0\,c_A=0}\,w} \tag{43}$$

$$Sh = \frac{\bar{i}^{t=0}\,w}{nFD_M\,c_M^{\infty}} \tag{44}$$

and

$$K_{LEV} = \frac{nFc_A^{\infty}D_A}{w\bar{i}^{t=0}}\,k_{LEV} \tag{45}$$

It can further be shown that in the Tafel kinetic regime, the dependence of the solution on Wa_L and $\frac{\alpha_a}{\alpha_c}$ vanishes.

The details of the numerical solution and the moving boundary scheme are described in reference [63]. The boundary element method involving quadratic elements was used, and the electrode boundary nodes were moved in proportion to the local current density calculated at each time step.

Highlights of the behavior predicted by this model are shown in Figs. 26–32. In each case the closely spaced curves show how, according to predictions, the electrode profile evolves during growth. A profile is shown for each pseudo-steady time step. The amount of metal deposited during each time step is sufficient to deposit a uniform film of width w with a thickness of one fiftieth of the resist wall height. As a basis for comparison among different cases, the point at which the average profile height has reached 90 percent of the resist-wall height is highlighted with a dashed curve. The simulations were terminated before the deposit "mushroomed" above the resist layer, since in practice patterned electrodeposits seldom intentionally exceed the resist thickness.

Fig. 26 corresponds to the base set of conditions for this study, which are summarized in dimensionless terms in the figure. The predominant characteristic of this

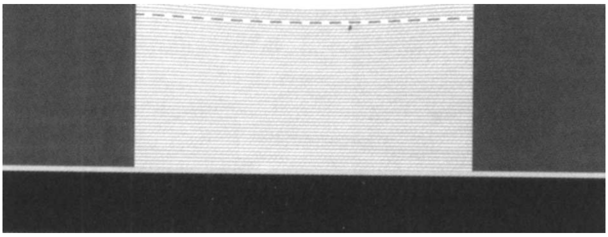

Fig. 26. Shape evolution predicted for the base case. $Sh = 0.5$, $K_{LEV} = 0$, $Wa_T = 520$, $Wa_L = 6500$, $\frac{\alpha_a}{\alpha_c} = 3$, $\gamma = 0.6$, $\frac{\alpha_c}{n} = 0.25$, $h/w = 0.5$, $\theta = 90°$, $\delta/w = 4$, $p/w = 10$, $s/w = 50$, (75% of limiting current at $t = 0$). (Copyright 1992 by International Business Machines Corporation; reprinted with permission [63]).

profile is its relative flatness. At 90 percent thickness the sides of the deposit are only 5 percent higher than the center. This is remarkable, since the conditions for this simulation were deliberately chosen to be harsher than typically used in practice. The fraction of limiting current at the onset of growth is 50 percent; one would normally operate below this point by using a lower current density, a higher metal ion concentration, or stronger agitation (which would produce a mass-transfer boundary layer thinner than 50 μm). It should be mentioned that the fraction of limiting current is of great importance; if this parameter is much less than unity, there is negligible contribution from metal ion transport via the concentration overpotential and the concentration-dependent exchange current density. At the opposite extreme, i.e., at the limiting current, growth is entirely dictated by metal-ion transport effects. Although the fraction of limiting current (the ratio of the applied current to the limiting current) is noted from case to case, it is not treated as an independent parameter because it is not related as closely to the external variables as are the geometric parameters and dimensionless groups identified earlier. Also, the fraction of limiting current actually varies as the profile evolves, making it difficult to compare two cases with the same fraction of limiting current.

Fig. 27 shows the result of reducing the current density by half (Wa_T doubled and Sh halved with respect to the base case). The nonuniformity at 90 percent of the resist height is thus reduced to a nearly undetectable 1.3 percent. It seems clear that at a modest fraction of limiting current vertically-walled cavities can be filled with a minimum of nonumiformity. The behavior shown in Figs. 26 and 27 agrees with the predictions by Hume et al. [48]. The vertical resist walls exert a collimating effect which promotes straight, uniform lines of diffusive flux. As the deposit profile rises toward the top of the cavity, this collimating action diminishes, and the radial enhancement of diffusion near the sides of the feature increases. Hence, most of the height nonuniformity is acquired toward the end of the deposition period.

Fig. 28 shows growth under base conditions, but at a resist wall angle of 70°. In this case, there is an enduring basis for radially enhanced diffusion near the sides of the feature, since the electrode profile forms an obtuse angle with the resist wall. Nonuniformity increases fairly steadily during growth and reaches 8 percent at

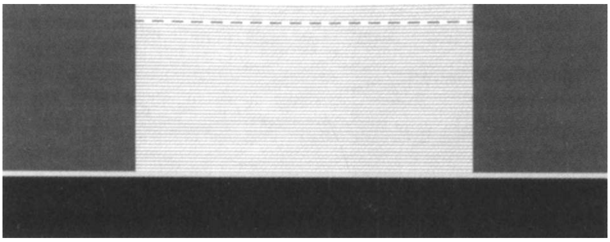

Fig. 27. Shape evolution predicted at half of the base current density (otherwise base conditions). $Sh = 0.25$, $K_{\mathrm{LEV}} = 0$, $Wa_T = 1040$, $Wa_L = 6500$, $\frac{\alpha_a}{\alpha_c} = 3$, $\gamma = 0.6$, $\frac{\alpha_c}{n} = 0.25$, $h/w = 0.5$, $\theta = 90°$, $\delta/w = 4$, $p/w = 10$, $s/w = 50$, (38% of limiting current at $t = 0$). (Copyright 1992 by International Business Machines Corporation; reprinted with permission [63]).

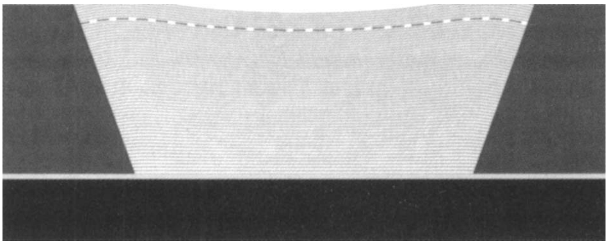

Fig. 28. Shape evolution predicted at base conditions with a wall angle of 70° (otherwise base conditions). $Sh = 0.5$, $K_{\mathrm{LEV}} = 0$, $Wa_T = 520$, $Wa_L = 6500$, $\frac{\alpha_a}{\alpha_c} = 3$, $\gamma = 0.6$, $\frac{\alpha_c}{n} = 0.25$, $h/w = 0.5$, $\theta = 70°$, $\delta/w = 4$, $p/w = 10$, $s/w = 50$, (68% of limiting current at $t = 0$). (Copyright 1992 by International Business Machines Corporation; reprinted with permission [63]).

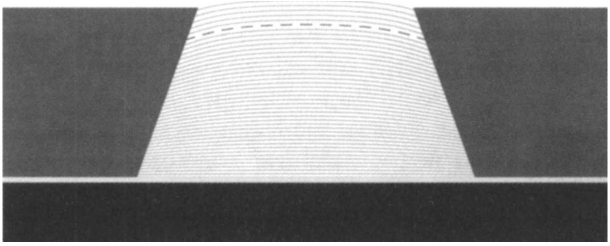

Fig. 29. Shape evolution predicted for a wall angle of 110° (otherwise base conditions). $Sh = 0.5$, $K_{\mathrm{LEV}} = 0$, $Wa_T = 520$, $Wa_L = 6500$, $\frac{\alpha_a}{\alpha_c} = 3$, $\gamma = 0.6$, $\frac{\alpha_c}{n} = 0.25$, $h/w = 0.5$, $\theta = 110°$, $\delta/w = 4$, $p/w = 10$, $s/w = 50$, (89% of limiting current at $t = 0$). (Copyright 1992 by International Business Machines Corporation; reprinted with permission [63]).

90 percent of the resist height. The final profile, which shows prominences near the two sides, is commonly observed in resist pattern plating [6] and is informally referred to as "rabbit ears."

A case with a wall angle of 110° is shown in Fig. 29. Here, diffusive transport to the sides of the feature is geometrically disfavored, and the profile develops a hump in the middle. Although all parameters except for the wall angle are the same as in the base case shown in Fig. 26, the initial fraction of limiting current is as high as 89 percent, because of the closed character of this cavity. Hence, the geometric diffusion effects are strongly felt, and the degree of nonuniformity exceeds 9 percent at 90 percent of the resist height.

In the preceding cases, the leveling parameter, K_{LEV}, was set at zero. Virtually all deviations from uniformity were caused by nonuniform depletion of the metal ion due to concentration field effects. Fig. 30 shows the predicted shape evolution at base conditions with K_{LEV} set at 1.0. A dramatic inversion of the earlier effect is

Fig. 30. Shape evolution predicted under strong leveling (otherwise base conditions). $Sh = 0.5$, $K_{\mathrm{LEV}} = 1$, $Wa_T = 520$, $Wa_L = 6500$, $\frac{\alpha_a}{\alpha_c} = 3$, $\gamma = 0.6$, $\frac{\alpha_c}{n} = 0.25$, $h/w = 0.5$, $\theta = 90°$, $\delta/w = 4$, $p/w = 10$, $s/w = 50$, (75% of limiting current at $t = 0$). (Copyright 1992 by International Business Machines Corporation; reprinted with permission [63]).

seen; instead of "rabbit ears", there is now a hump at the center of the deposit. As the deposit grows and the collimating effect of the vertical resist walls diminishes, strong local inhibition due to radially enhanced diffusion of the leveling agent causes the growth to decelerate dramatically near the sides of the feature. At 90 percent of the resist height, profile nonuniformity is 11 percent. Ironically, leveling agents can cause uneven growth under condition that would otherwise produce nearly flat profiles. This effect, i. e. formation of rounded metal features in baths with strong leveling power, has been observed in practice [65].

Fig. 31 reflects the same conditions as Fig. 16, except that in Fig. 31 K_{LEV} is reduced from 1.0 to 0.5. At this lower inhibition power, the leveling agent still retards growth at the sides of the feature, but this effect is less pronounced. At 90 percent height, the degree of nonuniformity remains below 5 percent.

The tendency for a diffusion-controlled leveling agent to suppress growth at the edges of a feature, where its supply is favored by radial diffusion, is most pronounced

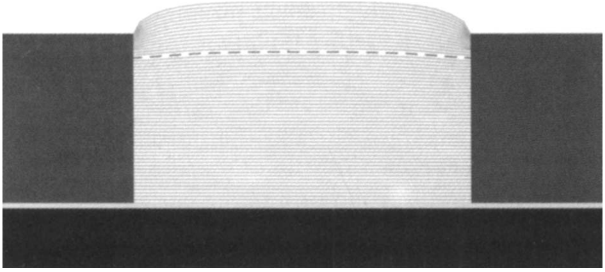

Fig. 31. Shape evolution predicted under moderate leveling (otherwise base conditions). $Sh = 0.5$, $K_{\mathrm{LEV}} = 0.5$, $Wa_T = 520$, $Wa_L = 6500$, $\frac{\alpha_a}{\alpha_c} = 3$, $\gamma = 0.6$, $\frac{\alpha_c}{n} = 0.25$, $h/w = 0.5$, $\theta = 90°$, $\delta/w = 4$, $p/w = 10$, $s/w = 50$, (75% of limiting current at $t = 0$). (Copyright 1992 by International Business Machines Corporation; reprinted with permission [63]).

under the conditions shown in Fig. 32. Here, the open wall angle enhances radial diffusion to the sides throughout the growth period. At 90 percent of the resist wall height, the deposit has a nonuniformity of 30 percent.

The described analysis illustrates some of the factors that may influence the shapes of features produced by through-mask electrodeposition. In review, there is little basis for nonuniform growth at rates well below the limiting current, especially if the resist walls are vertical. At moderate to high fractions of limiting current, nonuniform flux of the metal ion by diffusion, resulting from geometrical field effects, can cause nonuniform growth. Growth is faster where access by diffusion is geometrically favored. In the presence of diffusion-controlled additives that inhibit electrodeposition, the resulting profiles can be highly nonuniform, a tendency that is opposed to the behavior caused by metal ion depletion. Those portions of the profile that favor diffusion access grow more slowly. Leveling agents can actually cause undesired rounding of profiles that would otherwise be flat.

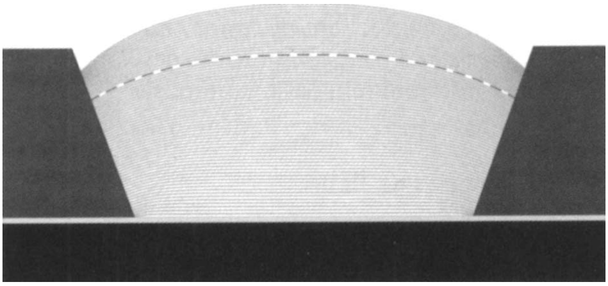

Fig. 32. Shape evolution predicted under strong leveling with a 70° wall (otherwise base conditions). $Sh = 0.5$, $K_{\mathrm{LEV}} = 0.5$, $Wa_T = 520$, $Wa_L = 6500$, $\frac{\alpha_a}{\alpha_c} = 3$, $\gamma = 0.6$, $\frac{\alpha_c}{n} = 0.25$, $h/w = 0.5$, $\theta = 70°$, $\delta/w = 4$, $p/w = 10$, $s/w = 50$, (75% of limiting current at $t = 0$). (Copyright 1992 by International Business Machines Corporation; reprinted with permission [63]).

4 Models for Electrochemical Microfabrication: Status and Future

In the three decades since digital computers were first used to predict electrochemical current distribution [66], the power and availability of computers have expanded to an almost unbelievable extent. Today, computers are employed to design and manufacture many products (not the least important among which are computers themselves). All evidence suggests that this trend will continue, and that advanced technology will depend more and more on simulation and virtual prototyping.

It is therefore appropriate to list a number of noteworthy general observations and trends related to microfabrication by electrodeposition, deposit uniformity, and the use of numerical simulation.

4.1 Toward a More Complete Physical Description of Electrodeposition

Enough is known about the fundamental forces that determine the current distribution to carry out fairly accurate simulations of simple systems. Although in the electronics industry predictions are currently quite useful for guiding the design and production of components made by patterned electrodeposition, there is ample opportunity for improvement, especially in the following areas.

4.1.1 Rigorous Treatment of Electrolyte-Phase Phenomena

As discussed above, rigorous treatment of convection has only recently become possible. Fallacies and limitations arising from models that are based on stagnant diffusion layers are coming to light. The quality of predictions will continue to improve as rigorous descriptions of coupled convection, diffusion, migration, and homogeneous reactions, including hydrolysis and complexation, are developed, confirmed by experiment, and incorporated into multidimensional models.

4.1.2 Electrodeposition from Additive-Containing Baths

There are too many factors left to be elucidated to afford complete agreement between theoretical prediction and measured behavior. One key example treated in this article is leveling. It is possible to develop a simple model to describe leveling action, based on established concepts. However, it is difficult at this point to describe actual leveling systems exactly. Many commercial plating baths contain several additives whose effects are combined. It is not always possible to observe the diffusion-influenced inhibition effect on macroelectrodes (as did Kruglikov et al. [59]). Leveling, in essence, is a phenomenon that occurs on the microscale and requires large differences in additive flux over very short distances. The properties associated with leveling may be impossible to detect on the macro scale. Rigorous models of leveling systems will require increased understanding of the effects of additives at both flat and topographic electrode surfaces.

4.1.3 Alloy Electrodeposition

A considerable amount of work remains to be done to develop models for alloy-deposition systems. These are of appreciable commercial significance, especially for magnetic-recording-head fabrication [9, 67] and in chip-connection technology [68]. Here, it is not only the thickness but also the composition of the deposit that must be kept uniform. The behavior of codepositing metals is sometimes quite unusual and mysterious. At present, many research projects focus on the mechanisms of alloy depositions. Much of this work is reviewed in another chapter of this volume [69].

The influence of side reactions (such as hydrogen evolution) on the deposition rate uniformity is another important consideration [70] both for alloy and pure metal deposition.

4.1.4 Atomic and Crystallographic Scale Phenomena

So far, engineering models of electrodeposition are primarily based on descriptions of matter as a continuum. As the dimensions of microfabricated structures continue to decrease far below the micron scale, however, such descriptions will become insufficient. Detailed accounting for kinks, steps, terraces, and microscopic roughness will become necessary. Scanning-tunneling microscopy and atomic-force microscopy may help promote understanding on this scale. Computational chemistry and molecular orbital modeling may contribute to engineering models of nanostructure fabrication.

4.2 Toward Sophisticated Tools for Computer-Aided Design

4.2.1 Geometric Detail

Recent advances in numerical methods and the increased availability of computing power have considerably facilitated simulation. No longer must we rely on one-dimensional idealization, analogy to classical solutions, analytical solutions obtained for limiting cases, etc. A recurring conclusion from investigations of current distribution on the feature scale is the realization that nonuniformity is primarily due to *multi-dimensional diffusion.* Such effects cannot be approximated by one-dimensional descriptions. Although this has been known for some time, erroneous explanations in terms of differences in thickness of one-dimensional boundary layers remain quite popular. Many structures of engineering interest cannot be approximated by two-dimensional or axisymmetric representations; these require three-dimensional models, which are gradually emerging.

The feature-scale model presented in Sec. 3 points to the fact that the geometry of the lithographically defined cavity may considerably affect the shape of the metal feature. Some basic information is obtained by applying the model to different simple geometries, such as straight resist walls inclined at different angles. Actual resist profiles are often curved and irregular; more exact predictions of feature shapes can be obtained by entering digitized profiles. The degree of geometrical realism and detail afforded by numerical models will continue to benefit greatly from the increasing availability of large memory, fast processors, graphical user interfaces, automatic mesh generation, object-oriented programming, and advances in solid geometric modeling.

4.2.2 Packaged Computer-Aided-Design Software

At present, electrochemical systems are outside the primary focus of computer-aided design software. One exception is the CELL-DESIGN package[3], an interactive program for small computers that solves two-dimensional and axisymmetrical electrochemical current distribution problems based on potential theory [71]. Another exception is COMCAPS[4], a three-dimensional boundary-element code which has been used to simulate cathodic protection of off-shore oil rigs [72]. The major areas in which commercial software packages have become available are computational fluid dynamics, electronic device simulation, mechanical and structural analysis, and heat transfer simulation. The broad scope, power, convenience, user interface, and pre- and post-processing capability of these commercial packages makes them very attractive. Several of these packages can be adapted to solve electrochemical problems such as those discussed above, which involve potential theory, nonlinear overpotential expressions, and shape evolution. The FIDAP package described above, mainly intended for fluid flow simulation,[5] has been substantially modified by Alkire, Sani, and co-workers [50, 54, 56, 64, 73] for electrochemical problems. The ability to describe convection and diffusion of more than one species which may be coupled by heterogeneous and homogeneous reactions, as well as the capability of three-dimensional modeling are noteworthy. However, adaptation of FIDAP to electrochemical problems requires extensive changes at the source-code level, work that requires special arrangement with the program designers. It is likely that in the near future the CAD industry will release more flexible packages that can be used directly for electrochemical simulation.

4.2.3 Integration of Electrodeposition into Multi-Step Process Models

The usefulness of eletrodeposition models will increase significantly when they can be combined with lithography models. Electrodeposition, after all, is only one step in a long process of making an electronic component. It may be interesting to find the combination of process parameters that affords optimum performance or process yield. The relation between lithographic shapes and metal feature shapes could be meaningfully explored by a multi-step simulation package. Such packages have been available for a decade or more and are used for semiconductor process sequences, including ion implantation, dopant drive-in, and thermal oxidation [74, 75]. A milestone in the maturation of electrodeposition process models will be reached when these have been integrated into computer-aided design (CAD) packages for general multi-step microfabrication. The convergence in sophistication

---

[3] CELL-DESIGN is a registered trademark of L-Chem, Inc., 13909 Larchmere Blvd., Shaker Heights, Ohio 44120.

[4] COMCAPS is a computer program developed by SINTEF, Division of materials and processes, 7034 Trondheim-NTH, Norway.

[5] FIDAP is a registered trademark of Fluid Dynamics Inc., Evanston Illinois.

of packaging and semiconductor technologies will help to bring this about. The development and deployment of engineering workstations with powerful central processing units and large memories has also facilitated progress in this area.

4.3 New Directions in Electrodeposition

Models of deposition-rate distribution and shape change are likely to evolve in new directions as progress continues in the areas of alloy plating [76], electrodeposition of resists [77, 78], electrodeposition of composite materials [79], electrodeposited compositionally modulated alloys [80], pulsed electrodeposition, and patterned electroless plating [81]. The success of electrodeposition in high-technology device fabrication will continue to depend on the degree to which rate-distribution effects can be understood, predicted, and controlled.

5 References

1. R. R. Tummala and E. J. Rymaszewski, Thin-Film Packaging, Microelectronics Packaging Handbook, Van Nostrand Reinhold, New York (1989).
2. D. P. Seraphim, R. Lasky, and C. Y. Li, Principles of Electronic Packaging, McGraw-Hill, New York (1989).
3. L. T. Romankiw, A Review of Plating Through Polymeric Resist Masks, Extended Abstracts of the Electrochemical Society, 79-2, No. Abstract No. 462, 1165-1166, The Electrochemical Society Inc., Pennington, NJ (1979).
4. L. T. Romankiw and T. A. Palumbo, Electrodeposition in the Electronic Industry, in: Proceedings of the Symposium on Electrodeposition Technology, Theory and Practice, L. T. Romankiw and D. R. Turner (eds.), The Electrochemical Society, Inc., Pennington, NJ (1987), 87-17, pp. 13-41.
5. L. T. Romankiw, Electrochemical Technology in Electronic Industry and Its Future, New Materials & New Processes, 3, JEC Press Inc., Cleveland (1985), pp. 39-51.
6. L. T. Romankiw, personal communication (1988)
7. K. Ohashi, M. Ito, and M. Watanabe, Application of Electroplating to Thin Film Heads: An Overview, in: Proceedings of the Symposium on Electrochemical Technology in Electronics, 1987 International Conference, L. T. Romankiw and T. Osaka (eds.), The Electrochemical Society Inc., Pennington, NJ (1988), 88-23, pp. 525-542.
8. R. E. Jones, IBM 3370 Film Head Design and Fabrication, IBM Disk Storage Technology, 6-9, IBM Corporation, San Jose, CA (1980).
9. L. T. Romankiw, Thin Film Inductive Heads: From One to Thirty-One Turns, in: Proceedings of the Symposium on Magnetic Materials, Processes, and Devices, L. T. Romankiw and D. A. Herman, Jr. (eds.), The Electrochemical Society, Inc., Pennington, NJ (1900), 90-8, pp. 39-53.
10. K. K. Chakravorty, C. P. Chien, J. M. Cech, M. H. Tanielian, and P. L. Young, High-Density Interconnection Using Photosensitive Polyimide and Electroplated Copper Conductor Lines, IEEE Comp., Hybrids., Manuf. Technol., 13, No. 1, pp. 200-206 (1990).
11. J. J. Barrett, High Definition Electroplated Copper Conductors on Silicon and Ceramic, Proceedings of the 5th International Microelectronics Conference, International Society of Hybrid Microelectronics, Tokyo, Japan (May 25-27, 1988), pp. 461-467.

12. N. G. Koopman, T. C. Reiley, and P. A. Totta, Chip-to-Package Interconnections, in: Microelectronics Packaging Handbook, R. R. Tummala and E. J. Rymaszewski (eds.), Van Nostrand Reinhold, New York (1989), pp. 425-427.
13. N. G. Koopman, T. C. Reiley, and P. A. Totta, Chip-to-Package Interconnections, in: Microelectronics Packaging Handbook, R. R. Tummala and E. J. Rymaszewski (eds.), Van Nostrand Reinhold, New York (1989), pp. 414-415.
14. L. C. Matthew, P. W. Coteus, A. P. Lanzetta, and W. P. Pawlowski, Flex Fabrication – Practical Problems and Design Considerations, in: Proceedings of the Fourth International TAB Symposium (February 16-19, San Jose, CA), S. Khadpe (ed.), Semiconductor Technology Center, Neffs, PA (1992), pp. 173-182.
15. R. R. Tummala, R. W. Keyes, W. D. Grobman, and S. Kapur, Thin-Film Packaging, in: Microelectronics Packaging Handbook, R. R. Tummala and E. J. Rymaszewski (eds.), Van Nostrand Reinhold, New York (1989), pp. 673-725.
16. G. W. Jones, J. M. Shaw, and D. E. Barr, Lithography in Electronic Packaging, in: Principles of Electronic Packaging, D. P. Seraphim, R. Lasky, and C. Y. Li (eds.), McGraw-Hill, New York (1989), pp. 372-393.
17. W. Chu, M. L. Schattenburg, and H. I. Smith, Low-Stress Gold Electroplating for X-Ray Masks, Microeletronic Engineering, 17, 223-226 (1992).
18. D. Ciarlo, Microfabrication Techniques and Applications, IEEE Potentials, 13-16 (October 1978).
19. E. W. Becker, W. Ehrfeld, P. Hagmann, A. Maner, and D. Munchmeyer, Fabrication of Microstructures with High Aspect Ratios and Great Structural Heights by Synchrotron Radiation Lithography, Galvanoforming, and Plastic Moulding (LIGA Process), Microelectronic Enigineering, 4, 35-56 (1986).
20. R. T. Howe, R. S. Muller, K. J. Gabriel, and W. S. N. Trimmer, Silicon Micromechanics: Sensors and Actuators on a Chip, IEEE Spectrum, 29-35 (July 1990).
21. B. Frazier, J. W. Babb, M. G. Allen, and D. G. Taylor, Design and Fabrication of Electroplated MMicromotor Structures, Micromechanical Sensors, Actuators, and Systems, DSC 32, 135-146, Dynamic Systems and Control Division, New York (1991).
22. J. O. Dukovic, Computation of Current Distribution in Electrodeposition, a Review, IBM J. Res. Develop., 34, No. 5, 693-705 (1990).
23. S. Mehdizadeh, J. Dukovic, P. C. Andricacos, L. T. Romankiw, and H. Y. Cheh, The Influence of Lithographic Patterning on Current Distribution: A Model for Microfabrication by Electrodeposition, J. Electrochem. Soc., 139, No. 1, 78-91 (1992).
24. G. A. Prentice and C. W. Tobias, A Survey of Numerical Methods and Solutions for Current Distribution Problems, J. Electrochem. Soc., 129, No. 2, 316-324 (1982).
25. S. Mehdizadeh, J. Dukovic, P. C. Andricacos, L. T. Romankiw, and H. Y. Cheh, Optimization of Electrodeposit Uniformity by the Use of Auxiliary Electrodes, J. Electrochem. Soc., 137, No. 1, 110-117 (1990).
26. E. K. Yung, L. T. Romankiw, and R. C. Alkire, Plating into Through-Holes and Blind Holes, J. Electrochem. Soc., 136, No. 1, 206-215 (1989).
27. T. Kessler and R. Alkire, Copper Plating of Multilayer Printed Wiring Boards, Plat. Surf. Finish., 63, No. 22, 22-27 (1980).
28. T. Kessler and R. C. Alkire, A Model for Copper Electroplating of Multilayer Printed Wiring Boards, J. Electrochem. Soc., 123, No. 7, 990-999 (1976).
29. R. C. Alkire and A. A. Mirarefi, The Current Distribution Within Tubular Electrodes Under Laminar Flow, J. Electrochem. Soc., 120, No. 11, 1507-1515 (1973).
30. M. Ben-Porat, J. Yahalom, and E. Rubin, Current Distribution during Electroplating Within a Tubular Electrode of High Ohmic Resistance, J. Electrochem. Soc., 130, No. 3, 559-567 (1983).
31. R. C. Alkire and J.-B. Ju, The Effect of an Impinging Fluid Jet on Mass Transfer and Current Distribution in a Circular Through-Hole, J. Electrochem. Soc., 134, No. 5, 1172-1180 (1987).

32. O. Lanzi and U. Landau, Analysis of Mass Transport and Ohmic Limitations in Through-Hole Plating, J. Electrochem. Soc., 135, No. 8, 1922-1930 (1988).
33. O. Lanzi III, U. Landau, and J. D. Reid, Effect of Local Kinetic Variations on Through-Hole Plating, J. Electrochem. Soc., 136, No. 2, 368-374 (1989).
34. A. M. Pesco and H. Y. Cheh, The Current Distribution within Plated Through-Holes II. The Effect of Periodic Electrolysis, J. Electrochem. Soc., 136, No. 2, 408-414 (1989).
35. A. M. Pesco and H. Y. Cheh, The current Distribution Within Plated Through-Holes I. The Effect of Electrolyte Flow Restriction During DC Electrolysis, J. Electrochem. Soc., 136, No. 2, 399-407 (1989).
36. E. K. Yung and L. T. Romankiw, Fundamental Study of Acid Copper Through-Hole Electroplating Process, J. Electrochem. Soc., 136, No. 3, 756-767 (1989).
37. L. T. Romankiw, S. Krongelb, E. E. Castellani, A. T. Pfeiffer, B. J. Stoeber, and J. D. Olsen, Advantages and Special Considerations in Fabricating Bubble Circuits by Electroplating and Sputter Etching, IEEE Trans. on Mag., MAG-10, No. 3, 828-831 (1974).
38. J. Horkans and L. T. Romankiw, Pulsed Potentiostatic Deposition of Gold from Solutions of the Au(I) Sulfite Complex, J. Electrochem. Soc., 124, No. 10, 1499-1505 (1977).
39. S. Mehdizadeh, J. Dudovic, P. C. Andricacos, L. T. Romankiw, and H. Y. Cheh, The Influence of Lithographic Patterning on Current Distribution in Electrochemical Microfabrication II. Experimental Study and Mass-Transfer Effects., in: Proceedings of the First International Symposium on Electrochemical Microfabrication, M. Datta, K. Sheppard, and D. Snyder (eds.), The Electrochemical Society Inc., Pennington, NJ (1991), 91-3, pp. 40-51.
40. S. Mehdizadeh, The Influence of Auxiliary Electrodes and Lithographic Patterning on Current Distribution in Electrodeposition, PhD thesis, Columbia University (1991), Chap. 4, pp. 112-159.
41. S. Krongelb, J. O. Dukovic, M. L. Komsa, S. Mehdizadeh, L. T. Romankiw, P. C. Andricacos, A. T. Pfeiffer, and K. Wong, The Application of Electrodeposition Processes to Advanced Package Fabrication, SPIE International Conference on Advances in Interconnection and Packaging, 1389, 249-256 (1990).
42. U. Landau, R. T. Galasco, and J. Tang, Current Distribution in Pattern Plating of Nonuniformly Spaced and Isolated Lines, Extended Abstracts of the 174th Meeting of the Electrochemical Society, 88-2, No. Abstract No. 330, 484-485, The Electrochemical Society Inc., Pennington, NJ (1988).
43. A. C. West, M. Matlosz, and D. Landolt, Normalized and Average Current Distribution on Unevenly Spaced Patterns, J. Electrochem. Soc., 138, No. 3, 728-735 (1991).
44. E. Rosset and C. Landolt, Precis. Eng., 11, No. 2, 79 (1989).
45. E. Rosset, M. Datta, and D. Landolt, J. Appl. Electrochem., 20, 69 (1990).
46. R. C. Alkire, T. Bergh, and R. L. Sani, Predicting Electrode Shape Change with Use of Finite Element Methods, J. Electrochem. Soc., 125, No. 12, 1981-1988 (1978).
47. R. C. Alkire and D. B. Reiser, Electrode Shape Change During Deposition onto an Array of Parallel Strips, Electrochim. Acta, 28, No. 10, 1309-1313 (1983).
48. E. C. Hume, III, W. M. Deen, and R. A. Brown, Mass Transfer Analysis of Electrodeposition Through Polymeric Masks, J. Electrochem. Soc., 131, No. 6, 1251-1258 (1984).
49. A. P. Peskin, The Use of Finite Element Method to Study Electrochemical Moving Boundary Problems, PhD thesis, University of Colorado, Boulder (1985).
50. M. K. Maslanik, Flow and Mass Transport Effects in Electrochemical Systems with Shape Change, PhD thesis, University of Colorado, Boulder (1989).
51. A. C. West, C. Madore, M. Matlosz, and D. Landolt, Shape Changes during Through-Mask Electrochemical Micromachining of Thin Metal Films, J. Electrochem. Soc., 139, No. 2, 499-506 (1992).
52. M. M. Menon and U. Landau, Modeling of Electrochemical Cells Including Diffusion, Migration, and Unsteady-State Effects, J. Electrochem. Soc., 134, No. 9, 2248-2253 (1987).

53. D. R. Baker, M. W. Verbrugge, and J. Newman, A Transformation for the Treatment of Diffusion and Migration. Application to Stationary Disk and Hemisphere Electrodes., J. Electroanal. Chem., 314, 23-44 (1991).
54. R. C. Alkire, D. B. Reiser, and R. L. Sani, Effect of Fluid Flow on Removal of Dissolution Products from Small Cavities, J. Electrochem. Soc., 131, No. 12, 2795-2800 (1984).
55. R. C. Alkire and H. Deligianni, The Role of Mass Transport on Anisotropic Electrochemical Pattern Etching, J. Electrochem. Soc., 135, No. 5, 1093-1100 (1988).
56. J. N. Harb and R. C. Alkire, Transport and Reaction during Pitting Corrosion of Ni in 0.5 M NaCl II. Flowing Fluid, J. Electrochem. Soc., 138, No. 12, 3568-3575 (1991).
57. K. G. Jordan and C. W. Tobias, Simulation of the Role of Convection in Electrodeposition into Microscopic Trenches, J. Electrochem. Soc., 138, No. 7, 1933-1939 (1991).
58. J. O. Dukovic and C. W. Tobias, Simulation of Leveling in Electrodeposition, J. Electrochem. Soc., 137, No. 12, 3748-3755 (1990).
59. S. S. Kruglikov, N. T. Kudryavtsev, G. F. Vorobiova, and A. Ya. Antonov, On the Mechanism of Leveling by Addition of Agents in Electrodeposition of Metals, Electrochimica Acta, 10, 253-261 (1965).
60. O. Kardos and D. G. Foulke, Applications of Mass Transfer Theory: Electrodeposition on Small-Scale Profiles, Advances in Electrochemistry and Electrochemical Engineering, 2, 145-233 (1962).
61. O. Kardos, Leveling and Microthrowing Power, Galvanotechnik und Oberflächenschutz, 8, 161, 185 (1967). (also in: Proceedings of "Surface 66", Basel, 1966, pp. 62-72).
62. K. G. Jordan and C. W. Tobias, The Effect of Inhibitor Transport on Leveling in Electrodeposition, J. Electrochem. Soc., 138, No. 5, 1251-1259 (1991).
63. J. O. Dukovic, Feature-Scale Simulation of Metal Deposition by Elctroplating, IBM J. Res. Develop., 37, No. 2, submitted (1993).
64. R. C. Alkire, H. Deligianni, and J.-B. Ju, Effect of Fluid Flow on Convective Transport in Small Cavities, J. Electrochem. Soc. (Submitted August 1989).
65. P. C. Andricacos, personal communication (1991).
66. J. A. Klingert, S. Lynn, and C. W. Tobias, Evaluation of Current Distribution in Electrode Systems by High-Speed Digital Computers, Electrochim. Acta, 9, 297-311 (1964).
67. S. H. Liao, Electrodeposition of Magnetic Materials for Thin-Film Heads, IEEE Trans. on Mag., 26, No. 1, 328-332 (1990).
68. E. K. Yung and I. Turlik, Electroplated Solder Joints for Flip-Chip Applications, IEEE Comp., Hybrids., Manuf. Technol., 14, No. 3, 549-559 (1991).
69. P. C. Andricacos and L. T. Romankiw, in: Advances in Electrochemical Science and Engineering, H. Gerischer and C. W. Tobias (eds.), Volume 3, VCH, Weinheim (1993).
70. R. C. Alkire and P.-Y. Lu, Effect of Hydrogen Evolution on Current Distribution during Electrodeposition at Vertical Electrodes, J. Electrochem. Soc., 126, No. 12, 2118-2124 (1979).
71. CELL-DESIGN: Computer Aided Design of Electrochemical Cells, L-CHEM, Inc., Shaker Heights, OH (1987).
72. P. O. Gartland and R. Johnsen, COMCAPS – Computer Modelling of Cathodic Protection Systems, Corrosion 85, Paper 319, NACE, Houston, TX (1985).
73. R. Alkire, M. Georgiadou, E. Mannheim, and R. M. Rynders, Modeling Electrochemical Fabrication Processes, in: Proceedings of the First International Symposium on Electrochemical Microfabrication, M. Datta, K. Sheppard, and D. Snyder (eds.), The Electrochemical Society Inc., Pennington, NJ (1991), 91-3, pp. 7-19.
74. Bhaskara Reddy Penumalli, A Comprehensive Two-Dimensional VLSI Process Simulation Program, BICEPS, IEEE Trans. Electron Devices, ED-30, No. 9, 986-992 (1983).
75. C. P. Ho, J. D. Plummer, S. E. Hansen, and R. W. Dutton, VLSI Process Modeling – SUPREM III, IEEE Trans. Electron Devices, ED-30, No. 11. 1438-1452 (1983).
76. M. Chomakova and S. Vitkova, Metal Microdistribution During Ni-Fe Alloy Deposition, Electrochim. Acta, 34, No. 8, 1197-1203 (1989).

77. T. Yamawaki, K. Wakashima, H. Terada, and K. Sasaki, Electrodeposition Photoresist for Production of Fine Pattern Printed Wiring Boards, Surface Mount International, Conference and Exposition Proceedings of the Technical Program, 1, 654–668, Surface Mount International (1991).
78. H. Nakahara, Electrodeposition of Primary Photoresists, Electronic Packaging & Production, 32, No. 2, 66–68 (1992).
79. J. P. Celis, J. R. Roos, C. Buelens, and J. Fransaer, Mechanism of Electrolytic Composite Plating: Survey and Trends, Trans. Inst. Metal Finish., 69, No. 4, 133–139 (1991).
80. D. S. Lashmore and M. P. Dariel, Electrodeposited Cu–Ni Textured Superlattices Use of Finite Element Methods, J. Electrochem. Soc., 135, No. 5, 1218–1221 (1988).
81. G. E. Georgiou, P. F. Bechtold, H. Luftman, and T. T. Sheng, Selective Electroless Plated Ni Contacts to CMOS Junctions with $CoSi_2$, J. Electrochem. Soc., 138, No. 12, 36189–3624 (1991).

Advances in Electrochemical Science and Engineering
Edited by Heinz Gerischer and Charles W. Tobias

The Principles and Techniques of Electrolytic Aluminum Deposition and Dissolution in Organoaluminum Electrolytes

Herbert Lehmkuhl[1], Klaus Mehler[1], and Uwe Landau[2]

[1] Max-Planck-Institut für Kohlenforschung, Kaiser-Wilhelm-Platz 1,
D-45470 Mülheim a. d. Ruhr, FRG
[2] MIB-Metallurgie und Oberflächentechnik und Innovationen in Berlin
GmbH & Co, Motzener Straße 6, D-12277 Berlin, FRG

Contents

List of Symbols

I_0	exchange current density (A/dm^2)
I	current
I_D	pure change transfer current density
L	characteristic length of the system (mm)
m	amount of metal deposited
M	relative amount of metal deposited m_c/m_f
ΔG	free enthalpy of formation (kJ/mol)
ΔH	enthalpy (kJ/mol)
ΔS	entropy (J/K · mol)
U	electrode potential (V)
U_H	electrode potential versus hydrogen el.
V_H	standard electrode potential
Wa	Wagner index
δ	chemical shift (NMR-spectr.; ppm)
ε	dielectric constant
η	overpotential
κ	electrolytic conductivity (mS · cm^{-1})
μ	coefficient of friction
ω	angular frequency of rotation

See also Table 9.

Abbreviations

PVD	physical vapor deposition
CVD	chemical vapor deposition
THF	tetrahydrofuran
DMF	*N,N*-dimethylformamide
DMSO	dimethylsulfoxide
TPAC	tetrapropylammonium chloride
TBAC	tetrabutylammonium chloride
RR	residual resistance ratio
GS	direct current-sulfuric acid technique
NS	anodizing technique
IVD	layer prepared from ionized aluminum in an electric field under vacuum

See also List of abbreviations, Table 1.

In Memory of
Karl Ziegler
(1898–1973)

1 Introduction

The worldwide consumption of nearly 22 million tons of aluminum (in 1987) shows that as an industrial material, aluminum has interesting performance qualities. Aluminum exhibits versatile technical properties in unique combinations. Aluminum is light; its weight is only about one third of that of iron with the same volume. Nonalloyed aluminum remains soft and ductile. Hard materials can be manufactured by alloying, for example with zinc, magnesium, silicon, or copper. Recently, Al–Li alloys have gained considerable interest because of their reduced density and their increased modulus of elasticity; some Al–Li variants can be super plastic molded. Aluminum forms a self-protecting oxide layer and is therefore highly resistant to weathering and exposure to sea water. The aluminum surface can be additionally protected by anodic oxidation or chromatizing. Owing to its high electrical and thermal conductivity, aluminum is indispensable for electronics and electrical engineering. Practically all electric lines consist of aluminum. Solar and heating technology are equally dependent on aluminum. Because aluminum does not present a health hazard, it has found important applications in the packaging industry. Finally, aluminum can easily be machined, industrially or manually, and recycled without any problems.

After oxygen and silicon, aluminum is the third most abundant element in the earth's crust, its abundance totaling 8%. Thus, it is plentiful and because it is not a toxic metal, it is not, like, for instance, lead and cadmium, subjected to legal limitations.

Of the 6 million metric tons of aluminum consumed annually in Europe, almost one third goes into the sphere of transportation. In every car, there is an average of 50 kg of aluminum. This proportion continuously grows, and in the year 2000 it is expected to reach 95 kg per automobile, which represents 9.5% of the total weight of a car.

Another fifth of the amount of aluminum produced is utilized in construction. A good 10% goes into packaging, especially as aluminum foil. Almost 10% of all aluminum is used in electronics and electrical engineering. Examples of applications in electrical engineering include housing for electric motors, high and low voltage cables, electric lines, contact rails, telephone lines, and condensors. In electronics, its application extends from supports for chip assembly to carrier and binding wires for microchips, to storage discs for computer systems. Eight percent of the total amount of aluminum is employed in robot and machine construction. Around 6% can be found again in western European households.

Presently, the proportion of aluminum recycled in Germany is about 35%. Recycling spares the valuable raw material sources and saves up to 95% of the energy necessary for primary manufacturing of the metal. For special purposes, raw aluminum refining is required. Examples of the application of ultra-pure aluminum with purities of 99.999–99.9999% Al include electrolytic condensors, electronic materials (vapor depositing and contact materials), and materials for low temperature electrical engineering [142, 174]. The quantitative demand for ultra-pure aluminum, which is considerably less than 1% of the raw aluminum demand (in 1983), is negligible, but financially quite significant. Especially the rapid development in the area of microelectronics is creating a growing demand for high purity aluminum [185, 205].

The recovery of aluminum metal is divided into two steps, i.e., the production of pure alumina (Bayer Process) and its molten salt electrolysis. Raw aluminum obtained by reduction electrolysis already has a high purity (99.5–99.7%). Refining methods for raw aluminum to obtain higher purities include the segregation process (99.94–99.99% Al) and three-layer electrolysis (99.99–99.998% Al) [142, 236]. Besides these, processes are available whereby the aluminum is anodically dissolved in an organic electrolyte and then cathodically deposited [37, 118, 217, 221]. The dissolution as well as the deposition process contribute to the electrolytic refining of aluminum.

A purity of 99.999–99.9999% Al can be reached by electrolysis from organoaluminum electrolytes. Employing this method, the "Vereinigte Aluminiumwerke AG (VAW)" has for the last 15 years produced one ton of ultra pure aluminum yearly. This process is especially suited to the separation of transition metals and elements such as scandium. This element, as well as uranium and thorium, have unfavorable partition coefficents and thus are not removed during purification via zone melting, [107, 185]. Due to the growing demand for ultra-pure aluminum in the electronics industry, a marked increase in production by "organic" electrolysis as one processing step in combination with three-layer electrolysis and zone melting is expected.

Owing to the outstanding performance qualities of aluminum, there has been no lack of attempts to coat metals with aluminum in order to combine the favorable properties of the base matrial with the specific properties of the aluminum covering layer. Today there are various methods available for plating workpieces with aluminum, for example:

- thermal spray coating,
- hot dipping,
- roll bonding,
- chemo-mechanical plating,
- PVD/CVD (physical or chemical vapor deposition),
- electrolytic plating.

Aluminum as well as aluminum-containing coatings can be deposited with the help of these techniques, which not only differ from one another with respect to procedure and cost, but also in terms of product quality.

Hot-dip aluminizing in a molten bath is only suitable for workpieces with simple shapes which can withstand thermal exposure during hot dipping. Similarly, spray coating is suited only to pieces with a simple geometry. In comparison to other processes, a rather thick layer is necessary to achieve a pore-free coating.

Roll bonding is essentially used only to coat plates and sheet metal. Chemo-mechanical coating, better known as mechanical plating, is conducted in a barrel-tumbling unit. Thus, only loose pieces can be treated. Coatings applied by this type of mechanical plating typically consist of aluminum alloys containing zinc and tin. The throwing power of the PVD process, in other words, the capability in which complex-shaped pieces are uniformly coated on all faces, is limited. In the United States airplane industry, the ion plating process was developed to replace the process of coating cadmium from aqueous solutions and thus to eliminate hydrogen embrittlement. By this process, workpieces can be plated with high purity aluminum, both in a barrel-type unit or supported on a frame. A disadvantage of this method is the necessity to periodically heat the substrate to circa 800 °C, which is clearly higher than the annealing temperature of many steels. At lower temperatures, the coating often reveals a cylindrical microstructure, which usually adversely affects many protective coating properties. The CVD technique shows a very good uniform distribution quality. However, the deposition rate is generally slow in comparison to other methods. Coating takes place in the temperature range of 500–1500 °C, which also leads to a high thermal strain on the workpieces. Plasma-supported processing allows reduction of the substrate temperature to 300 °C. However, at such temperatures, other reaction products are included in the precipitate, preventing deposition of high-purity layers.

The first attempt to electrolytically deposit an aluminum layer was carried out more than 100 years ago. Since then, other methods of electrolytic aluminum deposition were continued to be published. However, none stood up to careful scrutiny. The wish to electrodeposit a newly-to-be-erected statue of William Penn with aluminum led the city council of Philadelphia to be swindled. A charlatan claimed to be able to complete the electroplating process by using a secret recipe. The aluminum was to protect the statue from corrosion in the sea climate. The contractor had the city finance the construction of the world's largest eletroplating plant. Only subsequently would the defraud be publicized, when it became clear that zinc had been electrodeposited instead of aluminum [203].

Because of its very negative standard electrode potential of $-1.7\ V_H$, aluminum cannot be deposited from aqueous solutions. Therefore only molten salt and water-free inorganic or organic electrolyte systems are eligible for electrolytic deposition of aluminum. Only through the development of such nonaqueous systems [53, 54, 118, 217, 221] did it become possible to electrodeposit aluminum with the desired quality and properties.

This section provides a survey of the electrolytic deposition of aluminum out of organoaluminum electrolytes, from its discovery to its technical applications. First, the deposition of metals from nonaqueous organic electrolytes is generally discussed, and the corresponding problems and possibilities are pointed out. In detail, concrete examples of electrolytic aluminum deposition from organoaluminum electrolytes and their fundamental complex chemistry and electrochemistry are treated. In a further section, the properties of such deposited aluminum are described, and finally an overall view is given of the development in instrumentation from the first laboratory cell to a coating plant unit with a capacity of 90 m^2/h.

2 Nonaqueous Electrolyte Systems

2.1 General Introduction

Historically, the investigation of organic electrolyte systems with regard to their suitability and technical applicability for metal deposition and dissolution was, regrettably, neglected in favor of aqueous electrolyte systems. This statement proclaimed by Brenner in modified form during a seminar on electrolysis of organic solvents in 1958 has lost only little of its validity. The considerable practical impact of water on our everyday lives caused scientists, engineers, and technicians to focus nearly exclusively on aqueous electrolyte systems. Thus, electrolysis of nonaqueous solvents probably represents currently the most neglected field of electrochemistry, electrometallurgy, and electroplating. Presently, the predominant part of our fundamental knowledge about and technical experience with electrolytic processes is based on aqueous systems, and many of the observed phenomena may be specific to the solvent water. The study of electrolysis in a large number of different media is necessary to establish fundamental generalizations which can not be obtained on the basis of a single solvent.

Under standard conditions and in the absence of kinetic hindrance, the electrode potential U_H (versus a hydrogen electrode) determines the potential at which the corresponding metal will be deposited out of an aqueous solution. Therefore, metals that have a more negative electrode potential than the hydrogen electrode cannot be deposited from aqueous electrolytes. Kinetic barriers often disfavor the production of hydrogen over metal deposition. Thus, technically important metals, such as tin, nickel, and zinc can be electrolytically deposited out of aqueous solutions without any problems, even though their electrode potentials are lower than that of the hydrogen electrode.

The standard potentials of other metals, such as alkali metals, alkaline earth metals, aluminum, or titanium are so negative that these metals cannot be deposited from aqueous solutions. By choosing electrolytes which do not contain protons and strong complexing groups, it is possible to electrolytically deposit such metals which are not obtainable from aqueous electrolytes. Nonaqueous electrolytes may be either fused salts or solutions of metal compounds in organic or inorganic solvents.

Most metals can be electrolytically deposited from water-free melts of the corresponding metal salts. It is well known that aluminum, lithium, sodium, magnesium, and potassium are mass produced by electrolytic deposition from melts. Industrial processes for the melt-electrolytic production of beryllium, rare earth metals, titanium, zirconium, and thorium are also already in use. Pertinent publications [74, 137, 163] describe the electrolytic deposition of chromium, silicon, and titanium from melts. Cyanidic melts are used for the deposition of thick layers of platinum group metals. It is with this technique that, for instance, adhesion of platinum layers on titanium materials is obtained. Reports concerning the deposition of electrolytic aluminum layers [17, 71-73, 94, 96, 102, 164, 179] and aluminum refinement from fused salts [161] have been published. For these processes, fused salt electrolytes based on aluminum halides or aluminum hydrides are employed, together with organic compounds. From one electrolyte system, compact coatings up to 0.7 mm can be deposited. The results of electrochemical investigations of aluminum halide-containing melt systems are found in a series of publications [52, 86, 111, 155, 165]. Currentless aluminum deposition from fused salt has also been described [139].

The scope of electrolytic metal deposition from the melts is restricted by the limited number of suitable salt systems. In the case of refractory metals, fluoride-containing melts are needed in order to stabilize the metal oxidation state which is necessary for deposition. Because these fluoride melts are often difficult to manage and lead to problems with regard to corrosion and environmental pollution, their use has remained restricted to special applications.

Not withstanding a few exceptions, such as platinum and aluminum, electrolytic metal deposition from melts cannot normally produce dense coherent layers, which are usually required by surface technology. Coatings are often deposited from melt in powdery, spongy, or dendritic form. Even with eutectic melt mixtures, the temperatures are high. In many applications, this exposes the workpiece to be coated to great strain. Consequently, it is not surprising that salt melts, which are preferentially used for metal extraction, are not often employed in surface technology. As mentioned above, electrolytic aluminum deposition is an exception. Patents [232, 233] describe the deposition of aluminum from solution, e. g., from toluene, or from melts of aluminum halides and N-containing onium salts, especially N-heterocyclic compounds and pyridines, i. e., eutectic mixtures which are liquid at 20 °C.

Water-free inorganic solvents, such as ammonia, sulfur dioxide, and hydrazine, have been tested in terms of their suitability for electrolytic metal deposition. Liquid ammonia is used for a series of electrolytic metal deposition processes. Besides the low boiling point (−33 °C) of this solvent its toxicity is disadvantageous. It has been reported that group IA and IIA metals, such as lithium, sodium, magnesium, and beryllium can be deposited from solutions based on ammonia as a solvent [45]. However, only thin or incoherent layers are thus produced [43, 44]. Because it is possible to form anions of molybdenum, lead, selenium, and tellurium in ammonia, these elements can be anodically deposited. Thus, deposition of the semiconductor lead selenide has also been achieved with ammonia as a solvent.

Many of the difficulties associated with salt melts and water-free inorganic solvents can be avoided by utilizing organic solvents. As described in detail below, metals have been deposited from a series of electrolyte systems based on organic solvents. Contrary to popular opinion, the most suitable solvents for this purpose do not necessarily exhibit a high dielectric constant. Table 1 shows that several of the solvents used for electrolytic metal deposition, like tetrahydrofuran (THF), *N*-dimethylformamide (DMF), and dimethylsulfoxide (DMSO) have a very low dielectric constant ε in comparison to water. Indeed, there are conflicting requirements for the selection of a suitable solvent system. In order to achieve high conductivity and good metal salt solubility, the solvent should have strong polar groups. Unfortunately, this leads to strong coordination of the metal ions, shifting the deposition potentials of the metals to more negative values, i. e., values at which the solvent is in danger of decomposing.

Table 1. Limiting potential of some solvents at 25 °C (0.1 M $[NBu_4]ClO_4$, platinum electrode, potential at 0.1 mA/cm^2). Values, unless stated otherwise, quoted from Mann [145, 18].

Solvent	Abbreviation	Dielectric constant ε	U [V] vs. SCE	
			cathodic	anodic
Toluene		2.4	< −2.95[a]	+2.3
1,2-Dimethoxyethane	DME	3.5	−3.0[a]	+0.7[a]
Glacial acetic acid	HAc	6.2	−1.7[a]	+2.0[b]
Tetrahydrofuran	THF	7.6	−3.3[c]	+2.1[c]
Methylene chloride	MC	9.1	−1.7	+1.8
Pyridine	Py	12.0	−2.2	+3.3[d]
Acetone		21.0	−1.6	+1.6
Hexamethylphosphoric acid triamide	HMPT	30	−3.3[c]	+1.1[c]
Methanol	MeOH	31.5	−2.2[a]	+1.3
N-methylpyrrolidone	NMP	32	−3.3[a]	+1.4[c]
Nitromethane		35.7	−2.4[c]	+3.0[c]
Acetonitrile	ACN	36.2	−2.6	+2.7
N,*N*-Dimethylformamide	DMF	36.7	−2.7	+1.5
N,*N*-Dimethylacetamide	DMA	38	−2.6	+1.3
Sulfolane		44	−2.3[a]	+3.3
Dimethylsulfoxide	DMSO	46.6	−2.7	+1.3
Propylene carbonate	PC	65.2	−1.9	+1.7
Water		80	−2.9[a]	+1.4
85–96% Sulfuric acid		100	−1.0[a]	+2.1

[a] Mercury electrode. [b] Sodium acetate. [c] Lithium perchlorate. [d] According to other data, only up to 1.2 V.

Because of the sizes, forms, polarizability values and chemical properties of the constituent molecules, the solvent must be able to form a soluble ion complex with the metal compound or maintain an ionic complex in solution between the dissolved material and a suitable additive [150].

Table 1 points to a further important aspect of water-free organic electrolyte systems. The limiting potential, i.e., the value at which the organic solvent decomposes, shows a far broader applicable voltage window than aqueous systems. Furthermore, aromatic solvents which, except for toluene, are not listed in Table 1, such as naphthaline and diphenyl, have considerably wider voltage windows (3.91 and 4.28 V [81], respectively), than the solvent water. Such extensive voltage windows offer the capability of depositing metals which cannot be electrolytically precipitated from aqueous solution.

In Tables 2 and 3, some of the advantages and disadvantages of aqueous and nonaqueous organic electrolytes are listed. These must be taken into consideration so that the selected electrolyte system suits the application. Aqueous electrolyte solutions are advantageous because of their availability, comparably low price, simple handling, as well as nonflammability. A large number of salts are highly soluble in aqueous solutions, and the viscosity of such a solution is low. Many aqueous electrolyte systems are handled at low working temperature, well below 100 °C. Finally, water is a nontoxic solvent.

Table 2. Properties of aqueous electrolyte systems.

Positive	Negative
Availability	Decomposition voltage range at 1.23 V narrow
Low cost	Hydrogen side reactions
Simple handling	Hydrolysis of many dissolved materials
Nontoxicity	Reaction of some metals with water
Nonflammability	
High solubility of many salts	
Low viscosity	
Low working temperatures	

Table 3. Properties of nonaqueous organic electrolyte systems.

Positive	Negative
Broader decomposition voltage window (up to > 4 V) and therefore deposition of metals which is impossible in aqueous solution	Poisonous effect
No reaction with substrate	Easy inflammability.
No hydrogen evolution	Low conductivity.
Large number of complex ions possible	Relatively high cost
	Limited solubility of many salts
	Disintegration of change at the electrodes
	Moisture and oxygen sensitivity

However, the relatively narrow decomposition voltage window of water, which thermodynamically is only 1.23 V wide, is a disadvantage. During electroplating, the formation of hydrogen is often particularly undesirable. In primary materials to be coated, such as low-alloyed high-strength steel, titanium, or titanium alloys, the uptake of hydrogen leads to irreversible damage. In water, many dissolved materials are undesirably hydrolyzed. A series of base materials, especially non-noble metals, react with the solvent, i.e., water, forming an oxy- or hydroxy-surface layer which may adversely affect the adhesion of the electrodeposit.

The most important virtue of employing water-free organic solvents lies certainly in the mentioned broader decomposition voltage window, which in some systems exceeds 4 V. Thus it is possible to deposit metals which for the previously described reasons cannot be deposited from aqueous solution. The fact that cathodic hydrogen evolution is impossible in water-free aprotic organic systems adds to the advantage for electrolytic coating of hydrogen sensitive materials. Most organic solvents do not react with the materials to be coated, and they can thus be electrochemically coated without adhesion problems. In nonaqueous organic solvents, a large number of complex ions can exist, thereby providing a considerable resource for the development of electrolyte systems.

The disadvantages of nonaqueous organic electrolyte systems include easy flammability, in some cases toxicity of the solvent, and relatively high price. The limited solubility and/or low electrolytic dissociation of many metal compounds in organic solvents lead to low conductivity, thus allowing only low useful current densities. This problem of low conductivity can be overcome by adding conducting salts.

Inclusion of water in nonaqueous organic eletrolytes should be avoided by all means, so that the properties of the systems are not modified. Some organic solvents, for example aliphatic ethers, tetrahydrofuran, and many organic metal compounds react with oxygen. Oxygen must therefore be excluded from the electrolyte systems by appropriate processing techniques. Organoaluminum electrolytes react vigorously with water to generate alumoxanes and alkanes. Reaction with oxygen produces alkoxy-aluminum derivatives of the type $R_{3-n}Al(OR)_n$ ($n = 1 - 3$), as well as intense evolution of heat.

In developing electrolyte systems and apparatus for metal deposition from nonaqueous organic solutions, it is worthwhile to avoid the discussed disadvantages as far as possible without relinquishing the advantages. The development of "made-to-order" systems for metal deposition from organic electrolytes will only be possible when the chemical and electrochemical principles are better understood.

2.2 Survey of Metal Deposition from Nonaqueous Organic Electrolytes

According to the definition of Brenner [43], it has become common to classify electrolytic metal deposition from nonaqueous electrolytes according to two groups, i.e., "aqueous" and "nonaqueous". The "aqueous" group comprises all electrolyte systems from which metals or metallic alloys are deposited that can also be deposited from aqueous solutions. The "nonaqueous" group includes systems from which metals or metal alloys can be electrodeposited that cannot be plated from aqueous electrolytes.

2.2.1 "Aqueous" Group

Up until now, there has been little interest in electrolytic deposition of iron metals and chromium from nonaqueous solutions, because such deposits are easily obtained from aqueous electrolytes. On the other hand, adhesive layers can be applied to reactive metals like titanium, beryllium, and magnesium, for example through nickel deposition from nonaqueous solutions. By depositing such metals out of nonaqueous solutions, hydrogen sensitive materials, such as low-alloy high-strength steel, can be coated without danger of embrittlement. Materials coated in this way with a compact poreless metal layer can be further coated in an aqueous electrolyte, where the first layer acts as a hydrogen barrier. Chromium deposition is distinguished by a low cathodic current yield, although this is technically acceptable. Nonaqueous electrolytes make it possible to deposit chromium with a significantly higher current yield.

As early as 1930, deposition of nickel from organic electrolytes based on formamide and acetamide was reported [207]. Nickel acetate and nickel(II) bromide-hexammine were employed as salts. Metallic nickel coatings were deposited with high adhesive strength on reactive metals at a temperature of 100 °C and a current density of up to 3 A/dm^2. The experiments were carried out under totally water-free conditions. Nickel deposition from solutions consisting of nickel chloride and ethylene glycol was also reported [62]. Here, nickel was electroplated at a lower internal potential than that of aqueous baths containing nickel chloride, but without additives to reduce the potential. However, the throwing power of the nonaqueous baths was limited, so that only thin layers were obtained. Remarkably, the nickel anode dissolved completely and uniformly in the ethylene glycol bath.

The deposition of nickel from trifluoroacetate halide-alcohol baths was also investigated [188-194]. Lustrous, smooth nickel coatings were obtained from $Ni(CF_3COO)_2$-NH_4Cl-methanol baths at 2-22 A/dm^2 and at temperatures of 30-50 °C, from $Ni(CF_3COO)_2$-KBr-methanol at 2-14 A/dm^2 and 50 °C and from $Ni(CF_3COO)_2$-NH_4Br-methanol at 6-22 A/dm^2 and 50 °C. In all cases, the cathodic and anodic current yields were about 100%. The current density range for the deposition of smooth nickel coatings from ethanol is not as wide as with methanol. Cathodic and anodic current yields increase with increasing halide content. The hardness of the deposited nickel layers is considerably higher than that of the precipitate from Watt's bath.

Lustrous adhesive nickel layers can be obtained from baths containing nickel sulfamate, nickel chloride, boric acid, or dimethylformamide (DMF). At 60 °C, current densities of 3 A/dm^2 can be reached [152].

Reports about nickel deposition from baths consisting of acetone and methanol as solvents and nickel chloride and fluoroborate as salts have been published. The purity of the deposited layers decreased with increasing current density. Pure nickel coatings were electroplated at a current density of 1-1.5 A/dm^2 and a bath temperature of 15 °C (acetone) or 20 °C (methanol) [51]. The quality of the layers deposited from the methanol-based baths was still high, even after being stored for one year. These baths withstand the addition of small amounts of water without loss in quality of the layers. Metallic lustrous nickel layers are obtained by using the solvent dimethylsulfoxide (DMSO) with nickel nitrate or fluoroborate [116, 242]. The anodic and cathodic current yields are close to 100%. The measured conductivities, depending on the salt concentration, are between 10 and 15 mS · cm^{-1} at 60 °C. Pure, more than 50 μm thick nickel layers can be deposited from nonaqueous organic electrolytes based on aromatic solvent mixtures [81]. Cobalt coatings can be deposited out of nonaqueous DMF and DMSO solutions [12, 169, 242]. In DMF electrolyte, a current density of 1-6..4 A/dm^2 can be applied.

Chromium electrodeposits can also be obtained from electrolytes containing acetone and chromium chloride at current densities of 0.1-1 A/dm^2 and 15 °C. Nickel-chromium alloy coatings with up to 22% chromium can be deposited out of electrolytes produced by dissolving nickel fluoroborate and chromium chloride in methanol [51].

Uniform layers of iron, nickel, cobalt, copper, or their alloys, as well as tin-nickel alloys can be deposited from organic electrolytes based on half ethers of ethylene glycol. In order to avoid codeposition of hydrogen and the resulting danger of embrittlement of hydrogen-sensitive materials, water-free solutions of the metal salts of iron, cobalt, nickel, and tin are employed as electrolytes. The list of particularly suitable media includes water-free chlorides, bromides, and complex compounds of these metal chlorides and bromides with ethers (THF) or alcohols (ethanol) in water-free alkyl half ethers of C_2-C_3-alkylene glycols, mixtures of these solutions with water-free conducting salts, such as lithium chloride or bromide or the corresponding tetraorganoammonium halide. The corresponding metal is installed as the anode. The cathodic and anodic current yields are quantitative, based on the amount of deposited and dissolved metal. Hydrogen is not deposited [127].

Recommended electrolytic temperatures are between 50 and 80 °C. Uniform, and lustrous metal layers are obtained preeminently at 0.5 to 1.0 A/dm^2. With electrolytes containing compounds of various metals, the composition of the electrolytically produced alloys can be varied over a wide range. The described electrolytic systems are appropriate for electroplating intermediate layers on low-alloy high-strength steels, which must be coated without hydrogen embrittlement. These systems are especially suitable for replacing the nickel intermediate layer deposited out of aqueous solution, which serves as an adhesive agent for the following electrolytic aluminum plating step. In this way, hydrogen embrittlement can also be almost completely excluded during preliminary treatment.

Copper and palladium precipitates are obtained from aromatic solvent mixtures [1].

2.2.2 "Nonaqueous" Group

A series of technically meaningful metals, such as aluminum, titanium, and silicon are members of the "nonaqueous" group. Possible applications of the above mentioned metals in surface technology range from corrosion protection to semiconductor technology.

However, the "nonaqueous" group also includes metals such as lithium, magnesium, cerium, yttrium, beryllium, sodium, potassium, gallium, indium, thallium, and germanium, which have been deposited from organic electrolytes [43, 63, 143, 162, 181]. Patents describing electrolytes and processes for electrolytic sodium deposition from organometallic electrolytes were granted as early as the 1960s [224, 226, 227]. In the narrow temperature range between 64 and 70 °C, liquid potassium can be electrolytically deposited from $K[AlEt_4]$ dissolved in $K[Et_3AlOBu]$ [222]. Electrolytes containing propylene carbonate have also been employed for the deposition of potassium [217]. In 1980, the deposition of pseudo-amorphous silicon from electrolytes based on trichlorosilanes dissolved in propylene carbonate, with tetraalkylammonium chloride serving as a conducting salt, was reported [4]. Thin, nondoped silicon coatings on iron and non-iron materials are expected to protect against corrosion. Doped silicon films on appropriate substrates are inexpensive materials for photovoltaic cells. The choice of conducting salts has a considerable influence on the roughness of the silicon coatings. Deposits from electrolytes containing tetrapropylammonium chloride (TPAC) as a conducting salt show a finer crystalline texture than those obtained with tetrabutylammonium chloride (TBAC).

Titanium can likewise be electrodeposited from "nonaqueous" organic electrolytes. At circa 18 °C, 1-75 µm thick coatings are deposited from electrolytes containing dimethylsulfoxide (DMSO) [169]. The baths utilized do not exhibit high stability. Zirconium, hafnium, niobium, and aluminum are also expected to afford electroplated coatings from similar composite systems. Electroplating of titanium from electrolytes based on aromatic solvent mixtures has recently been reported [171].

Of all metals belonging to the "nonaqueous" group, electrodeposition of aluminum out of nonaqueous solvents has received the most attention. The beginning of this development is reviewed in reference [21]. Aluminum is the only metal that is electrodeposited on a commercial scale as a galvanic coating [6, 26, 28, 29, 31, 33, 35, 56, 66, 112-115, 182] as well as an electrolytically refined high-purity metal [37, 142, 184] from organic electrolytes. Additionally, there is a large number of publications describing the properties of electrodeposited aluminum precipitate [27, 30, 63, 97-99, 112, 118, 140, 149, 176, 180, 204, 206, 221].

Not only pure aluminum, but also aluminum alloys can be electrodeposited from organic electrolyte systems. Thus, codeposition of iron, nickel, and cobalt from systems composed of $AlBr_3$, LiBr, and toluene have been reported. However, only a small content up to a maximum of 1.4% (for instance, iron) is reached [175].

A patent has been granted concerning deposition of aluminum-titanium alloys [154]. In this case, the starting materials include aluminum and titanium bromides and toluene as a solvent. Precipitates containing up to 10% titanium were deposited. An alkylaluminum-containing electrolyte system is utilized for the deposition of aluminum-zinc alloys [60]. Zinc constitutes a maximum of 1-2% in the deposited alloys. Aluminum-copper alloys can be precipitated out of ethylbenzene-toluene aluminum bromide electrolytes [49, 76]. A copper content in the precipitate of up to 3.5% can be reached. Patents concerning deposition of aluminum-magnesium [147], aluminum-zinc, -cadmium, and -manganese alloys [200] have been granted. A molten-salt process for electroplating aluminum-manganese alloys has been developed on a technical scale [234, 235].

3 Electrolytic Aluminum Deposition from Nonaqueous Organic Electrolytes

For the electrolytic deposition of aluminum there are various types of aprotic organic electrolytes which can be distinguished by their aluminum source:

1. AlX_3 (Aluminum trihalides, especially $AlCl_3$, $AlBr_3$, their complexes with alkali metals, or onium halides).

2. AlH_3 (Aluminum hydrides as mixtures of Li $[AlH_4]$ and $AlCl_3$ in ethers).
3. AlR_3 (Aluminum trialkyls and their complexes with alkali metals or tetraalkylammonium halides, especially fluorides in aromatics or as melts).

In the electrolyte systems of group 1, the aluminum halides or their complexes are used as melts or in aromatic solvents. Deposition of aluminum from this type of electrolytes has been reported by a large number of authors [7, 46–50, 110, 151, 158–161, 165, 232, 233]. Electrolyte systems based on aluminum halides are often unstable, due to their differing cathodic and anodic current yields. Furthermore, corrosive hydrogen halide vapors can form, which are undesirable in closed electrolysis cells. Recently, patents have been granted concerning aluminum electroplating from a low melting composition comprising a mixture of 20 to 80 mol% of an aluminum trihalide and 80 to 20 mol% of an onium halide of the type:

1. bicyclic quarternary amidinium halide,
2. 1-alkylaminopyridinium halide,
3. trialkylimidazolium halide,
4. benzimidazolium halide,
5. alicyclic quarternary ammonium halide, or
6. asymmetric tetraalkyl ammonium halide $[NR^1R^2R^3R^4]$ X.

Bath temperatures of 20 to 100 °C are preferred. Current densities between 1 and 20 $A \cdot dm^{-2}$, electrolytic conductivities between 0.5 and 17 $mS \cdot cm^{-1}$ and current efficiencies of 95% or higher have been reached [232]. At present, there is no information about large-scale applications.

The so-called group 2 hydride baths are based on the work of Brenner [53, 54]. These baths consist of aluminum hydrides and chlorides, as well as alkali metal hydrides. Tetrahydrofuran is the most common solvent. These electrolytes were intensely investigated in the Netherlands [22–26, 55–60, 63, 82], in Japan [108, 198, 208–211], and in the former Soviet Union [68, 77–80, 103, 104, 109, 168, 173]. The development to a technical process (Real Process = room temperature electroplated aluminum) took place in the laboratories of Philips Research [6, 35]. The electroplating process can be carried out at ambient temperature; currently, the efficiency is 100%, and the deposited aluminum has a purity of 99.99% [6]. Pilot plant arrangements for continuous aluminum electroplating on wire, metal tape, and small parts have been developed. Aluminum layers with large surface areas targeted for electrolytic condensers can be deposited at a high current density. Industrial scale applications of these electrolytes are not known. Al–Mg alloys containing up to 13% Mg are obtained from mixtures of type 2 electrolytes and $MgBr_2$ [238].

Of all aluminum electrolyte systems, to our knowledge type 3 is today the technically most accepted. This type of electrolyte was discovered and intensely studied by Ziegler and Lehmkuhl [118, 217, 218, 221]. The companies Siemens AG, HGA, MBB, SEDEC, Interatom, and ALU 2000 have developed the industrial scale process (Sigal Process = Siemens galvanoaluminum). The used electrolytes consist of aluminumalkyls as well as alkali metal halides or quaternary onium salts, which are dissolved in aromatics (i.e., toluene). Electrolysis is carried out at temperatures around 90–100 °C. Electrolytes of this kind have demonstrated their high productivity even in long-term practical use. The high resistance of electrodeposited aluminum layers to corrosion is exploited especially in the automobile industry [27-31, 33, 112-115, 176, 178, 180, 204]. The same type of eletrolyte has been used for aluminum refinement for many years [37, 84, 107, 142, 185]. Purities of up to 99.999-99.9999% Al can be reached by working carefully.

The final performance limitation of aluminum alkyl electrolyte systems has not, by far, been reached. Substantially higher deposition rates than those realized today by eletrodeposition technology with organoaluminum electrolytes, i.e., 1-1.5 A/dm^2, are probably attainable [130]. As a result, the industrial efficiency of both galvanic aluminum deposition and eletrolytic aluminum refinement may be improved.

Chemical and electrochemical techniques were applied to study eletrolytic aluminum deposition and dissolution in type 1 organic eletrolyte systems. Current-potential curves were determined [158] to investigate the effect of smoothing agents on aluminum electrodeposition in aluminum bromide systems. With the help of a rotating disk electrode, the smoothing effect of 17 additives was checked. With the same type of electrolyte, the cathodic current-potential curves were recorded, and the exchange current density and activation energy at 40 °C were determined [12]. This investigation showed that an acceptable conductivity can only be obtained by adding hydrogen bromide.

The most extensive research results concern the hydride electrolyte system 2 [13-16, 68, 78, 82, 92, 93, 102, 209]. With the help of Raman spectroscopic measurements, the chemical constituents of the electrolyte were determined and the electrode reactions examined with chronoamperometric methods [82]. The catalytic role of hydride and the role of neutral and ionic aluminum components were thus detected. The dependence of the polarization parameters on the electrolyte composition shows a marked maximum from which the bath composition with the highest current distribution can be determined. The influence of the temperature and the composition on the electrode process kinetics was studied by Badawy et al. [13-16]. The results of Eckert et al. [68] show a dependence of the activation energy on the electrolyte composition of the hydride baths. The first electrochemical investigation results with respect to type 3 aluminum alkyl electrolyte were obtained by Kautek et al. [100, 101] and Tabataba-Vakili [186, 187, 133].

4 Electrolytic Aluminum Deposition and Dissolution in Organoaluminum Electrolytes

4.1 Historical Review

Between 1953 and 1955, Ziegler and his coworkers developed a simple and direct synthetic route to aluminum trialkyls from aluminum, hydrogen, and the corresponding alkene [213, 231]. Aluminum trialkyls, which are Lewis acids, show a strong tendency to react with alkali metal and tetraorganoammonium halides and pseudohalides to form salt-like complex compounds of the type $M[R_3AlX]$ (M = alkali metal, tetraorganoammonium; X = halide or pseudohalide) [120, 135, 215].

Consequently, in early 1953, research on these complex compounds was initiated to determine whether they were suitable for electrolytic aluminum deposition. The first trials ended in disappointment, because the electrolytes, employed as melts, yielded useless aluminum coatings containing large portions of alkali metal. Besides, the electrolytes showed a very low conductivity compared to aqueous systems. Attempts to improve the quality of the aluminum deposits by adding excess triethylaluminum led to unexpected observations. Hence, a detailed investigation of alkali metal fluoride-aluminum trialkyl systems was necessary.

A significant result of this study was the realization that besides the already known 1:1 complex, a 1:2 complex with the formula $M[R_3Al{-}X{-}AlR_3]$ also exists [118]. A conspicuous characteristic of this new compound in contrast to the 1:1 complex is the increase in electrical conductivity of the 1:2 complex by a factor of almost two, as exemplified by sodium fluoride-triethylaluminum complex shown in Table 4. The chemical investigation produced a large selection of electrolyte baths. From the subsequent numerous electrolysis trials, a general rule was deduced according to which aluminum as a compact, uniform mass, free of alkali metal admixture, can only be deposited from systems containing excesss aluminum trialkyl or aluminum dialkyl hydride in addition to the 1:1 complex [217].

Table 4. Specific conductivity in $mS \cdot cm^{-1}$ of 1:1- and 1:2-complexes of sodium fluoride with triethylaluminum [118] at 63 °C.

Complex	Type	Specific conductivity [$mS \cdot cm^{-1}$]
$Na[Et_3AlF]$	1:1	0.2
$Na[Et_3Al{-}F{-}AlEt_3]$	1:2	10.0

These conditions are fullfilled by the 1:2 complexes. The 1:2 complex compound of sodium fluoride and triethylaluminum turns out to be especially suitable. At room temperature, this complex is already in a molten state and has a high electrical conductivity.

Fig. 1 shows one of the first electrolytically deposited aluminum coatings to be obtained from this type of electrolyte. Since electrolytic aluminum deposition from this system has no true smoothening effect, thick layers become even rougher, as illustrated by the thickly coated cathode plate shown in Fig. 1. The cathodic deposition and the anodic dissolution of aluminum corresponded to almost 100% of the amount expected according to the Faraday rule, which is an important prerequisite for even considering using this electrolysis technique for technical applications. Independently of the layer thickness, the deposited aluminum layers are found to be extraordinarily pure. Spectroscopic investigations have revealed purities of up to 99.999%. Even when relatively impure raw aluminum with purities of 99.7% functions as the anode, very pure aluminum can be deposited. Therefore, obviously not only a technique of electroplating aluminum was discovered, but also a method of electrorefining aluminum. In their publications and patents, Ziegler and Lehmkuhl [118, 217, 221] already indicated that the described electrolytes may also be mixed with aromatic solvents, i. e., toluene, which do not decompose the organic aluminum compounds, do not greatly reduce the conductivity at moderate dilutions, and bestow a more brillant luster on the aluminum layers.

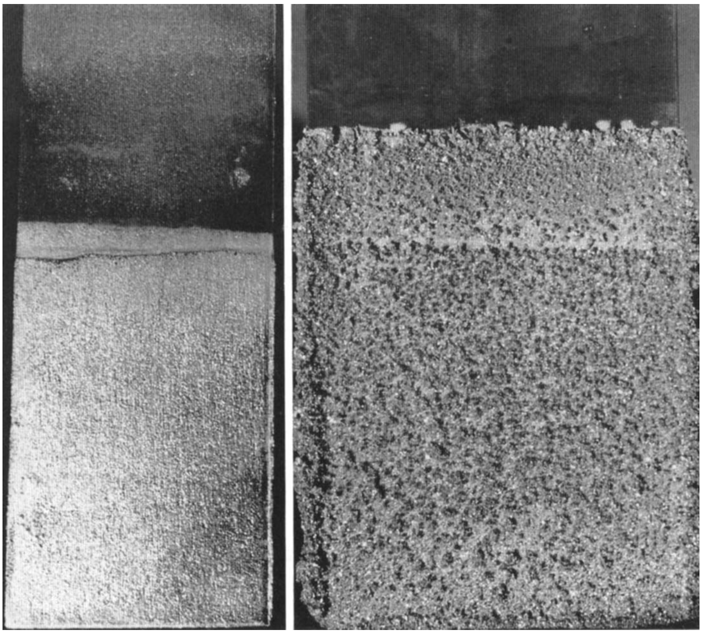

Fig. 1. From the series of first aluminum depositions from $Na[Et_3Al-F-AlEt_3]$. Left: coating for electroplating applications. Right: thick layer for refining applications.

4.2 Complex Chemical Behavior of Coordination Complexes of Alkali Metal Fluorides and Aluminum Trialkyls

Alkali metal halides reacting with aluminum trialkyls give complex compounds with four-coordinated aluminum of the type $M[R_3AlX]$. The tendency of formation of these complexes increases with the ionic volume of the alkali metal M and decreases with the ionic volume of the halogen X and the size of the alkyl group R on aluminum. Decisive factors within a series with a specific halide anion are: (1) the decrease in lattice energy from the lithium to the cesium halides, and (2) the reduction of the interaction energy between the Lewis acids R_3Al and the halide anion with increasing ionic radius (analogous to the decline of hydration energy of these ions) and with growing length of the hydrocarbon chain R in aluminum trialkyls. Lithium halides do not form any complexes with aluminum trialkyls. Trimethyl- and triethylaluminum undergo complex formation with the fluorides of Na to Cs, chlorides of K to Cs, and the bromides of only Rb and Cs. Alkali metal iodides, except for tetraalkylammonium iodides, do not form any complex compounds.

The fluorides of the alkali metals Na, K, Rb, and Cs, together with aluminum trialkyl, form two classes of complex compounds [118, 120, 135, 215, 217]. With a molar ratio of one for alkali metal/R_3Al, complexes of the type $M[R_3AlF]$ (1 : 1 complexes) result; with a molar ratio of 0.5, complexes of the type $M[R_6Al_2F]$ (1 : 2 complexes) are formed.

In the complex anion of a 1 : 1 complex, one Lewis acid R_3Al is coordinated to the Lewis base, i.e., the fluoride anion. In the complex anion of a 1 : 2 complex on the other hand, two R_3Al units are coordinated to the fluoride anion. The crystal structures of two of the 1 : 2 complexes of KF with R_3Al are known, with R = Me and Et [5, 153]. In both compounds, the fluorine atom is bound to two Al atoms, the Al–F–Al angle equals 180 °, and the Al–F bond length is 1.782 Å in the methyl complex [118] and 1.820 Å in the ethyl compound. The coordination geometry of Al in both cases is tetrahedral, see Fig. 2.

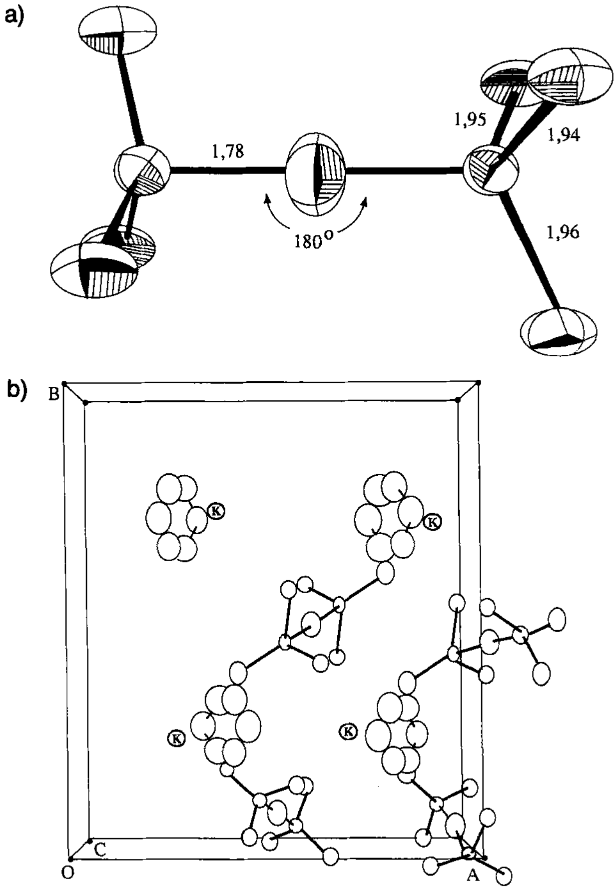

Fig. 2. Structure of $K[Me_3Al{-}F{-}AlMe_3] \cdot$ benzene [8]. (a) Molecular structure of the $[Me_3Al{-}F{-}AlMe_3]$ anion; (b) packing in crystal.

An analogous series of complex compounds is formed by aluminum trialkyls with LiH, NaH, NaCN, KH, KCN, CsCl, as well as a series with tetraorganoammonium halides [120, 135, 215, 219].

Melts or solutions of the 1 : 1 complexes of alkali metal fluorides with aluminum trialkyls show only a moderate electrolytic conductivity of $\kappa = 0.1$ to 4 mS · cm^{-1} at 100 °C. During electrolysis of these compounds, spongy cathodic deposits containing alkali metal are obtained [118, 217, 221].

The 1 : 2 complexes of the methyl or ethyl compounds show significantly higher specific conductivities. The conductivitity decreases with increasing size of the alkyl groups on aluminum. The conductivities of the Cs and K compounds are higher than those of the corresponding Na compounds [135, 215]. Based on the simple assumption that the melts of M[Et_3Al-F] (M = Na or K), contain only alkali metal cations and [Et_3Al-F]$^-$ anions and no undissociated complexes, the difference in the complex formation energy of the Na and K compounds of 23 kcal · mol^{-1} can be calculated from the difference in the lattice energies of NaF (218 kcal · mol^{-1}) and KF (195 kcal · mol^{-1}). Actually, this difference is about 13-15 kcal lower. This is due to the differing interaction between the alkali metal cation and the [Et_3Al-F]$^-$ anion. This interaction is 13-15 kcal · mol^{-1} stronger in the Na compound than in the K complex [120]. Since this effect counteracts electrolytic dissociation, the potassium fluoride complexes have significantly higher specific conductivities than analogous Na complexes. Table 5 and Fig. 3. provide a comparative survey of the specific conductivities of a variety of electrolytes.

The 1 : 2 complexes of alkali metal fluorides dissolve well in aromatic hydrocarbons, such as toluene or xylene, at least at higher temperatures.

The compounds which melt at high temperature partially crystallize upon cooling the hydrocarbon solution. Since organic Lewis bases, such as ethers or tertiary amines, in comparison to alkali metal fluorides show also a strong tendency to form

Table 5. Melting points and specific conductivities of molten organoaluminum 1 : 2 complexes of alkali metal fluorides [135].

Compound	mp. [°C]	Specific Conductivity of melt [mS · cm^{-1}]
Na[$Me_3Al-F-AlMe_3$]	~178	
Na[$Me_3Al-F-AlEt_3$]	65-68	18 (100 °C)
Na[$Et_3Al-F-AlEt_3$]	35	23 (100 °C)
K[$Me_3Al-F-AlMe_3$]	151-152	
K[$Me_3Al-F-AlEt_3$]	135-137	73 (150 °C)
K[$Me_3Al-F-Al(i Bu)_3$]	~25	8 (100 °C)
K[$Et_3Al-F-AlEt_3$]	127-129	73 (130 °C)
K[$Et_3Al-F-Al(i Bu)_3$]	liquid	
K[$(iBu)_3Al-F-Al(i Bu)_3$]	51-53	
Rb[$Et_3Al-F-AlEt_3$]	~135	

Abbreviation: Me = methyl [CH_3], Et = ethyl [C_2H_5], *i*Bu = isobutyl [$CH_2CH(CH_3)_2$].

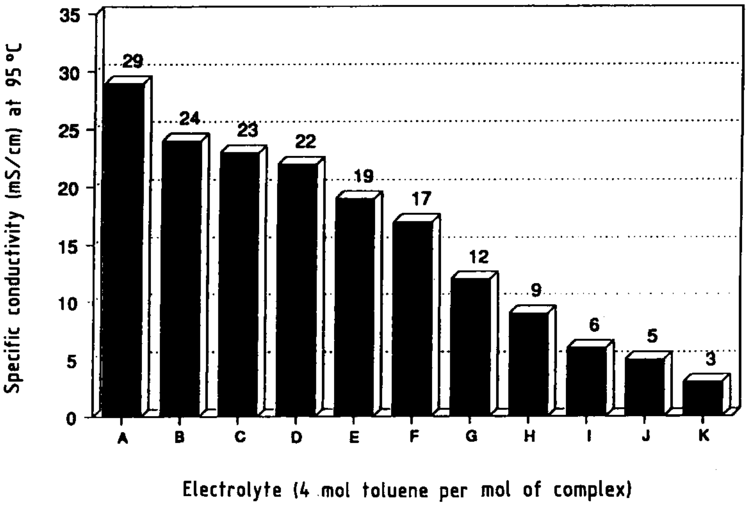

Fig. 3. Specific conductivities of organoaluminum electrolytes in toluene.
A: 0.75 KF $\cdot$ 2$AlEt_3$; 0.25 KF $\cdot$ 2$AlMe_3$; 0.3 $AlEt_3$
B: 0.75 KF $\cdot$ 2$AlEt_3$; 0.25 KF $\cdot$ 2$AlMe_3$
C: CsF $\cdot$ 2$AlEt_3$
D: KF $\cdot$ 2$AlEt_3$
E: 0.75 KF $\cdot$ 2$AlEt_3$; 0.25KF $\cdot$ 2Al$i$$Bu_3$
F: KF $\cdot$ $AlEt_3$ $\cdot$ $AlMe_3$
G: NaF $\cdot$ 2$AlEt_3$
H: KF $\cdot$ $AlMe_3$ $\cdot$ Al$i$$Bu_3$
I: KF $\cdot$ $AlEt_3$ $\cdot$ Al$i$$Bu_3$
J: 0.5 KF $\cdot$ 2$AlEt_3$; 0.5 KF $\cdot$ $AlEt_3$
K: 0.5 KF $\cdot$ $AlEt_3$ $\cdot$ $AliBu_3$; 0.5 KF $\cdot$ $AlEt_3$

complexes with aluminum trialkyls, ethers, and amines, such Lewis bases can only rarely be used as solvents. K[Et_3Al–F–$AlEt_3$] and Na[Me_3Al–F–$AlMe_3$] are stable in Et_2O, whereas Na[Me_3Al–F–$AlEt_3$] and Na[Et_3Al–F–$AlEt_3$] cleave to yield the 1 : 1 complex and $R_3Al \cdot OEt_2$. With stronger Lewis bases, i.e., trimethylamine, the complexes M[Et_3Al–F–$AlEt_3$] with M = K and Rb are cleaved giving the 1 : 1 complex, and with M = Na this results in NaF and $Et_3Al \cdot NMe_3$ [118, 120, 215].

Defined 1 : 2 complexes of alkali metal fluorides with two different alkylaluminum compounds are also known, for example Na[Me_3Al–F–$AlEt_3$], or a similar potassium complex K[Et_3Al–F–Al(iBu)$_3$] [118, 120, 135, 215, 217]. If the ratio of the two types of alkylaluminum in the 1 : 2 complex differs from 1 : 1, then a mixture of several defined complexes is present. During cooling to 20 or 0 °C, pure K[Et_3Al–F–$AlEt_3$] crystallizes out of the toluene solution of an electrolyte patented for aluminum electroplating [34] which has an overall composition of KF[1.6 $AlEt_3$ $\cdot$ 0.4 Al(iBu)$_3$]. This indicates that in such electrolytes where the aluminum components are not present in stoichiometric ratios, at least two, probably even three defined components coexist.

This is illustrated by the above mentioned case:
80 mol% K[Et_3Al–F–$AlEt_3$] together with 20 mol% K[(iBu)$_3$Al–F–Al($i$$Bu_3$)], or 60 mol% K[$Et_3Al$–F–$AlEt_3$] together with 40 mol% K[Et_3Al–F–Al(iBu)$_3$], or as a three-component system with 60–80 mol% K[Et_3Al–F–$AlEt_3$], up to 20 mol% K[(iBu)$_3$Al–F–Al(iBu)$_3$], and up to 40 mol% K[Et_3Al–F–Al(iBu)$_3$].

Defined 1 : 2 complexes with two different aluminum trialkyls in a stoichiometric ratio of 1 : 1 can be synthesized either from the individual components, i.e., alkali metal fluoride, AlR_3^1 and AlR_3^2 or by reacting the 1 : 1 complex of a particular alkylaluminum with a stoichiometric amount of a second type of alkylaluminum. Alternatively, the varying complex formation tendency of the aluminum trialkyls can be exploited by displacing one of the alkylaluminum groups of the 1 : 2 complex by a stronger complexing alkylaluminum [118], for example

$$\mathrm{Na[Et_3Al{-}F{-}AlEt_3] + 0.5\ (AlMe_3)_2 \longrightarrow Na[Me_3Al{-}F{-}AlEt_3] + 0.5\ (AlEt_3)_2} \qquad (1)$$

or

$$\mathrm{K[(\mathit{i}Bu)_3Al{-}F{-}Al(\mathit{i}Bu)_3] + 0.5\ (AlMe_3)_2 \longrightarrow K[Me_3Al{-}F{-}Al(\mathit{i}Bu)_3] + Al(\mathit{i}Bu)_3} \qquad (2)$$

The latter procedure requires the aluminum trialkyl units of the 1 : 2 complex and the noncomplexed Al_2R_6 dimer to be exchangeable and the trimethylaluminum to be more strongly coordinated to the fluoride than the corresponding ethyl or isobutyl group. Following addition of Al_2Me_6 according to Eq. (1), Al_2Et_6, not the more volatile Al_2Me_6, is distilled under vacuum while the reaction mixture is being warmed up [118, 120, 135].

Recently, Harrison et al. [85], in performing ^1H, ^{13}C, and ^{27}Al-NMR studies, observed a fast exchange between complexed and noncoordinated aluminum trialkyls in mixtures of $Na[Et_3Al{-}F{-}AlEt_3]$ and Al_2Et_6 in toluene. By performing line shape analysis of the temperature-dependent ^{13}C-NMR spectra, they determined the activation parameters of this exchange reaction. They found an activation enthalpy $\Delta H^{\#}$ of 20.4 $\mathrm{kcal \cdot mol^{-1}}$ and an activation entropy $\Delta S^{\#}$ of 18.7 $\mathrm{cal \cdot mol^{-1} \cdot K^{-1}}$ and postulated a dissociative mechanism, for the rate-determining step see Eq. (3a).

$$\mathrm{Na[Et_3Al{-}F{-}AlEt_3] \underset{k_{-1}}{\overset{k_1}{\rightleftharpoons}} Na[Et_3Al{-}F] + AlEt_3} \qquad (3a)$$

$$\mathrm{\overset{*}{A}l_2Et_6 \underset{k_{-2}}{\overset{k_2}{\rightleftharpoons}} 2\ \overset{*}{A}lEt_3} \qquad (3b)$$

$$\mathrm{Na[Et_3Al{-}F] + \overset{*}{A}lEt_3 \xrightarrow{k_{-1}} Na[Et_3Al{-}F{-}\overset{*}{A}lEt_3]} \qquad (3c)$$

k_{-1} und $k_2 \gg k_1$ (the exchanged aluminum trialkyl is marked *)

Since $Na[Et_3Al{-}F{-}AlEt_3]$, dissolved in toluene, is a good electrolytic conductor and a considerable proportion of the complex should exist as dissociated ions, an ionic exchange mechanism can be proposed (see Scheme 1).

In the course of further work, the electrochemical properties of electrolytes dissolved in toluene solutions containing not only the 1 : 2 complex, but also excess aluminum trialkyls were also investigated. These types of systems possess high limiting current densities, and high current densities can therefore be utilized without risking coprecipitation of alkali metal; however, the deposited aluminum is strongly dendritic [63, 130, 146]. It should be mentioned that in the meantime, by avoiding

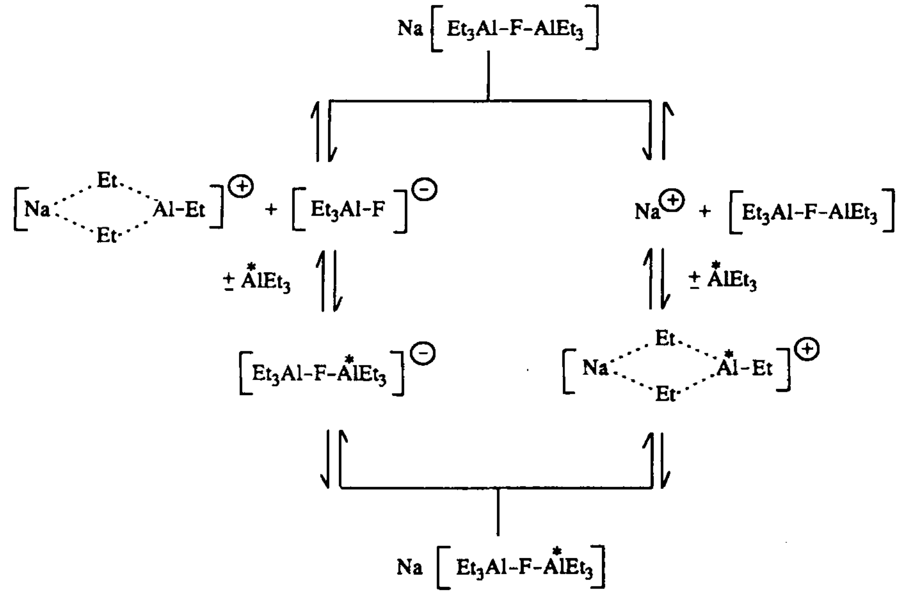

Scheme 1

the undesirable properties of such electrolytes by applying appropriate measures, the technique of depositing uniform aluminum layers has been significantly improved [128, 130].

From a chemical point of view, it is interesting to know whether these types of electrolytes contain alkali metal fluoride complexes of a higher order, like a 1 : 3 complex, or whether aluminum trialkyl in excess of the 1 : 2 composition remains uncoordinated. Hence the system NaF/m$AlEt_3$/3 toluene where m equals 1 to 4 was studied by NMR spectroscopy [181]. In the ^{1}H-NMR spectrum recorded at −10 °C, the signal of the CH_2 protons of Al_2Et_6 was shifted to negative δ-values, due to complexation of aluminum trialkyl to fluoride. At molar ratios where m equals 3 or 4, additional signals corresponding to the CH_2 protons of free Al_2Et_6 were observed in the spectra, but in the form of strongly broadened signals. This obviously results from the slower exchange of $AlEt_3$ between $Na[Et_3Al-F-AlEt_3]$ and Al_2Et_6 at 0 °C [85]. The ^{19}F spectra of the toluene solutions show signals at −183 and −172 ppm, representing the defined complexes $Na[Et_3Al-F]$ and $Na[Et_3Al-F-AlEt_3]$. At molar ratios of 2.5 to 4.0 for NaF/$AlEt_3$, the authors observed not only the signal for $Na[Et_3Al-F-AlEt_3]$ at −172 ppm, but also the appearance of a new ^{19}F-NMR signal at −166 ppm. They assigned this signal to a new, previously undescribed complex, i.e., $Na[Et_9Al_3F]$ (1 : 3 complex). Since it was already known that $Na[AlEt_3-F-AlEt_3]$ does not take up any additional aluminum trialkyl in the absence of a solvent and that it forms a two-phase liquid system with the 1 : 2 complex as a lower layer and the excess Al_2Et_6 as an upper layer [118, 120, 215, 217], the existence of such 1 : 3 complexes between NaF and triethylaluminum in toluene is doubtful.

Purchased and also self-produced distilled triethylaluminum always contains between 3 and more than 10 mol% diethylaluminum hydride if the compound is not carefully purified or prepared from crystalline $Na[AlEt_4]$ and $Et_2Al{-}Cl$, or treated with ethylene under pressure at circa 60 °C [122, 228]. It has been known for a long time that this diethylaluminum hydride has the capability to form complexes of a higher order, for instance with $Na[Et_3Al{-}F{-}AlEt_3]$ [220, 229, 230]. This suggests that in the investigation described in reference [181], the appearance of the ^{19}F-NMR signal at −166 ppm resulted from complexation of $Na[Et_3Al{-}F{-}AlEt_3]$ with diethylaluminum hydride, which was introduced with the added excess amount of aluminum triethylaluminum.

^{19}F-NMR investigation [136] (84.3 MHz; external standard: $CFCl_3$; $[D_8]$ toluene, −20 °C) verifies this claim. The ^{19}F-NMR signal of a 1.9 M toluene solution of $Na[Et_3Al{-}F]$ ($\delta = -185.3$ ppm) decreases upon addition of triethylaluminum (Et_3Al) and completely disappears when the molar ratio of both components is 1 : 1. A new signal originates at −172.1 ppm. The same signal is observed in the NMR spectra of toluene solutions of especially purified crystalline $Na[Et_3Al{-}F{-}AlEt_3]$ [118, 215, 217], supporting the assignment to the 1 : 2 complex mentioned in reference [181]. If the molar ratio of this 1 : 2 complex solution is shifted to 1 : 3 by adding further triethylaluminum, the ^{19}F-NMR spectrum does not change as long as the triethylaluminum is free of Et_2AlH. Otherwise, a ^{19}F-NMR signal of weak intensity appears at −166.6 ppm. This signal is the only signal which is observed when Et_2AlH is added to a toluene solution of $Na[Et_3Al{-}F{-}AlEt_3]$ to give a final molar ratio of 1 : 1. Thus , it can be concluded that $Na[Et_3Al{-}F{-}AlEt_3]$ forms stable complexes of a higher order with Et_2AlH, but not with $AlEt_3$.

This conclusion seems to contradict the observation that the specific conductivity of 2 to 2.5 M toluene solutions of 1 : 2 complexes or mixtures thereof, for example a final composition $KF[1.5\,AlEt_3 \cdot 0.5\,AlMe_3]$, increases upon addition on nonconducting aluminum trialkyls [39, 40, 125, 126]. Addition of 0.3 mol Et_3Al to one mole of the mentioned electrolyte, for instance, increases the specific conductivity from 24 to 29 $mS \cdot cm^{-1}$ at 100 °C (see Fig. 3). This effect, which is not observed in the melts of the 1 : 2 complex, can be restored by shifting the electrolytic dissociation equilibrium in the toluene solution towards the side where there are more ions by adding aluminum trialkyl [130], but not by formation of 1 : 3 complexes.

Oxidation of aluminum trialkyls or their complexes by oxygen yields partially or completely oxidized aluminum compounds of the type $R_nAl(OR)_{3-n}$ ($n = 2, 1, 0$) [216]. The number n is dependent on the trialkylaluminum/oxygen ratio. Likewise, the 1 : 2 complexes employed as electrolytes react with oxygen. Since the primary product, $(R_2AlOR)_m$ [119], can no longer be coordiated to $M[R_3Al{-}F]$, introduction of air and consequentially oxygen to an electrolyte yields a mixture of the 1 : 1 complex and alkoxydialkylaluminum, as illustrated in Eq. (4).

$$M[R_3Al{-}F{-}AlR_3] + 0.5\ O_2 \longrightarrow M[R_3Al{-}F] + 1/m\ (R_2AlOR)_m \qquad (4)$$

Since the 1 : 1 complexes, due to alkali metal deposition, lead to useless and partially impure aluminum coatings and show a significantly lower electrolytic conductivity than the 1 : 2 complexes, a significant increase of the concentration of the 1 : 1

complexes at the expense of the 1 : 2 complexes should be avoided. Two analytical methods are known for determining the amount of 1 : 1 and 1 : 2 complexes in a particular electrolyte, i.e., calorimetric titration [124] and an electrochemical technique [186]. If the composition with respect to both components is known, the amount of 1 : 2 complex in the electrolyte can be optimized by reacting the 1 : 1 complex with a corresponding amount of aluminum trialkyl. Loss of 1 : 2 complex as a result of increased formation of 1 : 1 complex during electrolysis may be caused by oxygen and/or water contamination or by nonquantitative dissolution of the aluminum anode. The latter can result from exceeding the particular anodic limiting current density or the presence of nondissolving metals with anodic potentials. Both of these are recognized by the evolution of gas. It is well known that during electrolysis of $Na[Et_3Al{-}F{-}AlEt_3]$ at copper anodes, quantitative equimolar amounts of ethylene and ethane are produced [118, 121, 220, 229, 230].

4.3 Electrochemical Behavior of Coordination Complexes of Alkali Metal Fluorides and Aluminum Trialkyls

The observation that only dark gray, spongy aluminum containing alkali metal is deposited by electrolysis of 1 : 1 complexes of alkali metal fluorides with aluminum trialkyls made it seem useful to try to suppress alkali metal deposition by adding aluminum trialkyls to the 1 : 1 complexes [118]. It is well known that aluminum trialkyls react easily with alkali metals, for example with sodium, to give alkali metal tetraalkyl aluminates and aluminum metal [135].

$$3\,Na + 2\,(Et_3Al)_2 \longrightarrow 3\,Na[Et_4Al] + Al \qquad (5)$$

Striking observations during the addition of aluminum trialkyls to the 1 : 1 complexes of the type $M[R_3Al{-}F]$ led to the discovery of the 1 : 2 complexes. Particularly remarkable is the great increase in the conductivity of the 1 : 1 complex melt or solution upon addition of nonconducting aluminum trialkyls [118, 135, 215, 217, 221].

Melts and solutions of these organoaluminum 1 : 2 complexes of the type $MX \cdot AlR^1_3 \cdot AlR^2_3$ or mixtures thereof were described in 1954. They were used as electrolytes for the deposition of aluminum [118, 217, 219]. In this formula, M represents an alkali metal or tetraorganoammonium ion, X stands for a halide or hydrogen, and R^1 and R^2 are alkyl groups. The complex aluminum alkyls AlR^1_3 and AlR^2_3 may be either identical or different. Small alkyl groups, such as methyl, ethyl, or butyl are recommended, because the specific conductivity of the complex decreases with increasing size of the alkyl groups without yielding any special advantages. Aromatic hydrocarbons, such as toluene, xylene, or tetralin are recommended as solvents. With increasing dilution with toluene or other solvents, the specific conductivity of the electrolyte decreases. Thus, only just enough solvent should be used to attain an optimum in conductivity, solubility, and throwing power.

An electrolyte containing less than two moles of aluminum trialkyl per mole MX is less useful for technical purposes because of a decrease in the specific conductivity and applicable current density and because of alkali metal codeposition. An aluminum trialkyl content in excess of two moles per mole of MX in toluene leads to deposition of coarser crystalline aluminum, dendritic growth [63, 130, 146], and reduced throwing power. Thus, these types of electrolytes are unsuitable for the deposition of uniform aluminum layers on workpieces with complicated shapes.

In comparison to the NaF complexes, the analogous KF complexes possess higher electrolytic conductivity [215] and higher throwing power [33, 130]. For technical purposes, the contrasting higher melting points and lower solubilities of the potassium fluoride complexes are disadvantageous. Due to the latter problem, the complex compounds often precipitate out of the solution, forming crystals as the electrolytes are cooled from operating temperatures between 90 and 100 °C to between 20 and 0 °C. This can lead to operational disturbances in the electrolytic cycle. In order to avoid this problem and still exploit the advantages of electrolytes containing potassium fluoride, solutions consisting of mixtures of several $K[R_3Al-F-AlR_3]$ complexes are recommended for technical operations [34, 129].

There are several examples:

1. 80 mol% $K[Et_3Al-F-AlEt_3]$ and 20 mol% $K[(iBu)_3Al-F-Al(iBu)_3]$ identical to $KF[1.6\,AlEt_3 \cdot 0.4\,Al(iBu)_3]$ or
2. 75 mol% $K[Et_3Al-F-AlEt_3]$ and 25 mol% $K[Me_3Al-F-AlMe_3]$ identical to $KF[1.5\,AlEt_3 \cdot 0.5\,AlMe_3]$ or
3. 50–75 mol% $K[Et_3Al-F-AlEt_3]$,
   25–12.5 mol% $K[Me_3Al-F-AlMe_3]$ and
   25–12.5 mol% $K[(iBu)_3Al-F-Al(iBu)_3]$.

In order to keep these mixtures of organoaluminum complexes in the liquid state which, during cooling to temperatures between 20 and 0 °C, remains homogeneous, at least 3–3.5 mol toluene/mol KF (limiting temperature 20 °C) or about 4 mol toluene/mol KF (limiting temperature 0 °C) are necessary. Significantly larger amounts of toluene are not recommended because of the corresponding decrease in conductivity. Other aromatic hydrocarbon solvents, such as meta-xylene or tetralin, can be used instead of toluene.

The specific conductivity of solutions with the same concentration decreases in the sequence toluene > meta-xylene > cumene > diphenylmethane > *p*-isopropylmethylbenzene > tetralin [242]. The decrease in conductivity in high-boiling hydrocarbons can be partially compensated for by increasing the temperature from 95 to around 130 °C [129, 130].

The behavior of the 1 : 2 complexes of alkali metal and tetraalkylammonium halides MX (MX = NaF, KF, KCl, $(CH_3)_4NCl$)) with triethylaluminum in various solvents was studied in detail [106]. As solvents, benzene, toluene, ethylbenzene, m-xylene (L^1), and high-boiling ethers (L^2) anisole, dipropylether, diisopropylether, dibutylether, tetrahydrofuran or 3 : 1 volume mixtures of L^1 and L^2 were utilized. The corresponding electrolyte containing 1.44 mol complex per 1 mol solvent was investigated with respect to its electroplating properties (solubility, specific conductivity, throwing power, current density loading capacity, and cathodic current yield). At 85 °C, the specific conductivity of $K[Et_3Al{-}F{-}AlEt_3]$ drops from 35 (extrapolated) to 15 mS/cm with increasing alkyl substitution on the aromatic hydrocarbon in the series benzene > toluene > ethylbenzene > xylene, without a significant improvement in solubility up to the operational temperature. In general, the specific conductivies of the studied complexes are lower in ethers and decrease in the sequence anisole > diisopropylether > THF > dipropylether equals dibutylether from 21 to 7 mS/cm.

In contrast to 1 : 1 complexes, electrolytes consisting of defined 1 : 2 complexes or mixtures thereof yield uniform, light gray, compact, and alkali metal-free aluminum layers [34, 118, 217, 221]. Exceptions seem to be those 1 : 2 complexes in which the larger portion of aluminum trialkyl is present as triisobutylaluminum. An example is $K[(iBu)_3Al{-}F{-}Al(iBu)_3]$ which, at a current density of only 0.4 A/dm^2, affords gray, potassium-containing deposits. Similarly, $K[Me_3Al{-}F{-}Al(iBu)_3]$ shows the same behavior at a higher current density. This does not apply to electrolytes containing a small portion of triisobutylaluminum, for example the electrolyte with the composition:

$KF \cdot 1.6\,AlEt_3 \cdot 0.4\,Al(iBu)_3 \cdot 3.4$ toluene [34]

The following systems have as yet been utilized for electroplating on the technical scale and are listed in chronological order:

$NaF \cdot 2\,AlEt_3 \cdot 3.4$ toluene (El I of Sigal® Process),

$KF \cdot 1.5\,AlEt_3 \cdot 0{,}5\,Al(iBu)_3 \cdot 4$ toluene (El II) and

$KF \cdot 1.5\,AlEt_3 \cdot 0.5\,AlMe_3 \cdot 4$ toluene (El III)

When aluminum is utilized as an anode, the metal dissolves during electrolysis. Based on the amount of cathodically deposited aluminum and anodically dissolved aluminum, the current yields, not withstanding a few exceptions, are quantitative [118, 186, 221]. Consequently, during electrolysis only aluminum metal is transported from the anode to the cathode. Apparent deviations from the Faraday rule with regard to aluminum deposition and dissolution actually result from alkali metal codeposition on the cathodic side with the particular electrolytes mentioned above, or in some cases from side reactions on the anodic side, which can be recognized by gas evolution at the anode.

With a melt of $K[(iBu)_3Al{-}F{-}Al(iBu)_3]$ and a current density of 0.4 A/dm^2, the weight loss of the anode was only 15% of the value calculated from the amount of current. With toluene-free melts of $Na[Et_3Al{-}F{-}AlEt_3]$, the anodic current yields are quantitative. The current yields, however, decrease upon addition of toluene. If 0.2 or 0.8 mol toluene per mole of complex is added, the anodic current yield sinks to about 70%, even with an anode consisting of refined Al (99.99% Al). Reducing the current density by half brings about no change either. A similar reduction of the anodic current yield to 80–90% is observed in toluene solutions of Na–K complex mixtures [130]. In contrast, both the melts and the solutions of ethyl-rich electrolytes containing only potassium as the cation, such as El II [186], El III, or $K[Et_3Al-F-AlMe_3]$, attain quantitative anodic current yields. The anodic current yield reduction, which is accompanied by gas evolution at the anode, is especially strong in the case of poor quality anodes and electrolytes containing a large amount of diethylaluminum hydride [130].

If the aluminum anode is replaced by one consisting of Na [226] or K [222] in the form of an amalgam, Zn, Cd, Hg [228], Ga, In, Tl [63, 196, 197, 228], Sn [228], Pb [118, 123, 212, 223, 225], Sb, Bi, Te [228], the metal will dissolve as an alkyl compound. Similarly, Mg anodes [225, 228] dissolve as a result of anodic oxidation. Fluoride-containing 1 : 2 complexes, on the other hand, coat the Mg-anode in a short while with an insulating layer of MgF_2. The metals, i.e., Zn, Cd, Ga, In, Tl, Bi, and Te, are practically quantitatively deposited at the cathode during electrolysis of this type in undivided cells. Thus, this technique can be used for the refinement of these metals [63, 196, 197]. Hg and Pb metal are partially deposited on aluminum. Anodes made of Si [228], Ge [63], or transition metals [118] are insoluble. Organoaluminum complex compounds are electrolytically destroyed at these anodes [229, 230]. In the most extensively studied system, i.e., $Na[Et_3Al-F-AlEt_3]$, about equimolar amounts of ethane and ethylene are liberated by the Al-bound ethyl groups at Cu anodes [118]. With electrolytes contaminated with diethylaluminum hydride during synthesis or purposely charged with Et_2AlH, hydrogen will form preferentially at Cu, Ag or brass anodes.

Based on this observation, pure aluminum is obtained by a two-step refinement technique whereby electrolysis is performed with an insoluble anode, i.e. Cu [229, 230].

$$(Et_3Al)_2 + 1.5\,H_2 + Al \xrightarrow{100-150\,°C;\ 50-200\ \text{bar}\ H_2} (Et_2AlH)_3 \tag{6a}$$

$$(Et_2AlH)_3 \xrightarrow{\text{electrolysis}} (Et_3Al)_2 + 1.5\,H_2 + Al \tag{6b}$$

An advantage of this method is that the impurities of a soluble aluminum anode are not included in the refined product. The chemical step (6a), in which the aluminum to be refined is converted to diethylaluminum hydride by reaction with triethylaluminum and hydrogen, is chemoselective for Al. The resulting diethylaluminum hydride is separated by distillation from the aluminum impurities, which remain unreacted.

With anodes derived from Au, Pd, Pt, Ni, Fe, or graphite, anodic production of hydrogen from Et_2AlH-containing electrolytes is minor [229, 230]. Besides small amounts of H_2, ethane and ethylene also evolve as a result of oxidation of the ethyl groups, and butane arises from the coupling of two ethyl groups. The ratio of ethane/ethylene is not equimolar, due to hydrogenation of ethylene to ethane by anodically formed hydrogen.

During electrolysis of the 1:2 complex of KF with trimethylaluminum, i.e., $K[Me_3Al-F-AlMe_3]$, ethane forms as a result of coupling of two methyl groups; also methane and a small amount of propane originate at a Cu anode (170 °C). The ratio of the three gases is dependent on the anode metal and the current density. With Cu, the decomposition voltage of the methyl complex was determined to be 0.77 V. Electrolysis of $Na[Pr_3Al-F-AlPr_3]$ at 100 °C between Cu electrodes yields an equimolar mixture of propane and propene plus *n*-hexane (47/51/2 at 1 A/dm^2). The $Na[Et_3Al-F-AlPr_3]$ complex upon electrolysis yields 70 mol% C_2- and 25 mol% C_3-hydrocarbons, as well as some butane and hexane at the Cu anode. This indicates that the ethyl groups are more easily anodically oxidized than the propyl groups. This conclusion is supported by the observed decomposition voltages for $Na[Et_3Al-F-AlEt_3]$ and $Na[Pr_3Al-F-AlPr_3]$ at copper electrodes at 100 °C and 0.32 and 0.62 V, respectively. Including $Na[Bu_3Al-F-AlBu_3]$ (0.35 V) and $K[Me_3Al-F-AlMe_3]$ (0.77 V) into the comparison demonstrates that the decomposition voltages for complexes with an uneven number of carbon atoms in the alkyl groups are higher than for those with an even number [229].

Defined 1:2 complexes and their mixtures are soluble in aromatic hydrocarbons. In some cases, the specific conductivity actually increases with moderate dilution. The specific conductivity of $[BuNEt_3][Et_3Al-I-AlEt_3]$, at 80 °C, for instance, increases from 10 mS · cm^{-1} for the melt to 15.5 mS · cm^{-1} for a 50% toluene solution. The conductivity of alkali metal fluoride complexes, slowly diminishes with increasing toluene addition. A similar effect is shown by xylene, but the decrease in conductivity upon dilution is more rapid. However, it has been shown that a moderate addition of toluene or xylene (molar ratio circa 1:1 to 1:4) is favorable for the appearance and maximum obtainable thickness of a homogenous aluminum layer [118, 217, 229]. Furthermore, the electrolytes become easier to handle, upon addition of toluene or xylene, due to a reduction in the spontaneous inflammability and the capability of the electrolytes to crystallize. The solubility between 0 and 20 °C of 1:2 complexes with low melting points is generally quite acceptable. 1:2 complexes with melting points above ca. 100 °C require higher temperatures to achieve sufficiently high solubility. For example, mixtures of complexes with high melting points, such as $K[Et_3Al-F-AlEt_3]$ or $Cs[Et_3Al-F-AlEt_3]$, with toluene or xylene (molar ratio 1:4) are maintained as homogeneous liquids at electrolysis temperatures of 90–100 °C. However, upon cooling, the corresponding organoaluminum complexes partially crystallize out of solution. To avoid crystallization, electrolytes consisting of several 1:2 complexes can be employed instead of a single defined complex. [34, 217].

The specific conductivities of 1:2 complex melts increase with decreasing size of the alkyl groups, and they are higher for K and Cs compounds than for sodium complexes with the same alkyl groups [215].

The starting materials for the synthesis of complexing aluminum trialkyls are easily accessible. Triethylaluminum and triisobutylaluminum are produced in large amounts from the corresponding olefin, aluminum, and hydrogen [213, 231]. Trimethylaluminum is also technically prepared from aluminum and methyl chloride [135]. In preparing appropriate electrolytes for the extraction of aluminum (refinement or plating), the quality of the alkali metal fluoride used is significant. Because high purity alkali metal fluorides are expensive, the reaction of crystallizable alkali metal tetraalkylaluminate with distillable dialkylaluminum fluoride, obtained from dialkylaluminumchloride and NaF [214], provides an attractive alternative route to 1:2 complexes:

$$4\ M[R_4Al] + (R_2AlF)_4 \longrightarrow 4\ M[R_3Al-F-AlR_3] \qquad (7)$$

4.4 The Refining Effect

In organometallic compounds, the metal atom is directly attached to a carbon atom of the organic group. Compounds featuring carbon bonds to almost any stable element of the periodic table, with the exception of the noble gases, are known. For a fundamental understanding of aluminum refinement from organoaluminum-containing electrolytes, it is necessary to recognize that the thermodynamic and especially the kinetic stability of these organo-element bonds are quite variable. This is especially true of many homoleptic, i.e., peralkylated transition metal compounds R_nM, in which the alkyl-metal interaction often lacks stability. This leads to disintegration reactions, such as α-H, β-H, or reductive elimination, as well as homolytic bond breaking. The homoleptic alkyl-main group metal compounds differ from the transition metal compounds in that the stability of the alkyl-metal interaction is generally higher. These varying kinetic and thermodynamic bond stabilities are certainly the basis for the refining effect between the purity of the dissolved aluminum anode and cathodically deposited aluminum. It was determined early that the refinement effect must be significant, a result obtained by comparative corrosion investigations of aluminum samples from different sources and with varying purities [118, 221]. Comparison with, at that time very precious samples, i.e., "5-niner aluminum", indicated comparable purity; quantitative analysis was not possible at the time, due to the lack of appropriate analytical methods. Later, investigations by Dötzer [63] showed that this refining process led to higher purity grades than expected on the basis of homoleptic metal alkyl bond stabilities. During refining electrolysis with anodes of raw aluminum in $Na[Et_3Al{-}F{-}AlEt_3]$ melts, it was noted that the sludge of the aluminum anode contained not only the transition metals Ti, Zr, V, Cr, Mo, Mn, Fe, Co, Ni, Cu, and Ag, but there was also an enrichment of the anode with the contaminating metals Mg, Ga, In, Zn, Pb, Sn, Sb, and Si [63], even though the homoleptic ethyl compounds of the latter elements are sufficiently stable. In contrast, if the elements Ga, In, Zn, Pb, Sn, Sb, Mg are used in pure form as anodes, they dissolve in the organoaluminum electrolyte as a result of anodic oxidation [63, 118, 121, 135, 196, 197, 212, 223, 225, 228]. However, Si or Ge anodes do not dissolve, even though the ethyl compounds of these metals are sufficiently stable. Dötzer concluded that the pure organometallic refinement effect is superimposed by the electrochemical purification process [63], thus making the refining of aluminum even more effective.

By using an anodic plate of technically pure aluminum (Al = 99.99%), metal with a residual content of impurities <5 ppm and a residual resistance ratio RR of 8.000–20.000 can be obtained after electrolytical refining in $Na[Et_3Al{-}F{-}AlEt_3] \cdot 1$ toluene at 100 °C and 0.35 A/dm². $RR = \frac{\rho_{293\,K}}{\rho_{4\,K}}$, ρ being the specific resistance of the metal at the temperature K. Subsequent zone melting makes it possible to reduce the level of impurities to <0.1 ppm and to achieve a residual resistance ratio of 100.000 [84, 107, 142, 185].

Combinations of the three process steps i.e., three-layer electrolysis, organoaluminum electrolysis, and zone melting can lead to aluminum with a nominal purity of >99.9999. Refinement with organoaluminum electrolytes was up until now conducted in a $Na[Et_3Al-F-AlEt_3] \cdot 1$ toluene systems at a low current density [142]. We have not been able to confirm reports suggesting that the densest aluminum deposits are only obtained with molar NaF to $AlEt_3$ ratios between 1:1.5 and 1:1.25. This is obviously also recognized by the authors who currently utilize a refining electrolyte with a molar $NaF/AlEt_3$ ratio of 1:2 [84]. Today, electrolyte systems are being tested which allow the application of a 10 times higher current density; these systems are derived from toluene or xylene solutions of mixtures of the complex compounds $K[Et_3Al-F-AlEt_3]$ with $K[(iBu)_3Al-F-Al(iBu_3)]$ and/or $K[Me_3Al-F-AlMe_3]$, as well as trialkylaluminum etherate in defined mixture ratios. Dibasic ethers of the glyme type are favored as complexing partners for aluminum trialkyls [128].

^{27}Al, ^{1}H, and ^{13}C-NMR investigations have shown that in the complex between $AlEt_3$ and $MeOCH_2CH_2OMe$ (molar ratio 1:1), the four-coordinated aluminum atom is bound to only one oxygen atom of the dibasic ether. The individual oxygen atoms are in a rapid equilibrium between the coordinated and the noncoordinated state [19].

The results of studies of such new refining electrolytes [128, 130], together with the analysis of the contamination of the aluminum raffinate by the GDMS method, reveal the following trends [132]:

1. If freshly prepared electrolytes are used, the impurities which originate from the chemicals of the electrolytes diminish with increasing electrolysis time. The quality of the used potassium fluoride determines the amount of impurities. With increasing electrolysis time, the presence of following contaminants in the raffinate diminishes: Si, Fe, Cu, Pb, K, Na.
2. During electrolysis, the content of the following metals in the cathodic deposit decreases with respect to their level in the anode metal: Si, Mn, Na, P, U from 24 to 7 ppb, Th from 51 to 11 ppb, and Sc from 43 to 9 ppb. The content of Cr remains almost constant compared to the anode. Ti increases slightly from 15 to 30 ppb. With a higher Ti content in the anode (115 ppb), a clear refinement effect is observed (24 ppb).
3. Doubling the current density from 1.4 to 2.8 A/dm^2 causes a loss in refinement for Mn (13 to 44 ppb), P (113 to 231 ppb), and Th (8 to 11 ppb). The residual resistance ratio RR sinks from 14.112 to 11.890.
4. The purity of aluminum raffinate obtained from organoaluminum electrolytes amounts to 99.9998% with respect to determinable contamination.

If cathode plates of titanium or certain titanium alloys are used, several mm thick aluminum layers can be peeled off without any difficulty (Fig. 4).

According to earlier radiochemical investigations by Spang and Cerny [63], the refining effect should be dependent upon the voltage, which is why a minimum cell voltage is recommended. Depending on the content of certain foreign metals in aluminum raffinate obtained from $Na[Et_3Al-F-AlEt_3]$ electrolytes between 0.2 and 2.3 A/dm^2, only a slight decrease in the refinement effect is observed with increasing current density. This was reported by Dötzer [63] and also by our own group [132], who used the electrolytes described in reference [128] at 0.35 to 3.0 A/dm^2.

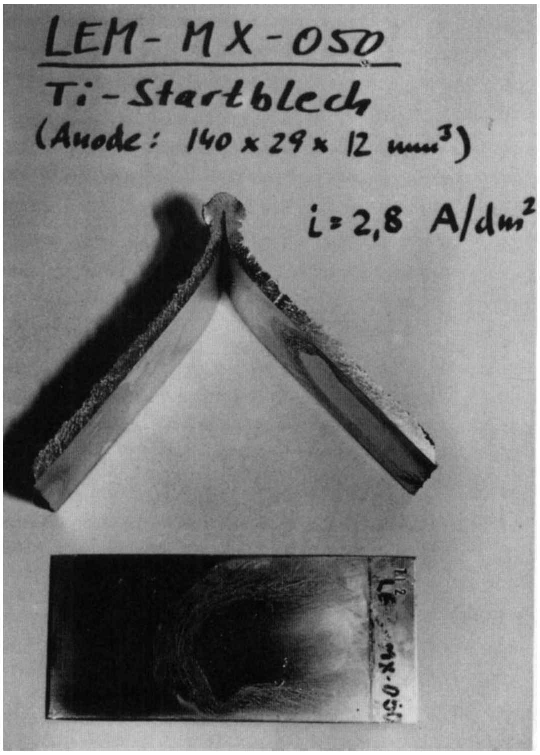

Fig. 4. An aluminum deposit removed from a titanium cathode [130, 132].

4.5 Electrochemical Investigations

Electrochemical studies to investigate the deposition and dissolution of aluminum in organoaluminum electrolytes were predominately carried out with the technical electrolytes used in the Sigal® Process at the electroplating plant of the SEDEC company (Berlin), i.e. El II ($KF \cdot 1.5 AlEt_3 \cdot 0.5 Al(iBu)_3 \cdot 4$ toluene) and El III ($KF \cdot 1.5 AlEt_3 \cdot 0.5 AlMe_3 \cdot 4$ toluene). The 1:2 complexes of NaF or KF with triethylaluminum were included for comparison. El II and El III were also modified by addition of aluminum trialkyls, see Table 6, especially systems S3 and S6. Table 6 lists several electrolytes of the same type as El II, but each treated in a different manner. A and T were originally identical, but A was used for a long time in the electroplating plant, while T was stored in a supply tank. A and T differ from one another mainly in their concentration of 1:2 and 1:1 complexes. It is obvious that during plating operations electrolyte A loses some of the 1:2 complex through hydrolysis and oxidation by water and oxygen, which are introduced into the system by the workpieces to be coated. H is a freshly delivered El II electrolyte and AR is the already used electrolyte A, regenerated by adding aluminum trialkyls. The S3 and

Table 6. Various electrolytes, studied electrochemically.

Electrolyte composition	System Symbol	Complex		AlR_3	κ	Toluene
		1 : 2	1 : 1		(mS · cm^{-1})	
		(mmol/g)		(mmol/g)	(100 °C)	(mmol/g)
KF · [$1.5Al(C_2H_5)_3$ $0.5Al(i\text{-}C_4H_9)_3$] + toluene	A	1.33	0.22	0	15.55	5.76
	El II T	1.37	0.09	0	22.2	5.76
	H	1.47	–	0	23.6	5.76
	AR	1.47	0	0	18.7	5.76
KF · [$0.5Al(CH_3)_3$ $1.5Al(C_2H_5)_3$ + toluene	El III	1.36	–	0	21.1	6.95
KF · [$1.5Al(C_2H_5)_3$ $0.5Al(i\text{-}C_4H_9)_3$] + $0.5Al(i\text{-}C_4H_9)_3$ + toluene [130]	S3	1.25	0	0.55	16.8	5.2
KF · [$0.5Al(CH_3)_3$ $1.5Al(C_2H_5)_3$] + $0.5Al(C_2H_5)_3$ + toluene [130]	V1	1.31	0	0.63	19.65	6.3
	S6 V2	1.02	0	0.46	16	7.4
	V3	0.73	0	0.32	11	8.4
NaF · $2Al(C_2H_5)_3$ + toluene		1.33	0.17	0	14	6.7

S6 electrolytes were prepared by adding triisobutylaluminum and triethylaluminum to El II and El III, respectively. The S6 electrolyte was diluted to the volume V1, V2, and V3, respectively (see Table 6) [133, 186, 187].

The amount of 1 : 1 and 1 : 2 complexes within the electrolyte may be determined by calorimetric titration [124]. Experimental details of the electrochemical measurements are found in references [186] and [187]. Cathodic and anodic current yields in excess of 99% for El II/T are listed in reference [186], while we determined those of El III [131].

4.5.1 Potentiodynamic Sweep of the Cathodic and Anodic Current-Potential Curves

Fig. 5 gives a general overview over the measured potentiodynamic part of the cathodic current-potential curve $\left(\frac{dU}{dt} = 5\ mV/s\right)$. The numbers mark regions of the current-potential curve in which there are characteristic changes in the appearance of the sample surface, noted by optical observation. In the region (1), the deposited aluminum layer shows a metallic luster. At the start of region (2), the edge of the metal deposit begins to change color to gray, and in region (4) the entire deposit is completely black. During the backsweep from (5) to (7), a continuous lightening process occurs, whereby at (7) the surface of the deposit again obtains a

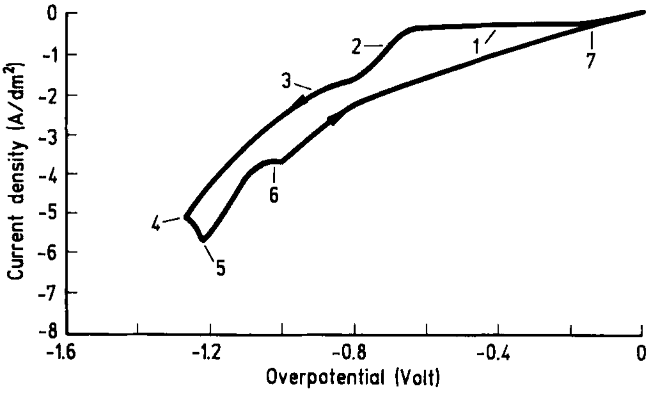

Fig. 5. Potentiodynamic cathodic current-potential curve for El II/T [186, 187], which provides a general overview over the aluminum deposition process over a wide current density range.

metallic luster. The darkening is due to coprecipitation of potassium [133, 186, 187]. The dark deposit becomes brighter as the electrode reaches (7), and it is allowed to remain in the electrolytes in the absence of a current. The observed hysteresis of the potentiodynamic current-potential curve is evidence of a very rough electrode surface.

The anodic portion of the potentiodynamic electrode curve shown in Fig. 6 likewise exhibits a special effect, i.e., the development of a current density maximum. This type of curve resembles those of metals that can be passivated. The cause of the current density maximum is examined in greater detail in Sec. 4.5.6.

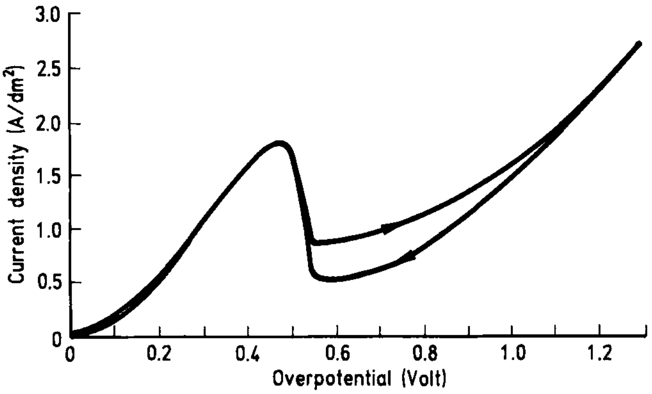

Fig. 6. The anodic portion of the potentiodynamic current-potential curve for El II/A (400 rpm) [186, 187], exhibiting a characteristic current density maximum.

4.5.2 Galvanodynamic Sweep of the Cathodic Current-Potential Curves

Preliminary potentiodynamic investigations have shown that aluminum deposition depends on stirring conditions, thus indicating mass transfer dependence of the aluminum deposition process. Fig. 7 shows that increasing stirring speeds enhance aluminum deposition rates in the studied voltage range. Thus, for practical electrolytic aluminum deposition, it is necessary to provide sufficient electrolyte motion close to the workpiece during coating at all applied current densities. With increasing negative cathodic potentials, the curves begin to reach somewhat of a limiting current density region. Through intensive stirring, this limiting cathodic current density region can be significantly raised. Cathodic current potential curves shown in Fig. 7 were obtained by changing the current density at a constant scan rate of 2.3 $A/dm^2 \cdot s$ and using different rotating electrode disk speeds. The limiting current density is obtained quite easily by galvanodynamic measurement. At this characteristic current density, the corresponding voltage signal sweeps quickly to very negative electrode potentials without too much interference from electrode roughening. It is well known that close to or at the limiting current density, metal deposits roughen very much, which makes it difficult to determine the true limiting current.

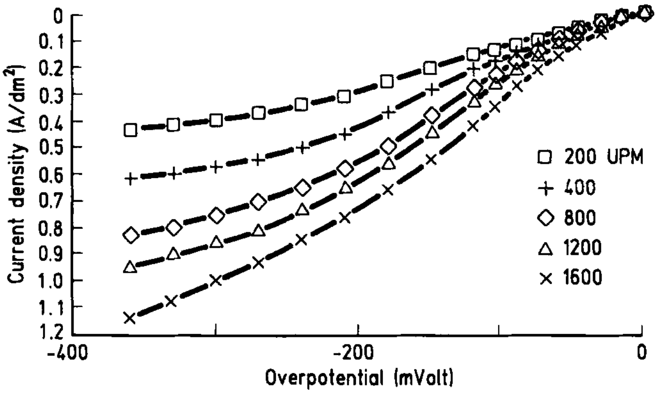

Fig. 7. Galvanodynamic cathodic current-potential curves at different rotation speeds of the disk electrode. These curves were used to study the influence of mass transfer on aluminum deposition. (EL II/A; 100 °C; scan rate: 2.3 $A/dm^2 \cdot s$).

Stationary Cathodic Current-Potential Curves

The limiting current density, obtained by galvanodynamic measurements, depends on the sweep rate. As a result, the limiting cathodic current density (maximum of deposition rate) -current sweep rate curve goes through a minimum. If the speed of the sweep is too slow, the cathode deposits roughen, whereas the stationary state is not reached if the sweep speed is too high. Therefore, the minimum current density-sweep rate curve was chosen as the true cathodic limiting current density at

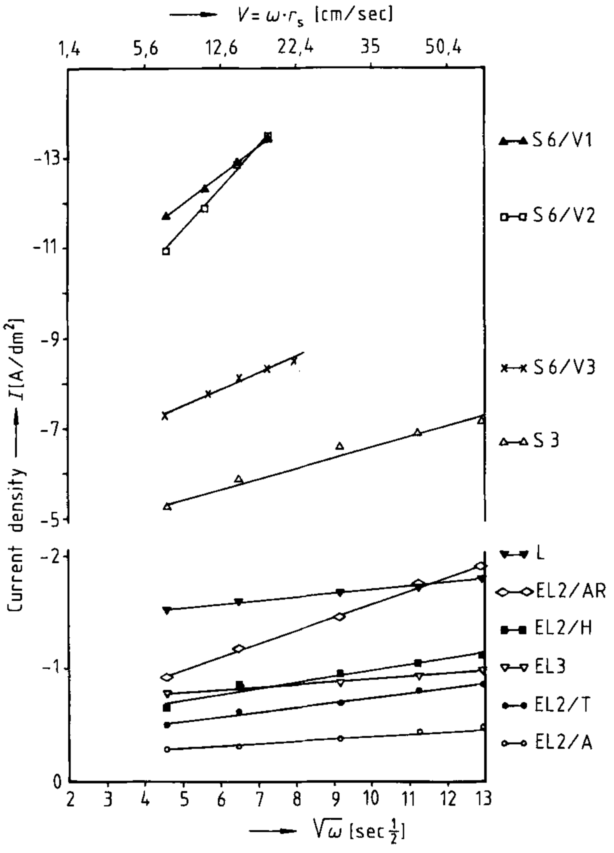

Fig. 8. Dependence of the cathodic limiting current density on the angular velocity of the rotating disk for different alkylaluminum electrolytes (100 °C; $\eta = -0.8\,V$) [186, 187].

given stirring conditions. This limiting current density value, plotted against the square root of the rotation speed of the disk electrode, gives straight lines which differ in terms of inclination and position for different electrolyte systems (Fig. 8).

However, the straight lines do not intersect with the zero point for $\sqrt{\omega} \rightarrow 0$, thus indicating that the measured "limiting" cathodic current density values are not diffusion-controlled limiting current densities according to the Levich-equation [138]. The deviation of pure diffusion control may be an indication of additional electrochemical or chemical hindrance [18, 95]. A steeper inclination of the slope indicates stronger diffusion control.

Two groups of electrolytes are shown in Fig. 8.

The electrolyte systems El I, II, and III resemble one another and show relatively low cathodic limiting current densities. The cathodic limiting current densities of the various El II electrolytes clearly ascend with increasing value of the 1 : 2/1 : 1 complex ratio, as related to electrolyte prehandling. The cathodic limiting current densities are five to ten times higher for electrolytes containing noncoordinated aluminum trialkyls in addition to the 1:2 complexes of alkali metal fluorides and aluminum trialkyls, i.e., S3 and S6. These electrolytes are unsuitable for technical use, due to their low throwing power and the tendency of the cathodically deposited aluminum to show dendritic growth. [130].

4.5.3 Determination of Characteristic Data for the Cathodic Charge-Transfer Reaction in Dependence of the Temperature

Current-potential curves depend on the stirring conditions in the investigated potential range. It was thus assumed that the aluminum deposition rate is determined by convective diffusion as well as by discharging.

By measuring the current density as a function of the angular frequency of rotation ω, the rate of the electrode reaction can be estimated by eliminating the influence of mass transfer by extrapolation of $\omega \to \infty$. According to Jahn and Vielstich [95], we may write:

$$\frac{1}{I} = \frac{1}{I_D} + \frac{1}{I_D} \cdot K \cdot \frac{1}{\sqrt{\omega}} \tag{8}$$

in which I_D is the pure charge transfer current density for a given overpotential, K is a constant, and the remaining parameters have already been defined. By plotting

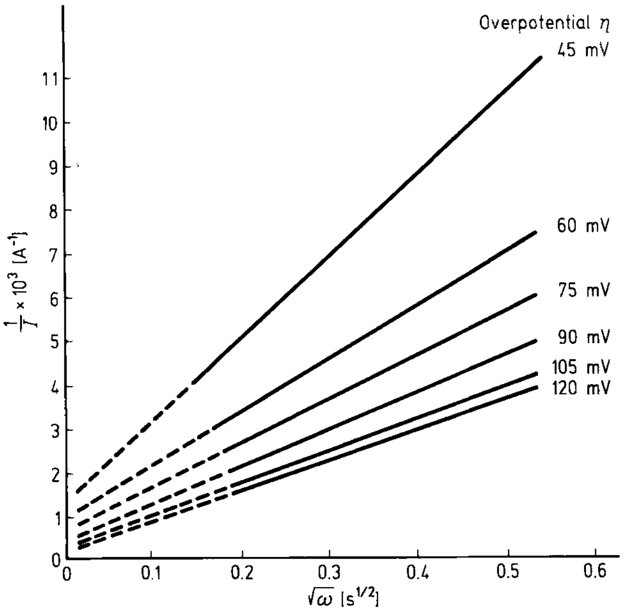

Fig. 9. Evaluation of a charge tranfer-current density plot, according to [95]. (EL II/T; 100 °C, electrode area: $3.848 \cdot 10^{-3}$ dm^2).

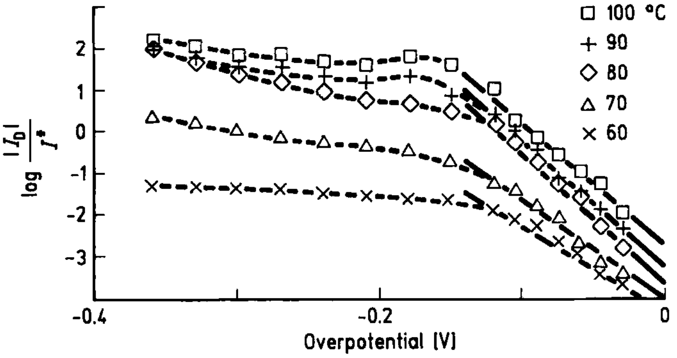

Fig. 10. Tafel plots for aluminum deposition at various temperatures (EL II/T) [186].

$\frac{1}{I}$ against $1/\sqrt{\omega}$, I_D can be determined from the y-intercept for a particular electrode potential.

Fig. 9 gives an example of how to determine the charge transfer current density. The plotted lines were evaluated according to the least squares method. The data were taken from the stationary potentiostatic current-potential curves at five different rotating electrode disk speeds.

In this manner, the assembly of current-potential curves shown in Fig. 10 were produced as a function of the electrolyte temperature of the electrolyte EL II/T. The electrode curves plotted on a semilogarithmic scale yield straight lines from 0 to about -0.12 V.

The Tafel coefficients are listed in Table 7. In the Tafel region, the coefficient ranges between 0.033 and 0.044 V over the investigated temperature range. As shown in Table 8, the exchange current density I_0 were determined from the Tafel slope by extrapolation to a value of $\eta = 0$. For the electrolyte systems, EL II/T and $KF \cdot 2AlEt_3 \cdot 4$ toluene, the exchange current densities I_0 at 100 °C were found to have similar values at 0.04 A/dm^2 [101, 186]. The plot of log $|I_0|$ against $1/T$ gives

Table 7. Tafel coefficients as a function of the temperature of aluminum deposition from alkylaluminum electrolyte (EL II/T).

Temp. (°C)	Tafel region b (V)
60	0.044
70	0.040
80	0.030
90	0.032
100	0.033

Table 8. Variation of the exchange current density for alkylaluminum electrolyte at various temperatures (EL II/T).

Temp. (°C)	$1/T$ [K^{-1}]	I_0 [A/dm^2]	$\log \frac{\lvert I_0 \rvert}{I^{1)}}$
60	3.00×10^{-3}	0.009	-2.046
70	2.92×10^{-3}	0.013	-1.886
80	2.83×10^{-3}	0.017	-1.769
90	2.76×10^{-3}	0.026	-1.585
100	2.68×10^{-3}	0.044	-1.357

($I^{1)} = 1$ A/dm^2)

a straight line, (Fig. 11) satisfying the Arrhenius equation. The activation energy of the cathodic process is computed from the slope of the line, according to Eq. (9).

$$\frac{\delta \log \lvert I_0 \rvert}{\delta (1/T)} = -\frac{E_a}{2.303 \cdot R} \tag{9}$$

The calculated value for the activation energy E_a at an overpotential of $\eta = 0$ is 39.9 ± 2.4 kJ/mol.

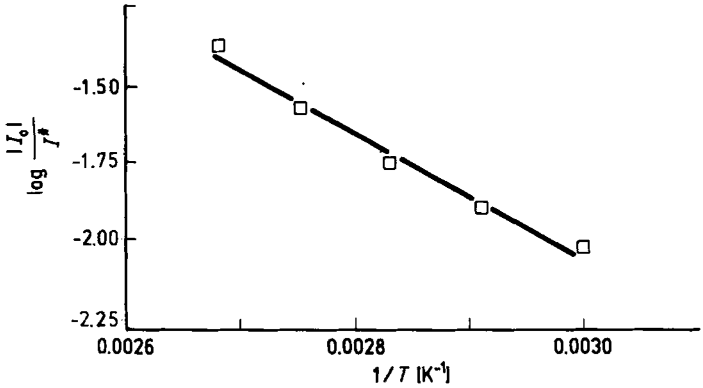

Fig. 11. Log of the exchange current density for aluminum deposition from alkylaluminum electrolytes as a function of $1/T$ (EL II/T) [186].

4.5.4 Dependence of the Potentiodynamic Anodic Curve on the Concentration of the 1:1 Complex

Based on previous experience, an optimized electrolyte system for aluminum plating on a technical scale should, if possible, only contain 1:2 complexes of the type $KF \cdot 2AlR_3$, where R may stand for ethyl and isobutyl and/or methyl groups, which are present in certain ratios [34, 129, 217]. As a solvent, toluene has proven successful, and its concentration should be 2 to 4 mol per mole of KF complex. As a result of water or oxygen contamination, the 1 : 2 complex will decompose to form the 1 : 1 complex. Eqs. (10) and (11) outline the chemistry of this decomposition reaction.

$$MF\cdot 2AlR_3 \xrightarrow{+H_2O} M[R_3AlF] + \frac{1}{n}\,\text{-}[RAlO]_{\overline{n}} + 2RH \tag{10}$$

$$MF\cdot 2AlR_3 \xrightarrow[+\frac{1}{2}O_2]{} M[R_3AlF] + R_2AlOR \tag{11}$$

Conversion of the 1 : 2 complex to the 1 : 1 complex by oxygen or water results also in the production of undesired decomposition products, reducing the specific conductivity, cathodic limiting current density, and throwing power, and thus reducing the coating quality.

The presence of the 1 : 1 complex in the electrolyte can be recognized from the shape of the potentiodynamic recorded anodic electrode curve. An El II electrolyte free of 1 : 1 complex gives rise to the anodic curve (b) exhibited in Fig. 12. After addition of the 1 : 1 complex, a curve (a) with a current density maximum develops. The peak height of this maximum depends on the rotating speed of the anode and increases with rising concentration of the 1 : 1 complex. The value of the current maximum I_{peak} is linearly dependent on $\sqrt{\omega}$, as well as on the concentration of the 1 : 1 complex. This concentration dependence can be used to determine the amount of 1 : 1 complex in the electrolyte [186].

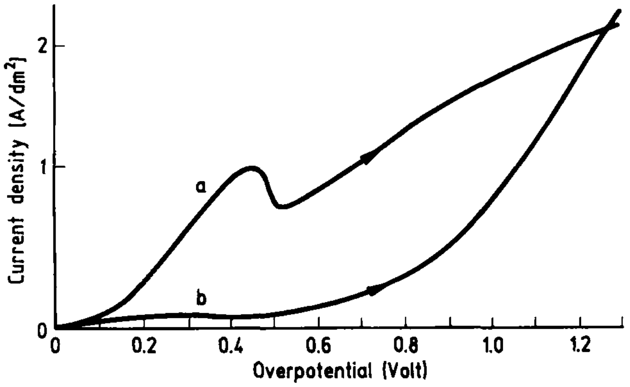

Fig. 12. Potentiodynamic anodic current-potential curve of aluminum dissolution in an alkylaluminum electrolyte (EL II/T): (a) after addition of 1 : 1 complex; (b) without 1 : 1 complex [186].

4.5.5 Throwing Power of Organoaluminum Electrolytes

Plating electrolytes are often characterized by their "throwing power", an empirical parameter which reflects the ability of the electrolyte system to deposit precipitates with an overall uniform layer thickness. It has become commonplace in electrochemical practice to express "throwing power" in terms of the so-called Wagner index *Wa*

$$Wa = \frac{1}{L} \cdot \kappa \cdot \frac{\delta \eta}{\delta I} \tag{12}$$

where κ is the conductivity of the electrolyte, L is the characteristic length of the system, and $\left(\frac{\delta \eta}{\delta I}\right)$ is the slope of the current-potential curve at a given electrode potential. A high Wagner index corresponds to a high coating uniformity [202].

In Fig. 13 the different electrolytes listed in Table 6 are compared to one another with respect to their throwing power, characterized by the Wagner index. Within one particular electrolyte system, the throwing power decreases with increasing current density [28, 33, 186, 187]. In comparison to the electrolytes El II and III, the throwing ability of El I, S3, and S6 is significantly lower. As a result, El I was replaced by either El II or El III in technical plating applications.

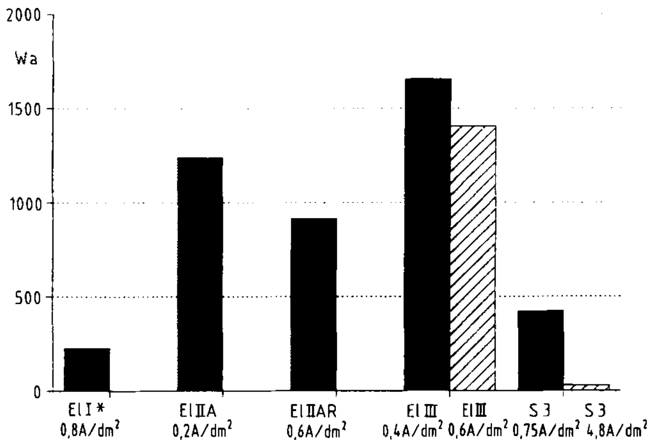

Fig. 13. The throwing power of various organoaluminum electrolytes, as defined by the Wagner index.

In practice, a general impression of the throwing power of an electrolyte can be obtained by observing deposition in a Hull [144], a Haring-Blum [75], or another suitable cell. To compare the throwing power of different organoaluminum electrolyte systems, a modified Haring-Blum cell was developed to allow work under inert atmosphere [130].

Two Cu cathodes, each with an effective surface area of $(11.5 \times 25)\text{mm}^2$, are placed within a frame composed of the glass ceramic Macor™. An anode made of pure aluminum is located between the two cathodes at a distance of 35 mm from one cathode and 5 mm from the second cathode. The top of the ceramic frame is equipped with the necessary power supplies and is attached to a round, plane ground cap, made of insulating material. This cover is placed on a matching glass cylinder with a plane ground rim. After drying and flushing with argon, the cell allows safe handling of air- and water-sensitive electrolytes (Fig. 14).

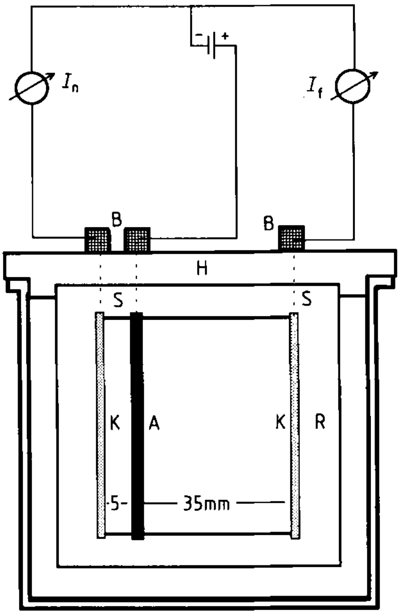

Fig. 14. Apparatus for the determination of the throwing power [130].
A = aluminum anode, K = copper cathode, R = ceramic frame, S = platinum power supply, B = contact socket, H = lid of indurated fabric

Because the cathodic and anodic current yields are quantitative in the current density regions selected for the investigated electrolytes, the amount m of metal deposited at a given time remains proportional to the current I in the corresponding current cycle [144]:

$$\mathrm{M} = \frac{m_c}{m_f} = \frac{I_c}{I_f} \tag{13}$$

Measurements to compare the throwing power of organoaluminum electrolytes were performed at 95 °C. The highest throwing power capabilities between 83 and 91% were shown by the defined 1 : 2 complexes of KF or CsF with Et_3Al, or Et_3Al and Me_3Al (1 : 1), or their mixtures, or certain mixtures of $KF[2AlEt_3]$ with $KF[2Al(iBu)_3]$ or $KF[AlEt_3Al(iBu)_3]$ [130]. $NaF[2AlEt_3]$ [33, 130] and KF electrolytes whose R_3Al/KF ratios are significant lower than 2 have a low throwing power. For the determination of the throwing power during production, a step-shaped cathode plate was utilized [31].

5 Mechanism of Electrolytic Aluminum Deposition and Dissolution

In 1954, Lehmkuhl in his dissertation discussed two alternative mechanisms for the cathodic deposition and anodic dissolution of aluminum from the new organoaluminum electrolytes [118]. One possibility is the preliminary deposition of alkali metals as a result of electrolytic dissociation of the 1 : 2 complex, resulting in alkali metal cations, and subsequent chemical reaction of this alkali metal with free or coordinated aluminum trialkyl, yielding aluminum metal and alkali metal tetraalkyl aluminate (see Scheme 2).

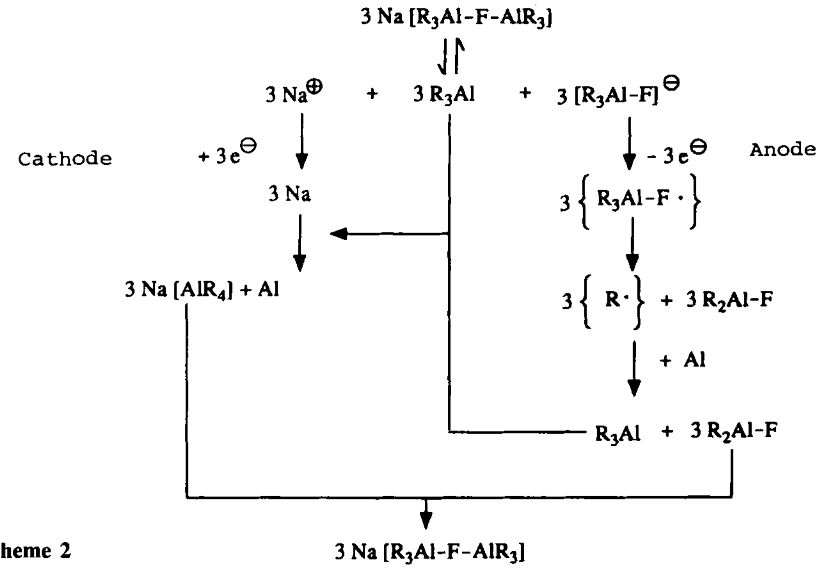

Scheme 2

An alternative mechanism with primary aluminum deposition claims formation of $[R_2Al]^{\oplus}$, $[RAl]^{2\oplus}$, or $Al^{3\oplus}$ cations by electrolytic dissociation of $M[R_3Al{-}F{-}AlR_3]$ complexes [63, 118, 221]. Formation of such cations by dissociation of organoaluminum compounds was unknown at the time. Shortly afterwards, Bonitz [39, 40] observed that aluminum trialkyl dimers possess a certain amount of intrinsic conductivity, and postulated the dissociation Eq. (14).

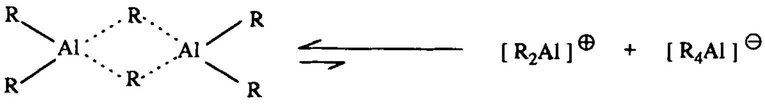

Addition of neutral Lewis bases, such as Et_2O, isoquinoline [39, 40], THF, pyridine, or NEt_3 [125, 126] to the R_6Al_2 dimer increased the specific conductivity, which reached a maximum at a molar ratio of one for Et_3Al/Lewis base. Obviously, the degree of dissociation of the aluminum trialkyls is enhanced by Lewis base addition. The assumption that the increased formation of ions from R_6Al_2 results from a stabilization of the coordinatively and electronically unsaturated $[R_2Al]^{\oplus}$ cation through coordination of two Lewis base molecules was verified by a measurement of the electrochemical transport in $Et_2AlCl \cdot$ pyridine and $Et_2AlCl \cdot 0.5\,NEt_3$ systems in a cell subdivided by a diaphragm. The results of the transport electrolysis in the $Et_2AlCl \cdot$ pyridine system may be interpreted as follows [126]:

1. The $Cl^{\ominus}$ ion is bound to the anion, the Lewis base to the cation.
2. Cation and anion diffuse at approximately the same speed.
3. Aluminum is found in the same stoichiometric ratio in both the cationic and the anionic species.

Hence the dissociation equilibrium (15) may be written as follows:

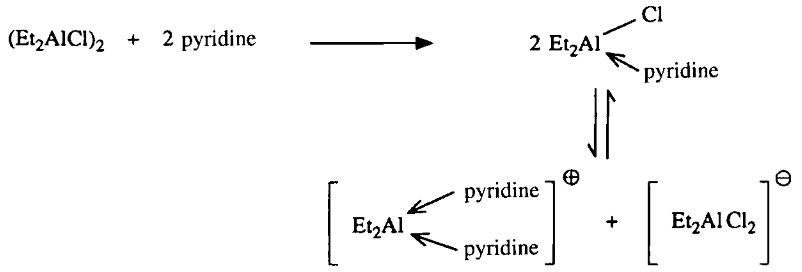

According to ^{27}Al-NMR investigations, the complex of triethylaluminum with the bidentate Lewis base 2,2′-bipyridyl (molar ratio 1 : 1) exists as an ionic complex with an $[Et_2Al]^{\oplus}$ cation.

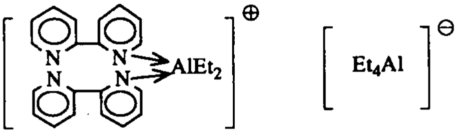

The molecular structures of $[Me_2Al]^{\oplus}$ coordinated by cyclic [15]crown-5-ether or [18]crown-6-ether in the crystalline state are known [41]. The structure of a dialkylaluminum cation stabilized through intramolecular chelate formation has also recently been described [69].

Because the $[R_2Al]^{\oplus}$ cation can be stabilized by neutral Lewis bases, we assume that this is also true of ionogenic Lewis base alkali metal alkyls R–M. Thus, 1 : 2 complexes of alkali metal halides with aluminum trialkyls, especially fluorides, may dissociate (3a) into $M^{\oplus}$ and $[R_3Al{-}F{-}AlR_3]^{\ominus}$, as shown by the molecular structure in the crystalline state. Yet there is another possibility, shown in Scheme 3b, i.e., dissociation into aluminum-containing cations and anions.

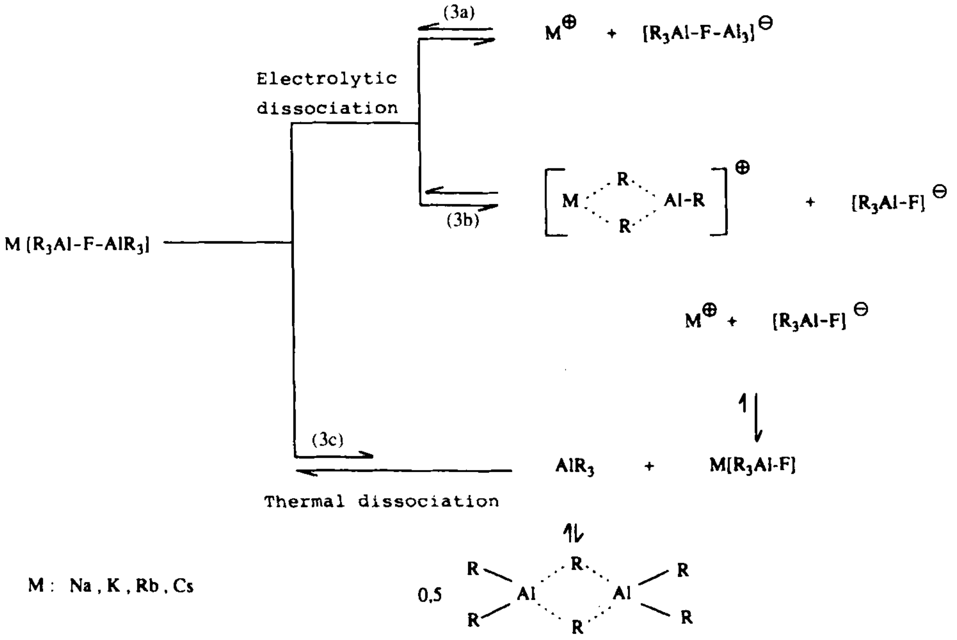

Scheme 3

It should be noted that since the discovery of 1 : 2 complexes with the formula $M[R_3Al{-}X{-}AlR_3]$ [215], the crystal structures of a large number of these compounds have been determined ($M = K$, $X = F$ and $R = Me$ [8], Et [5, 153]; $M = K$, $R = Me$ and $X = NO_3$ [9], N_3 [10]; or $M = Na$, $R = Me$ and $X = H$ [11]. None of these complexes has a crystalline structure which predetermines dissociation in solution according to Scheme (3b).

Under the plausible assumption that the $[M\ R_2Al{-}R]^{\oplus}$ cation is easier to reduce than the $M^{\oplus}$ cation, superposition of the dissociation equilibria (3a) and (3b) thus leads to deposition of aluminum metal from the organoaluminum cation at moderate cathode potentials and current densities. Only after a certain potential is exceeded does the deposition of alkali metal result from reduction of the $M^{\oplus}$ cation. The subsequent secondary chemical reaction of alkali metal with free or complex-bound aluminum trialkyls also leads to the formation of aluminum metal, but as a gray, powdery, nonadhesive coating. This can be observed during electrolysis if a certain current density at the cathodes is exceeded.

During the electrochemical investigations [186], two regions in the cathodic current-potential curve were studied. The region with a low negative overpotential yields Tafel slopes with rather low Tafel coefficients. The low Tafel coefficients indicate that a chemical equilibrium preceding the first electron transfer reaction might be the rate-determining step. In this region, deposition of high purity aluminum at quantitative current yields is observed. In the region with more negative overpotentials, obviously another type of cathodic reaction takes place. It has been shown experimentally that here potassium is codeposited with aluminum. The practical impact of the recognition of various regions lies in the fact that electrolytical coating as well as refining must be carried out in the potential region of the straight line at low negative overpotentials. Because of the dependence of the observed cathodic limiting current density on the temperature, the stirring speed, the concentration of the 1 : 2 complex, and the ratio of 1 : 2 to 1 : 1 complex, it is necessary for technical purposes to work at the highest possible temperature and 1 : 2 complex concentration, in the absence of 1 : 1 complex, and to mix thoroughly. The highest usable temperature is determined by the volatility of the solvent and the thermal stability of the organoaluminum complexes. In toluene solutions, operation temperatures of 90–100 °C have proven to be useful. The concentration limits are given by the solubility.

The sole cathodic deposition of Na from $Na[Et_3Al{-}F{-}AlEt_3]$ with mercury cathodes [118] was initially thought to support the reaction mechanism in Scheme 2, where alkali metal is always initially deposited. However, this reaction is easily explained by the great driving force for the formation of sodium amalgam. For a 0.2% sodium amalgam, the free enthalpy of formation is $\Delta G^{363} = -81.9\,\mathrm{kJ/mol}$, corresponding to 850 mV [123].

Based on the findings described in detail here and in Sec. 4, a reaction mechanism for the electrolytic deposition and dissolution of aluminum, such as the one shown in Scheme 4 exemplifying electrolysis of $K[R_3Al{-}F{-}AlR_3]$ can be discussed under the assumption that electrolysis is conducted below the experimentally determined limiting current density, so that no alkali metal is deposited. While developing this reaction scheme [134], it was assumed that the organo-aluminum cation is reduced to aluminum metal in three consecutive one-electron steps and not in one single, unlikely three-electron step. The low activation energy of aluminum deposition of about 40 kJ also points to one-electron steps constituting reduction.

The aluminum species with oxidation states between 2 and 0, which appear as intermediates, are presumed to be stabilized through interaction with the cathodic metal. There are no direct analogous compounds that can be isolated from solution. However, for two species mentioned in Scheme 4, i.e., $[KR_3Al^{II}\cdot]_{ad}$ and $[R_2Al^{II}\cdot]_{ad}$, corresponding dimers have been identified among the products of the reactions of potassium metal with triisobutylaluminum or with diisobutylaluminum chloride.

$$2\,R_3Al + 2\,K \longrightarrow K[R_3Al{-}AlR_3]K \tag{17}$$

$$2\,R_2AlCl + 2\,K \xrightarrow[-2\,KCl]{} R_2Al{-}AlR_2 \tag{18}$$

$$R = i{-}C_4H_9$$

The $R_2Al{-}AlR_2$ dimer in Eq. (18) can be further reduced with potassium metal [172] to yield $K[R_2Al{=}AlR]$. This compound, where aluminum has an oxidation state of +1, can be interpreted as a mixed dimer of the two species resulting from the second reduction step shown in Scheme 4, i.e., $K^{\oplus}[R_2Al^{I}:]_{ad}^{\ominus}$ and $[RAl^{I}:]_{ad}$.

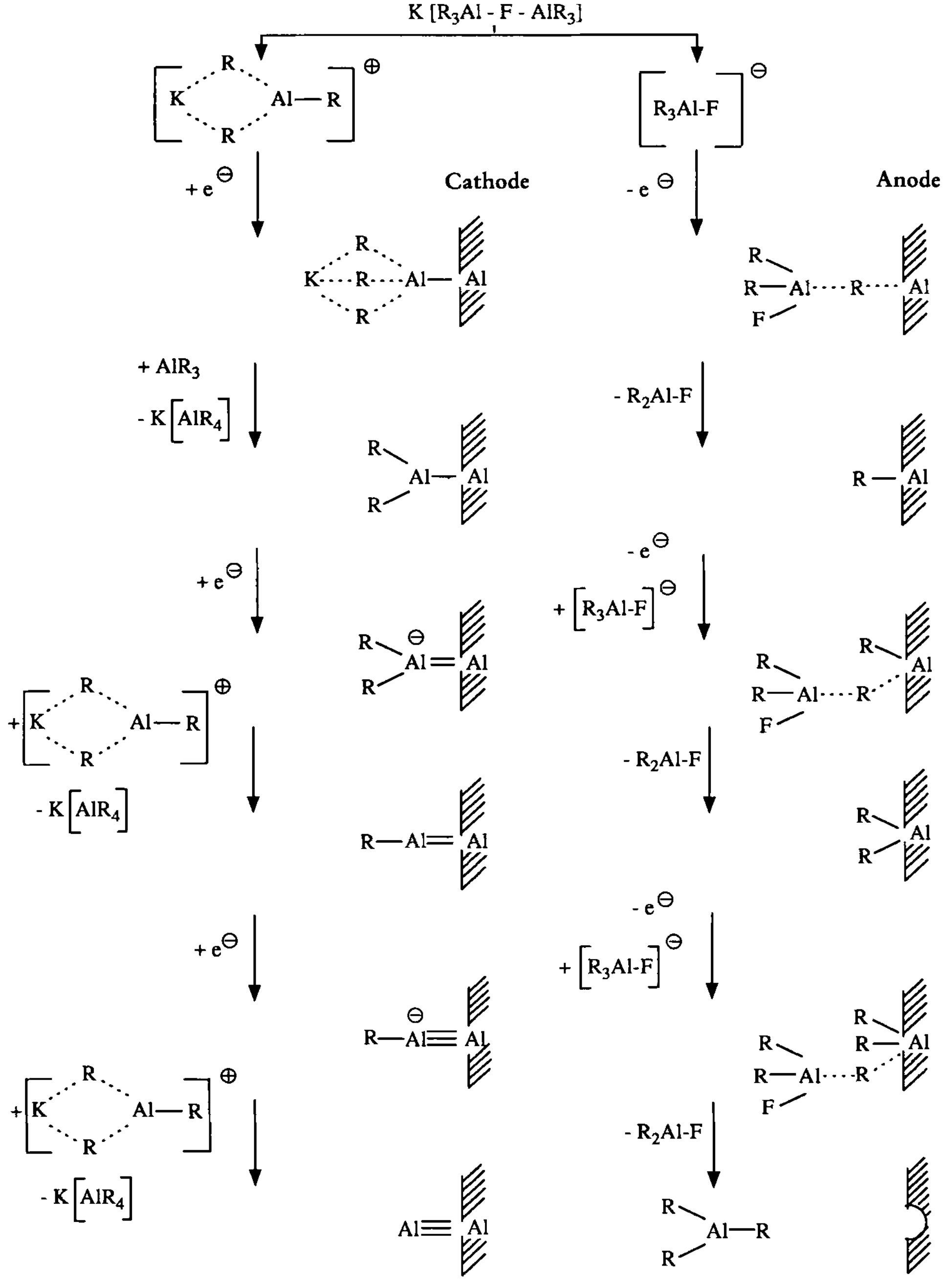
K [R₃Al - F - AlR₃]
Cathode
Anode
+ e⊖
- e⊖
+ AlR₃
- K[AlR₄]
- R₂Al-F
+ [R₃Al-F]⊖
R₃Al-F
K
Al
R

Scheme 4

From the product mixture of the reaction of diisobutylaluminum chloride with potassium, $K_2[Al_{12}(i\mathrm{Bu})_{12}]$ was recently isolated as a red crystalline solid by extraction with toluene. Its crystal structure was determined. The structure of $K_2[Al_{12}(i\mathrm{Bu})_{12}]$ reveals an Al_{12} icosahedron with a net charge of minus two. Three slightly different Al–Al bond lengths (2.679(5), 2.680(4), and 2.696(5) Å [89])were found within the icosahedron.

Concerning the anode process, Lehmkuhl [118] originally assumed that a free alkyl radical (R ·) is formed at the anode by oxidation of the $[R_3Al{-}F{-}AlR_3]^{\ominus}$ or $[R_3Al{-}F]^{\ominus}$ anions (Scheme 2). These radicals then react with the anode metal to form stable metal alkyls. Metals such as transition metals, which do not form stable homoleptic metal alkyls, either undergo disproportionation of the alkyl radicals to form alkanes and alkenes (1 : 1), or recombine to give dimers R–R. In contrast to the behavior of free alkyl radicals, it has been found that during electrolysis with insoluble anodes, the ratio of disproportion to recombination products is variable and depends on the specific anode metal [118, 229, 230]. We have accordingly modified our previous conception of the mechanism of anodic oxidation of organoaluminum complexes. There is direct interaction between the organoaluminum radical generated by release of an electron and the anode via an alkyl bridge, see Scheme 4. Because of the migration of neutral $R_2Al{-}F$ away from the anode, an alkyl linkage can be formed at the anode metal. With soluble anodes, the oxidation process is repeated until the metal in the metal alkyl R_nM reaches its stable oxidation state and the compound leaves the anode. Scheme 5 summarizes the anode and cathode reactions.

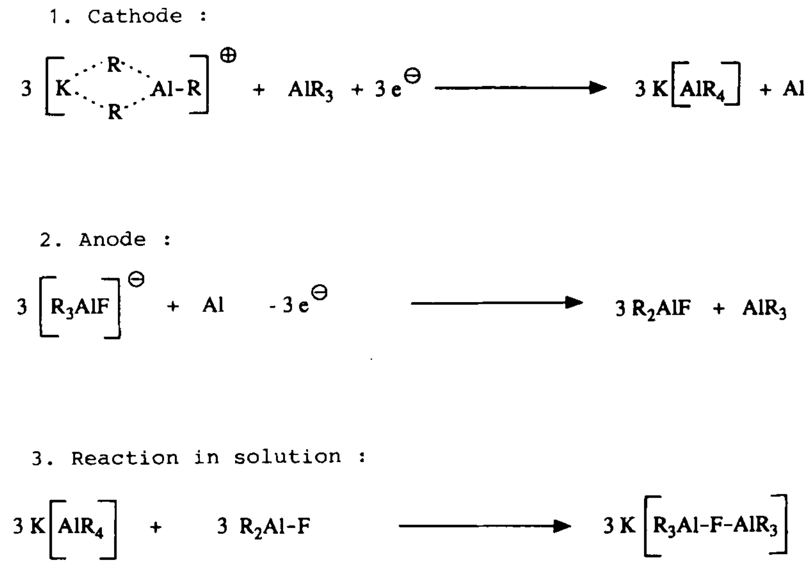

Scheme 5

Alkyl compounds of transition metals are often kinetically instable, since they generally display lower activation energies for the decomposition routes, i.e., reduction-elimination and/or β-H elimination, than the alkyl compounds of main group metals. With transition metal anodes, decomposition of the intermediary formed alkyl-metal complex therefore leads to the swift generation of disproportion and/or recombination products of the alkyl groups [121]. A diagram of these reactions is shown in Scheme 6, exemplified by the electrolysis of ethylaluminum compounds. Since the decomposition reactions resulting from alkyl-metal interaction proceed at different rates for different transition metals, the dependence of the anodic reaction products on the type of metal is easy to understand.

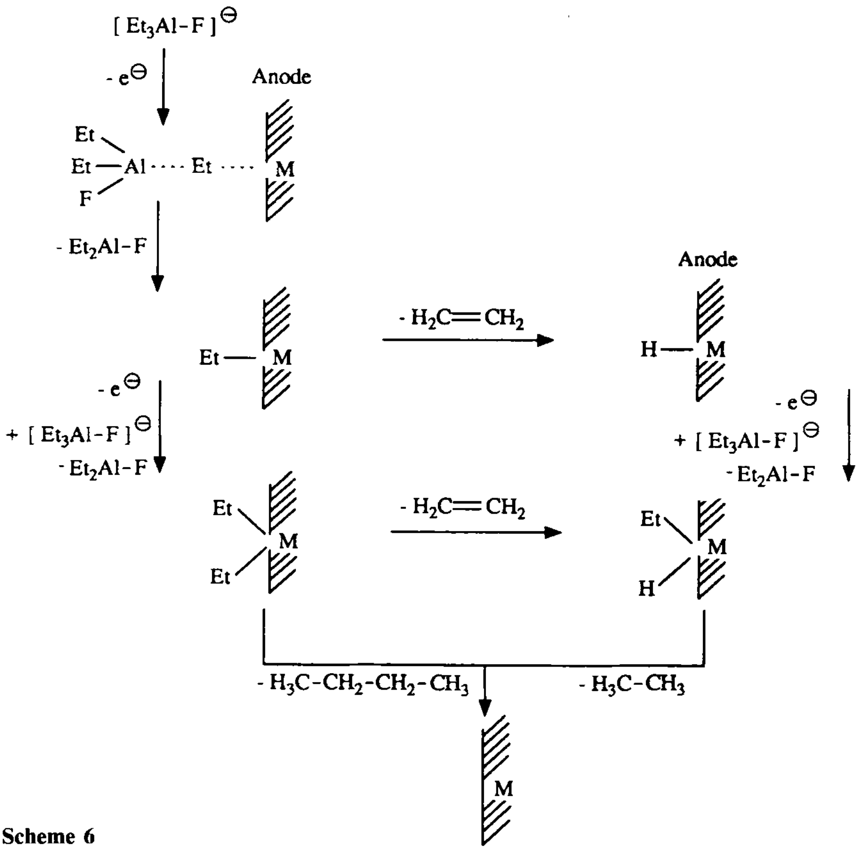

Scheme 6

6 Processing Techniques for Electrolytic Aluminum Deposition from Electrolytes Containing Aluminum Alkyls

6.1 Development of the Plant Design

Electrolytic deposition of metals out of nonaqueous media often involves materials which are very sensitive to water and/or react with oxygen. As pure materials or in concentrated solutions, aluminum trialkyl electrolytes are inflammable upon exposure to oxygen and give oxidized aluminum compounds of the type $R_nAl(OR)_{3-n}$ ($n = 0, 1, 2$). These are irreversibly destroyed by exposure to water; they hydrolyze and yield alumoxanes, such as $(R_2Al{-}O{-}AlR_2)_n$ or $(RAlO)_n$.

As a consequence, electrolysis of solutions containing aluminum alkyl must be conducted in the absence of oxygen and water in a sealed apparatus under an atmosphere of inert gas. For technical electrolysis cells, nitrogen is generally used, due to its lower cost. The charging and removal of electrodes must be conducted via a lock system, which prevents the admission of air and moisture. Furthermore, all pieces which are to be brought into the electrolytic cell must be completely dried.

The first laboratory apparatus made of glass for testing plating or refining aluminum via electrolysis of organoaluminum complexes are shown in Figs. 15 and 16. The refining apparatus was a cylindrical household jar with a ground glass rim and a matching planed aluminum lid on which the electrodes were fastened [118, 221].

Already in the first year after the discovery of electrolytic aluminum deposition from solutions containing aluminum alkyls, an apparatus for the continuous plating of wire was tested [118], see Fig. 17.

The first larger electrolysis cell of the type "highcell" with an electrolyte content of ca. 60 L was put into operation in the 1970s by Siemens-Labor (Erlangen). After loading a lock with articles to be coated, it was flooded with inert gas. Then the internal gate to the electrolytes could be opened and the workpieces brought into the electrolysis cell.

At about the same time, electrolytes containing aluminum alkyls were utilized by VAW (Bonn) for the production of ultra pure aluminum [142]. Fig. 18 shows the closed electrolysis cell used which already contains several hundred liters of bath.

An electrolysis cell with a content of 80 L for eight mounting frames (140 × 260 mm) was developed by Siemens (Erlangen) as a pilot plant for aluminum electrodeposition [65].

The first operational pilot cell by Siemens was followed by a larger cell with a capacity of 400 L, which was used by MBB (Ottobrunn). The unit was designed for a support frame of 400 × 450 mm.

In 1981, at the Dutch firm HGA, a semi-production plant with a bath volume of 2,200 L went into operation at an hourly output of 9 m^2 and an aluminum layer thickness of 10 μm. In a ring-shaped cell, articles mounted on 12 racks, each with a size of 500 × 800 mm, were plated simultaneously.

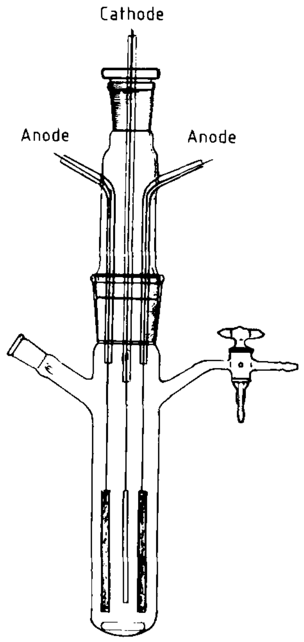

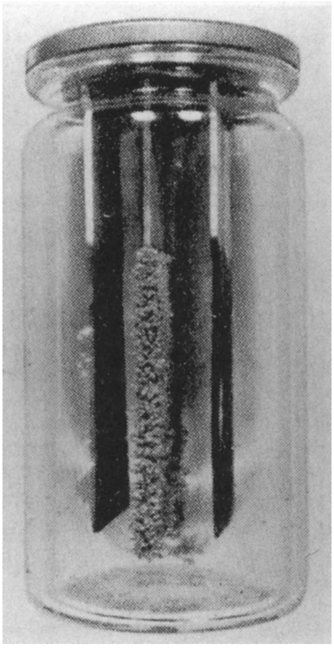

Fig. 15. A glass laboratory apparatus for plating with aluminum from organoaluminum electrolytes [118].

Fig. 16. A glass apparatus for aluminum refining from organoaluminum electrolytes [118, 221].

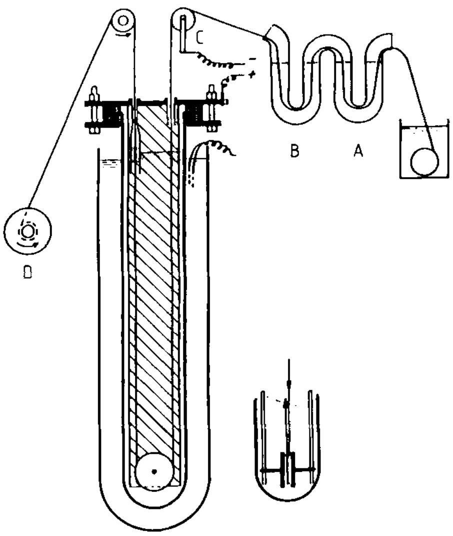

Fig. 17. A continuous operating unit for aluminum plating of wire [118].

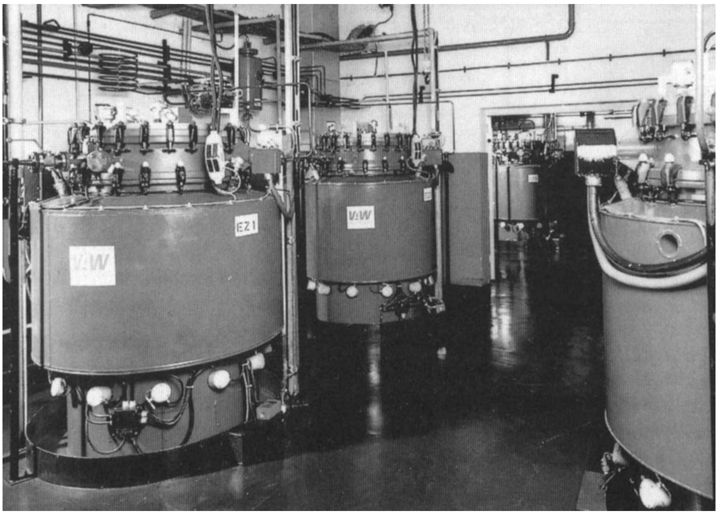

Fig. 18. The refining cells at VAW. (Photograph: Vereinigte Aluminium-Werke, Berlin-Bonn).

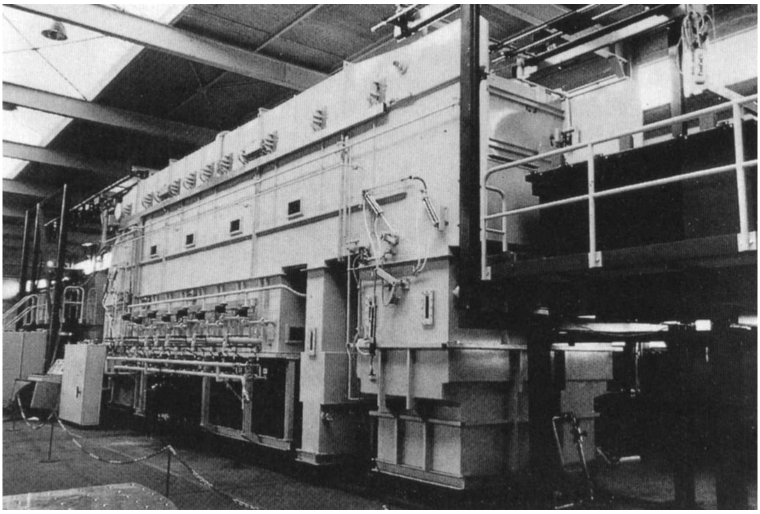

Fig. 19. 15 m^3 aluminum electroplating cell at SEDEC during assembly. (Photograph: SEDEC/Schempp und Decker, Berlin).

The first production plant in the world for electrolytic aluminum coating from organoaluminum complexes was put into operation by SEDEC (Berlin) in 1983. In order to shorten the processing time required by the HGA plant, this unit was designed as a rectangular cell. The production cell has an electrolyte volume of 15,000 L. The capacity of this automatic aluminum plating unit amounts to 32 m^2/h, with a layer thickness of 10 μm. Articles mounted on 32 frames, each 500 × 1000 mm in size, can be simultaneously coated. Fig. 19 shows the electrolysis

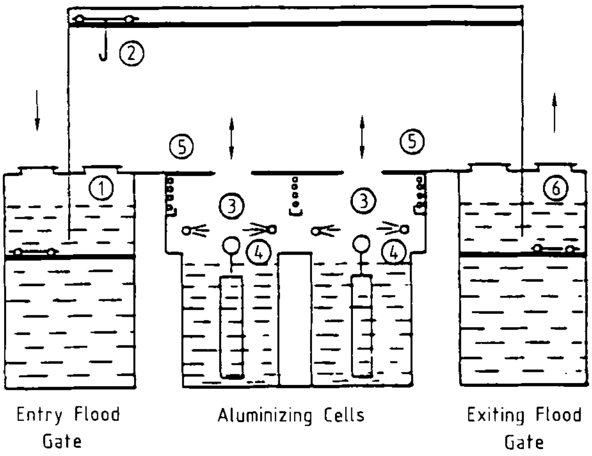

Fig. 20. Diagram of an aluminum electroplating cell with two flood gates, showing the sequence of product coating.

cell, as seen during construction. The cell is divided into eight electrolyzing compartments, each containing eight racks. In the diagram (Fig. 20) of the rectangular cell, the passage of the hardware is presented. The pretreated and dried pieces are introduced into a liquid floodgate (1) at the left-hand side of the cell and are transported to the inside of the nitrogen-filled electrolysis cell (5). Here, an automatically driven crane (2) lifts the loaded frame and places it inside a free electrolysis compartment (3).

After coating, the rack is lifted out of the cell, while the now aluminum-plated pieces are rinsed with solvent of the electrolyte system (4). Via the liquid floodgate to the right (6), the carriers with the coated pieces leave the electrolysis cell.

The solvent used for washing is obtained in very pure form by condensation of the continually evaporating electrolyte solvent (electrolyte temperature 90–100 °C) and is transferred to a collective container.

Another aluminum electroplating plant was erected in 1986 by firm G. A. N. in the Netherlands. In contrast to the Berlin unit, this installation is equipped with only one liquid port, a toluene immersion-type siphon. In order to further reduce the admission of oxygen into the electrolysis chamber, the unit was not designed as a flow-through unit, but rather for a batch process, where the single port acts both as an entering and an exiting gate. This construction is advantageous, because such a unit can be enlarged with less problems than a flow-through cell.

New plant developments are aiming in different directions. For the mass coating of supported pieces, INTERATOM (Bergisch Gladbach) constructed a new type of plant in 1989. Today, ALU 2000 (Bergisch Gladbach) operates aluminum electroplating cells with a 22.5 m^3 electrolyte volume and a plating capacity of 90 m^2/h with a layer thickness of 10 µm [31, 239]. Unlike the previous plant designs, these installations have vacuum rather than liquid ports (Fig. 21 and 22). Apparatus for the coating of loose pieces were tested [30, 32, 240]. Small units designed for specific purposes were developed for high-quality products [105].

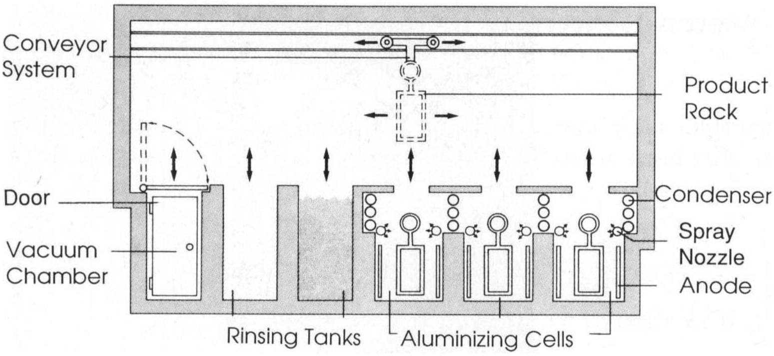

Fig. 21. Diagram of the Sigal aluminum plating unit with vacuum port.

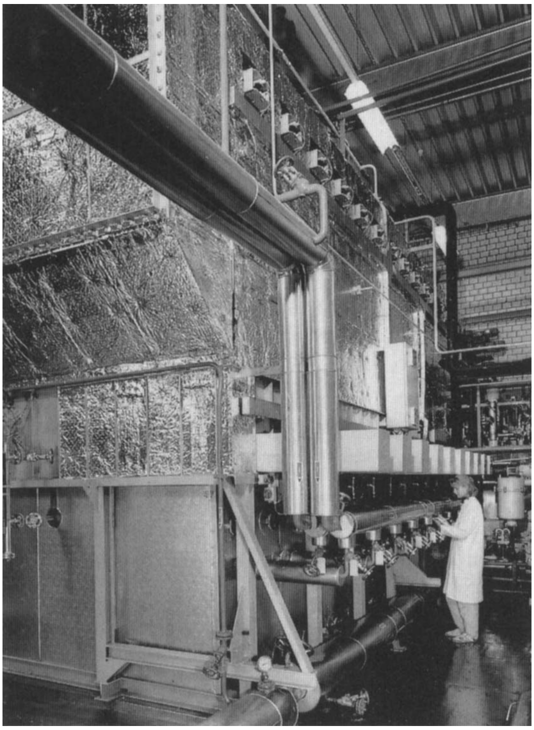

Fig. 22. Aluminum plating unit at ALU2000 in operation. (Photograph: ALU2000, Bergisch Gladbach).

6.2 Technical Aspects Concerning the Environment

In comparing electrolytic aluminum coating with conventional aqueous plating processes, it turns out that both proceed via the following process steps to afford electroplated pieces:

- pretreatment,
- electroplating,
- aftertreatment, if necessary.

Pretreatment is necessary to achieve a clean surface on the piece to be coated. To remove fat, oxides, and other impurities from the surface, defatting, etching, and descaling operations are carried out, which are then generally followed by a precoating step. In the case of aluminum plating, a prelayer of nickel, cobalt or iron or alloys of these metals (0.5–2 µm) is applied. Each treatment step is followed by one or more rounds of washing and conducted in such a manner as to minimize loss and to recycle valuable material [28, 29, 33, 127].

Since water reacts with organoaluminum compounds, destroying the electrolytes, all goods must be completely dried before subjecting them to aluminum plating. This drying step is not normally included in conventional coating processes. Dehydration with volatile fluorohydrocarbons [33] has been discontinued, due to ecological reasons. A further disadvantage of this type of drying results from the fact that fluorohydrocarbons can be carried downstream to the aluminum plating cell and cause irreversible damage to the organoaluminum electrolytes. New drying methods have been developed which are more favorable to the environment and more compatible with organoaluminum electrolyte systems [141, 239].

The aluminum plating cell is completely incapsulated. An alarm system monitors the outside of the electrolysis cell and is able to detect 100 ppm of solvents such as toluene, thus quickly recognizing a leak. Within the cell, the evaporating solvent is continuously recovered for washing purposes. Thus, a closed cleansing cycle exists, analogous to conventional aqueous electroplating processes, which is only partially realized by an ion exchanger. The organoaluminum electrolyte is continuously circulated throughout the closed system in order to filter and thermoequilibrate the electrolyte. The only waste materials are a small amount of sludge consisting mainly of impurities, originating from the anode, and solid, insoluble oxidation and/or hydrolysis products of the electrolytes.

The aluminizing process is a clean operation and the final products (Fig. 23), i.e., aluminum-coated metals, pose no environmental threat. We know today that aluminum can to a large extent replace cadmium as a corrosion-protective coating for work pieces [176]. Since cadmium is applied extensively in automobiles, aviation, on- and offshore industries, aluminum coating, i.e. both the aluminum electroplating process and the resulting coated pieces play an important role in environmental protection. The properties of the electrolytically produced aluminum layers on work pieces for aviation and space technology have been tested [183].

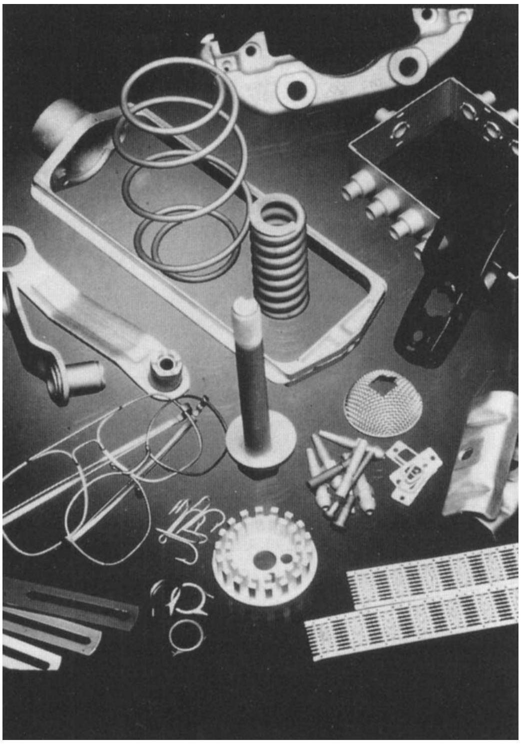

Fig. 23. Aluminum-coated work pieces. (Photograph: SEDEC/Schempp und Decker, Berlin).

7 Technological Properties of Aluminum Layers Electrolytically Deposited from Electrolytes Containing Aluminum Alkyls

Because of the concurrent refining effect, galvanoaluminum is deposited from organoaluminum electrolytes with a purity of >99.99%. This high purity contributes to many of the excellent properties of galvanoaluminum, as shown in Table 9.

Galvanoaluminum, due to its high purity, has a low electric resistance and a correspondingly high thermal conductivity. Its electric resistance is about 1.8 times higher than that of electrolytically deposited copper and silver layers, but it is only one third of that of cadmium layers [177].

Results of TEM investigations [97, 149] showed that galvanoaluminum deposits are microcrystalline, with a maximum grain diameter of 1 µm. Porefree layers were noted above ca. 8 µm. In comparison to other electrolytically deposited metals [167], the internal stress of galvanoaluminum layers was found to be very low. Independent

Table 9. Properties of galvanoaluminum

Purity	≥99.99%
Density	2.67 g/cm^3
Specific electric resistance	2.95 μΩ · cm
Thermal conductivity	218 J · s^{-1} · m^{-1} · K^{-1}
Ductility	very high
Elongation of rupture	>50%
Microhardness	21 HV
Microhardness, Anodized layer	490–530 HV
Internal tension	15 N/mm^2
Adhesion (Ring-Scher-Test) (always aluminum breaking)	70–90 N/mm^2
Pore-free coating from ca.	8 μm
Coefficient of friction (with lubricant)	$\mu \approx 0.16$

of the deposited layer thickness, electroplated aluminum layers have proven to be very ductile. A REM investigation of 20 μm thick galvanoaluminum layer deposited on a copper plate which was bent 180 degrees over a spine with a bending radius of 0.1 mm revealed that the aluminum layer showed no fissures [149]. The elongation of rupture of galvanoaluminum layers reaches values over 50%, which are significantly higher than the values for electrolytically deposited copper and gold.

Galvanoaluminum layers precipitated from electrolytes containing alkyl aluminum possess a much lower microhardness (21 HV) than other electrolytically deposited metals or aluminum layers deposited from other electrolyte systems. The soft galvanoaluminum deposits can be hardened considerably by a subsequent anodizing process. Because of the high purity of the aluminum layer, a transparent oxide layer is produced which can be colored as desired for decorative purposes. The obtainable hardness values are dependent on the selected anodizing technique.

With the direct current–sulfuric acid technique (GS), final hardness values are between 500 and 600 HV. Lower hardness values of 250–400 HV are reached by a special anodizing technique (NS). The latter procedure is preferred in practice, because, contrary to the GS process, it prevents attack on the base metal of pieces that are not completely aluminum plated, such as a hollow form.

One of the outstanding properties of galvanoaluminum is its high corrosion resistance. In a series of laboratory and short duration tests as well as studies corresponding to practical applications, galvanoaluminum demonstrated high efficiency, also in comparison to other surface coatings. In practice, protective surface layers are either uniformly attacked or pitted, or contact corrosion sets in if there is damage to the protective coating, exposing the base metal. The latter type of corrosion is the main problem, for example in automobile and airplane construction. In the following, comparable corrosion studies in laboratory, time-lapse, and practical tests are reported.

Electrochemical methods, such as potentiodynamic techniques and corrosion current measurements, can be applied [99] to simulate atmospheric contact corrosion of various layer combinations in electrolytes with varying acidity and oxygen concentration. In a sulfate environment, galvanoaluminum shows a cathodic corrosion protection ability for steel which is comparable to that of cadmium. In chloride-containing media, aluminum has a slightly higher tendency to solubilize than cadmium. Zinc, by comparison, dissolves quickly in all media, because with a corrosion potential of ca. -0.8 V at the oxide-free steel cathode, not only oxygen reduction, but also proton reduction takes place quickly.

These experimental results were for the most part verified by investigations involving salt spraying and Kesternich tests [149]: Prior to the trial, steel sheets, electrolytically coated with zinc, cadmium, and galvanoaluminum, received artificial crosswise damage to the base metal and were afterwards subjected for 500 h to a salt spraying test according to ASTM B117.

While at the end of this test zinc was completely corroded, galvanoaluminum and cadmium showed no sign of red rust. The corrosion-protective effect of the anodized layer is less than that of the nonanodized galvanoaluminum layer, because of the missing cathodic corrosion protection. Yellow chromated 12 µm thick galvanoaluminum and cadmium coatings exhibited no trace of red rust after 1000 h.

Galvanoaluminum layers thicker than 12 µm are extraordinarily corrosion resistant to exposure to SO_2, in which they surpass the performance of cadmium and zinc layers [31]. After 20 rounds of the SFW 2.0 L, DIN 50018 Kesternich test, in contrast to the ca. 12 µm thick, yellow chromated galvanoaluminum layers, the zinc and cadmium coatings were already heavily corroded. The SO_2 resistance of anodized galvanoaluminum can also be considered excellent in comparison to cadmium and zinc coatings.

Widening the range of competing surfaces, the high corrosion resistance of galvanoaluminum deposition was also verified under thermal stress in a salt-fog spray test. Thermal stress must be taken into consideration, for example, in automobile parts where the engine compartment temperature reaches more than 100 °C. Coatings must also guarantee sound corrosion resistance, even under these conditions.

Table 10 lists the results obtained with and without thermal stress for bolts coated with different systems [204, 239]. Because coatings on connecting elements can be damaged during assembly, which gives rise to contact corrosion, turned bolts were included in the test.

With galvanoaluminum coatings like zinc-nickel alloys, long duration times were reached. Regarding thermal and mechanical stress, the corrosion-protective effect of the zinc-nickel alloy layers is clearly inferior to that of galvanoaluminum. The short life span of IVD-aluminum deposits in comparison to galvanoaluminum is notable. This difference may result from the different microstructures of these two types of aluminum coatings [97, 156].

In contrast to salt spraying tests, the corrosion "driving" test involves attaching the pieces to be tested to a running motor vehicle. If the corresponding sample part can functionally replace the vehicle's original part, an exchange is carried out before the start of the test. If not, the sample piece is attached to a suitable place in the engine compartment. Such an investigation of various metallic and nonmetallic coating systems, conducted by a German automobile company, reveals the properties

Table 10. Life span [h] of M10 bolts in the ASTM B117 salt spraying for test [204].

Coating	Start of base metal corrosion [h]		
		after heating 24 h at 120 °C	
	w/o thermal stress	w/o turning	3 turns
Cyanidic zinc	288	144	96
Zinc nickel A	>1000	576	288
Zinc nickel B	>1000	576	288
Galvanic aluminum	>1000	>1000	480
Aluminum (IVD)	288	288	192

of the various layer systems in a critical corrosion environment over six years of operation. This test results certified the excellent corrosion resistance quality of galvanoaluminum layers at high thermal and corrosive stress.

During deposition of galvanoaluminum from organic aluminum electrolytes which do not contain aluminum hydride, coprecipitation of hydrogen is not observed. The danger of embrittlement through hydrogen as a result of coating low-alloyed high-strength steels with aluminum from such electrolytes is excluded. To improve the adhesion of galvanoaluminum layers on steel, a ca. 1 μm thick layer of nickel is electroplated onto the steel prior to aluminum electroplating. This intermediate layer can be obtained from either aqueous [149, 239] or nonaqueous organic nickel electrolytes [127].

The coefficients of friction of steel-galvano-aluminum couplings determined by the pin-disk method, are higher than those of steel-zinc or steel-cadmium combinations [176]. Lubricants which, for example, are admissible by the automobile industry significantly reduce the friction coefficient of the steel-galvano-aluminum combination which, on the average, is below that of the steel-zinc pairing. The deviation of the coefficients of friction of steel-galvanoaluminum (yellow chromated, lubricated) is below that of the similarly treated steel-zinc combination.

Comparative investigations to explore possible substituents for cadmium layers in motor vehicle construction also verified the high corrosion resistance of aluminum, as well as the advantageous avoidance of hydrogen embrittlement of the building unit [38].

Due to its high purity, galvanoaluminum has also been tested for applications in electronics, where galvanoaluminum has proven to adhere well to aluminum and gold wire [106]. The durability of the aluminum wire-galvanoaluminum bond after aging is clearly superior to other combinations, such as Al-wire/gold and Al-wire/silver [170].

The same investigation showed that copper-precoated ceramic plates coated with aluminum can be etched like copper circuit boards. A comparative study of galvanoaluminum layers and other electrolytically precipitated deposits was recently published [140].

Acknowledgements. The authors would like to thank Prof. Dr. Dr. h. c. Roland Kammel (Technische Universität Berlin) and Prof. Dr. Hans-Wilhelm Lieber (Technische Universität Berlin and Fachhochschule Berlin) for their great interest in and constant encouragement of the development of electrodeposited aluminum from organoaluminum electrolytes. The authors owe special thanks to Dr. Lorraine Aleandri-Hachgenei and to Ms. Helga Wasilewski for the English translation and completion of the manuscript, respectively.

8 References

1. A. P. Abbott, E. E. Loug, A. Bettey, D. J. Schiffrin, J. Electroanal. Chem. 261, 449 (1989).
2. E. F. Abrams, M. Kinna, Adv. Struct. Compos., Soc. Aerosp. Mater. Process Eng., Nat. Symp. Exhib., 12th 1967 AC-16; C.A. 70, 83512 n (1969).
3. E. F. Abrams, M. Kinna, Ref. Zh. Metall. 1976, Abstr. No. 4 I 804; C.A. 85, 64520 g (1976).
4. A. K. Agrawal, A. E. Austin, Novel Silicon Growth Methods, Electrochem. Soc. Symp., St. Louis (1980).
5. G. Allegra, G. Perego, Acta Crystallogr. 16, 185 (1963).
6. W. Altgeld, Metalloberfläche 40, 253 (1986).
7. H. Antoun, A. Hape, G. A. Capuano, J. Electrochem. Soc. 129, 40 (1982).
8. J. L. Atwood, W. R. Newberry, J. Organomet. Chem. 66, 15 (1974).
9. J. L. Atwood, K. D. Crissinger, R. D. Rogers, J. Organomet. Chem. 155, 1 (1978).
10. J. L. Atwood, W. R. Newberry, J. Organomet. Chem. 65, 145 (1974).
11. J. L. Atwood, D. C. Hrncir, R. D. Rogers, J. A. K. Howard, J. Am. Chem. Soc. 103, 6787 (1981).
12. N. Baba, Y. Takeuchi, S. Morisaki, J. Met. Finish. Soc. Jpn. 22, 175 (1971).
13. W. A. Badawy, N. Hilal, Ber. Bunsenges. Phys. Chem. 93, 56 (1989).
14. W. A. Badawy, B. A. Sabrak, N. Hilal, J. Appl. Electrochem. 16, 707 (1986).
15. W. A. Badawy, B. A. Sabrak, N. Hilal, J. Appl. Electrochem. 17, 357 (1987).
16. W. A. Badawy, B. A. Sabrak, N. Hilal, J. Appl. Electrochem. 18, 220 (1988).
17. V. A. Bagril, N. A. Kazdobin, Ukr. Khim. Zh. 45, 19 (1979).
18. F. Beck, Elektroorganische Chemie, Verlag Chemie, Weinheim (1974).
19. R. Benn, E. Janssen, H. Lehmkuhl, A. Rufińska, J. Organomet. Chem. 333, 155 (1987).
20. R. Benn, A. Rufińska, Angew. Chem. 98, 851 (1986); Angew. Chem. Int. Ed. Engl. 25, 861 (1986).
21. H. Benninghoff, Metalloberfläche 36, 13 (1982).
22. J. v. d. Berg, T. Daenen, G. Krijl, R. v. d. Leest, Philips Techn. Rev. 39, 218 (1980).
23. J. v. d. Berg, T. Daenen, G. Krijl, R. v. d. Leest, Sufaces 24, 8 (1985).
24. J. v. d. Berg, T. Daenen, G. Krijl, R. v. d. Leest, Metalloberfläche 35, 218 (1985).
25. J. v. d. Berg, G. v. Dijk, R. v. d. Leest, Interfinish, Tel Aviv (1984).
26. J. v. d. Berg, G. A. R. v. Dijk, R. E. v. d. Leest, Metal Finishing 83, 15 (1985).
27. K. Beyer, W. Röder, Metalloberfläche 34, 101 (1980).
28. S. Birkle, Jahrbuch Oberflächentechnik 40, 207 (1984).
29. S. Birkle, Metalloberfläche 40, 249 (1986).
30. S. Birkle, Korrosionsschutz am Kraftfahrzeug, 2. Tagung, Haus der Technik, Essen (5th-6th March 1987).
31. S. Birkle, Metalloberfläche 42, 511 (1988).
32. S. Birkle, J. Gehring, Europ. Patent 0209015 (Siemens AG), Prior. 9th July 1985; 15th May 1986.
33. S. Birkle, J. Gehring, K. Stöger, H. de Vries, Metall 36, 673 (1982).
34. S. Birkle, K. Stöger, Europ. Patent 0084816 (Siemens AG); Prior. 25th January 1982; C. A. 99, 148487 (1983).

35. Blasberg-Mitteilungen No. 4, 23 (1985).
36. J. O'M. Bockris, G. A. Razumney, Fundamental Aspects of Electrocrystallization, Plenum Press, New York (1967), p. 36.
37. A. Böhm, H. Ginsberg, W. Reuter, Aluminum 37, 267 (1961).
38. E. Böhm, J. Mann, Metalloberfläche 39, 449 (1985).
39. E. Bonitz, Angew. Chem. 67, 525 (1955).
40. E. Bonitz, Chem. Ber. 88, 742 (1955).
41. S. G. Bott, A. Alvanipour, S. D. Morley, D. A. Atwood, C. M. Means, A. W. Coleman, J. L. Atwood, Angew. Chem. 99, 476 (1987); Angew. Chem. Int. Ed. Engl. 26, 485 (1987).
42. A. Brenner, J. Electrochem. Soc. 106, 148 (1959).
43. A. Brenner, Adv. in Electrochemistry and Electrochem. Eng., 5, 205 (1967).
44. E. W. Brooman, Electrodeposition and Surface Treatment 2, 1 (1973-74).
45. E. W. Brooman, Plating and Surface Finishing 72, 142 (1985).
46. G. A. Capuano, W. G. Davenport, J. Electrochem. Soc. 118, 1688 (1971).
47. G. A. Capuano, W. G. Davenport, Plating 60, 251 (1973).
48. G. A. Capuano, W. G. Davenport, J. Electrochem. Soc. 131, 2595 (1984).
49. G. A. Capuano, W. G. Davenport, J. Appl. Electrochem. 9 (1979) 7.
50. G. A. Capuano, R. Lafortune, C. Gobeil, Plating and Surface Finishing 64, 49 (1977).
51. C. K. Chisholm, Trans. Institute of Metal Finishing 47, 134 (1969).
52. Y. Chryssonlakis, S. Kalogeropoulou, J. Appl. Electrochem. 17, 941 (1987).
53. J. H. Connor, A. Brenner, J. Electrochem. Soc. 103, 657 (1956).
54. D. E. Couch, A. Brenner, J. Electrochem. Soc. 99, 234 (1952).
55. T. E. G. Daenen, US Patent 4222827 (N. V. Philips), Prior 16th September 1980; C.A. 92, 84916 p (1980).
56. T. Daenen, J. v. d. Berg, G. A. R. v. Dijk, Trans. Institute of Metal Finishing 63, 104 (1985).
57. T. E. G. Daenen, G. A. R. v. Dijk, S. A. Stolk, US Patent 4381975 (N. V. Philips), Prior. 6th February 1981; C.A. 97, 171360 z. (1982).
58. T. E. G. Daenen, S. A. Stolk, DE 2806957 (N. V. Philips), Prior. 25th February 1977; US Patent 4145261; C.A. 89 170982 b (1978).
59. B. B. Damaskin, O. A. Petrii, V. V. Batrakov, Adsorption organischer Verbindungen an Elektroden, Akademie-Verlag, Berlin (1975), p. 246.
60. G. Dick, H. Tippmann, R. Suchentrunk, DE 3107384 (Messerschmitt-Bölkow-Blohm), Prior. 7th May 1986; C.A. 98, 24675 (1983).
61. G. v. Dijk, H. C. A. M. Smoorenburg, J. Electrochem. Soc. 131, 345 (1984).
62. A. J. Dill, Plating 59, 1048 (1972).
63. R. Dötzer, Chem. Ing. Tech. 36, 616 (1964).
64. R. Dötzer, DE 1200817 (Siemens AG), Prior. 30th March 1963; CA. 69, 15896 d (1965).
65. R. Dötzer, Chem. Ing. Tech. 45, 653 (1973).
66. R. Dötzer, E. Todt, H. G. Hauschild, DE 2453830 (Siemens AG), Prior. 13th November 1974; C.A. 85, 132849 y (1976).
67. P. Dudzik, Studienarbeit, Institut für Metallhüttenkunde, Technische Universität Berlin (1986).
68. J. Eckert, M. Galova, Electrochim. Acta. 26, 1169 (1981).
69. L. M. Engelhardt, U. Kynast, C. L. Raston, A. H. White, Angew. Chem. 99, 702 (1987); Angew. Chem. Int. Ed. Engl. 26, 681 (1987).
70. T. Erdey-Grúz, Kinetics of Electrode Processes, Akademiai Kiado, Budapest (1975), p. 68.
71. P. Fellner, M. Chrenkova-Paucirova, K. Matiasovsky, Surf. Technol. 14, 101-8 (1981); C. A. 96, 13073 h (1982).
72. P. Fellner, M. Chrenkova-Paucirova, K. Matiasovsky, Koroze Ochr. Mater. 26, 71-4 (1982); C.A. 98, 169113 y (1983).
73. P. Fellner, A. Silny, K. Matiasovsky, M. Chrenkova-Paucirova, Surf. Technol. 16, 15-21 (1982).
74. D. M. Ferry, G. S. Picard, B. L. Trémillon, J. Electrochem. Soc. 135, 1443 (1988).
75. H. Fischer, Elektrolytische Abscheidung und Elektrokristallisation von Metallen, Springer-Verlag, Berlin (1954), p. 316.

76. J. Gala, J. Branska, E. Lagiewka, Rudy Met. Niezelaz 26, 242 (1981).
77. M. Galova, Surf. Technol. 11, 357 (1980).
78. M. Galova, D. Kladekova, Surf. Technol. 11, 371 (1980).
79. M. Galova, D. Kladekova, L. Lux, Surf. Technol. 13, 315 (1981).
80. M. Galova, L. Lux, D. Kladekova, Hutn. Listy 39, 257 (1984).
81. G. Geblewicz, R. J. Potter, D. J. Schiffrin, Trans. Institute of Metal Finishing 64, 134 (1986).
82. M. W. M. Graef, J. Electrochem. Soc. 132, 1038 (1985).
83. Handelsblatt, 5.02.1986, p. 17.
84. W. D. Hannibal, G. Ibe, H. Pfundt, W. Reuter, G. Winkhaus, Metall 27, 203 (1973).
85. J. J. Harrison, D. L. Beach, D. C. Young, K. S. Seshardi, J. D. Nelligan, Organometallics 6, 343 (1987).
86. H. Hayashi, N. Hayashi, Z. Takehara, A. Katagiri, J. Electrochem. Soc. 136, 2606 (1989).
87. M. Hayes, A. T. Kuhn, W. Patefield, J. Power Sources 2, 121 (1977/78).
88. E. Heitz, G. Kreysa, Grundlagen der Technischen Elektrochemie, Verlag Chemie, Weinheim (1980), p. 254.
89. W. Hiller, K.-W. Klinkhammer, W. Uhl, J. Wagner, Angew. Chem. 103, 182 (1991); Angew. Chem. Int. Ed. Engl. 30, 179 (1991). The dimeric structure of a modified derivative of $R_2Al-AlR_2$ with $R = CH(SiMe_3)_2$ has recently been confirmed by X-ray analysis: Uhl, W., Z. Naturforsch. B43, 1113 (1988).
90. H. Hoberg, S. Krause, Angew. Chem. 90, 1013 (1978); Angew. Chem. Int. Ed. Engl. 17, 949 (1978).
91. H. Hoberg, S. Krause, Angew. Chem. 88, 760 (1976); Angew. Chem. Int. Ed. Engl. 15, 694 (1976).
92. J. N. Howarth, D. Pletcher, J. Chem. Soc., Faraday Trans. 1 83, 2787 (1987).
93. J. N. Howarth, D. Pletcher, J. Chem. Soc., Faraday Trans. 1 83, 2795 (1987).
94. K. Itoh, T. Ishikawa, R. Midorikawa, Sumitomo Light Metal Techn. Rep. 15, 1 (1974).
95. D. Jahn, W. Vielstich, J. Electrochem. Soc., 109, 849 (1962).
96. Japan Steel & Tube Corp., DE 1496937, Prior. 13th November 1964, 24th February 1965; C. A. 66, 91214 z (1967).
97. N. Kanani, F. Barth, R. Kammel, U. Landau, Aluminum 61, 643 (1985)
98. W. Kautek, Proc. 6. Österr. Chemietag, Linz (1985), p. 146.
99. W. Kautek, Corros. Sci. 28, 173. (1988).
100. W. Kautek, S. Birkle, DGO 26. Jahrestagung, Goslar (28th-30th September 1988).
101. W. Kautek, S. Birkle, Electrochim. Acta. 34 (1989) 1213.
102. V. A. Kazakov, H. Nakamura, M. Yoshio, Elektrokhimiya 21, 1331 (1985).
103. V. A. Kazakov, V. N. Titova, S. A. Smirnova, Zashch. Met. 15, 235 (1979); C. A. 90, 212148 n (1979).
104. D. Kladekova, M. Galova, Zbornik Vldeckyck Prac. Vysokej Skoly Technicky, Kosiciach, 133 (1984).
105. W. Keller, U. Landau, G. Gramm, Aluminum Journal 1990, 36.
106. K.-H. Kubatscha, Thesis, Georg-Simon-Ohm Fachhochschule, Nürnberg (1989).
107. T. Küsel, R. Sudhölter, Metall 42, 812, (1988).
108. M. Kume, J. Met. Finish. Soc. Jpn. 31, 487 (1980).
109. V. V. Kuznetsov, Elektrokhimija 16, 646 (1980).
110. R. Lafortune, J. T. Bourret, G. A. Capuano, Can. J. Chem. 56, 2375 (1978).
111. P. K. Lai, M. Skyllas-Kazacos, Elektrochim. Acta 32, 1443 (1987).
112. U. Landau, Galvanotechnik 77, 574 (1986).
113. U. Landau, Jahrbuch Oberflächentechnik 42, 121 (1986).
114. U. Landau, Jahrbuch Oberflächentechnik 43, 86 (1987).
115. U. Landau, Jahrbuch Oberflächentechnik 44, 126 (1988).
116. U. Landau, unpublished results.
117. H. H. Law, C. W. Tobias, The Electrochem. Soc. Proc. 81-86, 329 (1981).
118. H. Lehmkuhl, Dissertation, Rheinisch-Westfälische Technische Hochschule, Aachen (1954).

119. H. Lehmkuhl, unpublished results (1962).
120. H. Lehmkuhl, Angew. Chem. 75, 1090 (1963); Angew. Chem. Int. Ed. Engl. 3, 107 (1964).
121. H. Lehmkuhl, Organic Electrochemistry, Baizer, M. M. (ed.) Dekker, New York (1973), p. 621.
122. H. Lehmkuhl, W. Eisenbach, unpublished results.
123. H. Lehmkuhl, W. Grimme, Liebigs Ann. Chem. 705, 1 (1967).
124. H. Lehmkuhl, E. Janssen, J. Elsässer, Chem. Ztg. 110, 163 (1986).
125. H. Lehmkuhl, H. D. Kobs, Tetrahedron Lett. 29, 2505 (1965).
126. H. Lehmkuhl, H. D. Kobs, Liebigs Ann. Chem. 719, 11 (1968).
127. H. Lehmkuhl, K. Mehler, DE 3804303 (Studienges. Kohle), Prior. 12th February 1988.
128. H. Lehmkuhl, K. Mehler, Europ. Patent 0402760 (Studienges. Kohle), Prior. 10th June 1989.
129. H. Lehmkuhl, K. Mehler, Europ. Patent 0402761 (Studienges. Kohle), Prior. 10th June 1989.
130. H. Lehmkuhl, K. Mehler, unpublished results (1986).
131. H. Lehmkuhl, K. Mehler, unpublished results (1990-91).
132. H. Lehmkuhl, K. Mehler, (MPI Mülheim); J. Heil, (VAW AG, Grevenbroich) unpublished results (1990-91).
133. H. Lehmkuhl, K. Mehler, U. Landau, R. Kammel, H. W. Lieber, Galvanotechnik 82, 1586 (1991).
134. H. Lehmkuhl, K. Mehler, U. Landau, N. T. Tabataba-Vakili, The reaction scheme 21 was developed in the course of discussions.
135. H. Lehmkuhl, K. Ziegler, Methoden zur Herstellung und Umwandlung von organischen Aluminumverbindungen; Houben-Weyl-Müller: Methoden der organischen Chemie, Band 13/4; 4. Auflage, Thieme, Stuttgart (1970).
136. D. Lentz, J. Elsässer, H. Lehmkuhl, unpublished ^{19}F-NMR results (1986).
137. R. J. Lepinay, J. Bouteillon, S. Traore, D. Renak, M. J. Barbier, J. Appl. Electrochem. 17, 294 (1987).
138. V. G. Levich, Acta physiokhim. (USSR) 17, 257 (1942); Faraday Discuss. Chem. Soc. 1, 37 (1947).
139. Q. Li, H. A. Hjuler, R. W. Berg, N. J. Bjerrum, J. Electrochem. Soc. 136, 2940 (1989).
140. H. W. Lieber, H. Henning, BMFT-Bericht (1989).
141. H. W. Lieber, R. Kammel, H. Lehmkuhl, K. Mehler, U. Landau, unpublished results.
142. G. Lossmann, G. Winkhaus, Raffinationsverfahren in der Metallurgie, B2, Verlag Chemie, Weinheim (1983).
143. F. A. Lowenheim, Electroplating, McGraw-Hill Co., New York (1978).
144. W. Machu, Moderne Galvanotechnik, Verlag Chemie, Weinheim (1954), p. 198.
145. C. K. Mann, Electroanalytical Chemistry, Vol. 3, Bard, A. (ed.), Dekker, New York (1969).
146. A. Mayer, Plating and Surface Finishing 74, 78 (1987).
147. A. Mayer, US Patent 4778575 (United States Dept. of Energy), Prior. 21th January 1988; C. A. 110, 123847 (1989).
148. S. Meibuhr, E. Yeager, A. Kozawa, F. Hovorka, J. Electrochem. Soc. 110, 190 (1963).
149. Metaalinstitut TNO, Report No. 85M/016089 BLA/AKU (1985).
150. I. A. Menzies, Trans. Institute Metal Finishing 39, 172 (1962).
151. I. A. Menzies, D. B. Salt, Trans. Institute Metal Finishing 43, 186 (1965).
152. K. Michiyuki, Nagoya-Shikogyo Kenkyusho Kentya Hokoku 56, 21 (1977).
153. G. Natta, G. Allegra, G. Perego, A. Zambelli, J. Am. Chem. Soc. 83, 5033 (1961).
154. T. Nguyen, J. P. Wiaux, C. J. Vance, US Patent 4560446 (Eltech Systems Corp.), Prior. 14th December 1985; C. A. 103, 168769 b (1985).
155. Kh. Noninski, T. Tsvetkov, V. Noninski, Metalurgiya 36, 22 (1981).
156. W. Paatsch, Aluminum 53, 254 (1977).
157. R. Parsons, Electrochim. Acta 21, 681 (1976).
158. E. Peled, M. Elam, E. Gileadi, J. Appl. Electrochem. 11, 463 (1981).
159. E. Peled, E. Gileadi, Plating and Surface Finishing 62, 342 (1975).
160. E. Peled, E. Gileadi, J. Electrochem. Soc. 123, 15 (1976).

161. J. P. Pemsler, V. R. Koch, M. D. Dempsey, J. K. Litchfield, S. E. Stone, Energy Reduct. Tech. Met. Electrochem. Processes, Proc. Symp. 457-69, (1985); C. A. 104, 22316 a (1986).
162. O. Popovych, R. P. T. Tomkins, Nonaqueous Solution Chemistry, J. Wiley, New York (1981).
163. R. J. Potter, D. J. Schiffrin, J. Electrochem. Soc. 133, 547 (1986).
164. Q.-X. Quin, M. Skyllas-Kazacos, J. Electroanal. Chem. 168, 193 (1984).
165. G. F. Reynolds, C. J. Dymek, Proc. Electrochem. Soc. 86, 153 (1986).
166. R. J. Roethlein, J. Electrochem. Soc. 117, 714 (1970).
167. W. Safranek, The Properties of Electrodeposited Metals and Alloys, Elsevier Publ., New York (1974).
168. R. Saifullin, J. Eckert, N. V. Bortunov, Zashch. Met. 18, 792 (1982).
169. E. Santos, F. Dyment, Plating 60, 821 (1973); C. A. 79, 99733g (1973).
170. SCHERING AG, Berlin, personal communication.
171. D. J. Schiffrin, personal communication.
172. E. P. Schramm, Inorg. Chim. Acta 141, 69 (1988).
173. G. A. Serebryakov, I. F. Nichkov, S. P. Raspopin, E. A. Nivikov, Sov. J. Non-Ferrous Met. 12, 33 (1971).
174. H. G. Severin, Metall 38, 328 (1984).
175. L. Simanavicius, V. Ragaleviciene, Liiet, TSR Morksh. Akad. Darb. Scr. B5, 10 (1985).
176. H. Simon, Metalloberfläche 39, 13 (1985).
177. H. Simon, M. Thoma, Angew. Oberflächentechn. für Metallische Werkstoffe, C. Hanser, München-Wien (1985), pp. 76, 80, 81.
178. W. Simon, D. Boldin, Galvanotechnik 78, 954 (1987).
179. C. J. Smit, T. P. J. Peters, Light Met. 2, 253 (1986).
180. C. Strobl, Korrosionsschutz am Kraftfahrzeug, 2. Tagung, Haus der Technik, Essen (5th-6th March 1987).
181. M. S. Su, J. S. Gentry, C. B. Boss, C. G. Moreland, K. J. Bachmann, J. Electrochem. Soc. 132, 802 (1985).
182. R. Suchentrunk, Metall 35, 539 (1981).
183. R. Suchentrunk, H. Tippmann, Galvanotechn. 73, 2 (1983).
184. R. Sudhölter, Verunreinigung in Metallen Ber. Symp.; C. A. 92, 150554x (1980), 165 (1977).
185. R. Sudhölter, Aluminium 66, 339 (1990).
186. N. T. Tabataba-Vakili, Dissertation, Technische Universität, Berlin (1988).
187. N. T. Tabataba-Vakili, Galvanotechnik 82, 92 (1991).
188. T. Takei, J. Met. Finish. Soc. Jpn. 25, 343 (1974).
189. T. Takei, J. Met. Finish. Soc. Jpn. 25, 488 (1974).
190. T. Takei, J. Met. Finish. Soc. Jpn. 25, 533 (1974).
191. T. Takei, J. Met. Finish. Soc. Jpn. 26, 353 (1975).
192. T. Takei, J. Met. Finish. Soc. Jpn. 27, 601 (1976).
193. T. Takei, Electrochim. Acta 23, 1321 (1978).
194. T. Takei, Electrochim. Acta 23, 1325 (1978).
195. K. H. Thiele, Z. Anorg. Allg. Chem. 349, 33 (1967).
196. E. Todt, H. Hauschild, DE 1170658 (Siemens AG), Prior. 13th June 1961; C. A. 59, 3554 f. (1963).
197. E. Todt, H. Hauschild, DE 1483344 (Siemens AG), Prior. 15th December 1965; C. A. 70, 13647 (1969).
198. T. Tsuru, S. Kobayashi, K. Ohba, T. Inui, J. Met. Finish. Soc. Jpn. 31, 673 (1980).
199. T. Tsuru, W. Shimokawa, S. Kobayashi, T. Inui, J. Met. Finish. Soc. Jpn. 28, 272 (1977).
200. C. J. Vance, T. Nguyen, US Patent 4721656 (Eltech. Systems Corp.), Prior. 17th September 1984; C. A. 105, 31921 s (1986).
201. K. J. Vetter, Chem. Ing. Tech. 35, 343 (1963).
202. C. Wagner, J. Electrochem. Soc. 98, 116 (1951).
203. M. A. Weisberg, Plating and Surface Finishing 75, 24 (1986).

204. A. Wildemann, E. Runge, Korrosionsschutz am Kraftfahrzeug, 2. Tagung, Haus der Technik, Essen (5th-6th March 1987).
205. WIRTSCHAFTSWOCHE (3.11.1989), p. 64, 65.
206. W. Wittich, R. Suchentrunk, H. Kellerer, Metall 30, 943 (1976).
207. L. F. Yntema, L. F. Audrieth, J. Am. Chem. Soc. 52, 2693 (1930).
208. M. Yoshio, Kinzoku Hyomen Gijutsu 37, 367 (1986).
209. M. Yoshio, Metal Finishing 85, 33 (1987).
210. M. Yoshio, N. Ishibashi, J. Appl. Electrochem. 3, 321 (1973).
211. M. Yoshio, M. Matsuyuki, I. Iwasawa, J. Met. Finish. Soc. Jpn. 26, 416 (1975).
212. K. Ziegler, Bull. Soc. Chim. France, 1456 (1963).
213. K. Ziegler, H. G. Gellert, H. Lehmkuhl, W. Pfohl, K. Zosel, Liebigs Ann. Chem. 629, 1 (1960).
214. K. Ziegler, R. Köster, Liebigs Ann. Chem. 608, 1 (1957).
215. K. Ziegler, R. Köster, H. Lehmkuhl, K. Reinert, Liebigs Ann. Chem. 629, 33 (1960).
216. K. Ziegler, F. Krupp, K. Zosel, Liebigs Ann. Chem. 629, 241 (1960).
217. K. Ziegler, H. Lehmkuhl, DE 1047450; Prior. 28th July 1954; C. A. 52, 19619 d (1958).
218. K. Ziegler, H. Lehmkuhl, Angew. Chem. 67, 424 (1955).
219. K. Ziegler, H. Lehmkuhl, DE 1056377, Prior. 13th June 1955; C. A. 52, 19619 d (1958).
220. K. Ziegler, H. Lehmkuhl, DE 1101772, Prior. 9th April 1956.
221. K. Ziegler, H. Lehmkuhl, Z. Anorg. Allg. Chem. 283, 414 (1956).
222. K. Ziegler, H. Lehmkuhl, US Patent 3775270, Prior. 4th January 1970; C. A. 75, 83574 (1971).
223. K. Ziegler, H. Lehmkuhl, W. Eisenbach, unpublished results (1961). – W. Eisenbach, Dissertation, Rheinisch-Westfälische Technische Hochschule, Aachen (1961).
224. K. Ziegler, H. Lehmkuhl, W. Grimme, DE 1114330, Prior. 6th May 1959; C. A. 56, 4524 (1962).
225. K. Ziegler, H. Lehmkuhl, W. Grimme, unpublished results (1960); W. Grimme, Dissertation, Rheinisch-Westfälische Technische Hochschule, Aachen (1960).
226. K. Ziegler, H. Lehmkuhl, W. Grimme, DE 1146258, Prior. 30th June 1961; C. A. 58, 13458 (1963).
227. K. Ziegler, H. Lehmkuhl, W. Grimme, DE 1144490, Prior. 9th May 1961; C. A. 58, 9880 (1963).
228. K. Ziegler, H. Lehmkuhl, E. Hüther, unpublished results (1957); E. Hüther, Dissertation, Rheinisch-Westfälische Technische Hochschule, Aachen (1957), p. 34.
229. K. Ziegler, H. Lehmkuhl, E. Lindner, unpublished results (1957); E. Lindner, Dissertation, Rheinisch-Westfälische Technische Hochschule, Aachen (1957).
230. K. Ziegler, H. Lehmkuhl, E. Lindner, Chem. Ber. 92, 2320 (1959).
231. K. Ziegler, H. Lehmkuhl, W. Pfohl, DE 1118782, Prior. 25th May 1955; C. A. 55, 3435 d (1961).
232. Y. Kato, S. Takahashi, US Patent 4747916 (Nisshin Steel Co.), Prior. 3rd September 1987; C. A. 110, 47386 (1987).
233. S. Mori, K. Ida, H. Suzuki, S. Takahashi, I. Saeki, Europ. Patent 0398358 (Mitsubishi Petrochem. Co.; Nisshin Steel Co.), Prior. 18th May 1989; 22nd June 1989; 28th July 1989; 18th October 1989; C. A. 114, 216779 (1991).
234. T. Tsuda, Kinzoku 60, 25 (1990); C. A. 113, 175938 (1990).
235. T. Tsuda, H. Seto, J. Uchida, Y. Yamamoto, T. Siota, N. Usuki, A. Shibuya, R. Noumi, ASEF 6th Continuous Strip Plating Symposium, Pittsburgh (May 1990).
236. M. Kondo, H. Maeda, M. Mizuguchi, J. Met. 42, 36 (1990); C. A. 114, 194632 (1991).
237. M. Koike, K. Sekimoto, Kinzoku 42, 77 (1972); C. A. 80, 43337 (1974).
238. E. Eckert, Dechema-Monographien, Vol. 125, VCH Verlagsgesellschaft, Weinheim (1992), p. 425.
239. W. Frömberg, Oberfläche Surface 3, 13 (1992).
240. W. Kautek, W. Frömberg, J. A. de Hek, Metalloberfläche 46, 2 (1992).
241. V. E. Arnold, DE 2012846 (US Energy Comm.) Prior. 24th March 1969; C. A. 74, 9096 (1971).
242. H. Lehmkuhl, K. Mehler, unpublished results (1992).

Advances in Electrochemical Science and Engineering
Edited by Heinz Gerischer and Charles W. Tobias

Index